SYNTHESIS, BONDING, AND REACTIVITY OF GROUP 15 AMIDES

by

Katherine M. Marczenko

Submitted in partial fulfillment of the requirements
for the degree of Doctor of Philosophy

at

Dalhousie University
Halifax, Nova Scotia
July 2021

Satisfaction of one's curiosity is one of the greatest sources of happiness in life.

-Linus Pauling

Contents

List of Tables

List of Figures

Abstract

This thesis discusses the effects of ligand design on the chemistry of heavy Group 15 elements. The correlation of molecular geometry with frontier molecular orbital energies is a well-known principal. This principle was exploited to systematically tune the frontier molecular orbitals in heavy Group 15 amides. The geometry of antimony and bismuth complexes tethered with a N,N,N-triamido ligand deviate from idealized pyramidal geometries and showed planar metal centers. These compounds were examined in the solid, solution, and gas-phase. Gas-phase calculations were used to assess the change in properties of the bismuth compound upon planarization, such as the lower LUMO energies, and increased Lewis acidity, for which both steric and electronic effects were examined.

A new class of antimony hydrides that participate in the first example of additive-free hydrostibanation of C≡C, C=C, C=O, and N=N bonds was developed. These hydrometallation reactions were unlocked through changing the geometry of the ligand, and consequently tuning the energy of the Frontier Molecular Orbitals (FMOs). The careful choice of a bis(silylamino)naphthalene ligand accomplished the desired outcome and provides a second example of frontier molecular orbital engineering in this work. Mechanistic studies suggest that hydrostibanation proceeds via a radical mechanism. Recycling of the stinbinyl hydride during the hydrostibanation of terminal alkynes to yield the Z-olefin product was also achieved.

A one-step, high yield synthesis of thermally-robust bismuthanylstibanes provided the first examples of neutral Bi–Sb σ-bonds in the solid-state. The reaction chemistry of the Bi–Sb bond was debuted by showing the insertion of a sulfur atom, providing the first documented example of a Bi–S–Sb bonding moiety. DFT calculations indicated that the bis(silylamino)naphthalene scaffold is particularly efficient in increasing interaction energies through a combination of inductive effects and dispersion donor effects, foreshadowing the use of this ligand in the isolation of other labile bonding environments, such as bismuth carbamates.

These studies reveal design rules for the rational pursuit of catalytically relevant systems, and seamlessly connect the realms of fundamental and applied chemistry.

List of Abbreviations Used

ADF	Amsterdam Density Functional.
AIM	Atoms in Molecules.
AO	Atomic Orbital.
B3LYP	Becke-3-Parameter Exchange and Lee-Yang-Parr Correlation Hybrid Functional.
BJ	Becke-Johnson.
CCDC	Cambridge Crystallographic Data Center.
COSMO	Conductor-like Screening Model.
CP	Cross-Polarization.
DFT	Density Functional Theory.
EDA	Energy Decomposition Analysis.
EXSY	Exchange Spectroscopy.
FIA	Fluoride Ion Affinity.
FMOs	Frontier Molecular Orbitals.
FT	Fourier Transform.
GEI	Global Electrophilicity Index.
HOMO	Highest Occupied Molecular Orbital.
HRMS	High-Resolution Mass Spectrometry.
IR	Infrared.
LCP	Ligand Close Packing.

LUMO	Lowest Unoccupied Molecular Orbital.
MAS	Magic Angle Spinning.
MEPS	Molecular Electrostatic Potential Surface.
MO	Molecular Orbital.
NBO	Natural Bond Order.
NMR	Nuclear Magnetic Resonance.
NOESY	Nuclear Overhauser Effect Spectroscopy.
PCM	Polarizable Continuum Model.
PES	Potential Energy Surface.
TD-DFT	Time-Dependent Density Functional Theory.
TEMPO	(2,2,6,6-Tetramethylpiperidin-1-yl)oxyl.
TMS	Trimethyl Silyl.
TZ2P	Triple-Zeta with Two Polarization Functions Basis Set.
TZVPD	Valence Triple-Zeta Polarization with Diffuse Functions.
UV-Vis	Ultraviolet Visible Spectroscopy.
VBT	Valence Bond Theory.
VSEPR	Valence Shell Electron Pair Repulsion.
VT	Variable Temperature.
WBI	Wiberg Bond Index.

Acknowledgements

I would like to thank my supervisor, Dr. Saurabh Chitnis, for his guidance and mentorship over the past three years. It has been a pleasure working together in this evolving research area.

I would also like to thank all past and present members of the Chitnis lab for their hard-work, dedication, and many contributions to the various research projects and lab chores. I would specifically like to thank Marcus Kindervater and Chloe Louise Johnson - two of the first Chitnis lab students - for helping with lab set-up and establishing a friendly lab environment.

I would like to acknowledge my committee members Dr. Erin Johnson, Dr. Laura Turculet, and Dr. Mark Stradiotto, for their time spent attending committee meetings, reading various documents, and for all the guidance they have provided throughout my time at Dalhousie. I would like to give a special thanks to Dr. Erin Johnson, for reviewing the introduction chapter of my thesis and providing guidance on DFT calculations.

I would like to thank Dr. David Langalaan (Biochemistry) for sharing his resources and support for X-ray crystallography; Dr. Mike Lumsden for his expertise in all things related to NMR spectroscopy; and Xaio Feng for always going above and beyond when it came to analyzing sensitive samples by HRMS!

I would like to thank Dr. Marc Whalen for his commitment to student education and providing an environment that allowed me to explore several aspects of chemistry pedagogy.

I would like to thank the members of the fourth floor of the chemistry department who offered support in the form of friendly faces who never failed to lend a helping hand.

A special thanks to my parents, who have always encouraged me to pursue what I love. A heart-felt thanks to my partner, Alex, for participating in discussions pertaining to my research and always offering kind words of love and support. Thank you.

Chapter 1

Introduction

A quickly-evolving area of main-group chemistry is the investigation into the syntheses, bonding properties and reactivity of low/mid-valent compounds featuring the heaviest of the main group elements (5^{th} and 6^{th} row).[1] These compounds have stark reactivity differences compared with their lighter counterparts, and often contain very reactive centers that exhibit properties typical of transition metals.[2] Isolating these reactive species involves a combination of kinetic stabilization through the use of sterically demanding ligands and thermodynamic stabilization via coordination of the central atoms by Lewis bases or acids.[3] The heavy Group 15 elements often form neutral, monomeric compounds with suitable choice of substituents, making them attractive in this field of chemistry.

1.1 Light and Higher-row p-Block Elements

The elements of the p-block were long considered to be very similar due to the structure and reactivity of known compounds. The isolation of new and "unusual" p-block compounds over the past few decades has changed that notion and highlighted stark differences between light (rows 1 and 2) and higher-row (rows 3–6) main-group elements.[45678] The ability to synthesize compounds that were previously thought to be unisolable points towards a different narrative; one where the first and second row elements can in fact be considered anomalous and the higher-row elements behave

as expected.[9] Many higher-row p-block elements behave in a fashion similar to that of transition-metal elements, which has been a topic of recent reviews.[101112]

1.1.1 General Properties

The most fundamental difference between the light (e.g. B, C, N, O) and higher-row main-group elements is the large jump ($\sim$%50) in the covalent radius between the second and third rows of the periodic table (principle quantum number 2 to 3).[13] The "size" of an atom has a direct impact on its reactivity, and the larger the distance of the valence electrons from the nucleus, the larger the covalent radius. This increase gives rise to hypervalent species when the principle quantum number of the central element is greater than or equal to 3.[1415] The *s*- and *p*-valence electrons in the second row atoms occupy roughly the same region of space, whereas *p*-type valence electrons in higher-row atoms are considerably more diffuse than the corresponding *s*-type Atomic Orbital (AO)s.[16] Extreme increases in diffuseness is observed in sixth row elements, which is a direct consequence of relativistic effects and has major consequences for the chemical behaviour of very heavy elements.[17]

To describe the difference in the valence of elements of the second and higher-rows (i.e. hypervalency), two different models have been proposed:

- The formation of three-center, four-electon bonds.[18]
- The involvement of d-AOs, leading to hybrids.[16]

A three-center, four-electron bond negates the requirement for an explicit hypervalent bonding description at the central atom and can be explained using Molecular Orbital (MO) theory (Figure 1.1) or Valence Bond Theory (VBT) (Figure 1.2). According to Figure 1.1, three MOs can be constructed as linear combinations of the *p*-valence AOs of the central atom and two external atoms. Bonding, nonbonding, and antibonding MOs result from the combination of three relevant atomic orbitals, with the four electrons occupying the bonding MO delocalized across all three centers and a nonbonding orbital. This effectively forms a bonding orbital that consists

of two two-center-one-electron bonds. VBT describes the bonding in a hypervalent molecule, such as XeF_2, as a resonance averaged combination of three ionic structures (Figure 1.2). In the case of XeF_2, this is described through the combination of XeF^+ σ-MOs and a fluoride lone pair. The F^- lone pair acts as a 2-electron donor, while the XeF^+ σ*-antibonding orbital acts as a 2-electron acceptor. Overall, VBT justifies this bonding situation as favourable because of the small ionization potential of the central Xe atom and the high electronegativity of the outer atoms.[9]

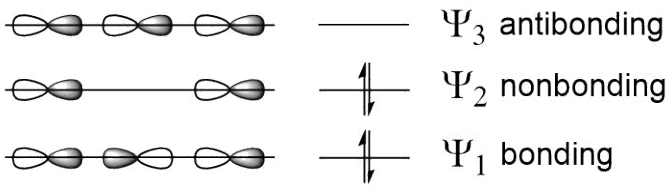

Figure 1.1: Molecular orbitals for a three-center four-electron σ-bond.

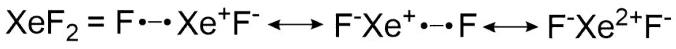

Figure 1.2: Valence bond theory explanation for the hypervalent bonding observed in XeF_2.

The other explanation for hypervalency in higher-row element compounds is the bonding contributions of *d*-orbitals. However, this is often wrongly stated as the reason why some higher-row element compounds are stable and isolable whereas others are not. Overall, Rundle's model (three-center, four-electron bond)[18] reflects the true situation more accurately than Pauling's model (e.g. sp^3d^n hybridization), because the population required by the hybridization model is in fact much lower.[16] Additionally, d-AOs are often involved in more complicated multi-center bonds, such as π-backbonding.[13] For example, the molecule PH_3F_2 is a known and stable compound whereas NH_3F_2 is not. The N–F bonds in the D_{3h} structure are very long and weak, presumably due to the small atomic radius of N and the inability to accommodate five atoms in its covalent shell (unlike phosphorous). The population of the *d*-AOs in $NH_3F_2(D_{3h})$ is negligible (0.05), whereas the population of the *d*-AOs in PH_3F_2 (D_{3h}) is more substantial (0.27).[19] However, the value of 0.27 is ultimately significantly lower than what's required by Pauling's sp^3d hybridization model (1-electron).

There are also stark geometric differences between the compounds of the elements of the second and higher rows, such as, the bond angles within the H_2E (E = O, S, Se, etc.) and EH_3 (E = N, P, As, etc.) class of compounds. The valence angles in H_2O and NH_3 are ca. 104°, whereas the angles in H_2S, H_2Se, PH_3, and AsH_3, are closer to 90°.[20] This is often understood as a result of hybridization, where *s*- and *p*-orbital sizes differ more dramatically progressing from NH_3 to PH_3 and higher-row element hydrides.[21] The poorer *s*- and *p*-orbital overlap decreases orbital mixing and hybridization, giving rise to 90° bond angles, characteristic of pure *p*-character. However, these geometric differences can also be explained using the Ligand Close Packing (LCP) model (Figure 1.3), which was introduced nearly 50 years after Valence Shell Electron Pair Repulsion (VSEPR) theory. Gillespie *et. al.* introduced the complimentary LCP theory (also abbreviated VSEPR-LCP) to explain almost all of the exceptions to the VSEPR model.[22] VSEPR-LCP attributes the observed 90° angles to inter-ligand repulsions, where the bond angles are determined by the "ligand radii" of the different E–H bonds involved. In this model, the lone pair of electrons take up as much space as possible, and it is the inter-ligand repulsions that are responsible for pushing the observed H–E–H angles out from 90°.[22] Unfortunately, the VSEPR-LCP model is not widely used today, although it is not clear why.[23]

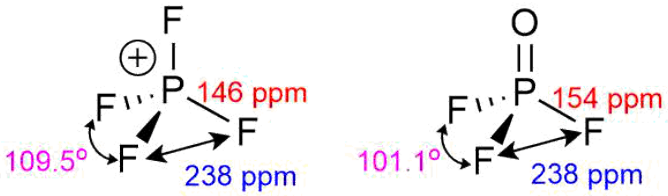

Figure 1.3: The molecular structures of PF_4^+ and PF_3O. The P-F-P bond angles are shown in pink; the F–F inter-ligand distance is shown in blue; and the P–F bond length is shown in red.The PF_4^+ ion has the VSEPR expected F–P–F bond angle of 109.5°, whereas the related PF_3O molecule has a smaller F–P–F bond angle of 101.1°. Despite these dramatic differences in bond angles, both molecules have identical F–F inter-ligand distances of 238pm.

Lastly, multiple bonding must be discussed in order to fully comprehend the differences between light and higher-row main-group elements. The strength of π-bonds is often incorrectly thought to decrease with higher rows of the periodic table.

An energy decomposition analysis was used to analyze the bonding contributions of Group 15 homonuclear diatomic molecules. This analysis demonstrated that an assumingly weak π-bond in multiple bonds between higher-row element molecules is not the reason they are much less stable than those of the first row of the periodic table (Table 1.1).[2] In fact, the small bond dissociation energy is the reason that sterically unprotected bonds often display high reactivity and low stability. The percentage contributions by ΔE_π to the orbital interactions in P_2, As_2, and Sb_2, are even slightly higher than in N_2, whereas the ΔE_π contribution in Bi_2 is slightly less than that in N_2. Ultimately, the contributions from electrostatic attraction to the bonding interactions in Sb_2 and Bi_2 is larger than the covalent bonding contributions, and the much stronger multiple bond of N_2 is caused by the relatively large σ-interactions, and not by a particularly strong π-interaction.

1.1.2 Comparison of p-Block Elements to Transition-metal Elements

The difficulty in stabilizing low-valent main-group compounds was often given as the reason main-group elements did not display reactivity analogous to that of transition-metal elements. The kinetic instability of the desired main-group compounds meant that open coordination sites and small Highest Occupied Molecular Orbital (HOMO)-Lowest Unoccupied Molecular Orbital (LUMO) gaps ($\leq$ 4eV) – two properties characteristic of transition-metal compounds – were hard to achieve.[11] It was eventually realized that extremely bulky ligands could prevent decomposition to oligomeric and polymeric derivatives, allowing for the isolation of several new classes of compounds that had energetically accessible frontier MOs.[6]

Multiple bonded higher-row main-group compounds were realized as one of these new classes that resemble transition-metal complexes because they contain energetically accessible frontier MOs.[247252627] These species have the potential to enable facile redox processes (i.e. oxidative addition, reductive elimination) through activation of small molecules and cleavage of strong σ-bonds. The first example of this was reported in 2005, when it was shown that a Ge alkyne analogue (Ar′GeGeAr′;

Term	$\mathbf{N_2}$	$\mathbf{P_2}$	$\mathbf{As_2}$	$\mathbf{Sb_2}$	$\mathbf{Bi_2}$
$\Delta\Delta E_{int}$	-240.2	-118.5	-97.3	-74.2	-64.6
$\Delta\Delta E_{Pauli}$	802.2	317.6	276.8	219.3	201.9
$\Delta\Delta E_{elstat}$	-312.8(30.0%)	-186.3(42.7%)	-181.5(48.5%)	-159.0(54.2%)	-50.8(56.6%)
$\Delta\Delta E_{orb}$	-729.6(70.0%)	-249.8(57.3%)	-192.7(51.5%)	-134.5(45.8%)	-43.2(37.4%)
$\Delta\Delta E_{\sigma}$	-478.7(65.6%)	-148.7(59.5%)	-116.2(60.3%)	-81.0(60.3%)	-72.4(62.6%)
$\Delta\Delta E_{\pi}$	-250.9(34.4%)	-101.1(40.5%)	-76.4(39.7%)	-53.4(39.7%)	-43.2(37.4%)

Table 1.1: Energy partitioning analysis (BP86/TZ2P) of the E–E bond in Group 15 homonuclear diatomics ($D_{\infty h}$). All energies are in kcal/mol. Reproduced from reference 2.

Ar′ = C_6H_3-2,6-$Dipp_2$, Dipp = C_6H_3-2,6-iPr_2) could split H_2 under ambient conditions to give the corresponding hydrogenated products via a synergistic interaction of FMOs.[28] Donation from the σ-orbital of H_2 into the LUMO of Ar′GeGeAr′ is accompanied by a synergistic electron donation from the π-HOMO orbital of the germanium species into the σ^*-orbital of H_2. This clearly demonstrates a mechanism of H_2 activation similar to that of transition-metal complexes. Since then, several other unsaturated higher-row main-group molecules have been shown to react with H_2 and other small molecules.[32930313233343536] The past two decades has seen an increase in main-group reactivity that mimics that of transition-metal complexes, including the development of Frustrated Lewis Pair chemistry for small molecule activation,[3337] Mg(I) compounds as soluble and selective reducing agents,[3839404142] homogeneous catalysis of group 2 elements,[43] and the stabilization of unusual low-valent or biradical p-block species.[44]

Many main-group research programs try to achieve catalytic redox cycling that is typically observed with precious transition-metal elements.[11] However, unlike transition-metals, reductive elimination at main-group elements is more challenging due to the high stability of the M^{n+2} state.[13] Organopnictogens are emerging as a class of compounds that readily cycle various oxidation states and are viable targets for catalytic redox cycles. As a recent review on this topic exists,[45] emphasis will be placed on organoantimony and organobismuth redox catalysis, which has been explored to a significantly lesser extent than that of the lighter elements.

Only one example of organo-antimony redox catalysis is currently known. Triphenylantimony dibromide was shown to catalytically oxidize α-hydroxyketones to α-diketones.[46] The same transformation can be achieved through the use of triphenylstibane as the catalyst under aerobic oxidation conditions (i.e. O_2) (Figure 1.4).[47] Interestingly, the analogous stoichiometric transformation with PPh_3 or $BiPh_3$ does not occur, presumably due to the chemical inertness of the P(V) and Bi(III) oxidation states.

Organobismuth redox catalysis is dominated by the inert pair effect, which makes oxidation from the +3 to +5 states very challenging.[13] The +1/+3 redox couple offers the opposite challenge, with reductive elimination being the most difficult step.

The first example of a catalytic cycle involving a Bi(I)/Bi(III) redox couple was unknown until recently.[48] Cornella *et. al.* demonstrated transfer-hydrogenation with ammonia-borane and a NCN-chelated Bi(I) catalyst that was originally synthesized by Dostál.[4950515253] This cycle presumably proceeds through an unstable Bi(III)-dihydride intermediate, although the only spectroscopic evidence of its formation was the detection of its protonated cation by High-Resolution Mass Spectrometry (HRMS). Cornella later demonstrated reductive deoxygenation of N_2O by the same NCN-chelated Bi(I) catalyst. The mechanistic pathway in this transformation is clearer, with an unstable Bi(III)-oxide serving as the catalytic intermediate.[54]

The first report of organopnictogen redox catalysis was surprisingly that of Barton *et. al.*, who reported the oxidative cleavage of α-glycols using triphenylbismuth and either N-bromosuccinidmide or tert-butyl hydrogen peroxide as a stoichiometric oxidant.[55] This transformation proceeded via a Bi(V) intermediate with catalyst loadings as low as 1%. Coles *et. al.* demonstrated radical-mediated organobismuth oxdiative coupling of TEMPO with phenylsilane (Figure 1.4). This transformation was accompanied by the loss of H_2 and was suspected to proceed via a Bi(III)-TEMPO radical oxidate and a Bi(III)-hydride. Earlier last year, Litchenberg *et. al.* reported a series of diorgano(bismuth)chalcogenides that underwent a similar transformation - namely the homogeneous photochemically-induced radical coupling of silanes with TEMPO.[56]

Cornella *et. al.* reported transition-metal like behaviour at a catalytically active bismuth center for the fluorination of aryl boronic esters via a redox cross-coupling reaction (Figure 1.4). The ligand framework utilized provided an intramolecular sulfoximine moiety as part of a bidentate diaryl ligand that stabilized the highly oxidizing +5 oxidation state.[57]

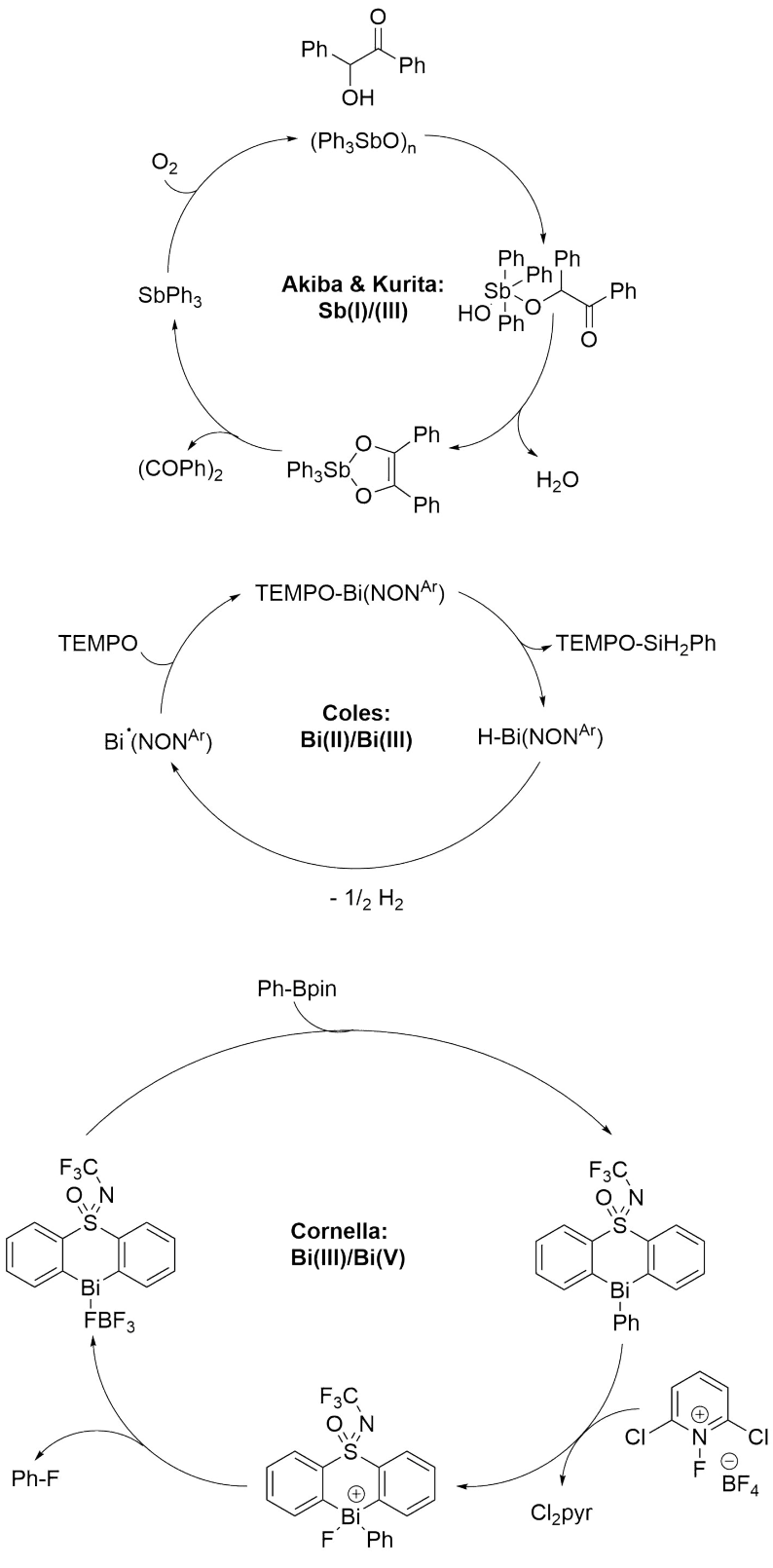

Figure 1.4: a) Sb(I)/(III) redox catalysis demonstrated by Akiba and Kurita. b) Bi(II)/Bi(III) redox catalysis demonstrated by Coles. c)Bi(III)/Bi(V) redox catalysis demonstrated by Cornella.

1.2 Heavy Group 15 Elements and Their Derivatives

1.2.1 Elemental Properties

The chemistry of antimony is much better explored than that of bismuth. Antimony is the fourth member of the pnictogen family and has a valence shell configuration of $5s^2 5p^3$. The chemistry of Sb is dominated by the +3 and +5 oxidation states; however, the -3 to +5 states are known. Sb(III) and Sb(V) often act as strong Lewis acids and display very weak Lewis base character.[585960]

Bismuth has a valence shell configuration of $6s^2 6p^3$ and is of particular interest because of its position as the heaviest nonradioactive element. Although there are numerous similarities between bismuth and its lighter counterparts, significant differences exist, arising from the low energy of the $6s^2$ electrons and the large coordination sphere of the metal.[17] Because the chemistry of bismuth is often dominated by relativistic and dispersion effects, it is a valuable element for testing predictions that cannot be tested using lighter elements that do no experience such electronic effects.[176162] The +5 oxidation state is found less often and is less stable for Bi than P, As, and Sb.[53] Its chemistry is therefore dominated by the +3 oxidation state, which demonstrates both Lewis acidity[63] and Lewis basicity.[64] Examples featuring oxidation states spanning –3 to +5 are known.[13]

1.2.2 Hydrides

Antimony hydrides have been studied more extensively than their bismuth counterparts.[65666768697071727374] Stibane, SbH_3, is an extremely toxic gas formed from the reaction of $SbCl_3$ and $NaBH_4$.[75] Dimerization with Sb–Sb bond formation and the release of H_2 is frequently observed for Sb–H compounds, including derivatives of R_2SbH, which yields distibanes R_2SbSbR_2 or metallic antimony.[76777879]

Me_2BiH and $MeBiH_2$ are formed from the reaction of the corresponding organobismuth halides with reducing agents such as $LiAlH_4$. Redox disproportionation at –45 °C gives bismuthane, BiH_3; a thermally unstable compound which decomposes above

–45 °C.[80] The only example of a room-temperature stable bismuth hydride, {2,6-$[C_6H_2(CH_3)_2]H_3C_6\}_2$BiH, was isolated through the use of bulky organic protecting groups (Figure 1.5).[81] No other molecular bismuth hydrides have been isolated, although such hydrides have been proposed as intermediates.[48828384]

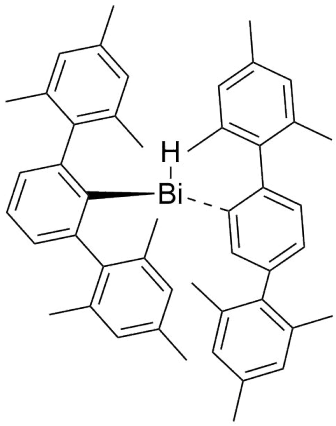

Figure 1.5: 2,6-$[C_6H_2(CH_3)_2]H_3C_6\}_2$BiH; the only known example of an isolable bismuth hydride.

1.2.3 Complexes with Group-15 Based Ligands

Many compounds where antimony is exclusively bonded to nitrogen atoms are known. Homoleptic tris-amido species, such as $Sb(NR_2)_3$, are formed through the reaction of $SbCl_3$ with secondary amines of alkali metal amides.[85] A limited number of Sb(V) amides have been prepared. The only known synthetic pathway towards such species is the conversion of Ph_3SbCl_2 to $Ph_3Sb(NMe_2)_2$. Neutral molecular compounds with Sb–P bonds are quite rare, but several anionic compounds have been reported.[86] Organophosphine-stabilized cationic antimony compounds have also been prepared.[87888990]

Bi(III) readily forms complexes with a wide range of nitrogen bases.[?91] Amido complexes of bismuth are often synthesized by the reaction of $BiCl_3$ with the appropriate lithium dialkyl amide.[92] Bismuth amides have evolved as useful reagents in C–H bond activation and reduction of carbon monoxide.[8293] The chemistry of bismuth with macrocyclic N-donor ligands is not extensive, but some compounds such as bismuth octaethylporphyrin nitrate[94] and bismuth tetraolylporphyrin nitrate[95]

have been prepared. Phosphines can also complex bismuth halides to form simple adducts.[9697]

1.3 Geometric Tuning

The physical and chemical properties of main-group compounds is in part dictated by the geometry and frontier molecular orbital arrangements of a molecule. VSEPR theory predicts and rationalizes the shapes (geometries) of molecules based on the electronic geometry (i.e. lone pairs on central atom, steric number).[20] Nevertheless, many exceptions to the model exist. The majority of the exceptions to the VSEPR model for molecules with non-metal central atoms can be explained if ligand-ligand respulsions, which are not explicitly considered in the VSEPR model, are taken into account.[22] Deviation from the VSEPR model is expected to give new electronic structures and reactivities, making strategic geometric tuning an attractive and emerging area of main-group chemistry.[98]

Pincer ligands bind tightly to coplanar sites, providing an inflexible ligand framework that allows for tuning of bond angles and effectively gives rise to non-VSEPR structures. Pincer complexes often show exceptional thermal stability, aiding high-temperature applications.[99] It has also been shown that many geometry-constrained compounds of p-block elements are capable of redox cycling catalysis.[100] This strategy has been exploited for accessing geometrically constrained Group 13, 14, and 15 compounds.

1.3.1 Geometry Constrained Group 13 Compounds

Group 13 complexes typically adopt a trigonal planar geometry. These complexes are typically Lewis acidic, with the degree of acidity being dependent on structure and the use of electronegative substituents. However, pincer ligands have been used to isolate "T-shaped" Group 13 compounds that are useful in exploring structure-reactivity relationships.[101]

Braunschweig *et. al.* isolated T-shaped AX_3 complexes through the coordination

of three transition metal atoms (Figure 1.6).[102] Metal-boron dative interactions and π-backbonding stabilized this unusual class of compounds. Martin *et. al.* utilized a triamido (NNN^{-3}) ligand to also give a T-shaped geometry at boron.[103] Other examples of geometrically distorting pincer ligands to give distorted T-shaped geometries at boron are present in the literature.[104]

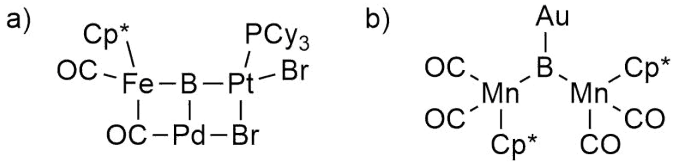

Figure 1.6: Non-VSEPR T-shaped boron compounds.

More recently, macrocyclic ligands have been employed to achieve geometrically constrained environments similar to what is observed with pincer ligands. In 2019, Greb *et. al* utilized a calix[4]pyrrole ligand to enforce a planar geometry at a tetracoordinate aluminum(III) anion (Figure 1.7).[105] Upon geometric deformation from VSEPR predicted T_d geometry to planar D_{4d} geometry, the LUMO energy dramatically decreased. The LUMO became localized at the central atom with almost pure *p*-character, giving rise to metal-centered Lewis acidity that unlocked bond activation reactions inaccessible to classical aluminate anions.[106][107]

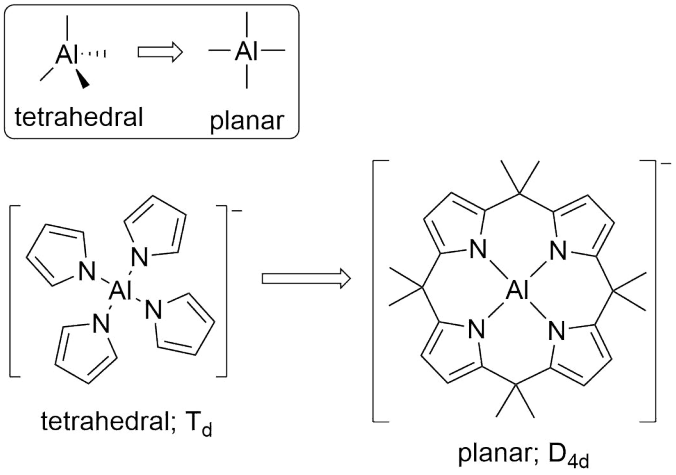

Figure 1.7: Geometric deformation from VSEPR predicted T_d geometry to planar D_{4d} geometry at an aluminum(III) anion.

1.3.2 Geometry Constrained Group 14 Compounds

Limited examples of geometrically constrained Group 14 compounds have been reported. Ardugeno *et al.* reported one of the first compounds in 1988; a discrete stannylene Sn(II) complex supported by a diketoimine-enolate (ONO^{-3}) ligand (Figure 1.8a). This discrete pseudo-trigonal-bipyramidal tin(II) species was amenable to oxidation by SO_2Cl_2 to give the corresponding Sn(IV) dichloride.[108] An analogous Ge(II) complex was postulated by Driess *et. al.*, although the presence of such an intermediate was only supported by secondary reaction products (Figure 1.8b).[109]

Recently, Greb and co-workers reported a variety of geometrically constrained Si(IV) compounds supported by triamido (NNN^{-3}) and amido diphenolato (ONO^{-3}) ligands (Figure 1.8c).[110][111] The monomeric derivatives show significant Lewis acidity at the silicon center due to distortions from tetrahedral towards planar geometries.[111] Roesky and co-workers isolated a geometrically constrained four coordinate chloro-stannylene stabilized by a chelating NCN ligand that was capable of activating P_4 under ambient conditions.[112] This provided a rare example of phosphorous activation by a Sn(I) compound at room temperature, mimicking reactivity typically observed for transition metal complexes.

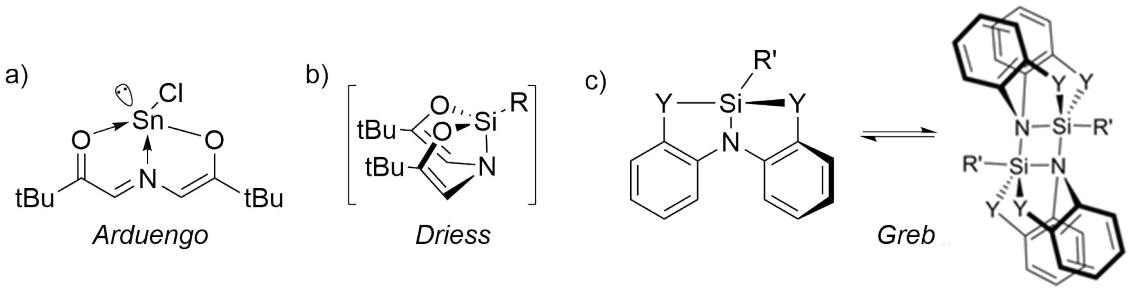

Figure 1.8: Geometrically constrained group 14 compounds based on the $HN[CH_2(O)TBu]_2$ ligand (a, b); geometrically constrained Si(IV)-NNN and -ONO compounds.

1.3.3 Geometry Constrained Group 15 Compounds

The use of pincer ligands in stabilizing geometrically constrained compounds is most prevalent for the Group 15 elements. As such, only key examples will be discussed,

and more emphasis will be placed on compounds containing a heavy Group 15 element as the central atom.

Arduengo and co-workers isolated the first 10-electron 3-coordinate pnictogen compounds (10–Pn–3 species); T-shaped pnictogen (P, As, Sb) complexes stabilized by a 5-aza-2,8-dioxa-3,7-di-*tert*-butyl-1-bicyclo[3.3.0]octa-3,6-diene ligand (ONO^{-3}).[113][114] The 10–Pn–3 designation is due to significant contribution of resonance form III (Figure 1.9)[115] to the overall electronic structure. Surprisingly, efforts towards the analogous bismuth complex gave a nine-coordinate 20-electron (20-Bi-9) complex.[116] Radosevich and co-workers later investigated the unusual electronic properties of 10–Pn–3 (Pn = P), which was shown to have significant electrophilic character at phosphorous - an uncommon property of tricoordinate phosphines.[117] This served as a platform for the catalytic reduction of azobenzene via a P(III)/P(V) redox cycle, and later the transition-metal like reactivity in N–H bond oxidative addition reactions.[118]

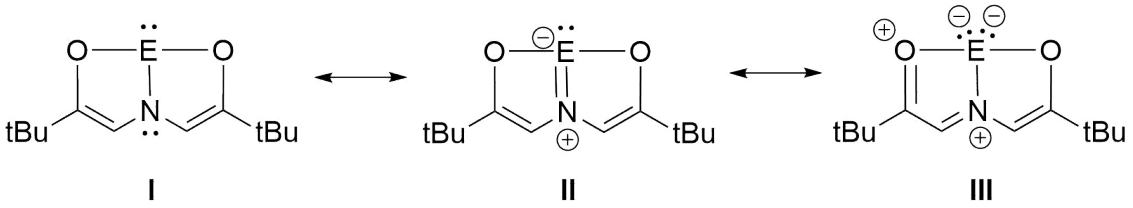

Figure 1.9: Resonance structures of Arduengo's 10–Pn–3 electron compounds (E = P, As, Sb).

In 2015, the research groups of Goicoechea and Aldridge reported a geometrically constrained phosphorous (III) compound using a N,N,-bis(3,5-di-tert-butyl-2-phenoxy)amine ligand.[119] The molecular structure differs from the planar geometry observed in the analogous 10–P–3 species, and instead contains C_s symmetry. The resulting complex is capable of activating the polar E–H bonds in water and ammonia; a desirable reaction for the transformation of inexpensive small molecules into value-added products. The ambiphilic nature of this P(III) compound was shown through reactions with both nucleophilic (^{t}BuOK) and electrophilic (MeOTf) substrates (Figure 1.10).[120]

The group of Wang reported on the synthesis and structures of a family of

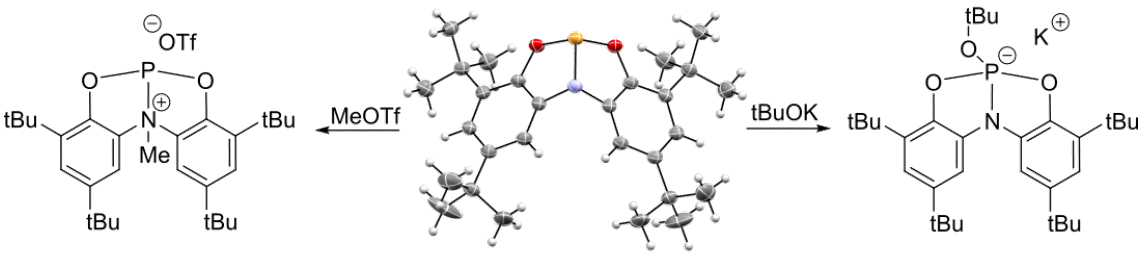

Figure 1.10: Single-crystal X-ray structure (thermal ellipsoids shown at 50% probability level) and reactivity of a geometrically constrained phosphorous (III) compound with a ONO-ligand towards nucleophilic (^{t}BuOK) and electrophilic (MeOTf) substrates.

10–Pn–3 molecules (Pn = P, As, Sb) with a tethered tris-amide ligand (Figure 1.11).[121] Importantly, the Bi derivative was not synthesized. Each compound has a planar T-shaped N_3 Pn core with shortened C–N bond lengths consistent with increased double bond character and the resonance structures shown in Figure 1.11. Reduction to the radical anions was accomplished using potassium in the presence of 2,2,2-cryptand.

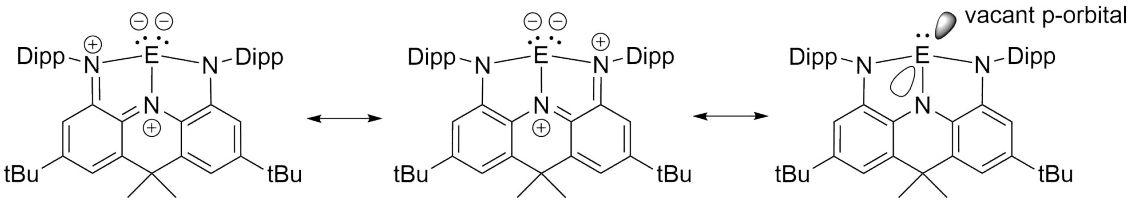

Figure 1.11: Resonance structures of the nontrigonal pnictogen compounds isolated by Wang *et. al.* (E = P, As, Sb).

In 2019, the Chitnis group reported on the synthesis of a redox confused Bismuth(I/III) triamide with a T-shaped planar ground state.[122] Its isolation was permitted through the use of a tethered triamide ligand, and its ambiphilic behaviour was demonstrated by coordination with an electrophilic (WCO_5) and nucleophilic (pyridine *N*-oxide) substrate.

Dostál and coworkers utilized a bulky N,C,N-chelating ligand to stabilize monomeric stibinidenes Sb(I) and bismuthinidenes Bi(I).[50] They were synthesize from the respective E(III) dichlorides that underwent reaction with K[B-(^{s}Bu)$_3$H] to form the

corresponding E(III) dihydride intermediates (E = Sb, Bi). These intermediates were susceptible to spontaneous reductive elimination of dihydrogen, yielding the targeted stibinidenes and bismuthinides. Dostál later achieved reversible C=C activation using the Sb(I) compound via a Sb(I)/Sb(III) redox couple (Figure 1.12).[123] As mentioned in section 1.1.2, Cornella later used the Bi(I) compound to catalyze the hydrogenation of azoarenes and nitroarenes using ammonia-borane.[48] It is worth emphasizing the importance in careful tuning of the constraining ligand to enable facile redox catalysis. The Cornella group demonstrated this with bismuth catalysts based on the tethered bis-anionic aryl ligands (Section 1.1.2, Figure 1.4).[5754] The tethered ligand assisted in stabilizing the geometry of the pentavalent intermediate by reducing the pseudorotational behaviour. The sulfonyl/sulfoximine group in the ligand backbone provided stabilizing Bi—O/N interactions for the Bi(V) intermediates.

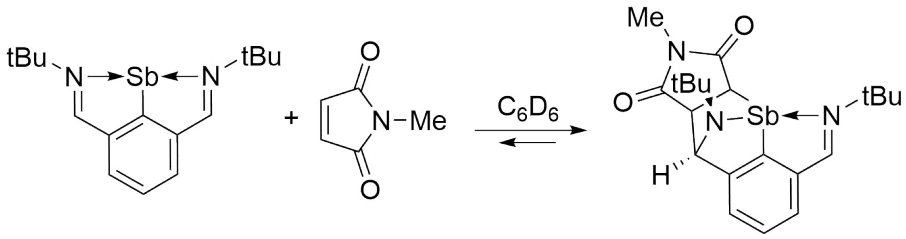

Figure 1.12: Stibinidene prepared by Dostál *et. al.* that is capable of reversible C=C bond activation through the reaction with methyl-maleimide.

1.4 Thesis Goals

The overall goal of this research is to extend and deepen our knowledge of the fundamental chemistry of antimony and bismuth. This was accomplished by examining the effects of ligand design on the structure and reactivity of higher-row Group 15 amides. These studies revealed reactivity patterns that contrast their lighter Group 15 counterparts, and complement what is typically observed with boranes.

Expanding on the principle publication by the Chitnis group, which documented the first example of a planar bismuth amide, Chapter 2 comprises a systematic

study that investigates periodic trends within a class of Group 15 amides, with the overarching goal of understanding how structure modulates reactivity at heavy centers. Antimony and bismuth centers constrained with a N,N,N-triamido ligand display significant Lewis acidity that is not observed with their lighter counterparts. The observed Lewis acidity is comparable to what is commonly seen with boranes - prototypical main-group Lewis acids that contain a vacant p-orbital perpendicular to the central atom. We subsequently sought to establish several pieces of work that contrast the Lewis acidity, and therefore the reactivity of boranes, stibanes, and bismuthanes.

First, we examined the effects of ligand design on the Lewis acidity of a planar bismuth triamide. The Lewis acidity of these bismuth Lewis acids was evaluated through a combination of experimental and computational methods. This work provides users with a framework to systematically tune the Lewis acidity of bismuth Lewis acids, and a quantitative comparison of the strength of boron and bismuth Lewis acids.

We then aimed to impart reactivity that is classical of lighter p-block elements at heavy Group 15 centers. The frontier molecular orbital energies of a new class of stibanes was tuned to achieve additive-free hydrostibination. The electrophilicity of the stibane is central to engaging unsaturated substrates. In a fashion complementary to hydroboration, anti-Markovnikov addition across a C≡C bond yields z-olefins. We explored the mechanism of this novel reaction and its use in the stoichiometric synthesis of z-olefins.

The last goal of this work was to create new and novel bonding at heavy Group 15 centers. Despite the isolation of a double bond between antimony and bismuth several decades ago, a single bond had yet to be isolated. Efforts towards isolating such a bonding motif, a bismuthanylstibane, were successful utilizing the napthyldiamino ligand framework. We were also successful in utilizing this ligand framework to isolate bismuth carbamates.

To summarize, the main objective of this report is to discuss the effects of ligand design on the chemistry of higher-row Group 15 elements, specifically antimony

and bismuth. Frontier molecular orbital engineering through strategic geometry deformation, developing new modes of reactivity, and achieving new bonding environments are the underlying themes of this report. These studies will reveal the design rules for rational pursuit of catalytically relevant systems.

Chapter 2

Investigations into the Structure, Bonding, and Reactivity of Group 15 Complexes Bearing a Geometry-Constraining Triamide Ligand

Portions of this work have appeared in **K. M. Marczenko**, J. A. Zurakowski,† M. B. Kindervater, S. Jee,† T. Hynes,† N. Roberts,† S. Park,† U. Werner-Zwanziger, M. Lumsden, D. N. Langelaan, S. S. Chitnis, *Chem. Eur. J.*, **2019**, 25, 8865-8874 (Full Paper; DOI: 10.1002/chem.201904361).

Contributions to the manuscript: KMM completed most of the experimental synthesis, all the X-ray crystallography, and some computational work. SSC completed most of the computational work and some experimental synthesis. KMM and JAZ completed NMR studies. JAZ and MKB completed UV-Vis spectroscopy studies. SJ conducted reactivity studies. TH, NR, and SP contributed to ligand synthesis. UWZ completed SS-NMR studies. ML provided input on 2D-NMR experiments. DNL provided access to a diffractometer. SSC supervised the project and wrote the manuscript. † denotes undergraduate author.

2.1 Introduction

A significant goal of electronic structure tuning in main group chemistry is the search for bond activation and catalysis that is similar to transition metals. Several recent examples demonstrate that tridentate ligands can distort classical VSEPR structures by creating a planar environment around the central element. Dutton and Martin used tethered triamide ligands to imposed a T-shaped planar geometry at boron (Figure 2.1).[104] Greb achieved a severely distorted tetrahedral arrangement at silicon that demonstrated novel dimerization modes (Figure 2.1).[110111] Other members of the Chitnis group recently showcased a bismuth complex of a triamide pincer ligand that has a planar geometry around Bi.[122] This compound displayed reactivity patterns of both Bi(I) and Bi(III) oxidation states. Importantly, a closely related phosphorus analogue (R = Me) was shown to be bent (Figure 2.1).[117] Tridentate-ligand bound planar Bi(I) compounds have recently emerged as catalysts in work by Cornella,[48] which demonstrates the importance of orbital engineering with pincer ligands to provoke nonclassical reactivity.

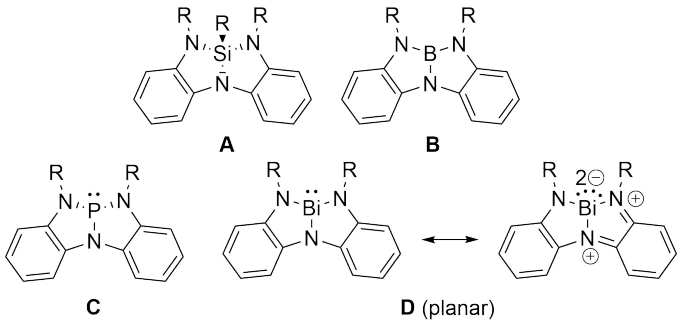

Figure 2.1: Select examples of main group elements within geometry-confining tridentate pincer ligands.

The literature currently contains several different classes of ligands that impose non-VSEPR geometries at various element centres; however, most of the efforts have focused on the lighter elements (B, Si, P, Al).[104111113110124] We decided that a systematic study examining how a geometry-constraining ligand changes the structure, electronics, and reactivity at the central element within a periodic group would be instructive. For this work, experimental data for novel complexes (E = Sb, Bi) will be discussed, and theoretical calculations involving the entire group are presented.

2.2 Results and Discussion

Lithiation of the triamide ligand followed by quenching with $SbCl_3$ failed to form compound **2.1-Sb** and instead led to reaction mixtures from which no pure material could be isolated. Instead, an aminolysis reaction between $Sb(NMe_2)_3$ and the triamide ligand afforded compound **2.1-Sb** in 67% yield (Figure 2.2a). As shown later, this compound is dimeric in the solid-state (**2.1-Sbdim**) and monomeric in solution (Figure 2.2b). Ligand coordination is a common strategy used to stabilize monomeric analogues of otherwise multimeric heavy main group element compounds.[125] We used this strategy to trap monomeric **2.1-Sb** in the solid-state. Repeating the aminolysis reaction in a sealed flask and cooling the resulting reaction mixture yielded the bis-dimethylamine adduct **2.1-Sb-(dma)$_2$**. This species is fragile and susceptible to amine loss under a stream of nitrogen or under vacuum to give dimeric, **2.1-Sb$_{dim}$**. Because of the volatile nature of the coordinated amines, no reproducible spectroscopic analysis could be performed on samples of **2.1-Sb-(dma)$_2$**. Compounds **2.1-Sb**, **2.1-Bi and 2.1-Sb-(dma)$_2$** are air-sensitive but stable under an atmosphere of dry nitrogen as solids and in hydrocarbon solutions. They decompose in halogenated solvents over a span of a few days.

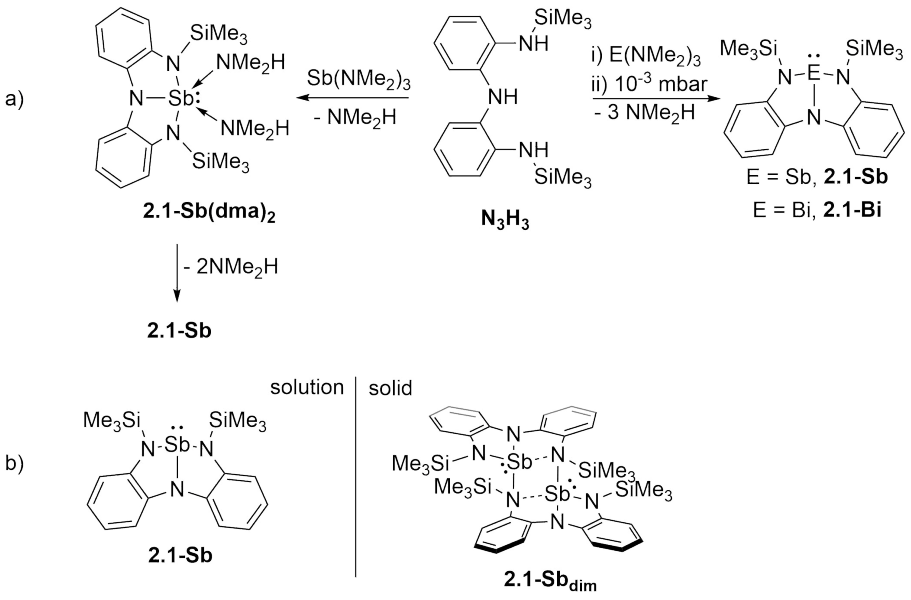

Figure 2.2: (a) Synthesis of compounds **2.1-Sb**, **2.1-Sb-(dma)$_2$**, and **2.1-Bi**, and (b) structure of **2.1-Sb** in solution and the solid-state.

2.2.1 Solid-State Structures

Solid-state Cross-Polarization (CP) Magic Angle Spinning (MAS) Nuclear Magnetic Resonance (NMR) spectroscopy and single-crystal X-ray diffraction were used to study the structures of compounds **2.1-Sb**, **2.1-Bi**, and **2.1-Sb-(dma)$_2$** in the solid-state (Figure 2.3). Compound **2.1-Bi** is monomeric, while single-crystal X-ray diffraction revealed that **2.1-Sb** is dimeric in the solid-state (**2.1-Sb$_{dim}$**) with two tetracoordinate antimony centers within a centrosymmetric molecule. Two modified monomeric units are horizontally displaced with respect to each other, forming Sb_2N_2 rings as the central motif (N–Sb–N angle 80.55°). The coordination geometry around Sb is best described as distorted seesaw with the outer N–Sb bonds occpuying the axial positions. The inversion center lies in the center of the planar Sb_2N_2 ring. The shortest Sb–N bonds involve the Sb–N1 (2.053(5) Å), Sb–N2 (2.075(4) Å), and Sb–N3' (2.136(5) Å) atoms, whereas the Sb–N3 distnce (2.633(4) Å) is significantly elongated. Thus, compound **2.1-Sb** is best described as an extended dinuclear compound, featuring bent Sb centers engaged in two intramolecular dative interactions rather than a donor-acceptor dimer assembled by dative interaction between two plaran SbN_3 cores. Such dimerization has also been observed by Greb with silicon analogues of constrained triamides, although in the silane case, the central rather than external nitrogen atoms acts as the bridging site.[110] The ^{13}C CP/MAS NMR spectrum of solid **2.1-Sb$_{dim}$** is consistent with its low symmetry and showed a complex superposition of lines arising from 12 independent aromatic carbon atoms per dinuclear molecule and the presence of two independent molecules in the unit cell (Figure A.11). In contrast, the ^{13}C CP/MAS NMR spectrum of solid **2.1-Bi** is expectedly very simple due to the twofold symmetry and a single independent molecule in the unit cell (Figure A.12).

Compound **2.1-Sb(dma)$_2$** represents a ligand-stabilized version of monomeric **2.1-Sb** and its formation is understood in terms of the metal-centered LUMO of **2.1$_{dim}$** (Figure A.14) being antibonding with respect to the Sb-N3' bond and the LUMO of the hypothetical monomer **2.1-Sb** being a p-type orbital at a planar antimony center. Consequently, the N_3Sb core involving the tridentate ligand in **2.1(dma)$_2$** is also planar (179.10(1)°), providing the first example of planar Lewis

acidity at neutral Sb(III) centers, which generally coordinate Lewis bases through Sb–X σ*-antibonding orbitals around a pyramidal SbX_3 molecule. The Sb–N1 bond length in **2.1-Sb(dma)$_2$** (2.069(2) Å) is essentially unchanged from its value in **2.1-Sb$_{dim}$** whereas the Sb–N2/3 lengths are comparable to the Sb–N2 length in **2.1-Sb$_{dim}$**, and nearly 0.5 Åshorter than the value for Sb–N3 in the dimer (Figure 2.3a/b).

Analogous phosphorus and arsenic derivatives were shown to be monomeric in the solid-state.[126117] These lighter derivatives adopt bent configurations around the central pnictogen, whereas **2.1-Bi** is planar (Figure 2.3c). Although monomeric planar **2.1-Sb** could not be isolated, the planar core of **2.1-Sb-(dma)$_2$** provides a model for the expected monomeric structure of **2.1-Sb** in the solid-state.

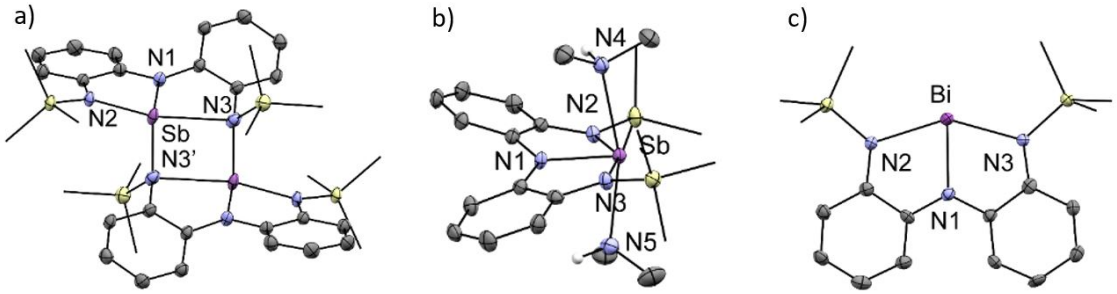

Figure 2.3: Views of the solid-state molecular structure of **2.1-Sb$_{dim}$** (a), **2.1-Sb-(dma)2** (b), and **2.1-Bi** (c). Nonessential hydrogen atoms have been omitted, and the silane groups are shown in wireframe for clarity. Thermal ellipsoids are drawn at the 50% probability level.

2.2.2 Solution-Phase Structures

The ^{1}H NMR spectra of **2.1-Sb** and **2.1-Bi** at 298 K in C_6D_6 exhibit four resonances in the aromatic region and a single resonance for the $SiMe_3$ group. Although this description is expected for **2.1-Bi** based on its C_2-symmetric solid-phase structure, it is inconsistent with the dimeric structure of **2.1-Sb** observed through X-ray crystallography and CP/MAS NMR spectroscopy. A Variable Temperature (VT) ^{1}H NMR study was used to understand the solution phase dynamics of **2.1-Sb** and **2.1-Bi**.

Upon cooling to 193 K in toluene-d_8, the ^{1}H NMR spectrum of **2.1-Bi** showed no

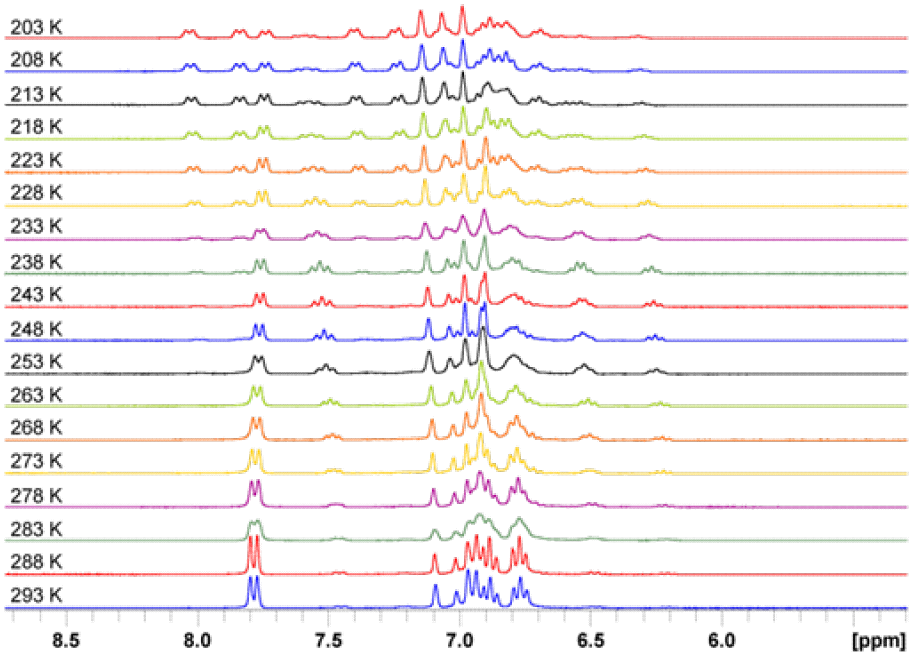

Figure 2.4: Variable temperature ^{1}H NMR spectra (aromatic region) for **2.1-Sb$_{dim}$**.

change in its spectrum suggesting a lack of monomer-dimer equilibria on the NMR timescale.[122] In contrast, the ^{1}H NMR spectrum of redissolved crystals of **2.1-Sb$_{dim}$** showed three species upon cooling, with the composition of the sample varying as a function of temperature (Figure 2.4, 2.5). The lack of signal decoalescence as a function of temperature, together with the appearance and disappearance of distinct signals upon cooling, allowed us to rule out a dynamic side-to-side motion in **2.1-Sb$_{dim}$** as the origin of the highly symmetric resonances observed at room temperature. Instead, the appearance of only four aromatic resonances at room temperature in solution is likely due to the conversion of formally covalent bonds to dative bonds, followed by dissociation to give a symmetric planar monomeric form (Figure 2.6). We propose temperature-dependent equilibria involving **2.1-Sb**, **2.1-Sb$_{dim}$**, and **2.1-Sb$_{dim}$'** rather than an intermediate-free "side-to-side" dynamic process. Exchange Spectroscopy (EXSY) (Figure A.9) produced cross peaks between the Trimethyl Silyl (TMS) protons of **2.1-Sb** and **2.1-Sb$_{dim}$**, also confirming an equilibrium process. A Nuclear Overhauser Effect Spectroscopy (NOESY) experiment of **2.1-Sb$_{dim}$** at 208 K confirmed the spatial proximity of one set of Si(CH$_3$)$_3$ protons to the aromatic protons *ortho* to the central nitrogen atom (Figure A.10), and the spatial proximity of the other set of Si(CH$_3$)$_3$ protons to the aromatic protons ortho

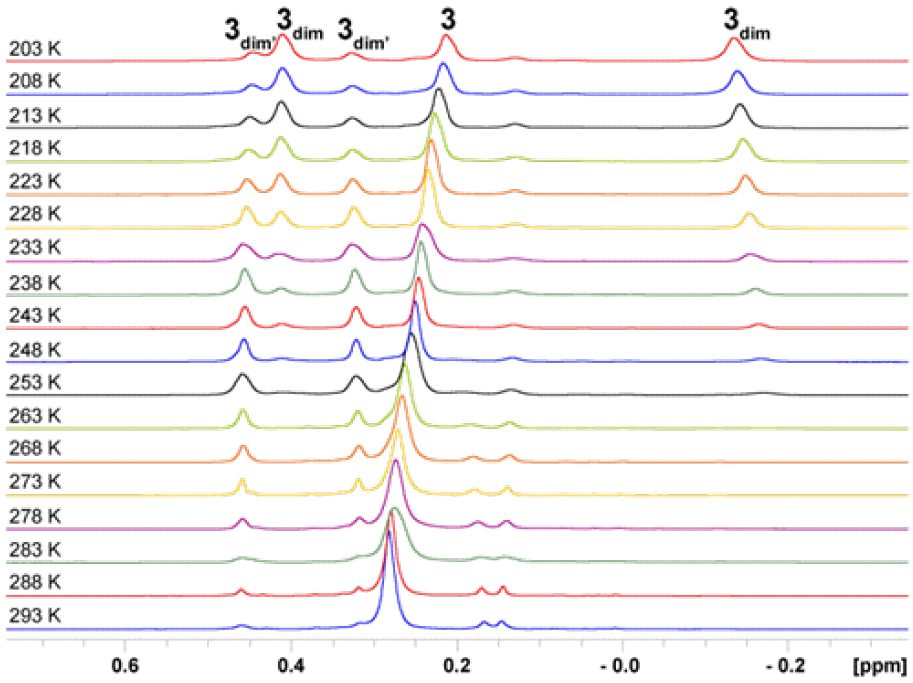

Figure 2.5: Variable temperature ^{1}H NMR spectra (TMS region) for **2.1-Sb$_{dim}$** ("**2.1-Sb**" abbreviated as "3" for space constraints).

to the external nitrogen atoms. The $Si(CH_3)_3$ signal assigned to monomeric **2.1-Sb** does not show proximity to the protons ortho to the central nitrogen atoms.

Conversion of the observed intensities to mole fractions (Figure 2.7) and construction of a van't Hoff plot (Figure 2.8) yielded thermodynamic parameters associated with the monomer-dimer equilibria (Table A.1). Our proposed sequence of events agrees with these parameters. Dimerization of **2.1-Sb** to give **2.1-Sb$_{dim'}$**, and the rearrangement of **2.1-Sb$_{dim'}$** to **2.1-Sb$_{dim}$** shows a sizeable negative entropy change. The reversible formation of covalent N–Sb bonds studied in these experiments provide rare quantitative thermodynamic data for dynamic covalent chemistry involving antimony centres.[123]

Further insight into the solution phase structures was obtained by comparison of the experimental and Time-Dependent Density Functional Theory (TD-DFT) calculated Ultraviolet Visible Spectroscopy (UV-Vis) spectra of compounds **2.1-Sb** and **2.1-Bi** (Figure 2.9). At 298 K, the spectra of **2.1-Sb** and **2.1-Bi** in pentane exhibit two absorptions in the visible range, and their relative positions agree with

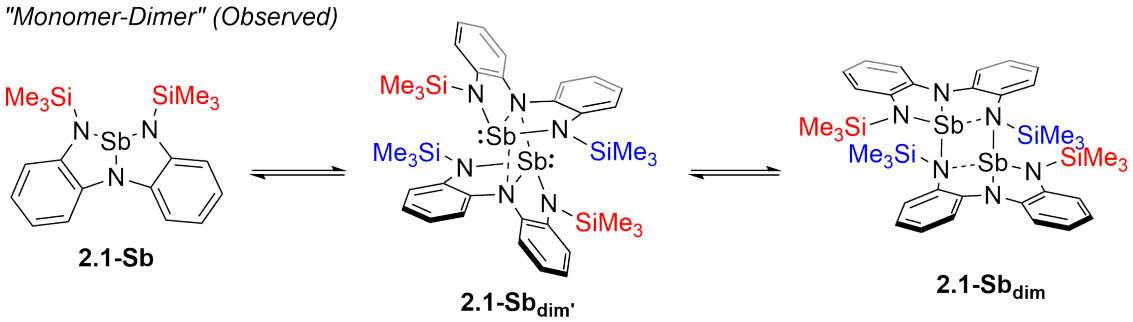

Figure 2.6: Proposed equilibria between **2.1-Sb**, **2.1-Sb$_{\mathbf{dim}}$'**, and **2.1-Sb$_{\mathbf{dim}}$** (top). Equilibria explaining a potential "side-to-side" motion between **2.1-Sb$_{\mathbf{dim*}}$** and **2.1-Sb$_{\mathbf{dim}}$** that was ruled out experimentally (bottom).

TD-DFT predictions for the monomeric planar forms. The calculated spectra for monomeric bent models or dimers **2.1-Sb$_{\mathbf{dim}}$** and hypothetical **2.1-Bi$_{\mathbf{dim}}$** differ significantly. Cooling a solution of **2.1-Sb** in pentane to 193 K (Figure 2.10), gave experimental data that is in agreement with conclusions from NMR spectroscopy that upon cooling a solution of **2.1-Sb** appreciable amounts of **2.1-Sb$_{\mathbf{dim}}$'** (calculated $\lambda_{max} = 407$ nm from TD-DFT) or **2.1-Sb$_{\mathbf{dim}}$** (calculated $\lambda_{max} = 395$ nm from TD-DFT) are formed. Thermodynamic parameters could not be obtained quantitatively from UV-VIS spectra due to substantial overlap between absorbance maxima for the three species.

To summarize, **2.1-Sb** exists as one planar monomeric and two dimeric species in solution, with the planar monomeric species being dominant at 298 K. Upon cooling, this species dimerizes first via weak dative bonds to give dimer **2.1-Sb$_{\mathbf{dim}}$'**, which subsequently rearranges to the more strongly bound (via covalent bonds) bent

form **2.1-Sb$_{dim}$** at the lowest temperatures studied. Crystallographic studies at 100 K show only the **2.1-Sb$_{dim}$** form. Compound **2.1-Bi** exists as a planar monomer in solution and solid states and shows no temperature-dependent dynamics. This diversity led to the investigation of the underlying electronic causes through Density Functional Theory (DFT) calculations.

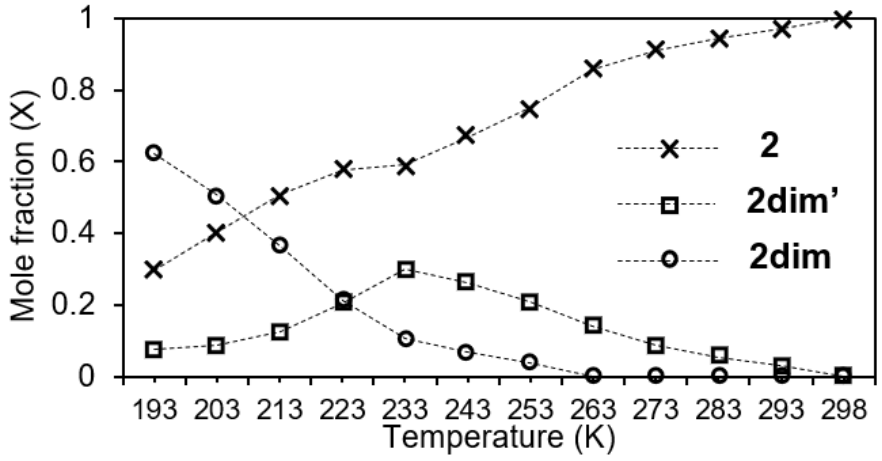

Figure 2.7: Mole fractions of **2.1-Sb**, **2.1-Sb$_{dim'}$**, and **2.1-Sb$_{dim}$** in a toluene-d_8 solution as a function of temperature.

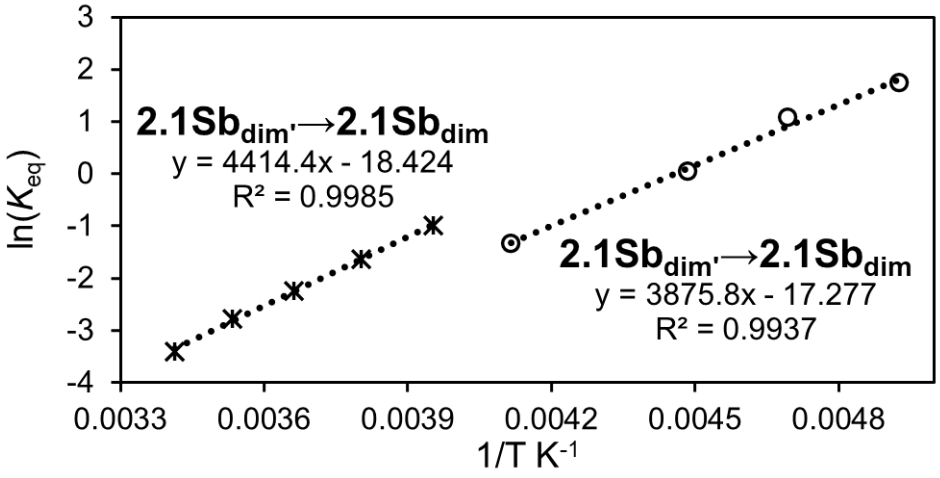

Figure 2.8: van't Hoff plot constructed with the mole fraction data.

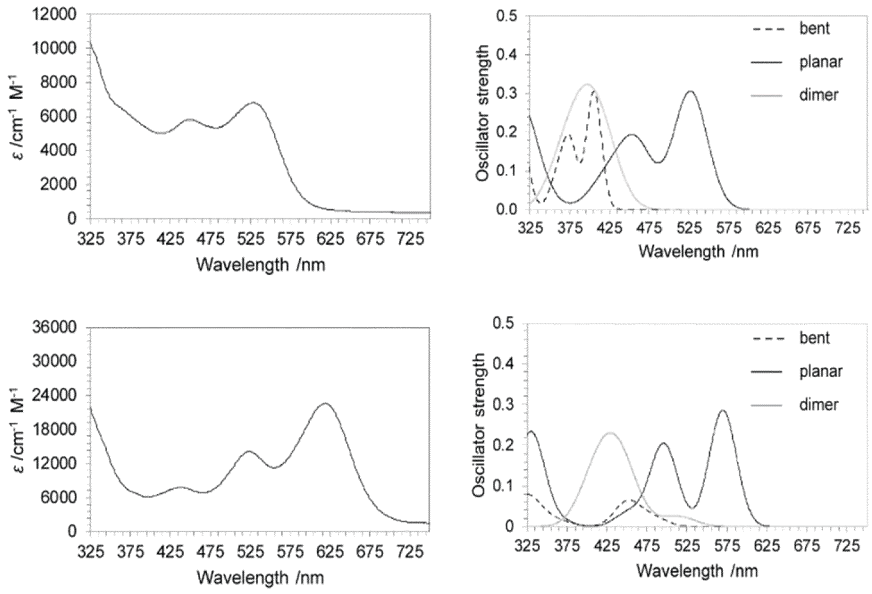

Figure 2.9: Experimental (left) and calculated (right) UV-Vis spectra of **2.1-Sb** (top) and **2.1-Bi** (bottom) in pentane at 298 K.

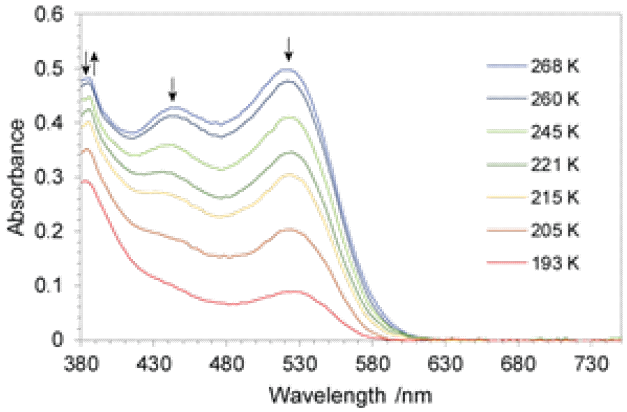

Figure 2.10: Variable temperature UV-Vis spectra of **2.1-Sb** in pentane. Bands assigned to the planar monomeric form decrease in intensity with temperature.

2.2.3 Gas-Phase Structures

The monomeric forms of compounds **2.1-P**, **2.1-As**, **2.1-Sb**, **2.1-Bi** were first considered, for which the optimized ground-state geometries are shown in Figure 2.11. Comparison of the calculated bond lengths and angles with the available structural data show good agreement with experimental lengths being within 0.05 Å.The optimized structures of monomeric **2.1-Sb** and **2.1-Bi** are planar with C_2 symmetry. Comparing the same bond length and angle parameters in monomeric **2.1-Sb** with the structure of **2.1-Sb-(dma)$_2$** showed minimal deviation. This suggests that despite the coordination of two ligands, **2.1-Sb-(dma)$_2$** provides an accurate model for the otherwise unisolable monomeric, planar **2.1-Sb**. The optimized ground state geometries for the monomeric forms of the phosphorus, PN_3TMS_2 (**2.1-P**), and arsenic, AsN_2TMS_2 (**2.1-As**), analogues were also computed. The calculations agree with crystallographic results[126] and reproduce a bent, rather than planar geometry, as the most stable configuration of **2.1-P** and **2.1-As**.

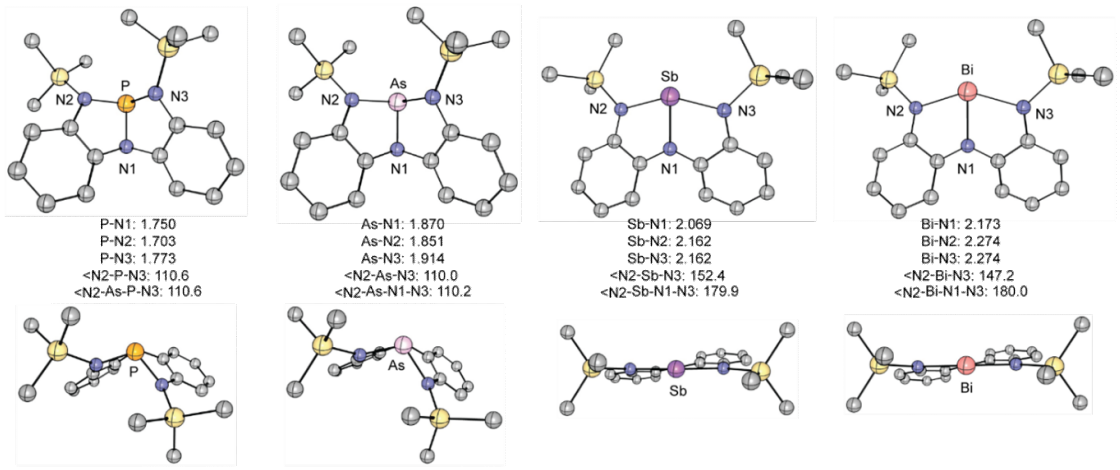

Figure 2.11: Calculated minima and selected metric parameters for the optimized structures of EN_3TMS_2 (E = P, As, Sb, Bi) at the PBE0-D3/def2-Valence Triple-Zeta Polarization with Diffuse Functions (TZVPD) level. Hydrogen atoms have been omitted for clarity.

Plots of the electron-density gradients within the two distinct EN_2C_2 rings for each compound (Figure A.16) are suggestive of a bonding situation where one of the rings expresses N-heterocyclic pnictenium cation like features - high planarity and high ellipticity (ϵ) at the E–N3 bond critical point (bcp) - whereas the other ring

contains an anionic amido substituent and exhibits reduced planarity and low ϵ at the E_2N_2 bcp. For example, the ellipticity at the P–N3 bcp is 0.21 and comparable to the value for the P–N1 bcp (0.19), but ϵ for the P–N2 bcp is only 0.06. The ring comprised of P–N1–C–C–N2 atoms is consistently substantially planar compared to the ring comprised of the P–N1–C–C–N3 atoms. This partial phosphenium-like character results in high P–N bond polarity,and is fully consistent with the reported facility of P–N bond heterolysis in analogues of **2.1-P**.[127]

The Natural Bond Order (NBO) and Atoms in Molecules (AIM) analyses for **2.1-Sb** and **2.1-Bi** support the more ionic E–N bonding in these compounds, which leads to lower values for the Wiberg Bond Index (WBI)s for E–N bonds (E = Sb, Bi) (Figure A.17). The ellipticity at the E–N2 and E–N3 bcps are on average higher than those found in **2.1-P** and **2.1-As** (0.19 for E = Sb, 0.18 for E = Bi) and the ϵ at the E–N1 bcps are the highest amongst all calculated values (0.25 for E =Sb, 0.23 for E= Bi). These data indicate greater *p*-delocalization over the planar heteroatom framework in **2.1-Sb** and **2.1-Bi** than in **2.1-P** and **2.1-As**.The NBOs of **2.1-Sb$_{\mathbf{dim}}$** support the presence of three covalent N–Sb bonds in a bent arrangement and one dative N—Sb bond with the WBI for the latter (0.16) being significantly smaller than the values for the former (0.44–0.54).

We then used an Energy Decomposition Analysis (EDA) scheme to investigate this system. This is a quantitative interpretation of bonding that allows the instantaneous interaction energy between two fragments to be expressed in three major terms: Pauli repulsion (ΔE_{Pauli}), orbital (ΔE_{orb}, i.e. covalent) interactions, and electrostatic (ΔE_{Elstat}, i.e. ionic) interactions (Figure 2.12). The sum of these terms is the interaction energy (ΔE_{int}) which is not experimentally observable as it is based on the fragments being frozen in the same geometry that they held in the full molecule (Figure 2.11; A* and B*). The classical bond dissociation energy (D_e) allows for relaxation of fragments to their equilibrium geometries and is an experimentally observable. The advantage of considering ΔE_{int} is that it reduces bonding down to purely electronic factors enabling easier comparison without contamination from fragment deformation energies (ΔE_{prep}). The $\Delta\Delta E$ values in Table 2.1 repre-

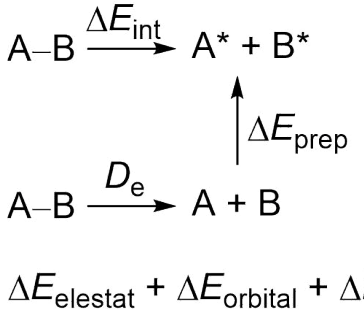

$$\Delta E_{\text{int}} = \Delta E_{\text{elestat}} + \Delta E_{\text{orbital}} + \Delta E_{\text{Pauli}}$$

Figure 2.12: Energy decomposition analysis of molecule AB. Molecular fragments A* and B* have the same geometry that they held in the molecule, and molecular fragments A and B are relaxed to their equilibrium geometries.

Term	**P**	**As**	**Sb**	**Bi**
$\Delta\Delta E_{int}$	6.1	-1.6	-5.4	-9.6
$\Delta\Delta E_{Pauli}$	28.1	18.1	45.9	50.4
$\Delta\Delta E_{elstat}$	39.0	37.0	26.3	24.3
$\Delta\Delta E_{orb}$	-63.5	-59.5	-81.1	-88.5
$\Delta\Delta E_{disp}$	1.7	1.8	1.9	1.8
$\Delta\Delta G_{298K}$	15.1	6.5	0.8	-2.4

Table 2.1: Energy decomposition analysis for transforming the bent conformations of 2.1(P–Bi) into the planar conformations as per Figure 2.13. All energies are in kcal/mol. The $\Delta\Delta E$ label is used because EDA results presented using ΔE refer to the decomposition of a molecule into its atomic constituents. In this table, the values refer to the difference between ΔE values for two molecules.

sent the instantaneous energy changes – broken down into the Pauli, orbital, electrostatic, dispersion, and solvation contributions – that accompany a change from the bent to the planar geometry for EN_3TMS_2 (E = P, As, Sb, Bi). The results capture the increased favourability of planarization going down the group (Figure 2.13). Orbital interactions are a significant stabilizing component in achieving the planar geometries, with the values increasing down the group (see $\Delta\Delta E_{orb}$). The destabilizing electrostatic interactions are also less for the heavier pnictogens (see $\Delta\Delta E_{elstat}$). The stabilizing orbital interactions ultimately outweigh the destabilizing electrostatic and Pauli repulsion leading to the experimentally observed trend that the preference for adopting a planar geometry increases in the order P < As < Sb < Bi.

The above trend is also observed when thermally corrected Gibbs energies (at 298

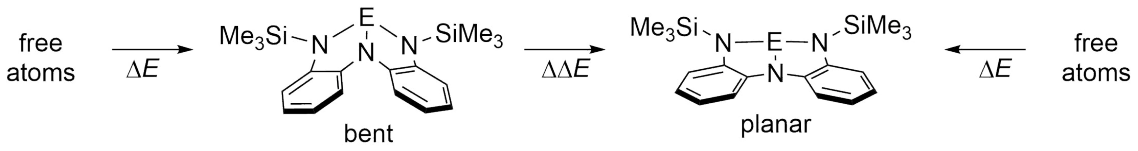

Figure 2.13: Conversion of the bent conformation into the planar conformation used for the energy decomposition analysis in Table 2.1.

K) are considered (see $\Delta\Delta G$ 298K values in Table 2.1). For compounds EN_3TMS_2 (E = P, As, and Sb), the planar structure models the transition state for edge-inversion and is uphill. This is reflected in the positive $\Delta\Delta G$ 298K values. The bismuth derivative is an exception, with its planar structure being the ground rather than the transition state, and consistently **2.1-Bi** is found to be planar in all phases. The decrease in energy for this inversion going down the group has been theoretically predicted before for the series EF_3 (E = N–Bi).[128129130]

Why does 2.1-Sb dimerize to give 2.1-Sbdim in the solid-state while 2.1-Bi does not? The gas-phase structures of **2.1-Sb$_{\mathbf{dim}}$** and the hypothetical compound **2.1-Bi$_{\mathbf{dim}}$** were optimized. The EDA results for the **2.1-Sb**→**2.1-Sb$_{\mathbf{dim}}$** and **2.1-Bi**→**2.1-Bi$_{\mathbf{dim}}$** dimerizations (Table 2.2) show that dispersive forces play a significant role (ca. 22 kcal mol^{-1}) in both cases. The dimerization process is more favourable for the antimony analogue (ΔE_{int} = –60.2 kcal mol^{-1}) than bismuth (ΔE_{int} = –47.9 kcal mol^{-1}). The significant difference in the stability of the two dimers is the destabilizing Pauli repulsion (ΔE_{Pauli}), which is higher in **2.1-Sb$_{\mathbf{dim}}$**. However, the stabilizing electrostatic and orbital energies are also more significant in **2.1-Sb$_{\mathbf{dim}}$**, leading to an overall more favourable interaction energy. The longer Bi–N3' bond in **2.1-Bi** may reduce the Pauli repulsion and electrostatic and orbital stabilization. The more diffuse valence orbitals of Bi compared with Sb will result in poorer overlap and contribute negatively to the stabilization of **2.1-Bi**. Considering these stabilizing and destabilizing factors for **2.1-Bi$_{\mathbf{dim}}$**, together with the higher preference of planarity for monomeric **2.1-Bi** (shown in Table 2.1), accounts for the experimental observations that **2.1-Sb$_{\mathbf{dim}}$** is accessible at 193 K in solution, but **2.1-Bi$_{\mathbf{dim}}$** is not detected.

Term	**2.1-Sb$_{dim}$**	**2.1-Bi$_{dim}$**
$\Delta\Delta E_{int}$	-60.2	-47.9
$\Delta\Delta E_{Pauli}$	431.6	336.7
$\Delta\Delta E_{elstat}$	-261.1 (53.1%)	-210.7 (54.7%)
$\Delta\Delta E_{orb}$	-206.3 (41.9%)	-149.7 (38.9%)
$\Delta\Delta E_{disp}$	22.8 (4.6%)	-22.1 (5.8%)
$\Delta\Delta E_{solv}$	-1.6 (0.3%)	-2.1 (0.5%)
r	2.147	2.294
D_{e}	12.6	11.3
$\Delta\Delta G_{298K}$	-7.4	-5.9

Table 2.2: Energy decomposition analysis for the formation of **2.1-Sb$_{dim}$** from **2.1-Sb** and hypothetical molecule **2.1-Bi$_{dim}$** from **2.1-Bi**. All energies are in kcal/mol. Percentages denote the fraction of attractive forces represented by each component. The value r denotes the distance between the monomers and is given in Å. D_{e} is the sum of ΔE_{int} and ΔE_{prep} and represents the true dimer dissociation energy (including geometric relaxation of monomers).

2.2.4 Implications for Reactivity

To assess whether the structural trends described above modulate the reactivity of this series of compounds, we analyzed their frontier orbital manifolds in both geometries (Figure A.15). All three *p*-orbitals are engaged in E–N σ-bonding in the bent case. In contrast, the planar geometry only engages two of three *p*-orbitals by virtue of 3-center-4-electron bonds involving the external E–N bonds. Consequently, in the planar geometry, a vacant *p*-orbital remains available perpendicular to the molecular plane at the central element and it is the LUMO in each case. Ligand oxidation transfers two electrons into this LUMO and was found to be responsible for the Bi(I) like reactivity reported for **2.1-Bi**.[122] The LUMO in the bent geometry is E–N σ^* in nature and appears *trans* to the central E–N bond as expected for the +III oxidation state of pnictogen amides.

Although the HOMO energies (Figure 2.14) are essentially unaltered by geometric perturbation, the LUMO energies are significantly lowered (approx. 1eV) upon planarization. The closing of the HOMO–LUMO gap is consistent with experimental UV/Vis spectra, where the calculated and observed HOMO-LUMO excitation bands are uniformly red shifted upon descending the group.

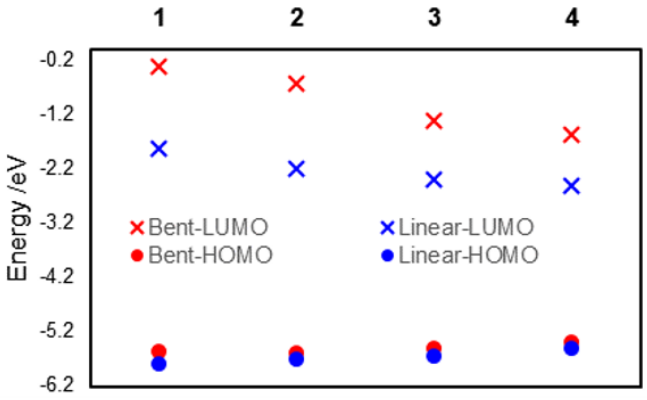

Figure 2.14: HOMO and LUMO energies for bent and planar derivatives of **2.1-P** (1), **2.1-As** (2), **2.1-Sb** (3), and **2.1-Bi** (4).

Given that the exceptional reactivity of geometrically constrained phosphorus complexes is thought to be initiated through a nucleophilic attack by substrate (e.g. amines, alcohols, water) upon the electrophilic phosphorus, we were particularly interested in implications of the above frontier orbital considerations on Lewis acidity at the central pnictogen. No reaction was observed between pyridine N-oxide or 4-di-methylamino pyridine and either **2.1-P** or **2.1-As** (Figure 2.15a). In contrast, 2:1 adducts **2.1-Sb-(pyo)$_2$** and **2.1-Bi-(pyo)$_2$** were readily isolated from reactions involving pyridine N-oxide and **2.1-Sb** or **2.1-Bi**, evidencing the increasing Lewis acidity of the predominantly planar compounds relative to their bent analogues (Figure 2.15b). Both compounds have been isolated and structurally characterized by crystallography (vide infra; Figure 3.12). Next, the Gutmann–Beckett method was used to experimentally compare the Lewis acidity of **2.1-Sb** and **2.1-Bi**. In the presence of excess Lewis acid, the ^{31}P NMR chemical shift of triethylphosphine oxide is shifted to more downfield values in **2.1-Bi** relative to **2.1-Sb** (Figure 2.16). Conversion of the chemical shifts to acceptor numbers gives values of 15 and 28 for the antimony and bismuth derivatives, respectively, evidencing the higher Lewis acidity for the heavier analogue. Solvent-corrected DFT calculations of the Fluoride Ion Affinity (FIA) and Global Electrophilicity Index (GEI)[131] (Equation 2.1) also confirm that **2.1-Bi** (FIA: 33kcal mol^{-1}, GEI: 2.70 eV) is more acidic than **2.1-Sb** (FIA: 28 kcal mol^{-1},GEI: 2.50 eV). The GEI provides an indication of the propensity of electron acceptors to acquire additional electronic charge. This electrophilicity

assessment is free from steric considerations and is solely dependent upon the electronic structure of the Lewis acid. FIAs are based on reaction enthalpies and were calculated by considering the sum of the reactions:

$$\mathrm{LA} + \mathrm{COF_3^-} \rightarrow \mathrm{LAF^-} + \mathrm{COF_2}$$

$$\underline{\mathrm{COF_2} + \mathrm{F^-} \rightarrow \mathrm{COF_3^-}}$$

$$\mathrm{LA} + \mathrm{F} \rightarrow \mathrm{LAF}$$

$$GEI = \frac{[0.5(E_{\mathrm{HOMO}} + E_{\mathrm{LUMO}})]^2}{2(E_{\mathrm{LUMO}} - E_{\mathrm{HOMO}})} \tag{2.1}$$

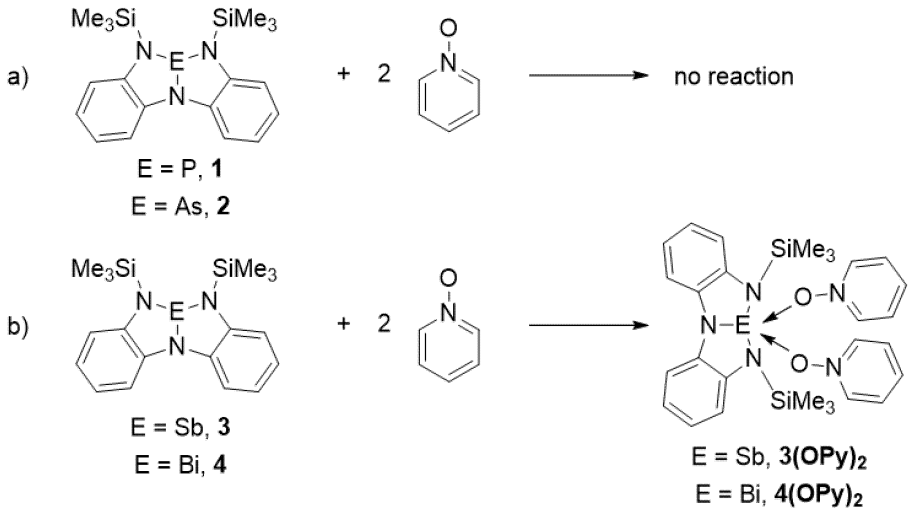

Figure 2.15: The reaction of pyridine N-oxide with **2.1-P** (1), **2.1-As** (2), **2.1-Sb** (3), and **2.1-Bi** (4).

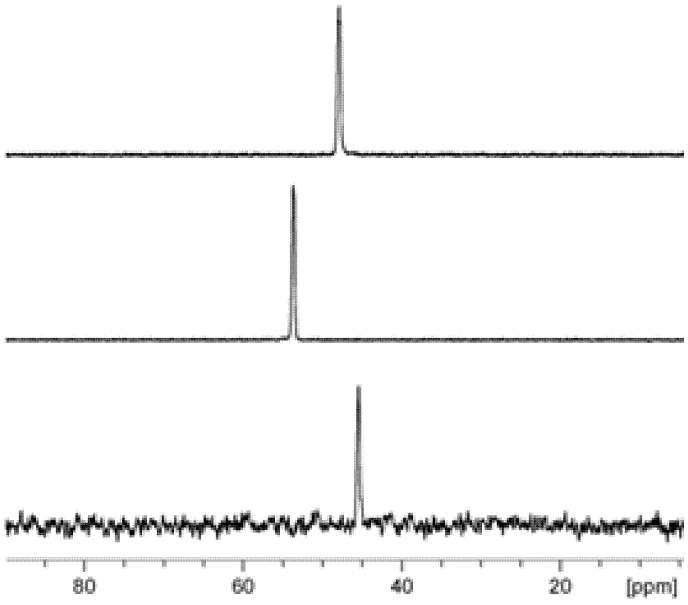

Figure 2.16: ^{31}P NMR spectra of a 3:1 mixture of **2.1-Sb** and Et_3PO (top), **2.1-Bi** and Et_3PO (middle), and uncoordinated Et_3PO in C_6D_6.

2.3 Conclusion

An investigation into the dynamic structure and bonding of antimony and bismuth triamides ligated by a geometry-constraining tridentate substituent was completed. These compounds were examined in the solid, solution, and gas-phase. Gas-phase calculations were also used to assess the geometric preference of phosphorus and arsenic derivatives. The fifth-row element antimony is identified as an inflection point between the behavior of the lighter pnictogens and bismuth. It exhibits a structural promiscuity that is unique amongst the studied compounds as shown by the equilibria involving **2.1-Sb**, **2.1-Sb$_{\mathbf{dim}}$'**, and **2.1-Sb$_{\mathbf{dim}}$**. By carefully studying these equilibria, we determined rare quantitative thermodynamic data for dynamic covalent chemistry involving antimony compounds. Compound **2.1-Bi** stands out due to its planar ground state and exhibits no dimerization due to large Pauli repulsion between the subunits as well as poor orbital overlap due to the long Bi–N bonds. The preference for adopting a planar geometry was found to increase descending the group (P, As < Sb < Bi). The main factor contributing to these trends was shown to be the electronegative difference across the E–N bond, which influences the electrostatic and orbital components of bonding. Structural preferences in this homologous series have consequences for reactivity.The Lewis acidity was experimentally found to increase in the order **2.1-P, 2.1-As** < **2.1-Sb** < **2.1-Bi**, which is predicted by considerations of their ground-state geometries and LUMO levels (the HOMO levels are unaltered by geometric deformation).

2.4 Experimental

2.4.1 General

Synthetic Procedures. All manipulations were performed using standard Schlenk and glovebox techniques under an atmosphere of dry nitrogen. Solvents were dried over Na/benzophenone (tetrahydrofuran, pentanes, hexanes, diethyl ether, toluene, benzene-d_6) or over calcium hydride (dichloromethane, acetonitrile, 1,2-difluorobenzene,

dichloromethane-d_2, acetonitrile-d_3, chloroform-d) and distilled prior to use. Reaction glassware was baked in a 130 °C oven for at least 1 h prior to use and assembled under nitrogen while hot.

Solution NMR Spectroscopy. Nuclear magnetic resonance spectra are referenced to tetramethylsilane (^{1}H, ^{13}C), 85% H_3PO_4 (^{31}P), $CFCl_3$ (^{19}F), or $B(OMe)_3$ (^{11}B) on a Bruker AV-300 spectrometer or a Bruker AV-500 spectrometer with residual solvent used for chemical shift calibration. Samples for NMR spectroscopy were prepared and sealed inside the glovebox with Parafilm before removal into ambient atmosphere. Heteronuclear NMR experiments were run using a sealed capillary containing benzene-d_6 placed within the NMR tube for solvent locking.

Solid-state NMR Spectroscopy. The ^{1}H and ^{13}C cross-polarization (CP) / Magic Angle Spinning (MAS) NMR experiments were carried out on a Bruker Avance DSX NMR spectrometer with a 9.4 T magnet (400.24 MHz ^{1}H, 100.64 MHz ^{13}C, Larmor frequencies) using a probe head for rotors of 4 mm diameter. The sample was packed into the rotor inside the glovebox and removed from the Parafilm sealed vial shortly before conducting the experiments.

Vibrational Spectroscopy. Infrared spectra were obtained on an Agilent Technologies CARY 630 Fourier Transform (FT) Infrared (IR) instrument equipped with a ZnSe ATR module. Raman spectra were obtained on a Thermo Scientific Nicolet NXR 9650 FT-Raman Spectrometer instrument equipped with a 1064 nm Nd:YVO_4 laser and InGaAs detector.

UV-Vis Spectroscopy. UV-VIS spectra were obtained on an Agilent CARY 100 spectrometer. Samples were prepared inside the glovebox in quartz cuvettes sealed with a Teflon plug prior to removal into the ambient atmosphere. Background correction was performed using a cuvette containing the analysis solvent. Variable temperature UV-Vis spectra were obtained on a portable Vernier SpectroVis spectrometer inside the glovebox. A cuvette containing the dissolved sample in pentane was cooled to ca. -100 °C using a cold port filled with copper beads. A thermocouple tip was placed in the cooled solution to provide real-time in-situ temperature measurements. The cuvette was removed from the beads and placed in the spectrometer

cavity. Spectra were obtained as the sample warmed to ambient temperature.

Melting Points. Melting points were obtained for samples sealed in glass capillaries and are uncorrected.

Crystallography. Single crystal diffraction experiments were performed on a Bruker D8-Quest Photon II diffractometer. The data was processed using the APEX III GUI software The XPREP program was used to confirm unit cell dimensions and crystal lattices. All calculations were carried out using the SHELXTL-plus and the Olex2 software packages for structure determination (ShelXT/Intrinsic phasing), solution refinement (ShelXL/Least squares), and molecular graphics. Space group choices were confirmed using Platon. The final refinements were obtained by introducing anisotropic thermal parameters and the recommended weightings for all atoms except the hydrogen atoms, which were placed at locations derived from a difference map and refined as riding contributions with isotropic displacement parameters that were 1.2 times those of the attached carbon atoms. Details for individual compounds are given with their characterization data.

Mass Spectrometry. Electro-Spray Ionization (ESI) and Atmospheric Pressure Chemical Ionization (APCI) spectra were obtained on a Bruker micrOTOF.

Commercial Reagents. 2-nitroaniline, 1-fluoro-2-nitrobenzene, pentafluorophenol: Oakwood Chemicals, used as received. Bismuth(III) chloride: Oakwood Chemicals, purified by vacuum sublimation (10^{-2} mbar, 200 °C). Chlorotrimethylsilane, triethylamine: Millipore Sigma, used after distillation under nitrogen. Phosphorus(III) chloride, *n*BuLi (1.6M/hexanes), lithium dimethylamide: Millipore Sigma, used as received.

Starting Materials. **SM1**: prepared by literature procedure[127] and purified by crystallization from DCM and washing with cold methanol. **SM2**: prepared by literature procedure.[132] Crude product was sufficiently pure for subsequent usage. N_3H_3: prepared by literature procedure.[133] Crude product was sufficiently pure for subsequent usage. **SM3**: prepared by literature procedure[134] and purified by sublimation. *Caution*: this compound is highly sensitive to temperature, light, and

moisture. We prepare it in the dark under rigorously anhydrous conditions, sublime it using the apparatus described in the cited reference, and immediately transfer it to a –30 °C freezer where it is stable for months in the dark. **SM4**: prepared by literature procedure[135] and purified by vacuum distillation.

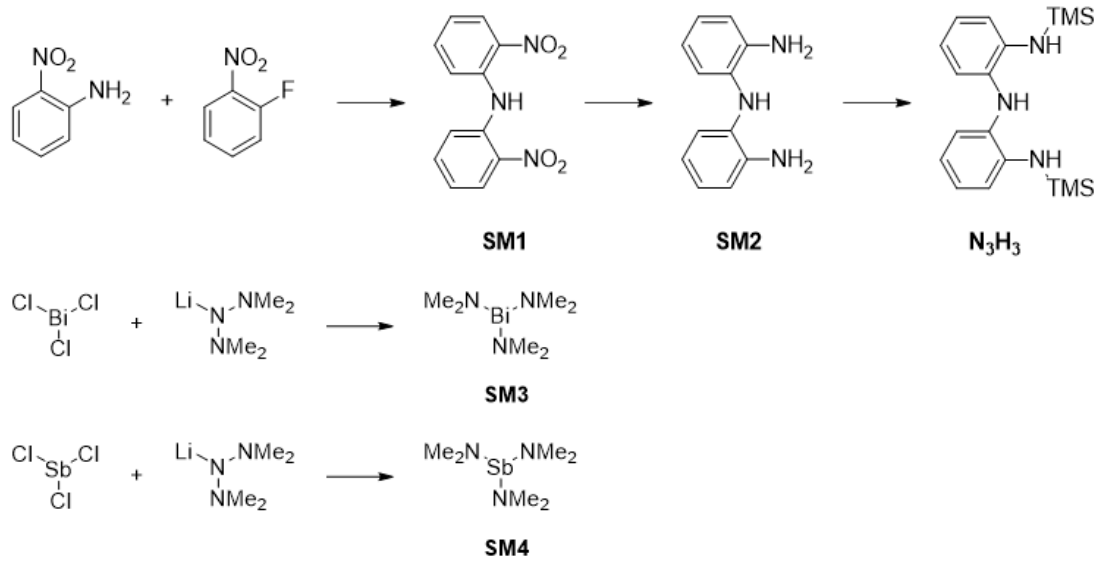

Due to the air-sensitive nature of the amides, elemental analyses were not obtained. However, bulk spectroscopic purity is clearly indicated by the spectra given for each compound.

2.4.2 Computational Methods

Geometry optimizations and frequency calculations for compounds **2.1P, 2.1As, 2.1Sb, 2.1Bi** (bent and planar geometries) were carried out at the PBE0-D3/def2-tzvpd level in Gaussian 16. NBO calculations were performed on structures optimized at the PBE0-D3/def2-tzvpd level for monomers and PBE0-D3/def2-tzvp level for dimers.

EDA calculations were performed using geometries optimized at the PBE0-D3/def2- tzvp//SCRF(Toluene) level in Gaussian 16. These geometries were exported to the Amsterdam Density Functional (ADF) suite where energy calculations were done at the PBE1-D3/TZ2P//COSMO(Toluene) level with scalar relativistic

correction. No significant difference was observed between small-core and large-core calculations and therefore, all calculations were performed using the large-core approximation for time efficiency.

UV-VIS calculations were performed using geometries optimized at the PBE0-D3/def2-tzvp//SCRF(Toluene) level in Gaussian 16. These geometries were exported to the Amsterdam Density Functional (ADF) suite where energy calculations were done using TDDFT at the BLYPD3(BJ)/TZ2P//COSMO(Toluene) level with scalar relativistic correction and large-core approximation. Davidson method was used and with 10 singlet-triplet excitations were calculated.

NMR calculations were performed using geometries optimized at the PBE0-D3/def2- tzvp//SCRF(Toluene) level in Gaussian 16. These geometries were exported to the Amsterdam Density Functional (ADF) suite where energy calculations were done using TDDFT at the BLYP-D3(BJ)/TZ2P-J//COSMO(Toluene) level with scalar relativistic correction and large-core approximation.

2.4.3 Synthesis and Characterization Data

Synthesis of 2.1-Sb

A solution of N_3H_3 (0.3439 g, 1 mmol) and $Sb(NMe_2)_3$ (0.2540 g, 1 mmol) were separately dissolved in ca. 4 mL n-hexane and cooled to –30 °C. The solution of $Sb(NMe_2)_3$ was dropwise added to the N_3H_3 solution over 1 minute to obtain a clear pale yellow-orange solution. The reaction was warmed to room temperature and stirred for 24 h to obtain a clear orange-red solution. Solvent and coordinated dimethylamine were removed under dynamic vacuum (10^{-3} mbar) over 20 h. Recrystallization of the resulting yellow powder from hexane yielded pure **2.1-Sb$_{\mathbf{dim}}$** as pale-yellow crystals. As described in the manuscript, this compound is dimeric in the solid state and exists (predominantly) as a monomer in solution.

Yield: 0.3331 g, 72%

Melting point: 112 °C, decomposes

^{1}H NMR (500 MHz, benzene-d_6): δ 7.86 (d, J = 7.9 Hz, 2 H, CAr-H), 6.99 (d, J = 7.8 Hz, 2 H, CAr-H), 6.93 (t, J = 7.6 Hz, 2 H, CAr-H), 6.82 (t, J = 7.9 Hz, 2 H, CAr-H), 0.27 (s, 18 H, $Si(CH_3)_3$) ^{13}C NMR (126 MHz, chloroform-d): δ 147.78 (CAr), 143.25 (CAr), 123.26 (CAr), 121.70 (CAr), 118.32 (CAr), 116.77 (CAr), 2.06 ($Si(CH_3)_3$)

Raman (cm^{-1}(int.)): 76(92), 98(86), 136(48), 187(53), 262(29), 289(26), 331(97), 377(24), 437(14), 485(15), 582(14), 607(33), 629(16), 664(22), 682(16), 712(16), 748(14), 793(14), 840(17), 876(16), 905(14), 1053(57), 1058(44), 1156(34), 1177(30), 1194(55), 1245(86), 1269(41), 1279(38), 1302(39), 1316(41), 1478(36), 1574(57), 1584(100), 2074(15), 2158(15), 2895(56), 2951(32), 3066(39), 3084(26).

HRMS (APCI-MS): calculated for $[M+1]^+$ = 462.0776 m/z for ^{121}Sb, observed = 462.0758 m/z for $_{121}$Sb, error = 3.96 ppm

X-ray for **2.1-Sb$_{dim}$**: $C_{18}H_{26}N_3SbSi_2$ (M =462.35 g/mol): triclinic, space group $P_{\bar{1}}$ (no. 2), a = 9.7953(4) Å, b = 10.9903(4) Å, c = 20.8263(8) Å, α = 95.4660(10)°, β = 99.2360(10)°, γ = 112.3310(10)°, V = 2016.80(14) Å^3, Z = 4, T = 100.03 K, μ(CuKα) = 12.018 mm^{-1}, D_{calc} = 1.523 g/cm^3, 54619 reflections measured (4.362° $\leq 2\theta \leq$ 148.96°), 8170 unique (R_{int} = 0.0345, R_{sigma} = 0.0215) which were used in all calculations. The final R_1 was 0.0515 ($I > 2\sigma(I)$) and wR2 was 0.1199 (all data). CCDC No. 1949725.

Synthesis of 2.1-Sb(dma)$_2$

This compound is unstable above –30 °C and cannot be isolated in pure form. It was prepared by reacting N_3H_3 and $Sb(NMe_2)_3$ in hexane as described for the synthesis of **2.1-Sb**. However instead of removing volatiles under vacuum, the crude reaction solution was cooled to –30 °C for several days to obtain crystals of **2.1-Sb(dma)$_2$** that immediately begin to lose the amine ligands when removed from the mother liquor. Therefore, the crystals must be kept cold (–30 °C), selected quickly before they warm up on the microscope slide (not precooled), and immediately mounted on the goniometer head bathed in a stream of cold nitrogen. Attempts to dry crystals of **2.1-Sb(dma)$_2$** either under vacuum or a stream of nitrogen gives a mixture of

2.1-Sb and **2.1-Sb(dma)$_2$** due to uncontrolled loss of the weakly bound ligands. Compound **2.1-Sb(dma)$_2$** disintegrated to **2.1-Sb** under the conditions used in electrospray ionization precluding accurate mass determination in the gas phase.

X-ray: $C_{22}H_{40}N_5SbSi_2$ (M =552.52 g/mol): monoclinic, space group $P2_1/c$ (no. 14), a = 9.7184(14) Å, b = 10.1220(14) Å, c = 27.102(4) Å, β = 96.704(2)°, V = 2647.8(6) Å^3, Z = 4, T = 125.01 K, μ(MoKα) = 1.151 mm^{-1}, D_{calc} = 1.386 g/cm^3, 32576 reflections measured (3.026° $\leq 2\theta \leq$ 58.368°), 6793 unique (R_{int} = 0.0895, R_{sigma} = 0.0814) which were used in all calculations. The final R_1 was 0.0454 ($I > 2\sigma(I)$) and wR_2 was 0.0976 (all data). CCDC No. 1949726

Synthesis of 2.1-Sb(pyo)$_2$

Compound **2.1-Sb** (0.0390 g, 0.09 mmol) and pyridine N-oxide (0.0160 g, 0.18 mmol) were added to a vial and toluene (ca. 2 mL) was added at ambient temperature. The reaction was stirred for an hour to obtain a dark red solution. The solution was concentrated under vacuum, layered with pentane and stored at –30 °C to yield crystalline **2.1-Sb(pyo)$_2$**.

Yield: 0.028 g, 50 %

Melting point: 98–102 °C

^{1}H NMR (500 MHz, benzene-d$_6$): δ 7.85 (dd, J = 8.0 Hz, 1.1 Hz, 2 H, CAr-H), 7.72 (m, 4H, CAr-H), 6.99 (dd, J = 7.9, 1.2 Hz, 2H, CAr-H), 6.93 (td, J = 8.2 Hz, 1.2 Hz, 2H, CAr-H), 6.81 (t, J = 7.5 Hz, 2 H, CAr-H), 6.09 (m, 6 H, CAr-H), 0.29 (s, 18 H, Si(CH$_3$)$_3$). ^{13}C NMR (126 MHz, benzene-d6): δ 147.07 (CAr), 143.81 (CAr), 139.25 (CAr), 125.45 (CAr), 122.92 (CAr), 122.71 (CAr), 121.12 (CAr), 118.29 (CAr), 116.89 (CAr), 1.91 (Si(CH$_3$)$_3$).

ESI-MS: (positive ion mode, [M+1]$^+$): The product from loss of two ligands was observed – 462.1 amu for ^{121}Sb and 464.1 amu for ^{123}Sb.

X-ray: $C_{28}H_{36}N_5O_2SbSi_2$ (M =652.55 g/mol): monoclinic, space group $C2/c$ (no. 15), a = 13.3092(12) Å, b = 10.4889(10) Å, c = 21.660(2) Å, β = 100.107(2)°, V = 2976.8(5) Å^3, Z = 4, T = 100.0 K, μ(CuKα) = 8.392 mm^{-1}, D_{calc} = 1.456 g/cm^3,

18652 reflections measured ($10.804^{o} \leq 2\theta \leq 144.314^{o}$), 2930 unique ($R_{int} = 0.0310$, $R_{sigma} = 0.0194$) which were used in all calculations. The final R_1 was 0.0324 ($I > 2\sigma(I)$) and wR_2 was 0.0856 (all data). CCDC No. 1949722.

Synthesis of 2.1-Bi(pyo)$_2$

Compound **2.1-Bi** (0.2748 g, 0.50 mmol) and pyridine N-oxide (0.0951 g, 1.0 mmol) were added to a vial and toluene (5 mL) was added at ambient temperature. The reaction was stirred for an hour to obtain a dark red solution. Volatiles were removed under vacuum to give a red-brown powder, which was recrystallized from THF/hexanes at –30 °C to yield **2.1-Bi(pyo)$_2$·THF**, which was characterized crystallographically. Removal of all solvent under dynamic vacuum yielded solvent-free **2.1-Bi(pyo)$_2$**. The ^{1}H and ^{13}C NMR spectra of this compound vary with concentration, presumably due to some degree of reversible coordination. Data given below are for a 0.125 M solution in C_6D_6.

Yield: 0.321 g, 69 %

Melting point: 139–140 °C, decomposes.

^{1}H NMR (500 MHz, benzene-d): δ 7.43 (m, 6 H, C_{Ar}-H), 7.01 (d, J = 7.8 Hz, 2H, C_{Ar}-H), 6.71 (t, J = 7.6 Hz, 2H, C_{Ar}-H), 6.34 (t, J = 7.2 Hz, 2 H, C_{Ar}-H), 6.06 (t, J = 7.6 Hz, 2 H, C_{Ar}-H), 5.91 (t, J = 6.5 Hz, 4 H, C_{Ar}-H), 0.62 (s, 18 H, $Si(CH_3)_3$) 13C NMR (126 MHz, benzene-d6): δ 149.69 (C_{Ar}), 148.63 (C_{Ar}), 139.45 (C_{Ar}), 127.63 (C_{Ar}), 124.80 (C_{Ar}), 120.50 (C_{Ar}), 119.45 (C_{Ar}), 117.90 (C_{Ar}), 114.19 (C_{Ar}), 2.35 ($Si(CH_3)_3$))

FT-IR (ATR, ZnSe crystal): 469 (w), 548 (w), 627 (m), 676 (m), 734 (s), 825 (vs), 879 (m), 927 (s), 1017 (w), 1045 (w), 1119 (w), 1155 (m), 1244 (s), 1282 (m), 1330, (w), 1445 (m), 1460 (s), 1475 (m), 1572 (m), 2891 (w), 2939 (m), 3046 (w)

ESI-MS: (positive ion mode, $[M+1]^{+}$): The product from loss of two ligands was observed – 550.2 amu

X-ray: $C_{60}H_{80}Bi_2N_{10}O_5Si_4$ (M =1551.66 g/mol): monoclinic, space group $P2_1/c$ (no. 14), a = 21.581(3) Å, b = 15.625(2) Å, c = 20.225(3) Å, $\beta = 108.420(2)^{o}$, V =

6470.5(14) $Å^3$, Z = 4, T = 124.97 K, μ(MoKμ) = 5.560 mm^{-1}, D_{calc} = 1.593 g/cm^3, 80958 reflections measured ($1.988^o \leq 2\theta \leq 58.578^o$), 16659 unique ($R_{int}$ = 0.0834, R_{sigma} = 0.0754) which were used in all calculations. The final R_1 was 0.0392 ($I > 2\sigma(I)$) and wR_2 was 0.0747 (all data). CCDC No. 1949724

Chapter 3

Lewis Acidity of a Vacant *p*-orbital Perpendicular to a Planar, Trivalent, Electropositive, and Neutral Main Group Element

Portions of this work have appeared in **K. M. Marczenko**, S. Jee,† S. S. Chitnis, *Organometallics*, **2020**, *39*, 4287–4296 (Full Paper; DOI: 10.1021/acs.organomet.0c00378).

Contributions to the manuscript: KMM and SJ completed DFT calculations. KMM completed ADF calculations. SSC assisted with calculations, wrote the manuscript, and supervised the project. † denotes undergraduate author.

3.1 Introduction

The use of main group compounds as Lewis acid catalysts, such as prototypical boranes, rely on the ability to easily tune the *p*-orbital (LUMO) energy (and therefore its Lewis acidity) through substituent variation.[136137138139140141] As previously discussed, the electronic structure of **2.1-Sb** and **2.1-Bi** shows a vacant *p*-orbital (LUMO) perpendicular to the molecular plane at the central element (Figure 3.1). Whereas the HOMO energies are essentially unchanged upon planarization, the LUMO energies are significantly lowered (ca. 1 eV), leading to increased Lewis

acidity at the planar centers. Experimental data further proved the presence of a vacant p-orbital available for coordination. A 2:1 adduct between pyridine N-oxide

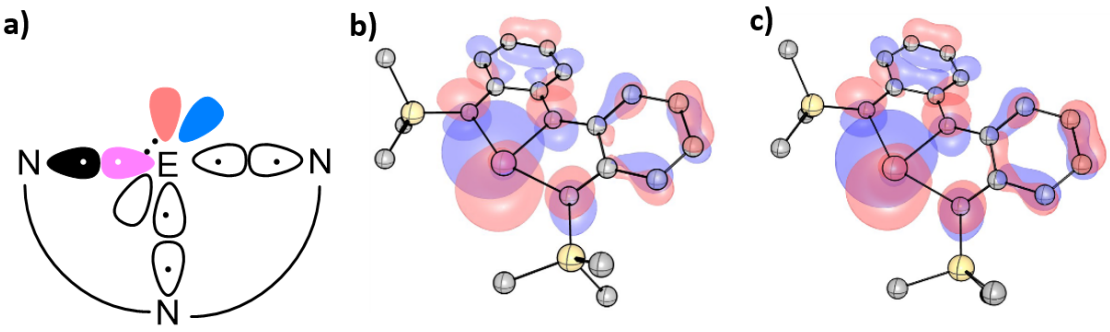

Figure 3.1: Bonding schemes for planar geometries (a). LUMOs of **2.1-Sb** (b), and **2.1-Bi** (c) in their minimum geometries.

and **2.1-Bi**, which was characterized by single-crystal X-ray diffraction, contains two molecules of base coordinating through the vacant p-orbital.[126] Additional 2:1 adducts of **2.1-Bi** and trimethylamine oxide or triethyl phosphine oxide were synthesized. Due to the weak interactions in these adducts, characterization was only completed using single-crystal X-ray crystallography (Figure 3.2). The crystal structures of **2.1-Bi(TMAO)$_2$** and **2.1-Bi(OPEt$_3$)$_2$** clearly show a distorted trigonal bipyramidal geometry around the Bi atom where two molecules of an oxygen base are coordinated to the bismuth atom through dative Bi—O bonding interactions (TMAO: 2.378(7), 2.386(8) Å; $OPEt_3$: 2.468(4), 2.466(4) Å). More importantly, the O–Bi–O angles span 166.0(3)–175.3(1)°, close to the idealized angle of 180°, indicating bonding through the vacant 6p-valence orbital at the metal center. The similarity in electronegativity of boron (2.04) and bismuth (2.02), and the experimentally verified presence of a vacant p-orbital, allows one to envision the use of planar BiN_3R_2 compounds in Lewis acid catalysis and achieve similar applications with these planar Bi compounds to what is commonly observed with boron compounds.[142] However, in order to fully realize their potential, we must first understand the influence of ligand design on Lewis acidity at the metal center.[143] This next section aims to use DFT calculations to observe the effect of tuning the ligand structure on the Lewis acidity of **2.1-Bi**. This will be addressed in terms of electronic and

steric effects. Once the influence of substitution on Lewis acidity is understood, future work can focus on applying it to creating new Lewis acid catalysts for synthetic organic transformations.

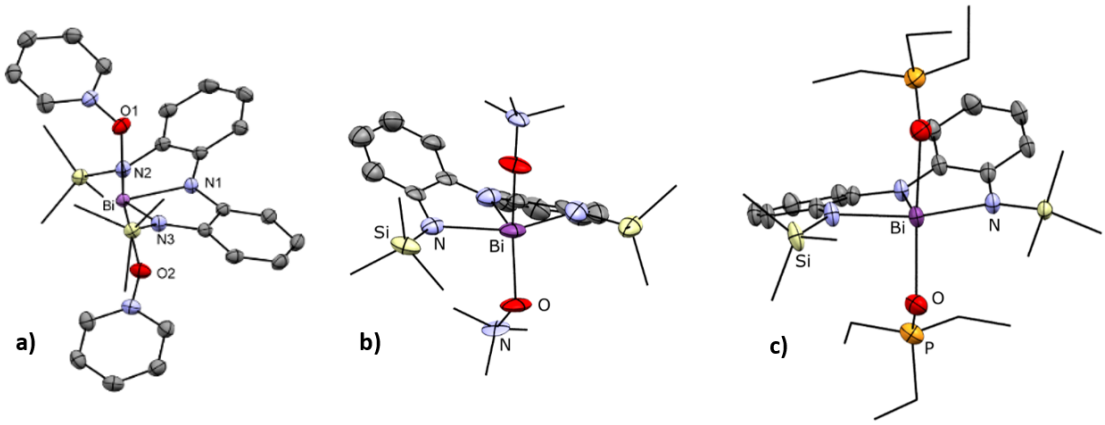

Figure 3.2: Single-crystal X-ray structures of **2.1-Bi(PNO)$_2$**, **2.1-Bi(TMAO)$_2$** and **2.1-Bi(Et$_2$PO)$_2$**. Thermal ellipsoids are shown at the 50% probability level, and hydrogen atoms have been removed for clarity.

3.2 Results and Discussion

3.2.1 Methods

All geometries were optimized in Gaussian 16[144] using the PBE0 functional[145146] with D3(Becke-Johnson (BJ)) dispersion correction[147148] and the def2-TZVP[149] basis set containing a relativistic small-core pseudopotential (ecp-46).[150] Frequency calculations were performed to confirm structures as true minima.

EDA calculations[151152153] were performed using the Amsterdam Density Functional (ADF) (2017)[154] package using the hybrid PBE0 functional, D3(BJ) dispersion correction, scalar relativistic correction,[155156157] and the AUG/ADZP[157] basis set. Closed shell neutral fragments were used in EDA calculations.

FIA calculations were performed using geometries optimized using the Becke-3-Parameter Exchange and Lee-Yang-Parr Correlation Hybrid Functional (B3LYP) functional with D3(BJ) dispersion correction. The cc-pVDZ basis set was used for

light atoms, and the aug-cc-pVDZ-PP[158] basis set was used at bismuth.

3.2.2 Origins of Lewis Acidity in X–Bi–Y

The electronic properties of **2.1-Bi** was varied by changing the substituents at the X and Y positions (Figure 3.3). The LUMO and HOMO of representative compound Me–Bi–H shows combinations of Bi $6p$ and N $2p$ atomic orbitals, reminiscent of π-bonding and π^*-antibonding interactions. This interaction is best considered as a "charge-shift bond"; where molecular stability is due to a combination of multiple ionic resonance forms rather than covalent sharing of electrons. Poor orbital overlap ultimately minimizes the electron density between the bonding centers. Regardless, the MO visualizations show a metal-based LUMO that was unchanged with substituent variation, indicating metal-based Lewis acidity in all examined derivatives.

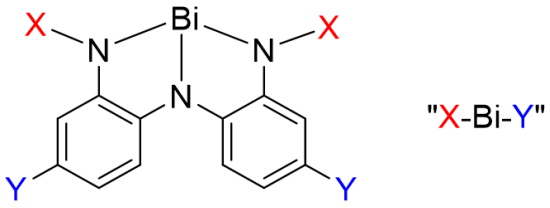

Figure 3.3: Substituent labelling of **2.1-Bi** acids.

3.2.3 Electron Affinity: Global Electrophilicity Index (GEI) and 1-Electron Reduction Energies

The metal based Lewis acidity was investigated using GEI calculations, which provide an indication of the propensity of **2.1-Bi** to acquire additional electronic charge. A plot of LUMO energies and GEI values (Figure 3.4) of the studied set of compounds shows that these parameters vary smoothly, with more Lewis acidic centers containing a lower LUMO energy and higher GEI value. The ability of electronegative substituents to lower the LUMO energy and boost the GEI is demonstrated when X = CF_3 > TMS Me (see CF_3–Bi–H, TMS–Bi–H, and Me–Bi–H) and/or Y = CF_3 > Br > H > Me > OMe (see Me–Bi–CF_3, Me–Bi–Br, Me–Bi–H, Me–Bi–Me, and Me–Bi–OMe).

These trends are understood in terms of electronegativity effects, with more electronegative substituents increasing the Lewis acidity of the metal center. The position of the Y substituent on the aryl ring was also shown to influence the GEI and LUMO energies, with TMS–Bi–Br showing a lower LUMO energy and higher GEI than TMS–Bi–Br_{int}. This indicates that substituents *meta* to the internal nitrogen have a less profound influence on the Lewis acidity of the metal center than substituents *meta* to the external nitrogen atoms. It was also shown that substitution at the X position (N atoms) has a larger influence than substitution at the Y position (aryl ring) through comparison of the GEI and LUMO energies of CF_3–Bi–Me and Me–Bi–CF_3 (Figure 3.4).

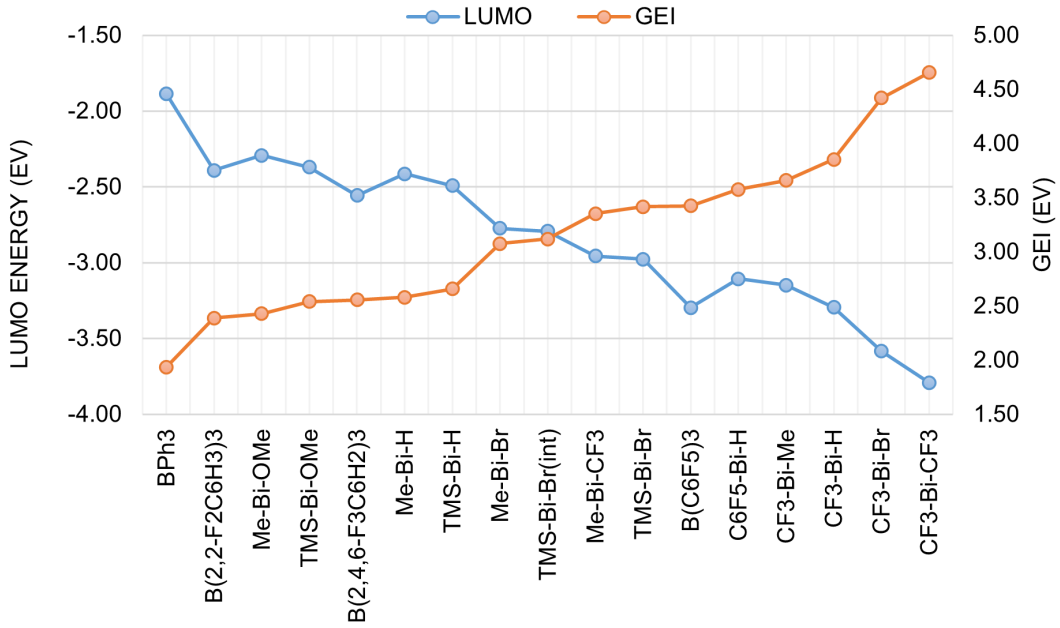

Figure 3.4: LUMO energies and GEI values for derivatives of selected bismuth and boron Lewis acids at the PBE0(D3(BJ))def2-TZVP level in the gas phase.

The observed difference is presumably due to the substituent proximity to the site of Lewis acidity (the vacant *p*-orbital on the metal center). Notably several derivatives of X–Bi–Y are found by this measure to be stronger Lewis acids than the commonly employed borane Lewis acid, $B(C_6F_5)_3$ (Figure 3.4).

The electron affinities of this group of Lewis acids was estimated by calculating the energy change upon addition of one electron with and without geometric relaxation. Minor geometric changes occur upon the addition of one electron; the

Bi–$N_{internal}$ and Bi–$N_{external}$ distances are elongated by approximately 0.05 and 0.02 Å, respectively. The minor geometric changes compliment the small energy differences observed between frozen and optimized geometries upon reduction (Figure 3.5). The reduction energies align with the trend predicted for LUMO energies and GEI values, and together, these calculated values demonstrate that it is possible to tune the Lewis acidity of **3.1-Bi** through careful ligand choice. These calculations also demonstrate that some derivatives are more Lewis acidic or comparable to calculated values for polyfluorinated boranes (see values for $B(C_6F_5)_3$).

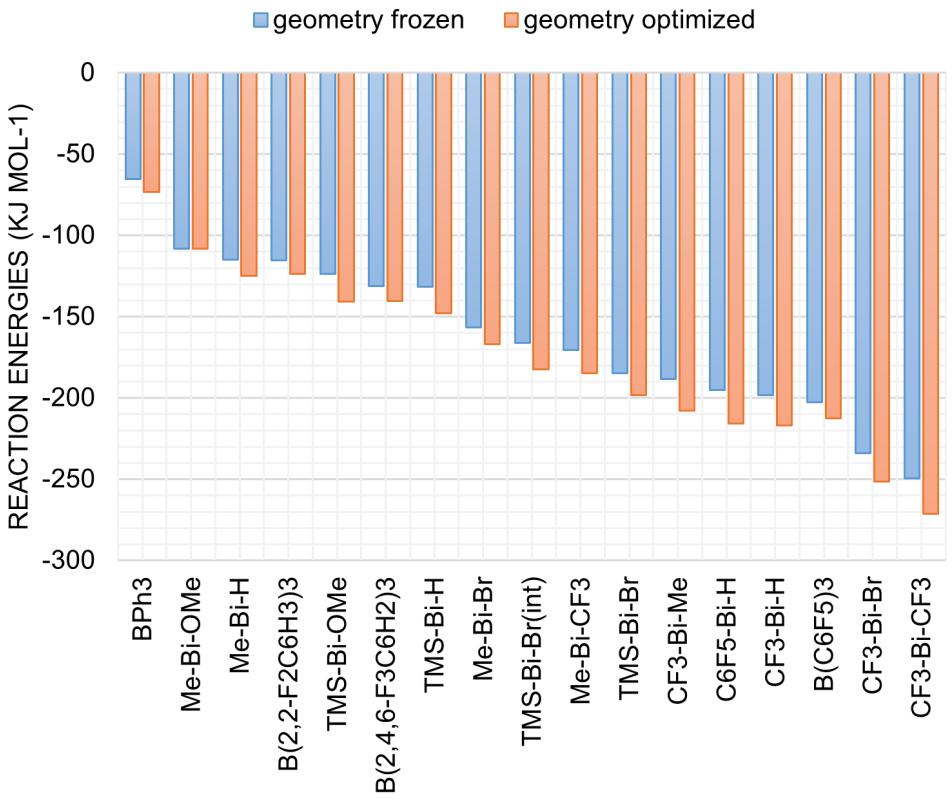

Figure 3.5: One electron reduction energies with and without geometry optimization for selected bismuth and boron Lewis acids at the PBE0(D3(BJ))/def2-TZVP level in the gas phase.

3.2.4 Ligand Affinity: Ligand Coordination Energies, Fluoride Ion Affinities (FIAs) and HSAB Considerations

While the previous section considered the intrinsic electronic properties of **2.1-Bi** with different ligand substituents, section 3.2.4 aims to consider ligand binding

affinity, which is the primary experimental consideration in the context of catalysis. We chose to examine the binding affinity of **2.1-Bi** towards trimethylamine oxide (a relatively small ligand) to minimize steric effects. Upon coordination of **2.1-Bi** to TMAO, the LUMO remains metal-centered and is a partially filled *p*-orbital (Figure 3.6). In contrast, the LUMO of the 1:1 adducts of Me_3NO with triarylboranes lie on the aryl rings and does not allow coordination of a second ligand. The coordination of a second molecule of TMAO to **2.1-Bi** is exothermic and of equal energy to the addition of the first ligand (Figure 3.7).

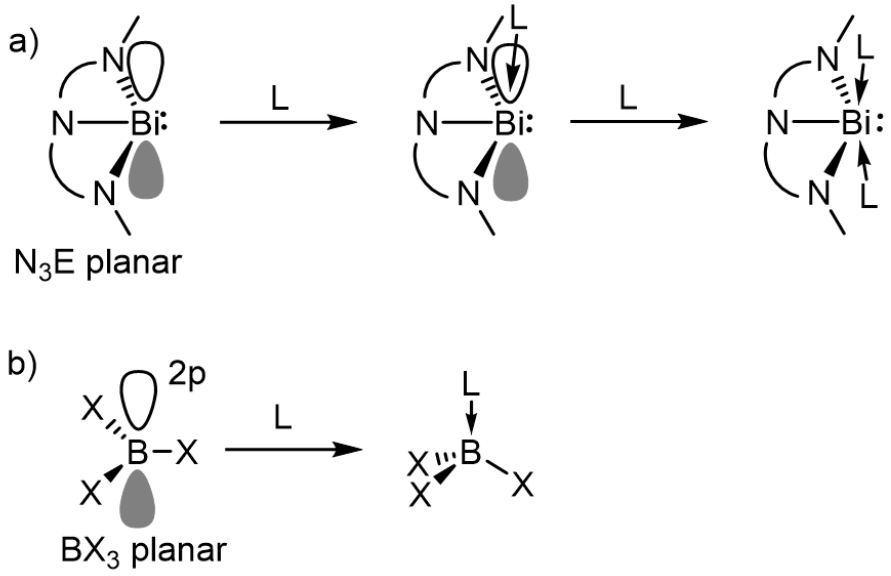

Figure 3.6: Orbital availability for (a) ligand coordination in planar bismuth compounds and (b) boranes.

This indicates a degree of unquenched Lewis acidity at the metal center and demonstrates that the origin of the Lewis acidity in this system is partially dependent on orbital availability. In contrast, boranes are small and the second lobe of the *p*-orbital is unavailable for addition of a second ligand to a ligand-borane adduct. This was further investigated using an energy decomposition analysis (EDA) involving the 1:1 and 1:2 adducts between CF_3–Bi–CF_3 and $ONMe_3$ (Table 3.1). The ΔE_{int} values confirm that the addition of the second ligand is as favorable as the first one in CF_3–Bi–CF_3. The ΔE_{orb} term is the stabilizing factor in both 1:1 and 1:2 adducts, accounting for $> 65\%$ of the contributions to the total attractive interactions. The analogous EDA results for $B(C_6F_5)_3$ show a larger relative contribution

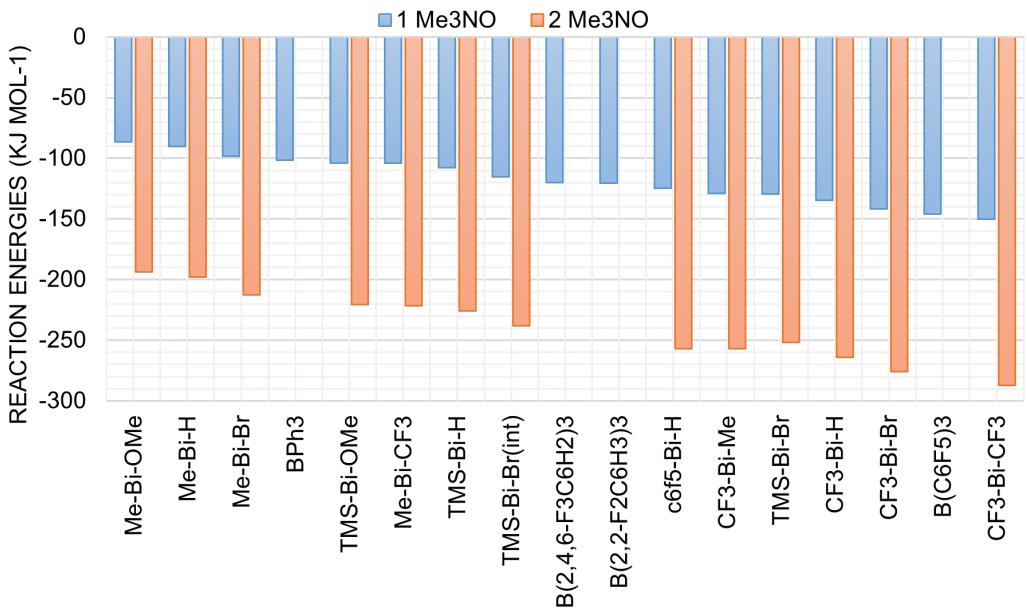

Figure 3.7: Calculated reaction energies for addition of one or two Me_3NO ligands to bismuth and boron-based Lewis acids.

from orbital interactions (ca. 75%), presumably due to the similar sizes and better overlap of the $2p$–$2s$ bonding orbitals than the $6p$–$2p$ orbitals in the bismuth derivative. The dominance of orbital interaction contrasts the long-established history of noncovalent metal–oxygen interactions in hypervalent bismuth complexes[159] and further highlights the unique origins of Lewis acidity in X–Bi–Y compounds (via a vacant $6p$ orbital, not a σ-hole interaction), furthering validating the analogy to triarylboranes. As expected, dispersion plays a minor role, consisting of only 3% of the favorable bonding interactions. Although Pauli repulsive forces increase as a second ligand is coordinated, the electrostatic and orbital contributions increase in magnitude to overcome the Pauli repulsive forces, with the relative contributions remaining approximately equivalent to what is observed in the 1:1 adducts.

Fluoride ion affinites were calculated for derivatives of **2.1-Bi** in the gas-phase. Although our previous work has demonstrated the need for a solvent model when considering the absolute Lewis acidity in the gas-phase,[160] FIA calculations without a solvent model are still valid as long as relative trends and not absolute values are discussed. The Lewis acidity trends observed with LUMO energies and GEI values are well aligned with calculated FIA values (Figure 3.8). Electonegative substituents

Parameter	CF_3–Bi–CF_3 + 1 Me_3NO	CF_3–Bi–CF_3 + 2 Me_3NO	$B(C_6F_5)_3$ + 1 Me3NO
ΔE_{int}	-114.1	-289.8	-277.1
ΔE_{Pauli}	1101.8	1836.3	2601.8
ΔE_{elstat}	-373.3(29.9%)	-603.8 (28.4%)	-685.5 (23.8%)
ΔE_{orb}	-834.7 (66.9%)	-1452.3 (68.3%)	-2156.7 (74.9%)
ΔE_{disp}	-37.9 (3.0%)	-70.0 (3.3%)	-36.7 (1.3%)

Table 3.1: Energy Decomposition Analysis for the 1:1 and 1:2 adducts of Me_3NO and CF_3–Bi–CF_3 and the 1:1 adduct of Me_3NO and $B(C_6F_5)_3$. The ΔE values are given in kJ mol^{-1}. ΔE_{int} (interaction energy) is the energy change upon E–O bond formation starting from fragments frozen in the geometry found in the bonded compound, assuming closed shell fragments. Values in parentheses denote percentages of overall attractive interactions.

in the X position have a more significant impact on the FIA than electronegative substituents in the Y position. The FIA of TMS–Bi–Br is within error of the FIA of TMS–Bi–Br_{int}, indicating that the placement of substituent *meta* to the internal or external nitrogen atoms may have a smaller influence on the overall Lewis acidity than predicted by GEI and LUMO energy values. Small differences exist within the relative Lewis acidities of perfluorinated boranes and derivatives of **2.1-Bi** when compared to predictions based on GEI and LUMO energy values.

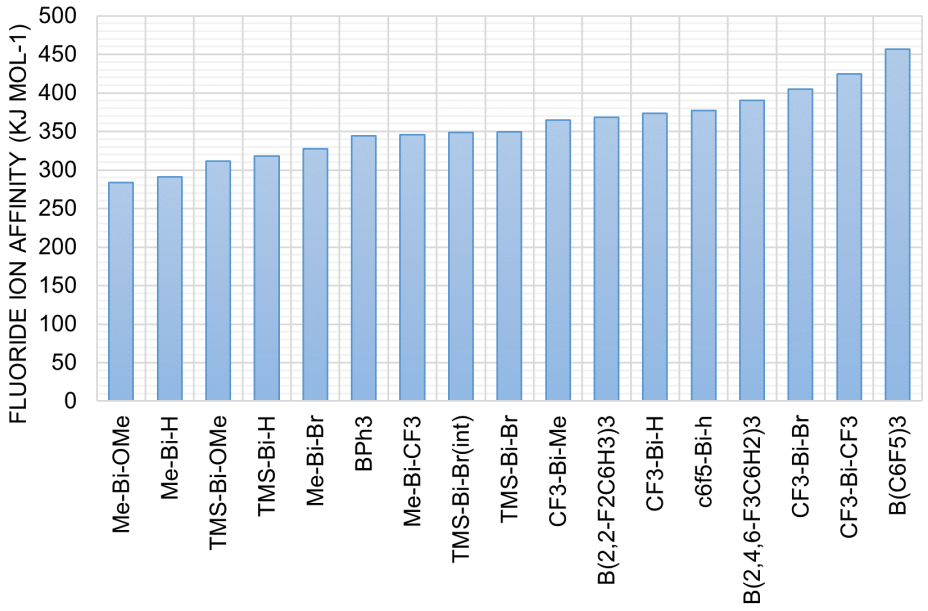

Figure 3.8: FIA values for derivatives of selected bismuth and boron Lewis acids at the PBE0(D3(BJ))/def2-TZVP level in the gas phase.

For example, FIA values predict $B(C_6F_5)_3$ (FIA 456 kJ mol^{-1}) to be a stronger Lewis acid than CF_3–Bi–CF_3 (FIA 424 kJ mol^{-1}), whereas the GEI predicts $B(C_6F_5)_3$ (GEI 3.42 eV) to be a weaker Lewis acid than CF_3–Bi–CF_3 (GEI 4.65 eV). Because overall Lewis acidity trends are maintained, small differences in the specific ordering of Lewis acid strength are not discussed at length.

We also attempted to classify the acidity of **2.1-Bi** using Pearson's Hard and Soft Acid and Base (HSAB) principle.[161] Because all experimental efforts towards isolating adducts between **2.1-Bi** and soft donors (i.e. Me_3PS) failed, we turned to DFT methods. The coordination strength of CF_3–Bi–CF_3 towards Me_3PS (–106.1

kJ mol^{-1}) is slightly less than the coordination strength towards Me_3PO (–127.4 kJ mol^{-1}). Analogous calculations towards $B(C_6F_5)_3$ show significantly different coordination preferences (Me_3PS –69.2 kJ mol^{-1}; Me_3PO –123.7 kJ mol^{-1}). We therefore conclude that unlike the computationally and experimentally verified classification of perfluorinated boranes as a hard acceptor,[142] derivatives of **2.1-Bi** lie on the border between hard and soft and do not show a preference in their interactions with hard or soft acids.

3.3 Conclusion

An assessment of the Lewis acidity of the planar bismuth Lewis acid was completed using DFT methods. The effects of sterics and electronics (electron-donating and electron-withdrawing substituents on the ligand) indicate that CF_3–Bi–CF_3 has the strongest Lewis acidity and is comparable in strength to perfluorinated boranes such as $B(C_6F_5)_3$. Unlike boranes, however, the bismuth derived Lewis acids can readily coordinate more than one ligand (potentially setting the stage for future ligand coupling reactions) and show no preference for hard or soft Lewis base interactions.

Chapter 4

Synthesis and Reactivity of Antimony and Bismuth Hydrides

Portions of this work have appeared in **K. M. Marczenko**, J. A. Zurakowski,† K. L. Bamford, J. W. M. MacMillan,† S. S. Chitnis, *Angew. Chem. Int. Ed.*, **2019**, *58*, 18096-18101 (Full Paper; DOI: 10.1002/anie.201911842), and J. M. MacMillan,† **K. M. Marczenko**, E. R. Johnson, S. S. Chitnis, *Chem. Eur. J.*, **2020**, *26*, 17134-17142 (Full Paper; DOI: 10.1002/chem.202003153).

Contributions to the manuscript: KMM completed all X-ray crystallography. KMM and JAZ completed synthetic work and reactivity studies. KLB and SSC conceived the original idea. JMM completed mechanistic studies. SSC supervised the project. EJ and SSC performed the computational studies and wrote the manuscripts. † denotes undergraduate author.

4.1 Introduction

Diagonal relationships are often found between pairs of adjacent atoms in the 2nd and 3rd rows of the periodic table. These pairs exhibit similar properties and can be used as a predictor of reactivity.[162] For example, carbon and phosphorus both have similar electronegativities, exhibit allotropes, and can form strong double and

triple bonds. Chapter 2 discussed bismuth and antimony complexes within a constrained triamide environment, whose molecular and electronic structures are similar to boranes. Each featured a neutral, planar, trivalent p-block element with a vacant p-orbital perpendicular to the molecular plane.[122126] Given the similarity in the Pauling electronegativity of boron (2.04), bismuth (2.02), and antimony (2.03), we were interested in investigating the potential of a diagonal relationship between light Group 13 elements and heavy Group 15 elements. We recognized that the LUMO of binary halides SbX_3 and BiX_3 consists of two E–X σ^* orbitals that are of similar symmetry to the vacant p-orbital of boranes (Figure 4.1). As a result, SbX_3 and BiX_3 exhibit Lewis acidic behaviour to a variety of ligands and participate in metathesis chemistry – both classic features of boranes.[163164165166167]

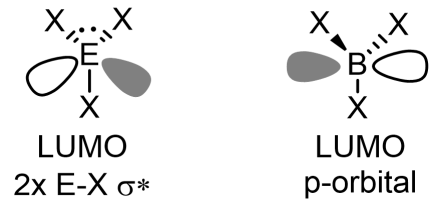

Figure 4.1: Similarity of LUMOs of Group 15 and Group 13 elements.

However, spontaneous and catalyst-free hydroboration (another classical reaction of boranes) has no counterpart in antimony or bismuth chemistry, although examples of hydrophosphanation and hydroarsanation are known. The low kinetic stability of bismuth hydrides has allowed for the isolation of a single example in the solid-state, preventing the development of hydrobismuthanation reactivity.[81]

In contrast, antimony hydrides are relatively stable, and several examples have been isolated.[66717273168741691701711172] Previous work by Breuing[173] and Huang[174] showed overall hydrostibanation of C=C and C=O bonds with diphenylstibane. Importantly, this required radical initiators, transition metal catalysts, and/or main-group Lewis acid mediators. Nesmeyanov and Brandt also reported that they observed hydrostibanation of azobenzene and phenylacetylene. However, evidence for this reaction was based on infrared and mass spectrometric analyses of reaction mixtures and the scope and mechanism of the reaction was not explored.[175176] Therefore, catalyst and additive-free hydrostibanation has not yet been established.

We hypothesized that Breunig and Huang did not observe hydrostibanation un-

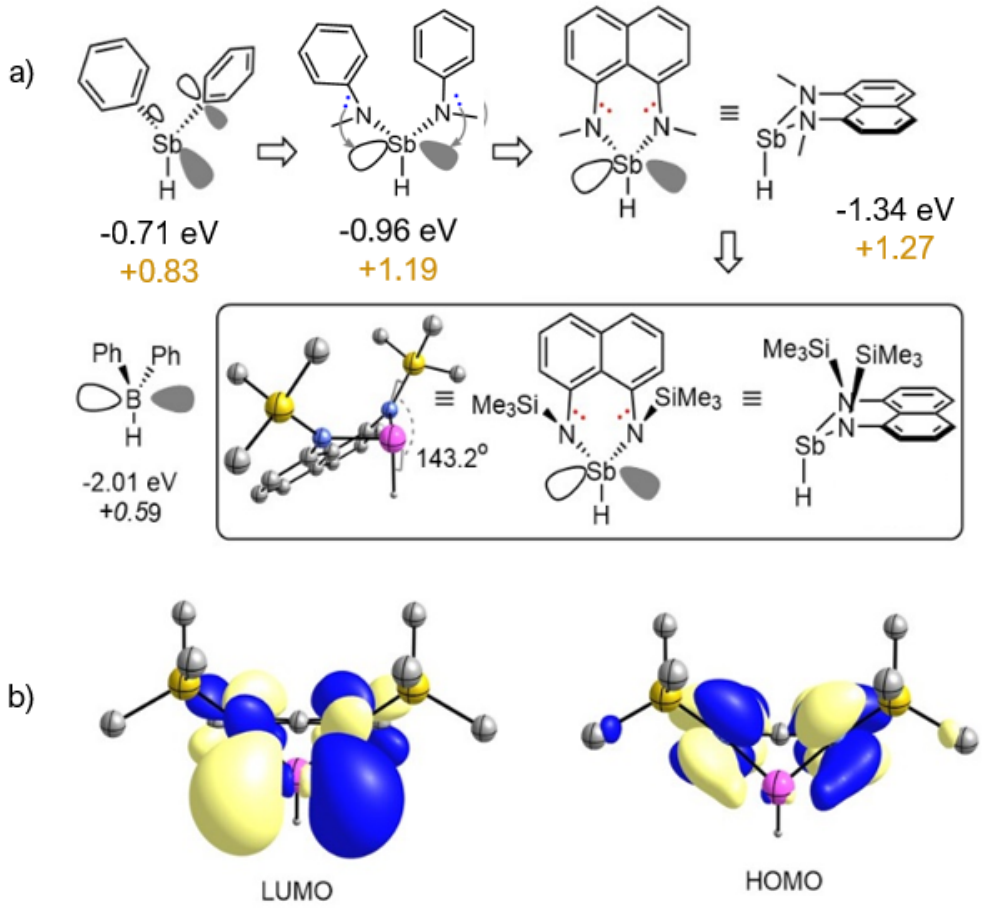

Figure 4.2: a) Significant LUMO contributions, LUMO eigenvalues (eV), and NBO partial charges (gold font) for Sb atoms in the considered stibanes and Ph_2BH, b) calculated LUMO and HOMO for **4a**.

der catalyst-free conditions with Ph_2SbH due to i) extensive delocalization of the LUMO over the adjacent phenyl rings and ii) the high energy of the LUMO (–0.71 eV, PBE1/def2-TZVP level). The diffuse nature and high energy of the LUMO render the stibane incapable of engaging unsaturated substrates. Amino substituents increase the Sb–X bond polarity resulting in less mixing of the atomic orbitals and a metal centered LUMO. Natural bond orbital (NBO) partial charges (Figure 4.2) indicate that amino groups also increase electropositivity at the Sb center.

However, because N(lone pair)→Sb(σ^*) back donation (curly arrows in Figure 4.2a) is possible from the amino substituents to the Sb center, the LUMO energy is

not significantly lowered, and gives a high energy of –0.42 eV in $(Me_2N)_2SbH$. Our chosen diamino naphthalene ligand framework requires a distortion of the amines to fit the antimony atom within the NC_3N bay,[177178179] causing the N lone pairs to twist away from the plane of the Sb–N σ^* LUMO, lowering the LUMO energy to –1.34 eV (Figure 4.2b). The silyl group on the amino substituents are easily varied using different silane precursors, providing steric protection against bimolecular H_2 loss.[716673169] Therefore, the use of a fused naphthyl substituent that provides i) a sterically shielded metal hydride, and ii) a metal-centred LUMO that is significantly lower in energy than in Ph_2SbH.

4.2 Hydrostibanation

4.2.1 Synthesis and Characterization

Lithiation of 1,8-naphthalene diamine followed by quenching with the appropriate chlorosilane yielded ligands **4.1(a–c)** in high yields (Figure 4.3a). Chlorostibanes **4.2(a–c)** were obtained in 52–69% yields by lithiating the respective ligand and quenching with $SbCl_3$. X-ray crystallography was used to establish the solid-state structures of the chlorosilanes. Each derivate features a three-coordinate pyramidal antimony center coordinated to a chloride atom and a bidentate ligand. The structural aspects of the chlorostibanes (i.e. bond lengths and angles) do not vary significantly.

Dissolving the chlorostibanes in hexane and addition to a solution of $LiHBEt_3$ in hexane/THF at –30°C yielded antimony hydrides **4.3(a–c)**. Although these reactions proceeded in reasonable yields for hydrides **4.3b** (77%) and **4.3c** (58%), hydride **4.3a** was found to be a thermally unstable oil and was only characterized spectroscopically as part of a reaction mixture. Hydrides **4.3b** and **4.3c** are air-sensitive but indefinitely stable in the solid-state under an inert atmosphere of dry nitrogen. They are not stable in halogenated solvents, insensitive to ambient light, and slowly decompose to the respective ligand and metallic Sb upon heating above 50 °C. The hydride positions in the X-ray crystal structures of **4.3b** and **4.3c** were

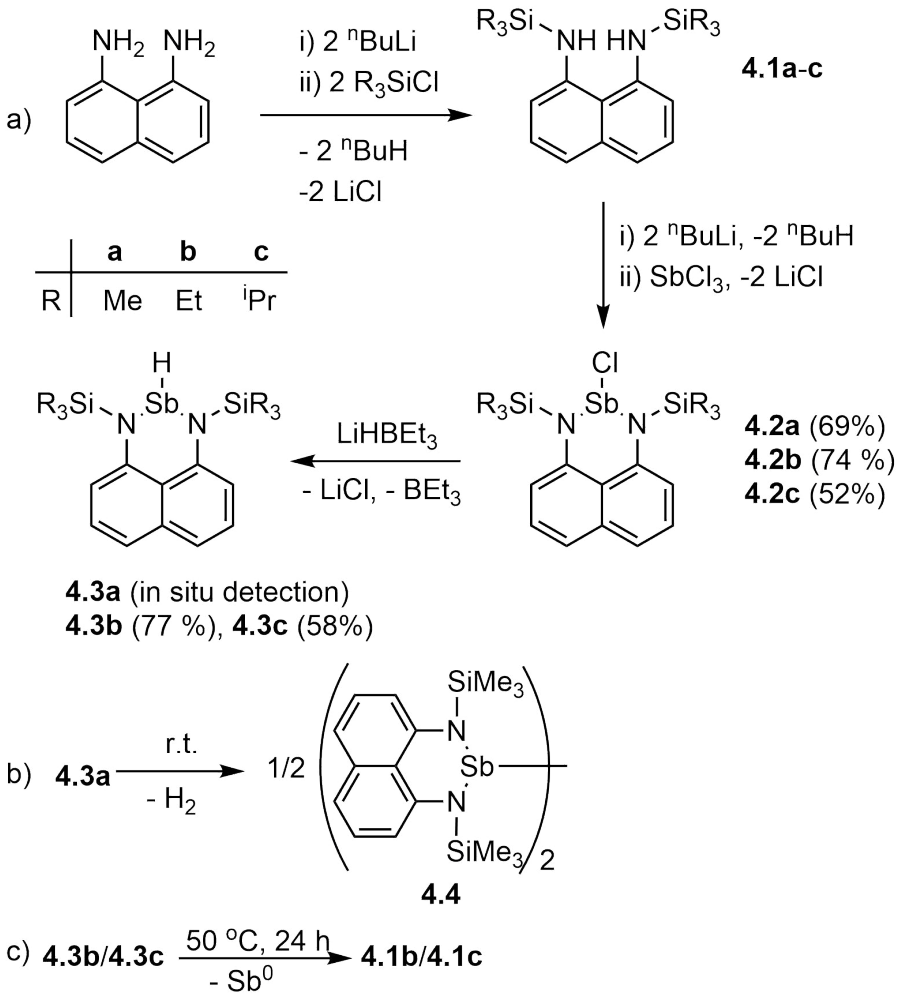

Figure 4.3: a) Synthesis of compounds **4.1**, **4.2**, and **4.3**. b) Decomposition of **4.3a** to give **4.4**. c) Thermal decomposition of **4.3b** and **4.3c** in C_6D_6.

unambiguously established using electron density found within the difference map. The three-coordinate antimony centers have a pyramidal geometry with approximately equivalent Sb–N bond lengths (Figure 4.4). The Si–N–Sb–H dihedral angles have values of 146.7(1)° in **4.3b** and 143.9(1)° in **4.3c**, which is comparable to the value calculated for **4.3a** (143.2°).

The ^{1}H NMR spectra of the stibanes in C_6D_6 show sharp resonances for the Sb–H fragment with the chemical shift values increase with the steric bulk of the N-silyl group (9.65 ppm for **4.3a**, 9.88 ppm for **4.3b**, and 10.04 ppm for **4.3c**). Infrared spectroscopy revealed Sb–H stretching frequencies of 1883 cm^{-1} and 1863 cm^{-1} for **4.3b** and **4.3c**.

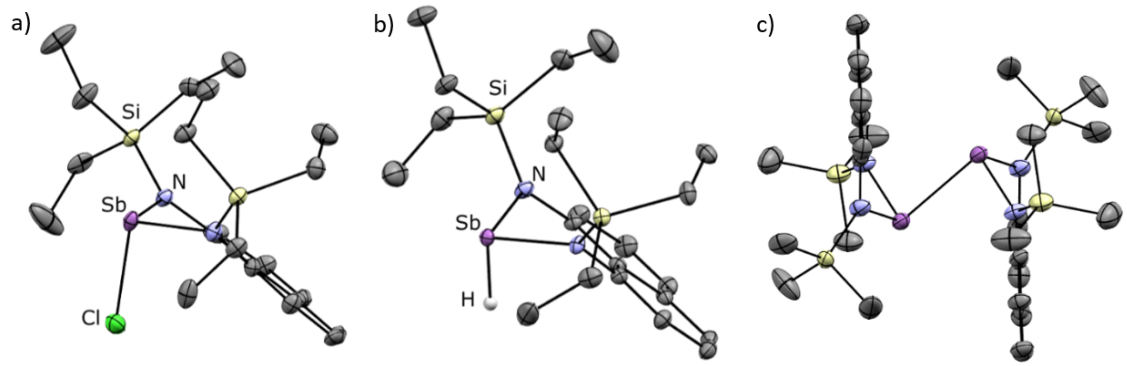

Figure 4.4: Molecular structures of **4.2b** (a), **4.3b** (b), and dimer **4.4** (c) in the solid-state as determined by X-ray crystallography. Thermal ellipsoids are drawn at the 50% probability level. Nonessential hydrogen atoms have been omitted.

4.2.2 Reactivity

Hydride **4.3b** was chosen to test hydrostibanation reactivity due to its high synthetic yield and relatively low cost of the chlorosilane precursor. The hydridic nature of the Sb–H bond was assessed by combining **4.3b** with $[Ph_3C][B(C_6F_5)_4]$. The ^{1}H NMR showed the disappearance of the hydride signal and appearance of Ph_3CH, demonstrating H^- transfer from **4.3b**. Attempts to crystallize the stibenium cation by-product have thus far failed.

Alkynes. The addition of phenylacetylene to **4.3b** (Figure 4.5) in C_6D_6 at room temperature showed complete disappearance of the Sb–H and acetylene signals after 24 hours. The ^{1}H NMR spectrum of the crude reaction mixture showed the formation of a single product, **4.5**, containing two olefinic resonances at 6.32 and 7.07 ppm ($^3J_{HH}$ = 12.4 Hz), indicating anti-Markovnikov addition and a single isomer. Single-crystal X-ray diffraction unambiguously confirmed the formation of the Z isomer (Figure 4.6). Similar results were observed for 4-methyl-phenylacetylene and 4-trifluoromethyl-phenylacetylene.

Alkenes. Hydrostibanation of electron-rich and electron-poor alkenes was also achieved (Figure 4.5). The reaction between 3-vinylanisole and **4.3b** required 5 days to reach 60% product conversion to **4.6** at room temperature. The crude ^{1}H NMR spectrum showed two new methylene resonances, indicating the formation of the desired hydrostibanation product. The reaction of **4.3b** with acrylonitrile

proceeded much faster and showed quantitative conversion after 24 hours, yielding **4.7**. The ^{1}H and two-dimensional COSY NMR spectra for this compound indicate anti-Markovnikov addition (Figure B.28). This was also confirmed by X-ray crystallography (Figure 4.6). The crystal structure shows intermolecular Sb—NCR interactions comprising a dimer and indicating unquenched Lewis acidity at the antimony center, as suggested by the LUMO being highly localized on the metal.

Aldehydes. No reaction was observed between **4.3b** and benzaldehyde or p-anisaldehyde over a 24-hour period at room temperature. However, when **4.3b** was added to p-trifluoromethyl benzaldehyde in hexane, conversion to the alkoxy stibane **4.8** was detected in 96% yield (Figure 4.5). The product could not be separated from excess aldehyde due to the oily nature of the reactant. Still, HRMS and the appearance of a methylene resonance at 4.48 ppm in the ^{1}H NMR spectrum confirmed its formation. DFT calculations indicate that hydrostibanation is favourable for both electron-rich and electron-poor aldehydes ($\Delta G_{reaction}$ p-anisaldehyde = –10.1 kcal mol^{-1}; $\Delta G_{reaction}$ p-trifluoromethyl benzaldehyde = –14.8 kcal mol^{-1}). Therefore, the lack of a reaction involving electron-rich substrates is viewed as a kinetic obstacle, suggesting that the aldehyde acts as an electrophile in the rate-limiting step.

Azobenzene. The addition of **4.3b** to trans-azobenzene in C_6D_6 resulted in the formation of **4.9** in 94% yield, as indicated by the N–H resonance at 5.02 ppm in the ^{1}H NMR spectrum, an N–H stretch in the infrared spectrum at 3353 cm^{-1}, and the single-crystal X-ray structure (Figure 4.6). A small amount (6%) of diphenylhydrazine was detected by ^{1}H NMR spectroscopy, indicating hydrogenation of azobenzene (Figure 4.5). The Sb–Sb bonded species **4.10** (trace amounts) was also identified by X-ray crystallography, accounting for the observed redox chemistry.

Other Substrates. The attempted hydrostibanation of CO_2, acetone, acetophenone, CO, or CH_3CN was unsuccessful due to the multiple bond strength in these substrates. The hydrostibanation of sterically hindered substrates such as 1,2-diphenyl-acetylene and benzophenone was also unsuccessful. These observations highlight the current limitations of hydrostibanation, which may be conquerable with additional ligand tuning.

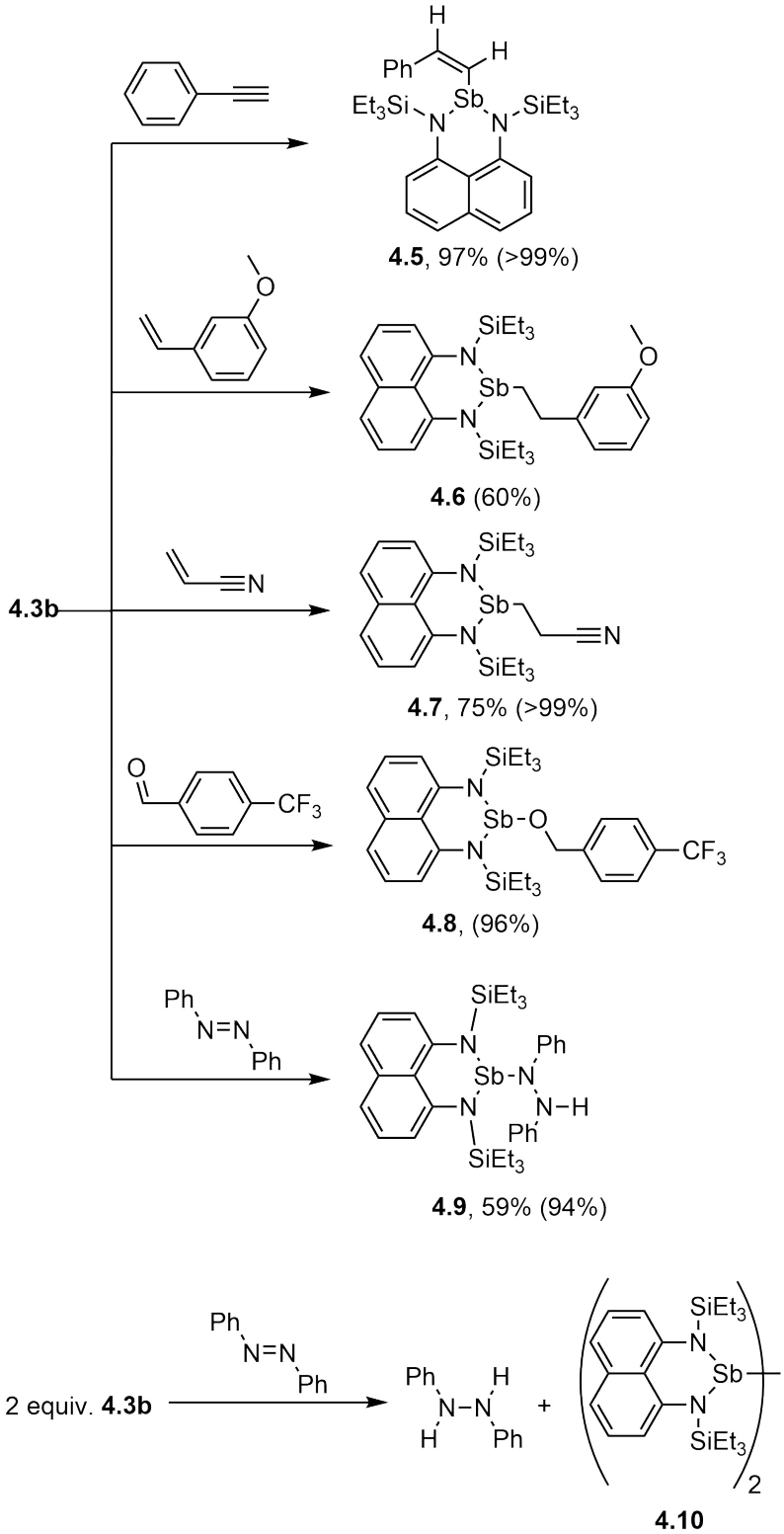

Figure 4.5: Hydrostibanation reactivity of **4.3b**. Yields are for isolated materials. Yields in parentheses were determined from NMR spectroscopy.

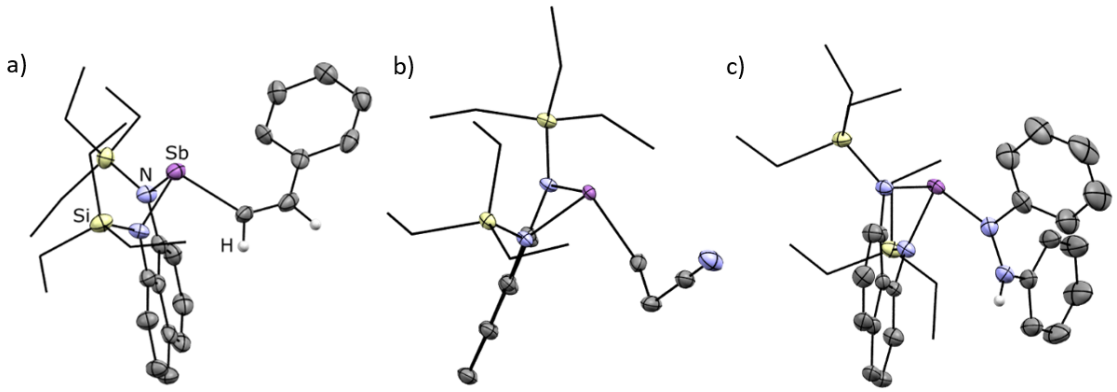

Figure 4.6: Single-crystal X-ray structures of **4.5** (a), **4.7** (b), and **4.9** (c). Thermally ellipsoids are shown at the 50% probability level. Some hydrogen atoms have been remove and silane substituents are shown in wireframe for clarity.

4.2.3 Mechanism

Kinetic experiments were conducted to determine if the hydrostibination of phenylacetylene proceeded through a mechanism with ionic or radical based intermediates. Time-resolved ^{1}H NMR spectroscopy was used to monitor the progress of the reaction through the disappearance of the Sb–H resonance at 9.88 ppm. Concentration vs. time-plots showed that the hydrostibination of phenylacetylene proceeds via 2nd order kinetics, with a 1^{rst} order dependence on each reactant (rate = k_b[stibine][acetylene]). We next investigated the influence of solvent polarity, alkyene substitution, and radical based additives (Table 4.1). Two main observations were gathered from this data:

- A dramatic increase in the reaction rate is observed when the solvent polarity is reduced from C_6D_6 to C_6D_{12} (Table 4.1 (entry 2); Figure 4.7).
- A dramatic decrease in the reaction rate is observed when radical scavengers (O_2, (2,2,6,6-Tetramethylpiperidin-1-yl)oxyl (TEMPO)) are present during the reaction (Table 4.1 (entries 1, 4, and 5); Figures 4.8 and 4.9).

Combined, these observations indicate that a mechanism with radical intermediates is more probable than a model with ionic species (Figure 4.10).

Entry	Arylacetylene	Conditions	$k_b[x10^{-2}M^{-1}s^{-1}]$
1	^{Tol}Ac	C_6D_6, 300K, N_2	0.436±0.019
2	^{Tol}Ac	C_6D_{12}, 300K, N_2	3.587±0.200
3	^{Ph}Ac	C_6D_6, 300K, N_2	0.900±0.080
4	^{Ph}Ac	C_6D_6, 300K, N_2, TEMPO	0.060±0.008
5	^{Tol}Ac	C_6D_6, 300K, O_2	0.030±0.002
6	^{Tol}Ac	C_6D_6, 300K, N_2, UV	0.639±0.026
7	^{FTol}Ac	C_6D_6, 300K, N_2	4.60±0.600
8	^{Tol}Ac	C_6D_6, 305K, N_2	0.677±0.003
9	^{Tol}Ac	C_6D_6, 310K, N_2	1.125±0.023
10	^{Tol}Ac	C_6D_6, 315K, N_2	1.365±0.033

Table 4.1: Bimolecular rate constants of arylacetylene hydrostibanation under varying conditions. ^{Ph}Ac=*p*-H-phenylacetylene, ^{Tol}Ac=*p*-CH_3-phenylacetylene, and ^{FTol}Ac=*p*-CF_3-phenylacetylene.

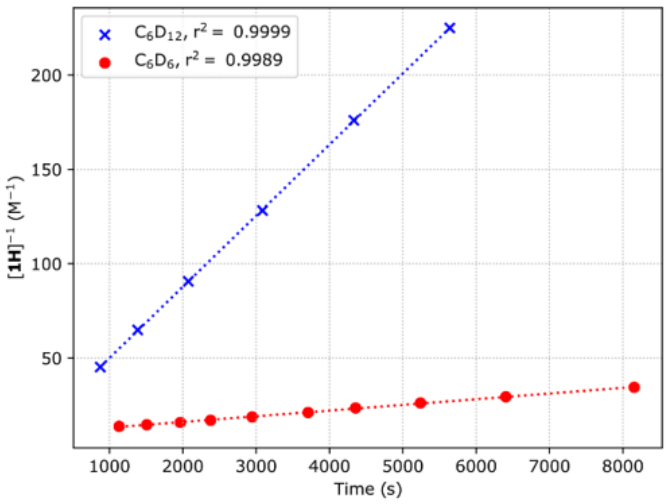

Figure 4.7: Linearized rate data for the hydrostibanation of **^{FTol}Ac** with **4.2b** in C_6D_6 and C_6D_{12}.

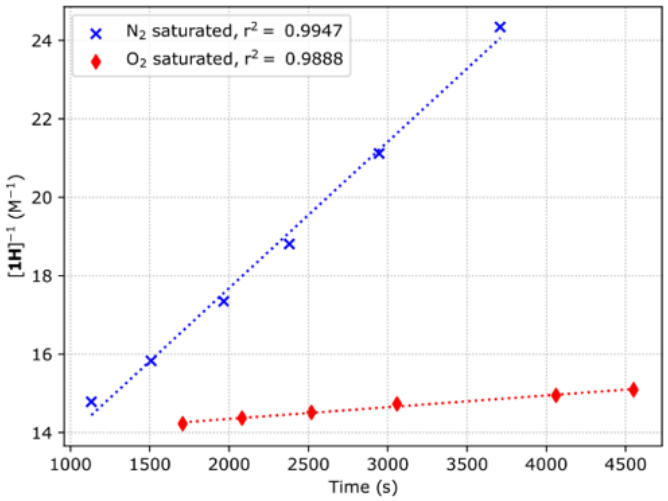

Figure 4.8: Linearized rate data for the hydrostibanation of $^{\mathbf{Tol}}$**Ac** with **4.2b** under and N_2 or O_2 atmosphere.

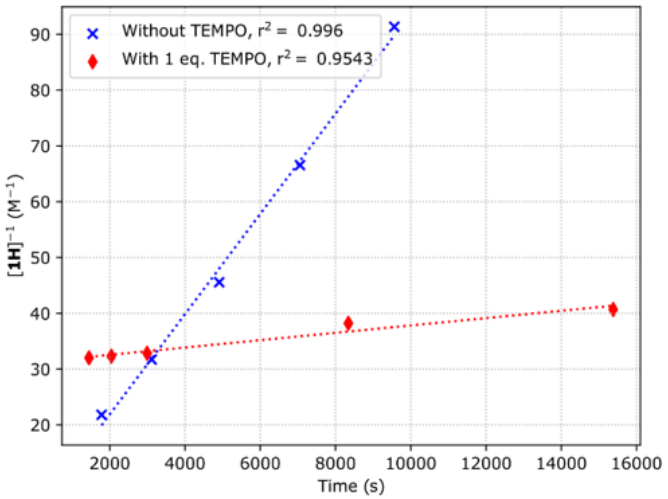

Figure 4.9: Linearized rate data for the hydrostibanation of $^{\mathbf{FTol}}$**Ac** with **4.2b** with or without added TEMPO.

Comparison of the k_b for *p*-H-phenylacetylene, *p*-CH_3-phenylacetylene, and *p*-CF_3-phenylacetylene show clear evidence of an increased reaction rate as the electronegativity of the *para* substituent is increased. This observed trend (^{FTol}Ac > > ^{Ph}PhAc > T^{Fol}Ac) points to a rate determining step where the aryl acetylene behaves as an electrophile (increased electron withdrawing ability correlates to increased electrophilicity).

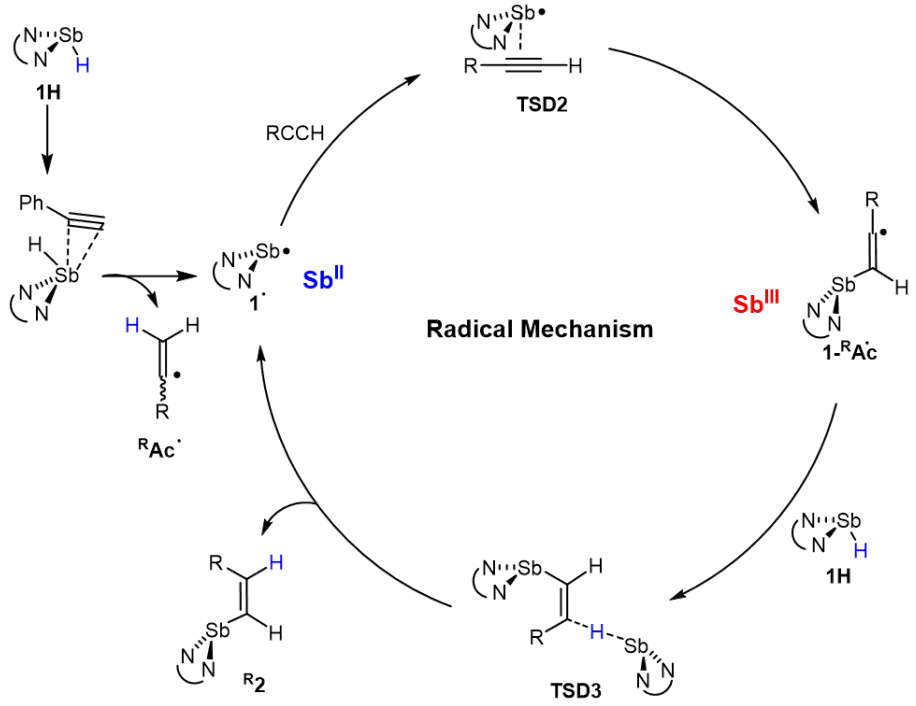

Figure 4.10: The radical mechanism considered in this study.

We then turned towards DFT calculations in collaboration with Prof. Erin R. Johnson (Dalhousie University). The calculated Potential Energy Surface (PES) for the proposed mechanism (Figure 4.11) showed no prohibitive barriers. Transfer of an H atom from **4.3b** to PhAc gives PhAcH and Int1, which is 16.1 kcal mol^{-1} uphill, and the rate limiting step. This step should exhibit bimolecular kinetics, which is in good agreement with our experimentally observed second-order kinetics. The stibinyl radical Int1 adds to an equivalent of PhAc in a stepwise fashion to give stable intermediate Int2 (-0.9 kcal mol^{-1} downhill), which undergoes rearrangement to give Int3 via a 5.4 kcal mol^{-1} high transition state (TS1). As these steps involve coordination of radical Int1 to PhAc, the presence of a donor solvent can compete with PhAc for coordination and slow down the reaction, which is consistent with the

observed relative reaction rates in C_6D_6 and C_6D_{12} (Figure 4.7). Once radical Int3 forms a stable adduct with **4.3b** (Int4, 2.3 kcal mol^{-1} downhill), H-atom transfer via TS2 to Int5 occurs. The structure of TS2 explains the observed Z-olefin selectivity due to the *anti* addition of the H atom. High steric bulk of the stibinyl fragments makes it impossible to arrange in a *syn* configuration, which would be required for formation of the E-alkene. The loosely bound (5.5 kcal mol^{-1}) adduct dissociates to regenerate the stibinyl radical Int1 and yield the hydrostibanation product (^{R}2). It is also important to note that the calculated ΔG values for the H-atom transfer from **4.3b** to TolAc and FTolAc are 16.9 kcal mol^{-1} and 14.2 kcal mol^{-1}, respectively. There, electron deficient arylacetylenes are predicted to undergo more rapid hydrostibanation, as is observed experimentally.

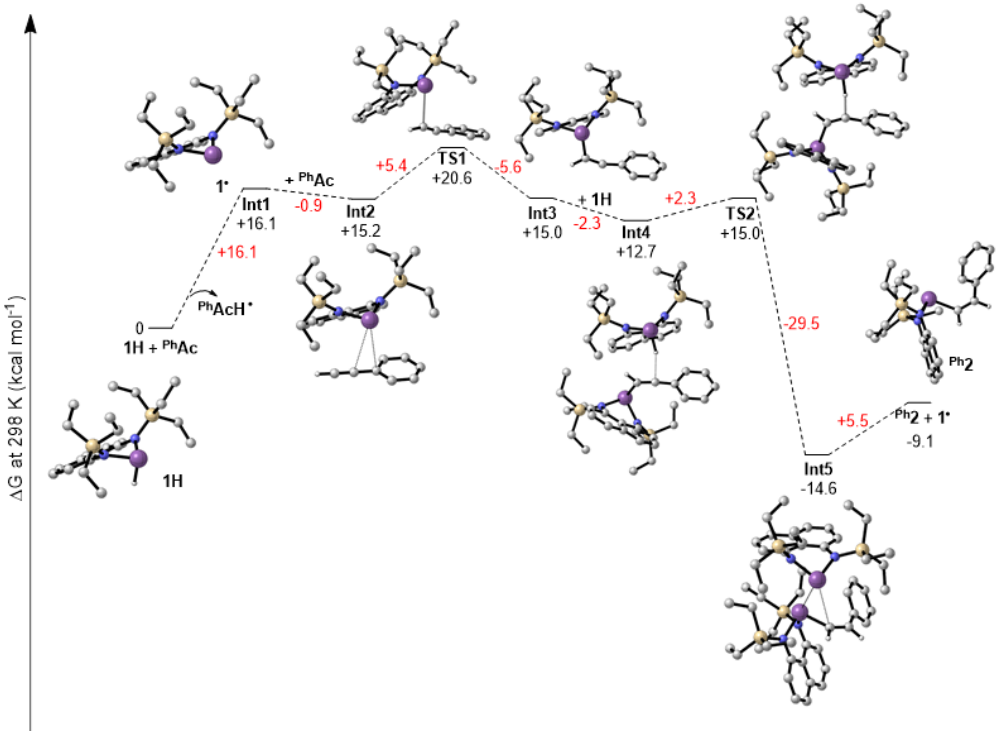

Figure 4.11: DFT-calculated PES for the hydrostibanation of $^{\mathbf{FTol}}$**Ac** with **4.2c** as per the proposed radical mechanism.

4.2.4 Efforts Towards Catalytic Applications

Hydroelementation of phenylacetylenes to give the z-olefin is a characteristic unique to hydrostibanation. Attempts were made to establish step-wise regeneration of the

stibnyl hydride from the iodination of the hydrostibanation product of phenylacetyl (Figure 4.12). The ultimate goal of this part of the project is to achieve high-yield synthesis of z-olefins with catalytic amounts of the stibanyl hydride.

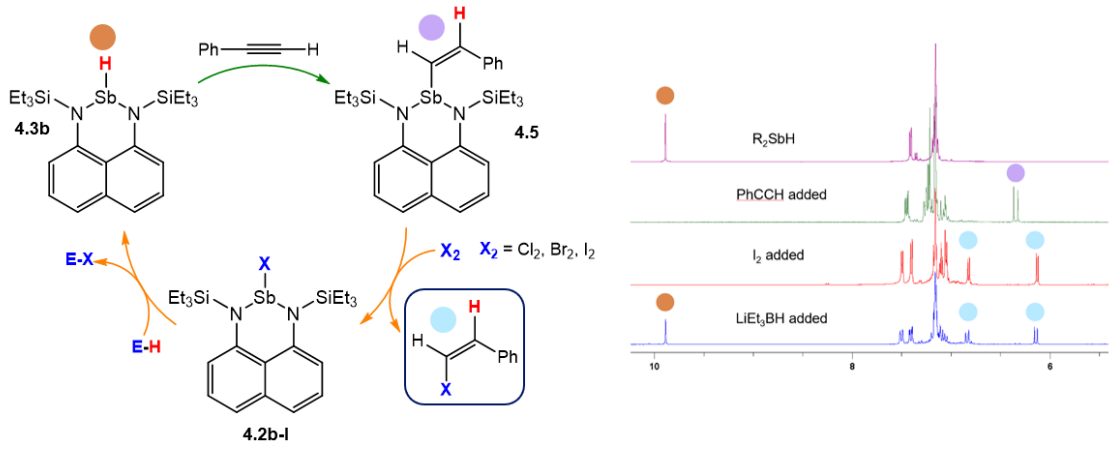

Figure 4.12: Proposed cycle for the generation of z-olefins from catalytic amounts of **4.3b** (left). ^{1}H NMR spectroscopic evidence of one-pot synthesis of z-olefins accompanied with regeneration of **4.3b** (right).

The reaction of compound **4.5** with 1 molar equivalent of methyliodide, methyl triflate, and molecular iodine was examined. Only I_2 was successful in oxidizing **4.5** to the corresponding z-iodo-olefin **4.5-I** and stibanyl iodide **4.2b-I**. Complete conversion was observed within ten minutes at room temperature. Reduction of **4.2b-I** to **4.2b** was accomplished using a 1.0M solution of $LiHBEt_3$ in THF. Unfortunately, combination of phenylacetylene, I_2 and milder reducing agents such as 9-BBN, resulted in the net addition of H–I across the phenylacetylene C≡C triple bond with formation of α-iodostyrene as the major product. This indicates that our chosen oxidizing agent is not compatible with potential reducing agents, ultimately hindering their combined use in a catalytic cycle. However, their compatibility in a stoichiometric one-pot cycle was validated (Figure 4.12 - right), confirming stepwise regeneration of the stibinyl hydride from the iodination of the hydrostibanation products of phenylacetylene. Purification of the desired vinyl iodide product can be accomplished via high-temperature (100 °C) distillation.

4.3 Efforts towards Secondary Bismuthanes

Chlorobismuthanes **4.11(a–c)** were obtained in moderate yields by lithiating the respective ligand **4.1(a–c)** and quenching with $BiCl_3$ (Figure 4.11). X-ray crystallography was used to establish the solid-state structures of the chlorobismuthanes **4.11a** and **4.11b** (Figure 4.12). All attempts to crystallize chlorobismuthane **4.11c** have thus far failed. Each derivative features a three-coordinate pyramidal bismuth center coordinated to a chloride atom and a bidentate ligand. In a similar fashion to the chlorostibanes, the structural aspects of the chlorobismuthanes do not vary significantly and therefore are not discussed. Attempts to synthesize the diaminobismuthanes using the route described above for diaminostibanes **4.3(a–c)** were unsuccessful (Figure 4.11). Addition of $LiHBEt_3$/ THF (1.0 M) to chlorobismuthanes at –30 °C afforded reaction mixtures containing free ligand, unreacted chlorobismuthane, and an unidentified side product. Repeating the reaction at –70 °C afforded higher conversion to the free ligand and side product. Concentration of the crude reaction mixture and storage in the freezer at –30 °C afforded crystals of the side product which was identified by X-ray crystallography as the dibismuthane **4.12** (Figure 4.12). Attempts to rationally synthesize the dibismuthane by reduction of the chlorobismuthane **4.11b** with magnesium were unsuccessful.

Because all efforts to isolate a bismuth hydride were unsuccessful, a "surrogate" approach for hydrobismuthanation was examined. Oestreich et al. established the cyclohexa-2,5-dien-1-yl group as a leaving group at silicon to achieve formal SiH_4 chemistry using stable and easy-to-handle surragates.[180181] Attempts were made to used the approach outlined by Oestreich to isolate the cyclohexadiene derivative **4.13** (Figure 4.11b) which could act as a source of Bi-H. Once isolated, a catalytic amount of tris(pentafluoro)borane could catalyze hydride migration from the CH_2 fragment of the cyclohexadiene substituent to the metal to generate the bismuth hydride accompanied by the loss of benzene (Figure 4.11c). If completed in the presence of unsaturated substrates, hydrobismuthanation may occur before the decomposition of the transient bismuth hydride. ^{1}H NMR spectroscopy of the cyclohexadiene derivative showed a mixture of unconverted starting material and the targeted product **4.13-Bi**, which was identified by the distinct cyclohexadiene

olefin resonances (5.04, 5.11, 5.19 ppm). Attempts to crystallize cyclohexadiene derivative **4.13-Bi** have thus far failed, but the antimony derivative **4.13-Sb** was isolated (Figure 4.15). Heating the unpurified reaction mixture containing **4.13-Bi** to 50 °C for 2 hours gave the dibismuthane **4.12**, H_2 and benzene providing a proof-of-concept that bismuth hydrides can be generated from a bismuth cyclohexadienyl group (Figure 4.11d), even though they have not at present been trapped.

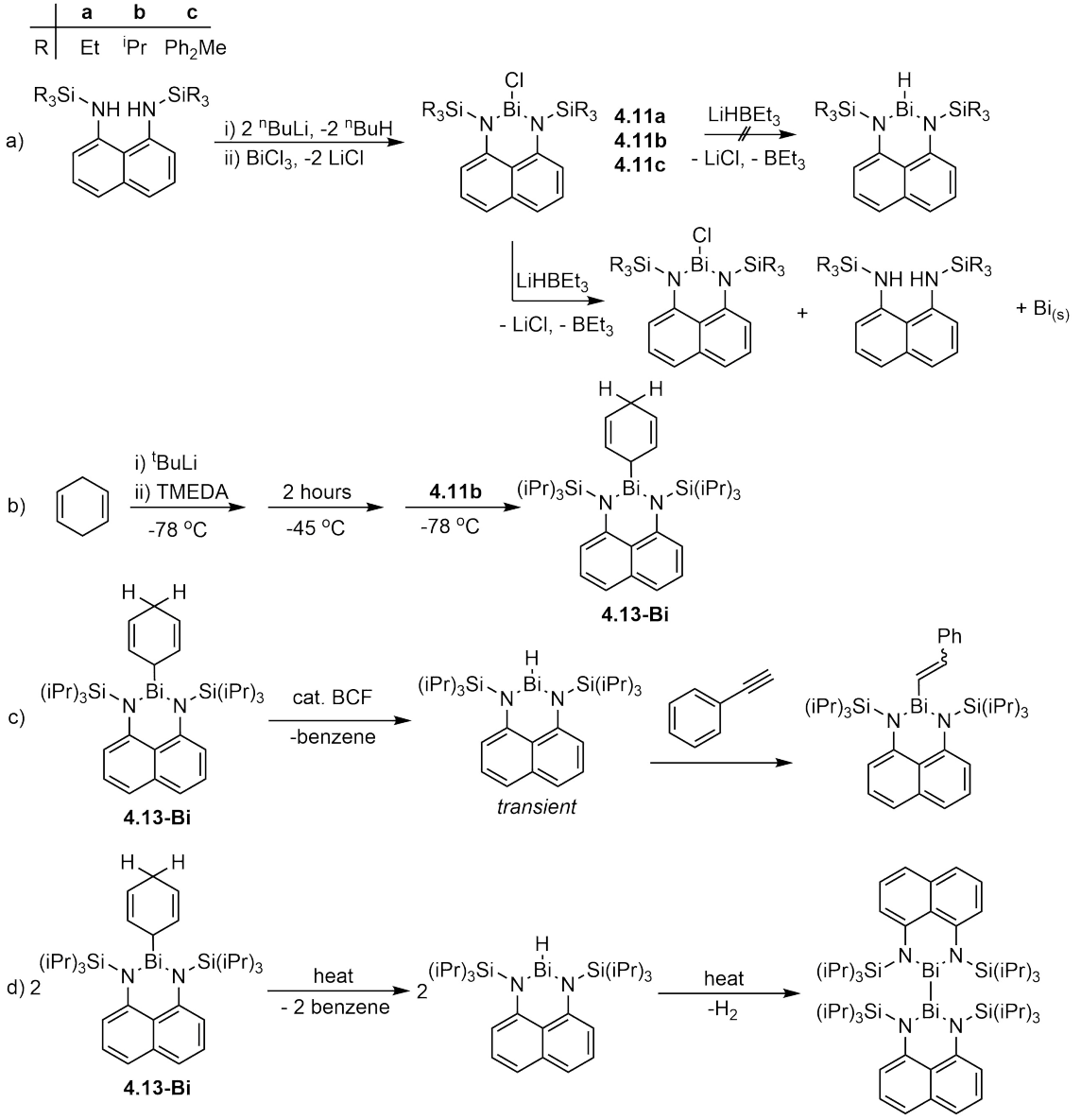

Figure 4.13: a) Synthesis of compounds **4.11(a–c)**. b) Synthesis of **4.13-Bi**. c) Proposed surrogate approach towards hydrobismuthanation. d) Formation of a transient bismuth hydride.

Due to difficulties synthesizing the cyclohexadiene derivatives, attempts were made to generate a transient bismuth hydride in solution from a dibismuthane. This could catalytically convert azobenzene to phenylhydrazine in the presence of ammonia borane via a BiII/BiIII redox couple (Figure 4.16). A 10 mol% loading resulted in 20% conversion, which was determined to be within the error of the methods used. We concluded that catalytic hydrogenation was not achieved, and that stoichiometric conversion occurred (^{1}H NMR spectra showed phenylhydrazine and borazine). This proceeded via a transient bismuth hydride using a dibismuthane initiator.

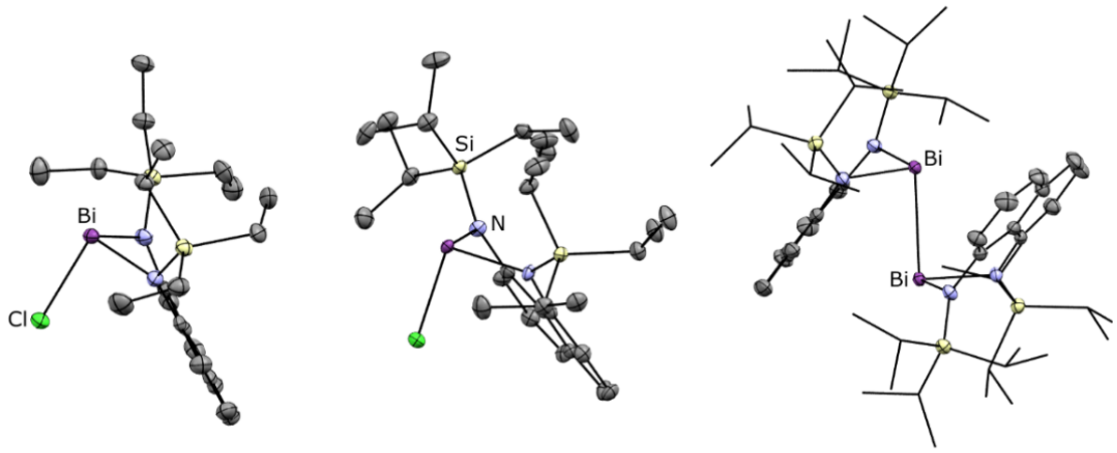

Figure 4.14: Single-crystal X-ray structures of **4.11a**, **4.11b**, and **4.12**. Thermal ellipsoids are shown at the 50% probability level and hydrogen atoms are removed for clarity.

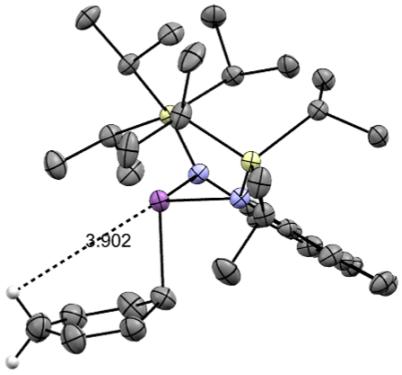

Figure 4.15: Single-crystal X-ray structure of **4.13-Sb**. The distance between the Sb atom and cyclohexadiene hydrogen atom is highlighted. Thermal ellipsoids are shown at the 50% probability level and some hydrogen atoms are removed for clarity.

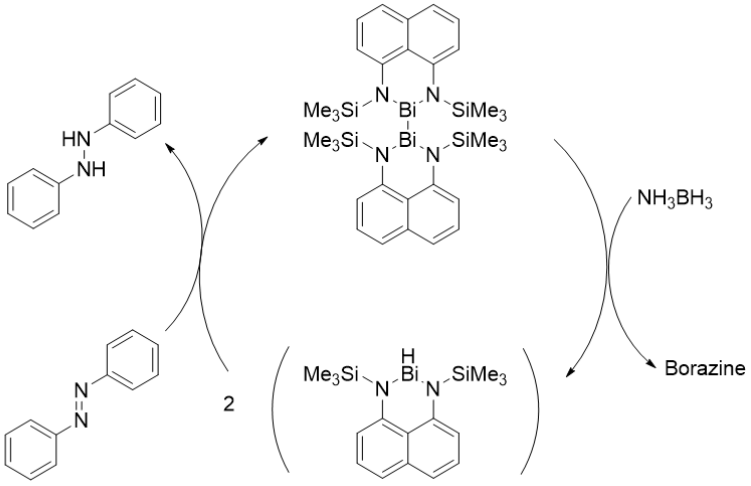

Figure 4.16: Proposed catalytic cyclic for the transfer hydrogenation of azobenzene using a dibismuthene based catalyst.

4.4 Conclusions

In conclusion, this chapter highlighted a new class of antimony hydrides. These stibanes provided access to the first example of additive-free hydrostibanation of C≡C, C=C, C=O, and N=N bonds in high yield. These hydrometallation reactions were accessed through strategic ligand design choices, which involved the use of a naphthalene diamine ligand framework. These results provide evidence for a nonintuitive diagonal relationship between light Group 13 elements and heavy Group 15 elements. Mechanistic studies on the hydrostibanation of phenylacetylene revealed a radical pathway.

Attempts to isolate bismuth hydrides using a 1,8-naphthalene diamine framework have thus far been unsuccessful, with traces of free ligand and metallic bismuth being the major products. The ligand framework has not provided enough steric bulk to prevent dimerization and H_2 elimination. The formation of H_2 and benzene when a cyclohexadiene substituted bismuth compound was heated provides proof-of-concept that bismuth hydrides can be generated from a bismuth cyclohexadienyl group. This is currently being investigated further.

4.5 Experimental

4.5.1 General

Synthetic procedures.All manipulations were performed using standard Schlenk and glovebox techniques under an atmosphere of dry nitrogen. Solvents were dried over Na/benzophenone (tetrahydrofuran, pentanes, hexanes, diethyl ether, toluene, benzene-d_6) or over calcium hydride (dichloromethane, acetonitrile, 1,2-difluorobenzene, dichloromethane-d_2, acetonitrile-d_3, chloroform-d) and distilled prior to use. Reaction glassware was baked in a 130 ^{o}C oven for at least 1 h prior to use and assembled under nitrogen while hot.

Solution NMR Spectroscopy. Nuclear magnetic resonance spectra are referenced to tetramethylsilane (^{1}H, ^{1}C), 85% H_3PO_4 (^{31}P), $CFCl_3$ (^{19}F), or $B(OMe)_3$

(^{11}B) on a Bruker AV-300 spectrometer or a Bruker AV-500 spectrometer with residual solvent used for chemical shift calibration. Samples for NMR spectroscopy were prepared and sealed inside the glovebox with Parafilm before removal into ambient atmosphere. Heteronuclear NMR experiments were run using a sealed capillary containing benzene-d_6 placed within the NMR tube for solvent locking.

Vibrational Spectroscopy. Infrared spectra were obtained on an Agilent Technologies CARY 630 FTIR instrument equipped with a ZnSe ATR module. Raman spectra were obtained on a Thermo Scientific Nicolet NXR 9650 FT-Raman Spectrometer instrument equipped with a 1064 nm Nd:YVO4 laser and InGaAs detector.

Melting Points. Melting points were obtained for samples sealed in glass capillaries and are uncorrected.

Crystallography. Single crystal diffraction experiments were performed on a Bruker D8-Quest Photon II diffractometer. The data was processed using the APEX III GUI software The XPREP program was used to confirm unit cell dimensions and crystal lattices. All calculations were carried out using the SHELXTL-plus and the Olex2 software packages for structure determination (ShelXT/Intrinsic phasing), solution refinement (ShelXL/Least squares), and molecular graphics. Space group choices were confirmed using Platon. The final refinements were obtained by introducing anisotropic thermal parameters and the recommended weightings for all atoms except the hydrogen atoms, which were placed at locations derived from a difference map and refined as riding contributions with isotropic displacement parameters that were 1.2 times those of the attached carbon atoms. Details for individual compounds are given with their characterization data.

Mass Spectrometry. Electro-Spray Ionization (ESI) and Atmospheric Pressure Chemical Ionization (APCI) spectra were obtained on a Bruker micrOTOF.

Commercial reagents. Naphthalene diamine was obtained from Oakwood Chemicals. Chlorosilanes were obtained from Alfa. *n*Butylltihium (1.6 M in hexanes) was obtained from Acros. $SbCl_3$ was obtained from Alfa and sublimed prior to use. $LiHBEt_3$ (1.0 M in THF) was obtained from Alfa. All hydrostibanation substrates

were obtained from Sigma and distilled prior to use.

Starting materials. Ligands **4.1a-c** were synthesized according to the literature procedure.[182] Compound **4.11** was synthesized according to the procedure of Roesky *et. al.*[84]

4.6 Synthesis and Characterization Data

General synthetic procedure for 4.2a-c. Naphthalene diamine (4.71 g, 10 mmol) was dissolved in THF (ca. 50 mL) and cooled to –89 °C (2-propanol and liquid nitrogen). To this, 12.5 mL of a solution of *n*-Butyllithium (1.6 M in hexanes, 20 mmol) was slowly added, resulting in the formation of a dark brown to green solution. The solution was warmed to room temperature and stirred for 18 hours. Next, a solution of $SbCl_3$ (2.28 g, 10 mmol) in THF (ca. 50 mL) was prepared and cooled to –89 °C. The solution of lithiated ligand was added dropwise to the cooled flask containing the $SbCl_3$ in THF, which resulted in the formation of a dark brown to red solution. The reaction was warmed to room temperature, wrapped in foil to eliminate exposure to light, and stirred for 3 hours. The reaction was evaporated to dryness and the residue dissolved in ca. 30 mL of pentane then filtered, yielding a light-yellow solution. Recrystallization at –25 °C gave the respective chlorides as a yellow powder.

Compound 4.2a:

Yield: 3.1719 g, 69%

Melting point: 66.3–69.1 °C, decomp.

^{1}H NMR (300 MHz, benzene-d_6): δ 7.40 (dd, J = 8.2, 1.0 Hz, 2H, Ar-H), 7.17 (t, J = 7.5 Hz, 2H, Ar-H), 7.05 (dd, J = 7.6, 1.2 Hz, 2H, Ar-H), 0.21 (s, 18H, 2 x $Si(CH_3)_3$)

$^{13}C\{^1H\}$ NMR (75 MHz, benzene-d_6): δ 143.2 (CAr), 137.6 (CAr), 125.9 (CAr), 124.6 (CAr), 123.2 (CAr), 118.4 (CAr), 2.59 ($Si(CH_3)_3$).

FTIR (cm^{-1} (relative int.)): 3056.2(2), 2952.3(1), 2939.4(16), 2888.6(1), 1958.8(1), 1922.1(2), 1607.2(4), 1563.6(21), 1501.4(1), 1442.4(1), 1426.4(5), 1405.9(1), 1373.9(9), 1334.9(7), 1321.4(2), 1274.8(6), 1264.5(4), 1248.4(42), 1173.7(4), 1061.1(31), 1041.6(18), 965.5(2), 893(14), 872.7(42), 836.4(100), 814.2(6), 784.7(2), 764.5(54), 676.4(9), 655.4(1), 637.6(2), 621.6(5), 605.3(9), 533.8(4), 516.8(1), 502.2(1), 477.8(5).

HRMS: The sample decomposed in the spectrometer precluding mass spectrometric characterization.

X-ray: Crystals were grown from a saturated hexane solution. $C_{16}H_{24}ClN_2SbSi_2$ (M =457.75 g/mol): monoclinic, space group $P2_1/c$ (no. 14), a = 8.8039(3) Å, b = 9.0250(3) Å, c = 24.7328(7) Å, β = 94.6200(10)°, V = 1958.76(11) Å^3, Z = 4, T = 120.0 K, μ(CuKα) = 13.576 mm^{-1}, D_{calc} = 1.552 g/cm^3, 46262 reflections measured (7.172° $\leq 2\theta \leq$ 144.8°), 3850 unique (R_{int} = 0.0358, R_{sigma} = 0.0155) which were used in all calculations. The final R_1 was 0.0220 ($I > 2\sigma(I)$) and wR_2 was 0.0570 (all data). CCDC No. 1957859.

Compound 4.2b:

Yield: 4.0335 g, 74%

Melting point: 95.0–98.0 °C

^{1}H NMR (500 MHz, benzene-d_6): δ 7.39 (dd, J = 8.1, 1.2 Hz, 2H, Ar-H), 7.17 (t, J = 7.7 Hz, 2H, Ar-H), 7.08 (dd, J = 7.8, 1.1 Hz, 2H, Ar-H), 0.92 (t, J = 7.6 Hz, 12H, 2 x Et_3Si), 0.85-0.72 (m, 18H, 2 x Et_3Si).

$^{13}C\{^1H\}$ (126 MHz, benzene-d_6): δ 143.1 (CAr), 137.6 (CAr), 125.9 (CAr), 124.1 (CAr), 123.1 (CAr), 117.5 (2 x Et_3Si), 7.3 (CAr), 6.4 (2 x Et_3Si).

FTIR (cm^{-1} (relative int.)): 3054.8(10), 2954.2(59), 2933.4(1), 2909.6(10), 2873(21), 2800.1(1), 2732.4(1), 2028.9(2), 1958.8(7), 1899.6(2), 1609(1), 1562.8(76), 1511.6(<1), 1459.5(22), 1429(16), 1422.5(<1), 1375.8(47), 1335(25), 1270.8(100), 1235.2(10), 1174.7(16), 1094.9(1), 1055.9(97), 1041.6(2), 1015.8(<1), 999.1(61), 960.3(<1), 887.8(9), 864.4(57), 821.5(48), 784.4(16), 767.6(90), 753.6(29), 719.9(7), 695.8(12), 625.1(7), 594.5(<1), 582.4(9), 534(16), 501.6(4), 480(15), 469.9(<1).

HRMS (APCI, $[M+1]^+$): calculated = 541.1222 m/z, observed = 541.1216 m/z, error = 0.05 ppm.

X-ray: Crystals were grown from a saturated hexane solution. $C_{22}H_{36}ClN_2SbSi_2$ (M =541.91 g/mol): triclinic, space group $PP_{\bar{1}}$ (no. 2), a = 8.2080(7) Å, b = 11.0460(9) Å, c = 14.4920(12) Å, α = 106.468(3)°, β = 93.127(4)°, γ = 94.583(3)°, V = 1251.89(18) Å^3, Z = 2, T = 100.0 K, μ(CuKα) = 10.708 mm^{-1}, D_{calc} = 1.438 g/cm^3, 29786 reflections measured (6.38° $\leq 2\delta \leq$ 145°), 4914 unique (R_{int} = 0.0466, R_{sigma} = 0.0298) which were used in all calculations. The final R_1 was 0.0342 ($I > 2\sigma(I)$) and wR_2 was 0.0999 (all data). CCDC No. 1954405.

Elemental analysis: Calcd. C: 48.76, H: 6.70, N: 5.17; Expt. C: 48.43, H: 6.75, N: 5.02.

Compound 4.2c:

Yield: 3.1620 g, 52%

Melting point: 147.6–150.0 °C

^{1}H NMR (500 MHz, benzene-d_6): δ 7.37 (d, J = 7.9 Hz, 2H, Ar-H), 7.17 (t, J = 7.8 Hz, 2H, Ar-H), 7.08 (d, J = 7.6 Hz, 2H, Ar-H), 1.42 (sept, J = 7.6 Hz, 6H, $Si(CH(CH_3)_2)_3$), 1.15 (d, J = 7.6 Hz, 18H, $Si(CH(CH_3)_2)_3$), 1.07 (d, J = 7.5 Hz, 18H, $Si(CH(CH_3)_2)_3$).

$^{13}C\{^1H\}$ (126 MHz, benzene-d_6): δ 142.95 (CAr), 137.55 (CAr), 125.52 (CAr), 124.39 (CAr), 123.17 (CAr), 118.07 (CAr), 19.06 ($Si(CH(CH_3)_2)_3$), 14.64 ($Si(CH(CH_3)_2)_3$).

FTIR (cm^{-1} (relative int.)): 2943.5(61), 2926.1(<1), 2888.9(5), 2865.8(39), 2028.8(6), 1958.8(24), 1606.5(1), 1563.3(50), 1463.2(31), 1427.9(9), 1390.2(<1), 1373.2(17), 1332.1(9), 1268(79), 1244.1(<1), 1174.9(5), 1099.3(1), 1050.6(70), 1040.7(1), 1016.6(11), 986.4(2), 919.1(7), 880.5(13), 856.9(45), 810.2(100), 784.6(5), 756.6(3), 744.9(74), 67.3(1), 652.9(34), 635.3(8), 623.6(1), 587.9(6), 535.5(2), 526.4(6), 515.9(2).

HRMS (ESI-MS, $[M+1]^+$): calculated = 625.2155 m/z, observed = 625.2177 m/z, error = 3.39 ppm.

X-ray: For connectivity information only. Crystals were grown from a saturated hexane solution. $C_{28}H_{48}ClN_2SbSi_2$ (M =626.06 g/mol): monoclinic, space group $P2_1/n$ (no. 14), a = 8.3167(4) Å, b = 31.6223(16) Å, c = 11.9888(6) Å, β = 104.415(2)°, V = 3053.7(3) Å^3, Z = 4, T = 99.95 K, μ(CuKα) = 8.851 mm^{-1}, D_{calc} = 1.362 g/cm^3, 40672 reflections measured ($5.59° \leq 2\theta \leq 112.18°$), 3957 unique ($R_{int}$ = 0.0422, R_{sigma} = 0.0196) which were used in all calculations. The final R_1 was 0.0436 ($I > 2\sigma(I)$) and wR_2 was 0.1071 (all data). CCDC No. 1954398.

Elemental analysis: Calcd. C: 53.72, H: 7.73, N: 4.47; Expt. C: 54.10, H: 8.10, N: 4.47.

Compound 4.3a:

A cooled (–25 °C) solution of **4.2a** (0.1360 g, 0.30 mmol) in hexanes (ca. 5 mL) was added dropwise to a vigorously stirred cold (–25 °C) suspension of $LiHBEt_3$ (0.3 mL of a 1.0 M solution in THF) in ca. 5 mL hexanes. The reaction was allowed to warm up to ambient temperature and stirred for 30 minutes to yield a yellow-orange suspension with some black precipitate. The reaction mixture was dried thoroughly, extracted with hexanes, filtered through a fine frit, and concentration under vacuum. Attempts to isolate **4.3a** in the solid state repeatedly gave mixtures containing crystals of compound **4.4** due to thermal decomposition (see manuscript for details). Therefore, this compound has only been characterized as a mixture without isolation.

An updated procedure was later developed due to varying concentrations of $LiHBEt_3$. With this procedure a titration of **4.2b** with $LiHBEt_3$ was performed to determine the accurate concentration of $LiHBEt_3$ in THF. A solution of **4.2b** (0.2 mmol) in hexanes was cooled to –25 °C. To this, 0.1 molar equivalents of $LiHBEt_3$ (1.0 M solution in THF) were slowly added with stirring. ^{1}H NMR spectroscopy was used to monitor the progress of the reaction after each addition. The solution of **4.2b** was considered fully titrated when the ^{1}H NMR spectrum no longer revealed the presence of **4.2b** and solely contained **4.3b**. The determined concentration was used in the large-scale synthesis of **4.3b**. A suspension of $LiHBEt_3$ (0.52 mL of a 1.0 M solution in THF) was added to a cooled solution (–25 °C) of **4.2b** (0.3253

g, 0.52 mmol) in hexanes (ca. 10 mL). The reaction was allowed to warm up to ambient temperature and stirred for 30 minutes to yield a yellow suspension with white precipitate. The reaction mixture was filtered through a fine frit and concentrated under vacuum. Storage at –25 °C yielded **4.3b** as yellow crystals, which were isolated by decanting the mother liquor and drying under vacuum.

^{1}H NMR (500 MHz, benzene-d_6): δ 9.65 (s, 1H, Sb–H), 7.43 (d, J = 7.9 Hz, 2H, Ar-H), 7.21-7.14 (m, 4H, Ar-H), 0.30 (s, 18H, 2 x $SiMe_3$).

^{13}C{^{1}H} (75 MHz, benzene-d_6): δ 150.7 (CAr), 138.1 (CAr), 126.0 (CAr), 125.0 (CAr), 122.7 (CAr), 117.3 (CAr), 3.01 ($SiMe_3$).

FTIR (cm^{-1} (relative int.)): 2956.2(24), 1958.8(8), 1562.9(41), 1512.5(6), 1422.8(14), 1373.8(11), 1333.9(7), 1251.2(76), 1058.8(55), 876.1(18), 837.9(100), 758.8(38), 684.8(5), 532.7(8).

Compound 4.3b:

A cooled (–25 °C) solution of **4.2b** (2.4458 g, 4.52 mmol) in hexanes (ca. 40 mL) was added dropwise to a vigorously stirred cold (–25 °C) suspension of $LiHBEt_3$ (4.52 mL of a 1.0 M solution in THF) in ca. 20 mL hexanes. The reaction was allowed to warm up to ambient temperature and stirred for 30 minutes to yield a yellow suspension with some black precipitate. The reaction mixture was dried thoroughly, extracted with hexanes, filtered through a fine frit, and concentration under vacuum. Storage at –25 °C yielded **4.3b** as yellow crystals over three crops, which were isolated by decanting the mother liquor and drying under vacuum.

Yield: 1.7808 g, 77%

Melting point: 104.5–108 °C

^{1}H NMR (500 MHz, benzene-d_6): δ 9.88 (s, 1H, Sb–H), 7.40 (dd, J = 7.9, 1.4 Hz, 2H, Ar-H), 7.16 (t, J = 7.5 Hz, 2H, Ar-H), 7.13 (dd, J = 7.5, 1.4 Hz, 2H, Ar-H), 0.97-0.92 (m, 15H, 2 x $SiEt_3$), 0.92-0.76 (m, 12H, 2 x $SiEt_3$).

^{13}C{^{1}H} (126 MHz, benzene-d_6): δ 150.7 (CAr), 138.2 (CAr), 126.5 (CAr), 125.0

(CAr), 122.6 (CAr), 116.1 (CAr), 7.5 ($SiEt_3$), 6.6 ($SiEt_3$).

FTIR (cm^{-1} (relative int.)): 2946.6(38), 2908.5(8), 2867.9(7), 1883.8(17), 1558.4(63), 1455.1(10), 1423(23), 1371.9(39), 1328.7(24), 1272.4(100), 1232.8(10), 1174.1(12), 1062.9(100), 1039.7(9), 1001.6(50), 897.2(42), 872.6(21), 816.6(35), 780.9(6), 771(39), 755.8(87), 719.3(27), 698.6(14), 671.9(8), 642.6(17), 531.3(20), 468.4(6).

HRMS (APCI-MS, $[M+1]^+$): calculated = 507.1606 m/z, observed = 507.1605 m/z, error = 0.19 ppm.

X-ray: Crystals were grown from a saturated hexane solution. $C_{22}H_{37}N_2SbSi_2$ (M =507.46 g/mol): monoclinic, space group $P2_1$ (no. 4), a = 7.2849(4) Å, b = 21.5587(12) Å, c = 15.5806(9) Å, β = 92.957(2)°, V = 2443.7(2) $Å^3$, Z = 4, T = 100.0 K, μ(MoKα) = 1.237 mm^{-1}, D_{calc} = 1.379 g/cm^3, 14278 reflections measured ($5.236° \leq 2\theta \leq 80.398°$), 14278 unique ($R_{int}$ = 0.0446, R_{sigma} = 0.0286) which were used in all calculations. The final R_1 was 0.0234 ($I > 2\sigma(I)$) and wR_2 was 0.0473 (all data). CCDC No. 1954397.

Elemental analysis: Calcd. C: 52.07, H: 7.35, N: 5.52; Expt. C: 49.60, H: 7.01, N: 5.28.

Compound 4.3c:

A cooled (–25 °C) solution of **4.2c** (0.3253 g, 0.52 mmol) in hexanes (ca. 10 mL) was added dropwise to a vigorously stirred cold (–25 °C) suspension of $LiHBEt_3$ (0.52 mL of a 1.0 M solution in THF) in ca. 5 mL hexanes. The reaction was allowed to warm up to ambient temperature and stirred for 30 minutes to yield a yellow suspension with some black precipitate. The reaction mixture was dried thoroughly, extracted with hexanes, filtered through a fine frit, and concentration under vacuum. Storage at –25 °C yielded **4c** as yellow crystals, which were isolated by decanting the mother liquor and drying under vacuum.

Yield: 0.1770 g, 58%

Melting point: 134.7-138.1 °C

^{1}H NMR (500 MHz, benzene-d_6): δ 10.04 (s, 1H, Sb–H), 7.39 (dd, J = 7.1, 2.6 Hz, 2H, Ar-H), 7.18-7.12 (m, 4H, Ar-H, overlaps with solvent signal), 1.51 (sept, J = 7.5 Hz, $HC(CH_3)_2$), 1.18 (d, J = 7.5 Hz, $HC(CH_3)_2$) , 1.10 (d, J = 7.5 Hz, $HC(CH_3)_2$).

$^{13}C\{^{1}H\}$ (126 MHz, benzene-$_6$): δ 150.7 (CAr), 137.9 (CAr), 126.2 (CAr), 124.3 (CAr), 122.3 (CAr), 115.9 (CAr), 18.9 ($Si(CH(CH_3)_2)_3$), 18.8 ($Si(CH(CH_3)_2)_3$), 14.4 ($Si(CH(CH_3)_2)_3$).

FTIR: 3051.3, 2966.4, 2945.2, 2866.1, 2912.4, 2727.5, 1959.6, 1863.2, 1564.2, 1462.0, 1450.4, 1436.2, 1373.3, 1325.1, 1269.1, 1249.8, 1174.6, 1053.1, 1039.6, 1016.5, 1004.9, 991.4, 918.0, 875.9, 856.3, 812.0, 779.2, 758.0, 740.6, 680.9, 653.8, 640.3, 624.9, 561.3, 530.4, 514.9, 489.9, 482.2.

HRMS (APCI-MS, $[M+1]^+$): calculated = 591.2545 m/z, observed = 591.2543 m/z, error = 0.33 ppm.

X-ray: Crystals were grown from a saturated hexane solution. $C_{28}H_{49}N_2SbSi_2$ (M =591.62 g/mol): monoclinic, space group $P2_1/c$ (no. 14), a = 11.4969(5) Å, b = 14.0998(6) Å, c = 18.6866(8) Å, β = 103.038(2)°, V = 2951.1(2) Å^3, Z = 4, T = 100.0 K, μ(CuKα) = 8.314 mm^{-1}, D_{calc} = 1.332 g/cm^3, 43969 reflections measured (7.894° $\leq 2\theta \leq$ 149.136°), 5921 unique (R_{int} = 0.0499, R_{sigma} = 0.0358) which were used in all calculations. The final R_1 was 0.0248 ($I > 2\sigma(I)$) and wR_2 was 0.0593 (all data). CCDC No. 1954401.

Elemental analysis: Calcd. C: 56.84, H: 8.35, N: 4.73; Expt. C: 56.74, H: 8.73, N: 4.74.

Compound 4.4:

Only a few crystals of this side-product were isolated from the thermal decomposition of **4.3a** (see manuscript for details).

X-ray: $C_{16}H_{24}N_2SbSi_2$ (M =422.30 g/mol): monoclinic, space group $P2_1/n$ (no. 14), a = 10.7905(4) Å, b = 12.2257(4) Å, c = 14.2711(5) Å, β = 90.924(2)°, V = 1882.42(11) Å^3, Z = 4, T = 120.0 K, μ(CuKα) = 12.801 mm^{-1}, D_{calc} = 1.490 g/cm^3, 54660 reflections measured (9.526° $\leq 2\theta \leq$ 144.966°), 3719 unique (R_{int} = 0.0527,

R_{sigma} = 0.0206) which were used in all calculations. The final R_1 was 0.0375 (I > 2σ(I)) and wR_2 was 0.1164 (all data).

Compound 4.5:

Freshly distilled phenylacetylene (0.5 mmol) was added to a solution of **4.3b** (0.2501 g, 0.5 mmol) in hexane (5 mL) and the resulting yellow solution stirred at ambient temperature for 24 h. The resulting dark yellow solution was filtered and dried thoroughly to obtain an oil. The oil solidified upon standing at –25 °C overnight to give a fine yellow powder. Colourless blocks suitable for diffraction were obtained by leaving the oil to stand at ambient temperature.

Yield: 0.2974 g, 97%

Melting point: 77.9–79.7 °C

^{1}H NMR (500 MHz, C_6D_6): δ 7.43 (dd, J = 6.7, 3.1 Hz, 2H, Ar-H), 7.24 (d, J = 5.1 Hz, 2H, Ar-H), 7.21 (d, J = 3.4 Hz, 2H, Ar-H), 7.20 (s, 2H, Ar-H), 7.15 (t, J = 6.2 Hz, 2H, Ar-H, overlap with solvent resonance), 7.07 (d, J = 12.7 Hz, 1H, C=C-H), 7.04, (tt, J = 7.4, 1.3 Hz, 1H, Ar-H), 6.32 (d, J = 12.7 Hz, 1H, C=C-H), 1.07-0.79 (m, 30H, 2 x $SiEt_3$).

^{13}C{^{1}H} (500 MHz, C_6D_6): δ 147.4 (C=C), 146.7 (C=C), 143.1 (CAr), 137.9 (CAr), 128.8 (CAr), 128.33 (CAr), 128.31 (CAr), 125.6 (CAr), 125.3 (CAr), 122.6 (CAr), 118.5 (CAr), 7.7 ($SiEt_3$), 6.9 ($SiEt_3$).

FTIR (cm^{-1} (relative int.)): 3053(13), 2952.4(75), 2908.2(8), 2874.4(21), 2730.9(1), 2029.1(<1), 1958.7(2), 1902.1(1), 1808.9(1), 1561.8(77), 1491.9(7), 1458.1(11), 1442.2(1), 1425.2(23), 1374.4(41), 1330.2(26), 1271.8(101), 1236.8(14), 1174.5(10), 1058.7(94), 1040.1(10), 1001.9(42), 969.8(4), 878.1(1), 866(54), 816.2(49), 782.5(5), 765.7(89), 754.8(20), 704.1(17), 653.7(3), 628.2(5), 590.6(6), 533(12), 503.6(7), 486.8(16).

HRMS (APCI, $[M+1]^1$): calculated = 609.2076 m/z, observed = 609.2068 m/z, error = 1.26 ppm.

X-ray: Crystals were grown upon storage of the neat oil at room temperature.

$C_{30}H_{43}N_2SbSi_2$ (M =609.59 g/mol): monoclinic, space group $P2_1/n$ (no. 14), a = 18.7685(10) Å, b = 8.6053(5) Å, c = 20.2990(11) Å, β = 115.443(2)°, V = 2960.5(3) Å^3, Z = 4, T = 120.0 K, μ(CuKα) = 8.311 mm^{-1}, D_{calc} = 1.368 g/cm^3, 48265 reflections measured (5.37° ≤ 2θ ≤ 141.228°), 5637 unique (R_{int} = 0.0629, R_{sigma} = 0.0337) which were used in all calculations. The final R_1 was 0.0843 (I > 2σ(I)) and wR_2 was 0.1836 (all data). CCDC No. 1954402.

Elemental analysis: Calcd. C: 59.11, H: 7.11, N: 4.60; Expt. C: 57.65, H: 6.82, N: 4.67.

Compound 4.6:

3-vinylanisole was added to a solution of **4.3b** (0.0500 g, 0.1 mmol) in C_6D_6) and the resulting yellow solution monitored by ^{1}H NMR spectroscopy. Even after >140 h, only ca. 50% conversion was observed. This compound was not isolated but characterized spectroscopically as a mixture of reactants and products.

^{1}H NMR (500 MHz, C_6D_6): δ 7.39 (dd, J = 7.6, 1.6 Hz, 2H, Ar-H), 7.14, (dd, J = 5.5, 1.4 Hz, 1H, Ar-H), 7.05 (t, J = 7.8 Hz, 1H, Ar-H), 6.98 (d, J = 7.9 Hz, 1H, Ar-H), 6.48 (d, J = 7.5 Hz, 1H, Ar-H), 6.39 (t, J = 1.6 Hz, 1H, Ar-H), 3.30 (s, 3H, OMe), 2.58 (t, J = 8.3 Hz, 2H, CH2), 1.43 (t, J = 8.3 Hz, 2H, CH2), 0.94 (s, 15H, 2 x $SiEt_3$), 0.93-0.76 (m, 12H, 2 x $SiEt_3$)

HRMS (APCI-MS, [M+1]^1): calculated = 641.2338 m/z, observed = 641.2358 m/z, error = 3.10 ppm

Compound 4.7:

Freshly distilled acrylonitrile (5 mL) was added to solid **4b** (0.2501 g, 0.5 mmol) and the resulting yellow solution stirred at ambient temperature for 24 h. A pale-yellow suspension was obtained which was dried under vacuum. The pale-yellow powder obtained was washed with cold (–30 °C) pentane (3 x 2 mL) and dried thoroughly. Colourless blocks suitable for diffraction were obtained by cooling the pentane pentane washes to –30 °C.

Yield: 0.2097 g, 75%

Melting point: 94.7–95.9 °C

^{1}H NMR (500 MHz, C_6D_6): δ 7.37 (dd, J = 7.8, 0.9 Hz, 2H, Ar-H), 7.14 (t, J = 7.9 Hz, 2H, Ar-H), 7.09 (dd, J = 7.6, 0.9 Hz, 2H, Ar-H), 1.64 (t, J = 7.4 Hz, 2H, CH2), 0.98-0.75 (overlapping m, 32H, 2 x $SiEt_3$ and CH_2).

$^{13}C\{^1H\}$ (500 MHz, C_6D_6): δ 145.3 (C≡N), 137.7 (Ar-H), 125.6 (Ar-H), 124.1 (Ar-H), 122.7 (Ar-H), 120.0 (Ar-H), 118.4 (Ar-H), 22.9 (CH2), 12.3 (CH2), 7.6 ($SiEt_3$), 6.7 ($SiEt_3$).

FTIR (cm^{-1} (relative int.)): 3051(10), 3035(2), 2952(54), 2934(1), 2910(12), 2874(19), 2802(1), 2733(2), 2244(10), 2029(3), 1959(9), 1902(3), 1724(5), 1603(6), 1561(64), 1455(17), 1426(8), 1411(21), 1376(44), 1329(27), 1275(90), 1246(4), 1235(12), 1175(9), 1137(5), 1060(88), 1040(21), 999(38), 967(5), 903(7), 876(61), 817(74), 782(22), 769(34), 756(100), 735(4), 719(18), 694(28), 672(7), 629(8), 594(5), 580(11), 549(3), 531(14), 505(5), 482(14), 472(1).

HRMS (APCI-MS, $[M+1]^1$): calculated = 560.1872 m/z, observed = 560.1877 m/z, error = 0.38 ppm.

X-ray: Crystals were grown from a saturated pentane solution. $C_{25}H_{40}N_3SbSi_2$ (M =560.53 g/mol): orthorhombic, space group *Aea*2 (no. 41), a = 21.5449(10) Å, b = 15.7690(8) Å, c = 16.0973(8) Å, V = 5468.9(5) Å^3, Z = 8, T = 100.0 K, μ(MoKα) = 1.113 mm^{-1}, D_{calc} = 1.362 g/cm^3, 500488 reflections measured (5.166° ≤ 2θ ≤ 96.252°), 26229 unique (R_{int} = 0.0493, R_{sigma} = 0.0206) which were used in all calculations. The final R_1 was 0.0257 (I > 2σ(I)) and wR_2 was 0.0585 (all data). CCDC No. 1954404.

Elemental analysis: Calcd. C: 53.57, H: 7.19, N: 7.50; Expt. C: 52.11, H: 8.35, N: 7.56.

Compound 4.8:

Freshly distilled p-trifluoromethyl benzaldehyde (2 mL) was added to a solution of **4.2b** (0.2501 g, 0.5 mmol) in 5 mL hexane and the resulting yellow solution stirred at ambient temperature for 24 h. A pale-yellow solution was obtained which was

dried under vacuum to obtain an oil. The product was not isolated but characterized spectroscopically in the presence of 6 equivalents of p-trifluoromethyl benzaldehyde.

^{1}H NMR (500 MHz, C_6D_6): δ 7.33 (d, J = 8.4, 2H, Ar-H), 7.15 (m, 2H, Ar-H), 7.13 (t, J = 7.8 Hz, 2H, Ar-H), 6.63 (d, J = 7.8 Hz, 2H, CH2), 4.48 (s, 2H, CH2), 0.95-0.73 (overlapping m, 30H, 2 x $SiEt_3$)

HRMS (APCI-MS, $[M+1]^1$): calculated = 681.1899 m/z, observed = 681.1921 m/z, error = 3.29 ppm

Compound 4.9:

A solution of azobenzene (0.0911 g, 0.5 mmol) in hexane (2 mL) was added dropwise to a solution of **4b** (0.2501 g, 0.5 mmol) in hexane (2 mL). The resulting orange solution was stirred for 24 h and then dried under vacuum. The resulting oil was dissolved in a minimum amount of pentane and cooled to -25 °C for 48 h. This yielded dark yellow crystals along with some light-yellow crystals. The dark yellow crystals were manually separated from the lighter ones and washed with 3 x 0.5 mL cold pentane. Drying the crystals under vacuum yielded the product.

Yield: 0.2031 g, 59%

Melting point: 95.5–98.2 °C

^{1}H NMR (500 MHz, C_6D_6): δ 7.33 (d, J = 6.9 Hz, 2H, Ar-H), 7.09 (m, 1H, Ar-H), 7.04 (m, 3H, Ar-H), 7.01 (t, J = 7.9 Hz, 4H, Ar-H), 6.91 (dd, J = 8.5, 1.3 Hz, 2H, Ar-H), 6.69 (tdt, J = 7.3, 3.3, 1.0 Hz, 2H, Ar-H), 5.02 (s, 1H, N-H), 1.06-0.0.68 (broad, 30H, 2 x $SiEt_3$).

$^{13}C\{^1H\}$ (500 MHz, C_6D_6): δ 152.7 (CAr), 149.7 (CAr), 144.3 (CAr), 137.4 (CAr), 129.4 (CAr), 129.3 (CAr), 125.9 (CAr), 123.6 (CAr), 123.0 (CAr), 119.4 (CAr), 119.3 (CAr), 114.1 (CAr), 112.7 (CAr), 117.8 (CAr), 7.7 ($SiEt_3$), 6.9 ($SiEt_3$).

FTIR (cm^{-1} (relative int.)): 3353.6(8), 3052.7(12), 2954.7(61), 2908.2(6), 2875.3(25), 2732(1), 2028.9(1), 1958.7(4), 1912.7(1), 1820.4(1), 1597.4(38), 1561.7(69), 1493.4(64), 1461.9(2), 1425.7(12), 1414.7(1), 1373.7(31), 1331.8(11), 1306.4(3), 1271.1(100),

1240.1(23), 1174.7(11), 1153.7(2), 1124(1), 1056.1(89), 1039.8(6), 1002.6(30), 854.8(52), 818(48), 783.3(10), 765.6(16), 752.1(97), 717.4(3), 691.1(32), 627.9(5), 573.5(4), 533.7(16), 504.9(4), 482.8(8).

HRMS (APCI, $[M+1]^1$): calculated = 689.2450 m/z, observed = 689.2474 m/z, error = 3.46 ppm.

Elemental analysis: Calcd. C: 59.21, H: 6.87, N: 8.12; Expt. C: 58.82, H: 7.17, N: 8.19.

X-ray: Crystals were grown from a pentane solution. $C_{34}H_{47}N_4SbSi_2$ (M =689.68 g/mol): monoclinic, space group $P2_1/c$ (no. 14), a = 16.2602(13) Å, b = 12.5808(10) Å, c = 16.9219(13) Å, β = 105.743(3)°, V = 3331.8(5) Å^3, Z = 4, T = 120.0 K, μ(CuKα) = 7.470 mm^{-1}, D_{calc} = 1.375 g/cm^3, 78853 reflections measured (5.646° $\leq 2\theta \leq$ 144.976°), 6552 unique (R_{int} = 0.0362, R_{sigma} = 0.0157) which were used in all calculations. The final R_1 was 0.0346 ($I > 2\sigma(I)$) and wR_2 was 0.0922 (all data). CCDC No. 1954400.

Compound 4.10:

A few crystals of this side-product were isolated from the reaction between 4.2b and azobenzene. Crystallography identified it as a distibine believed to form from hydrogenation of azobenzene.

Yield: 0.0474 g

Melting point: 165.0–170.0 °C decomp.

^{1}H NMR (500 MHz, C_6D_6): δ 7.36 (dd, J = 8.1, 1.1 Hz, 4H, Ar-H), 7.19 (dd, J = 7.2, 1.1 Hz, 4H, Ar-H), 7.13 (t, J = 7.6 Hz, 4H, Ar-H), 0.92-0.69 (overlapping multiplets, 60H, 4 x $SiEt_3$)

^{13}C{^{1}H} (500 MHz, C_6D_6): δ 152.7 (CAr), 149.7 (CAr), 144.3 (CAr), 137.4 (CAr), 129.4 (CAr), 129.3 (CAr), 125.9 (CAr), 123.6 (CAr), 123.0 (CAr), 119.4 (CAr), 119.3 (CAr), 114.1 (CAr), 112.7 (CAr), 117.8 (CAr), 7.7 ($SiEt_3$), 6.9 ($SiEt_3$).

FTIR (cm^{-1} (relative int.)): 3052(11), , 2951(68), 2915(5), 2873(23), 2728(1), 2366(2), 2342(1), 2028(3), 1958(10), 1601(3), 1582(2), 1560(63), 1516(1), 1457(15), 1417(26), 1371(34), 1328(23), 1269(98), 1234(20), 1171(4), 1096(4), 1057(82), 1040(6), 1000(56), 968(5), 878(24), 855(87), 805(73), 782(6), 751(100), 721(20), 692(24), 625(5), 591(5), 576(1), 530(17), 500(3) 478(7).

HRMS: The sample decomposed in the spectrometer precluding mass spectrometric characterization.

X-ray: Crystals were grown from a pentane solution cooled to -25 °C. $C_{22}H_{36}N_2SbSi_2$ (M =506.46 g/mol): monoclinic, space group $P2_1/c$ (no. 14), a = 10.4827(3) Å, b = 12.2446(3) Å, c = 19.3638(5) Å, β = 102.0770(10)°, V = 2430.46(11) Å^3, Z = 4, T = 120.0 K, μ(CuKα) = 10.004 mm^{-1}, D_{calc} = 1.384 g/cm^3, 45100 reflections measured (11.256° $\leq 2\theta \leq$ 144.502°), 4759 unique (R_{int} = 0.0353, R_{sigma} = 0.0188) which were used in all calculations. The final R_1 was 0.0258 ($I > 2\sigma(I)$) and wR_2 was 0.0675 (all data). CCDC No. 1954399.

4.6.1 Computational Details

All calculations were performed with the Gaussian 09[183] and postg[184] programs, using the B3LYP[185186] functional and the exchange-hole dipole moment (XDM) dispersion correction.[187] Geometry optimizations and frequency calculations used a mixed basis set, consisting of 6-31G* for C, H, and Si, 6-31+G* for N and F, and the polarized SBKJC basis set[188] and associated effective core potential (ECP)[189] for Sb. Subsequent single-point energies were performed with the 6-311+G(2d,2p) basis set for all elements except Sb, for which def2-SVPD[190191192] was used. The XDM damping function parameters were set to a1 = 0, a2 = 3.7737 Å, and a1 = 0.4376, a2 = 2.1607 Å, for the geometry optimizations and single-point energy calculations, respectively. Thermal free-energy corrections were evaluated assuming an ideal gas with a molar volume of 1 L and a temperature of 298.15 K. To investigate possible ionic intermediates, a polarizable continuum model (PCM)[193] of benzene solvent was employed in the single-point energy calculations.

Chapter 5

Bismuthanylstibanes

Portions of this work were adapted from Ref. 193 (**K. M. Marczenko**, S. S. Chitnis, *Chem. Comm.*, **2020**, *56*, 8015-8018) with permission from The Royal Society of Chemistry (Communication; DOI: 10.1039/d0cc00254b).[194]

Contributions to the manuscript: KMM completed all experimental work, all X-ray crystallography, and wrote the first draft of the manuscript. SSC completed computational work, wrote the final version of the manuscript, and supervised the project.

5.1 Introduction

Multiple bonding between heavy p-block elements (principle number n>2) has been a topic of much interest of the past several decades.[4195196] Numerous compounds containing homo- and hetero-nuclear single and multiple bonds have been isolated, giving way to new reactivity paradigms.[4711197] During our pursuit of fundamental research in the area of heavy Group 15 chemistry, we were surprised to note that although a Bi–Sb π-bond is known,[198] neutral compounds containing a σ-bond in an R_2BiSbR_2 type species remain unisolated in the solid state. Such species were hypothesized to exist in solution based on spectroscopic evidence.[199] Specifically,

Me_2SbBiR_2 was presumed to undergo rapid scrambling in solution to give combinations of dipnictanes at ambient temperature. This is likely due to the kinetic lability of neutral Bi–Sb bonds, as the introduction of molecular charge has enabled characterization of four charged compounds exhibiting Bi–Sb interactions (Figure 5.1).[200,201,202] These ions are likely persistent due to stabilization from lattice enthalpy and the high barrier to scrambling. The successful isolation of these ionic examples led us to seek the neutral σ-bonded derivative that is known for most element pairs in the p-block but remained unisolated between Bi and Sb centers.

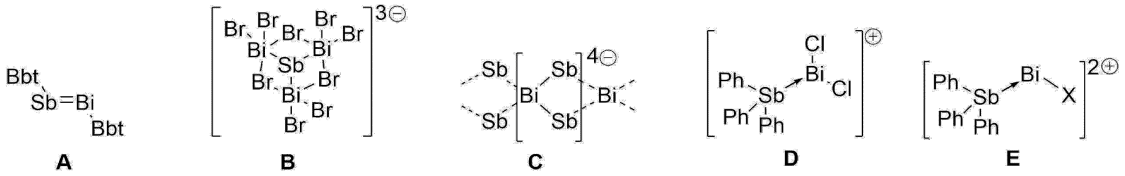

Figure 5.1: Isolated compounds containing Bi–Sb bonds. See text for references. Bbt = o,o−$(CH(SiMe_3)_2)_2$−p−$C(SiMe_3)$−Ph.

We choose the naphthalene diamine substituent for this chemistry as it allows for easy access to aminobismuthanes, chlorostibanes, and chlorobismuthanes, which through careful combination with the Sb–H functional group, may provide access to the first example of an isolable Bi–Sb σ-bond via dehydrohalogenation, reduction, or aminolysis reactions. We therefore made several attempts to target this connectivity.[198] Interestingly, the only know example of a Bi–Sb π-bonded compound was isolated through dehydrohalogenation reactivitions.

5.2 Results and Discussion

Attempts to form bismuthanylstibanes through traditional dehydrohalogenation reactions and magnesium reductions[198] failed (Figure 5.2a,b). Reaction mixtures containing antimony and bismuth metal deposits, and traces of free ligand were formed. We next imagined the reaction of a stibanide anion[203,204] with chlorobismuthane[84] **4.11a** (Figure 5.2c), but all attempts to synthesize the deprotonated lithium salt of **4.3b** with a strong base such as nBuLi or $LiNMe_2$ failed. Layering the reaction mixture with diethyl ether at 0 °C gave a red precipitate, which was identified by X-ray

crystallography as polystibane $(EtSb)_4Sb_8$. The asymmetric unit of this compound consists of four EtSb fragments connected by a tetracyclic Sb_8 cage (Figue 5.3a). Although the pathway towards this tetracyclic motif is unknown, it has been previously observed by Breuing and Roesky,[205204] and its formation was not investigated in further detail.

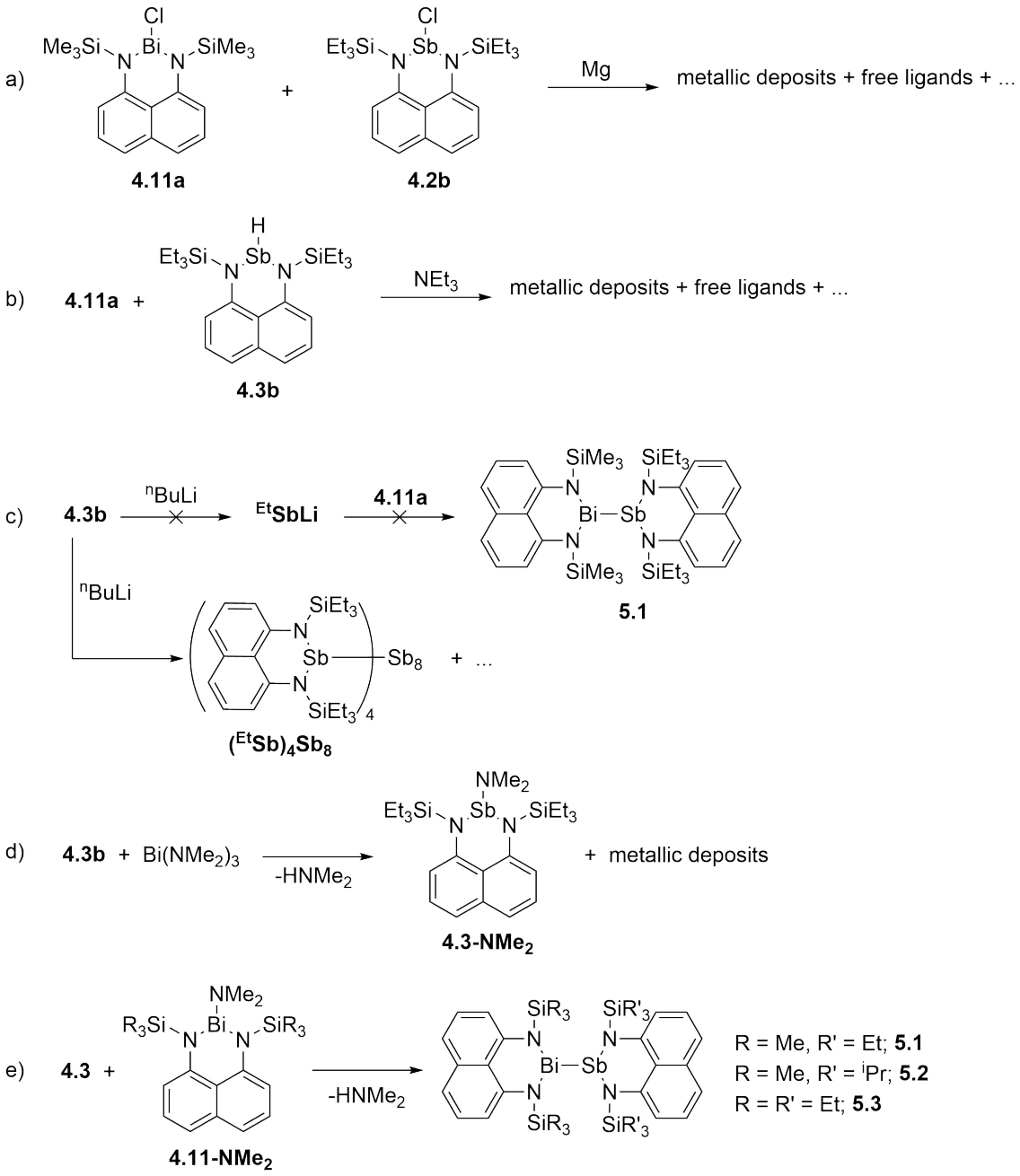

Figure 5.2: Syntheses of aminostibane **4.3-NMe$_2$** and bismuthanylstibanes **5.1**, 5.2, and **5.3**.

We next attempted aminolysis using the Sb–H functional group and a bismuth amide. The reaction between **4.3b** and $Bi(NMe_2)_3$ (in hexane at 0 °C and –78 °C) gave a light yellow solution and a black precipitate (Figure 5.2d). Analysis of the crude reaction mixture by ^{1}H NMR spectroscopy showed the formation of the corresponding antimony amide, abbreviated as **4.3-NMe$_2$**, and free $HNMe_2$, indicating proton removal from the stibane. The identity of **4.3-NMe$_2$** was confirmed by the independent reaction of **4.3b** and $LiNMe_2$. Compound **4.3-NMe$_2$** presumably formed due to the decomposition of a transient Sb–Bi bonded species. We hoped that the use of a tethered naphthalene diamine framework would prevent decomposition and allow isolation of an Sb–Bi bonded species. Dropwise addition of a hexane solution of **4.3b** to a hexane solution of bismuth amide, **4.11-NMe$_2$**, at –30 °C yielded a dark red solution over ten minutes (Figure 5.2e). Concentration of the reaction mixture yielded bright red crystals of the first Bi–Sb σ-bonded compound – a bismuthanylstibane **5.1**. The silane substituents were easily varied using different precursors to give **5.2** and **5.3**. The progress of the reaction is easily monitored using ^{1}H NMR spectroscopy, which shows the disappearance of the hydride single and formation of $HNMe_2$.

The structures of all bismuthanylstibanes were determined by single-crystal X-ray diffraction, providing the first structural data for Bi–Sb σ-bonds. The asymmetric units contain a bimetallic structure with trigonal pyramidal antimony and bismuth atoms (Figure 5.3b). The lone pair sites on each of the metallic atoms are oriented in opposite directions achieving maximum spatial distance between the two distinct naphthalene diamine ligand frameworks. A Bi/Sb substitutional disorder was detected in **5.3**, which prevents an in-depth discussion of the geometric parameters of this structure. The Sb–Bi, Sb–N, and Bi–N bond lengths in **5.1** and **5.2** do not significantly vary when the silane substituents are changed, indicating that this type of "outer sphere" bulk has little influence on the immediate bond parameters of the Bi–Sb bond. The N–Bi–N angle is slightly more contracted than the N–Sb–N angle in both cases (see deposited CIFs). The Bi–Sb bonds in **5.1** (2.9775(9) Å) and **5.2** (2.9764(7) Å) are comparable in length to the value in TbtBi=SbTbt (Tbt = o,o-($CH(SiMe_3)_2$)2-p-$C(SiMe_3)$-Ph).[198]

A solution of **5.1** in C_6D_6 was heated to 100 °C in a J-Young tube for 72 h to assess the stability of the Bi–Sb bond. No decomposition or metal redistribution was observed over this period, despite ^{R}Bi–Bi^{R} and $^{R'}$Sb–Sb$^{R'}$ (R = Me, R′ = Et) being isolable compounds, and in sharp contrast to the facile redistribution previously reported for alkyl/aryl-substituted Bi–Sb bonds even at room temperature.[199]

DFT calculations were performed on **5.1**, $Ph_2BiSbPh_2$, and $(Me_2N)2BiSb(NMe_2)_2$ to explore the specific influence of the bis(silylamino)naphthalene framework and reconcile the high stability of the prepared compounds. Energy decomposition analysis (EDA)[206] revealed that the Bi–Sb bonding interaction in **5.2** (ΔE_{int} = –72.03 kcal mol^{-1}) is significantly stronger than the corresponding interactions in the

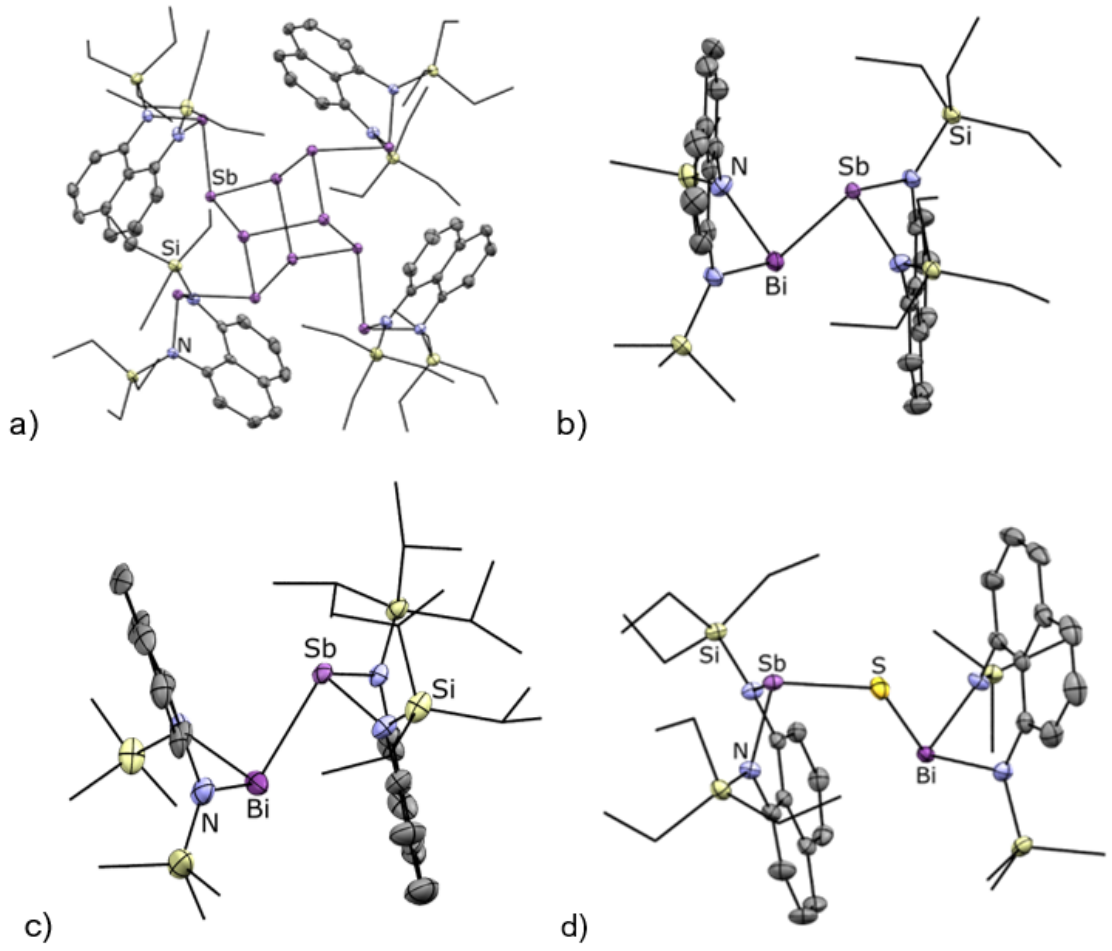

Figure 5.3: Single-crystal X-ray structures of a) $(EtSb)_4Sb_8$, b) **5.1**, c) **5.2**, and d) **5.4**. Thermal ellipsoids are shown at the 50% probability level. Hydrogen atoms have been omitted and silyl groups are shown in wireframe for clarity.

Parameter	**5.1**	$(Me_2N)_2BiSb(NMe_2)_2$	$Ph_2BiSbPh_2$
ΔE_{int}	-72.03	-46.72	-52.55
ΔE_{Pauli}	329.36	238.66	224.41
ΔE_{elstat}	-126.07	-88.05	-96.26
ΔE_{orb}	-236.29	-182.19	159.15
ΔE_{disp}	-39.03	-15.14	-21.55
ΔE_{prep}	0.81	6.12	0.68
$\Delta E(-D_e)$	-71.22	-40.60	-51.87
d/A	3.003	2.981	2.940
q_{Sb}	1.15	0.92	0.64
q_{Bi}	1.12	0.93	0.68

Table 5.1: Energy Decomposition Analysis for selected Bi–Sb bonded compounds at the BP86-D3/Triple-Zeta with Two Polarization Functions Basis Set (TZ2P) level in kcal mol^{-1}. qSb and qBi denote the NBO determined partial atomic charges.

$Ph_2BiSbPh_2$ (ΔE_{int} = –52.55 kcal mol^{-1}) or $(Me_2N)2BiSb(NMe_2)_2$ (ΔE_{int} = –46.72 kcal mol^{-1}). Table 5.1 displays the orbital (ΔE_{orb}) and electrostatic (ΔE_{Elstat}) components of the interaction energy. These values are more stabilizing in the amino-substituted compounds than in the phenyl-substituted compounds. Attachment of the metal atoms to electronegative nitrogen atoms increases their partial charge as evidenced by the significant difference in NBO determined partial atomic charges (Table 5.1) of Sb and Bi in **5.1** (qSb 1.15; qBi 1.12) and $Ph_2BiSbPh_2$ (qSb 0.64; qBi 0.68). This also increases the stabilization of the electrostatic component by making the metals stronger electron density acceptors. Attractive dispersion forces[207] between the bulky trialkyl silyl groups[62] also provide additional stabilization in **5.1** (ΔE_{disp} = –39.03 kcal mol^{-1}). Notably, the contribution of dispersion forces is greater than the sum of ΔE_{Pauli}, ΔE_{Elstat}, and $\Delta E_{Orbital}$. These results showcase the unique ability of the bis(silylamino)naphthalene scaffold for stabilizing the otherwise weak Bi–Sb bond by peripheral dispersive attraction – an underappreciated feature that may enable the isolation of other fragile bonds.

The reactivity of **5.1** towards a variety of unsaturated substrates was examined (Figure 5.4). No reaction between **5.1** and azobenzene, phenylacetylene, or pyridine N-oxide was observed after several days in the presence of UV light or refluxing C_6D_6. Photochemical or thermal disproportionation to homonuclear single-bonded species was also not observed at any point of these reactivity studies. Heating solutions of

5.1 and ammonia borane gave **4.3b**, as well as bis(trimethylsilylamino)naphthalene and bis(triethylsilylamino)naphthalene in a 10:2 ratio along with metallic deposits. Although **4.3b** is a stable metal hydride, any transiently formed bismuth analogue presumably undergoes reductive elimination of bis(trimethylsilylamino)naphthalene due to the known instability of Bi–H bonds,[81] and deposits metallic bismuth. Inser-

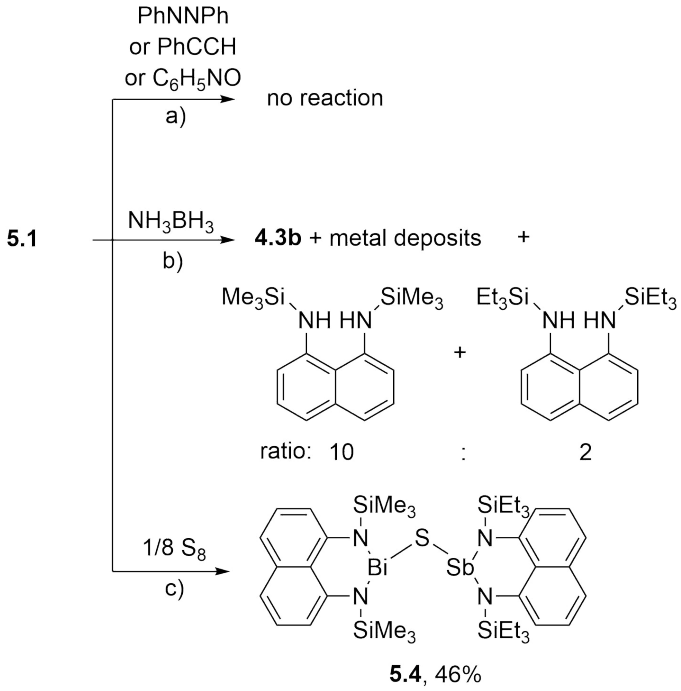

Figure 5.4: Reactivity of **5.1** with a variety of substrates.

tion of a sulfur atom into the Sb–Bi bond was achieved by heating a solution of **5.1** and S_8 in toluene at 100 °C for 1 hour. This gave full conversion to **5.4**, which provides the first documented example of an Sb–S–Bi bonding moiety (Figure 5.4c). A Cambridge Crystallographic Data Center (CCDC) search further revealed that **5.4** is only the third structurally characterized example of an Sb–Z–Bi moiety, where Z is any element of the periodic table.[208209] Compound **5.4** was fully characterized, and the structure was determined by X-ray crystallography. The Sb–S (2.3838(8) Å) and Bi–S (2.5456(7) Å) bond lengths are within range of mean E–S bond lengths observed for antimony sulphides and bismuth sulphides (Sb–S: 2.527±0.173 Å; Bi–S: 2.791±0.177 Å) and the Sb–S–Bi angle (116.06(3)°) is as expected for a bent geometry at sulphur. The N–Bi–S bonding angles (91.52(6), 91.15(6)°) are significantly more contracted than the N–Sb–S angles (101.50(6), 102.49(6)°). The N–E–N

(E=Sb: 89.35(8); E=Bi: 83.86(8)°) angles around Sb are comparable to those found in **5.1** and **5.2**, however significantly contracted with respect to the bismuth atom.

The field of bismuth antimony alloys is an attractive area of materials chemistry due to the potential of BiSb alloys being the best n-type thermoelectric material at low temperatures (20–200 K). Current methods do not have a single-source precursor leading to poor morphological control and broad size distribution. The deposition of SbBi nanocrystals was accomplished from dual-source precursors through the reduction of antimony and bismuth amides in the presence of olyelamine.[210] Reactivity studies of compounds with Sb–Bi bonds and reducing agents (e.g. LiHBEt3) will be undertaken to develop application of these compounds as single-source precursors for depositing BiSb nanocrystals.

5.3 Conclusions

Thermally-robust bismuthanylstibanes were synthesized in a one-step, high yield reaction, providing the first examples of neutral Bi–Sb σ-bonds in the solid-state. DFT calculations indicate that the bis(silylamino)naphthalene scaffold is well-suited for supporting otherwise labile bonds because it increases interaction energies through a combination of inductive effects and the dispersion effects. We also examined the reaction chemistry of the Bi–Sb bond by showing the insertion of a sulphur atom. This provides the first documented example of a Bi–S–Sb bonding moiety. We are currently examining the reactivity of this bond and the application of bismuthanylstibanes compounds as single-source precursors for depositing BiSb nanocrystals.

5.4 Experimental

5.4.1 General

Synthetic procedures.All manipulations were performed using standard Schlenk and glovebox techniques under an atmosphere of dry nitrogen. Solvents were dried over Na/benzophenone (tetrahydrofuran, pentanes, hexanes, benzene-d_6) or over

calcium hydride (dichloromethane, chloroform-d). Reaction glassware was baked in a 160 °C oven for at least 1 h prior to use and assembled under nitrogen while hot.

Solution NMR Spectroscopy. Nuclear magnetic resonance spectra are referenced to tetramethylsilane (^{1}H, ^{13}C) on a Bruker AV-300 spectrometer or a Bruker AV-500 spectrometer with residual solvent used for chemical shift calibration. Samples for NMR spectroscopy were prepared and sealed inside the glovebox with Parafilm or in a J-Young tube before removal into ambient atmosphere.

Vibrational Spectroscopy. Infrared spectra were obtained on a Thermo Scientific Nicolet NXR 9650 FT-Infrared Spectrometer instrument equipped with a 1064 nm Nd:YVO4 laser and InGaAs detector, on KBr plates. Details for individual compounds are given with their characterization data. Peak intensities are normalized to 100 and given in parentheses.

Melting Points. Melting points were obtained for samples sealed in glass capillaries and are uncorrected.

Crystallography. Single crystal diffraction experiments were performed on a Bruker D8-Quest Photon II diffractometer. The data was processed using the APEX III GUI software The XPREP program was used to confirm unit cell dimensions and crystal lattices. All calculations were carried out using the SHELXTL-plus and the Olex2 software packages for structure determination (ShelXT/Intrinsic phasing), solution refinement (ShelXL/Least squares), and molecular graphics. Space group choices were confirmed using Platon. The final refinements were obtained by introducing anisotropic thermal parameters and the recommended weightings for all atoms except the hydrogen atoms, which were placed at locations derived from a difference map and refined as riding contributions with isotropic displacement parameters that were 1.2 times those of the attached carbon atoms. Details for individual compounds are given with their characterization data. Crystallographic data has been deposited with the Cambridge Structural Database under numbers: 1975977-1975980.

Mass Spectrometry. Atmospheric Pressure Chemical Ionization (APCI) spectra

were obtained on a Bruker MicroTOF.

Commercial reagents. 1,8-Naphthalene diamine was obtained from Oakwood Chemicals. Chlorosilanes were obtained from Alfa. *n*Butylltihium (1.6 M in hexanes) was obtained from Acros. $SbCl_3$ and $BiCl_3$ were obtained from Alfa and sublimed prior to use. $LiNMe_2$ was obtained from Sigma Aldrich and used as received.

Known starting materials. Compounds **4.3b** and **4.2b** were synthesized according to the procedure of Chitnis *et. al.*[211] Compound **4.11a** was synthesized according to the procedure of Stalke *et. al.*[84]

5.4.2 Synthesis and Characterization

Representative procedure for the synthesis of bismuthanylstibanes ($^{R}BiSb^{R}$).

Compound **4.3b** (1.4460 g, 2.85 mmol) was dissolved in hexane (ca. 50 mL) and cooled to –30 °C. To this, compound **4.11a** (1.5792 g, 2.85 mmol) in a solution of hexane (ca. 50 mL) was slowly added, resulting in the formation of a dark red solution. The solution was warmed to room temperature and stirred for 5 hours. The reaction mixture was concentrated and placed in the freezer for recrystallization at –25 °C which gave the respective diaminobismuthanylstibanes as a red powder.

Compound 5.1:

Yield: 2.2047 g, 76%

^{1}H NMR (300 MHz, benzene-d_6): δ 7.30-7.08 (m, 12H, Ar-H), 0.89-0.86 (m, 18H, 2 x Et_3Si), 0.70-0.69 (m, 12H, 2 x Et_3Si), 0.15 (s, 18H, 2 x Me_3Si).

$^{13}C\{^{1}H\}$ (75 MHz, benzene-d_6): δ 154.3 (CAr), 151.4 (CAr), 138.2 (CAr), 137.7 (CAr), 136.9 (CAr), 126.2 (CAr), 124.7 (CAr), 124.4 (CAr), 122.1 (CAr), 120.4 (CAr), 116.8 (CAr), 116.01 (CAr), 7.4 (2 x Et_3Si), 6.7 (2 x Et_3Si), 3.13 (2 x Me_3Si).

FTIR (cm^{-1} (relative int.)): 3051(7), 2950(25), 2906(2), 2872(5), 1959(13), 1555(55), 1511(1), 1460(1), 1453(6), 1429(2), 1422(19), 1384(4), 1371(34), 1324(33), 1312(3),

1271(100), 1249(33), 1174(7), 1155(1), 1126(3), 1103(1), 1057(81), 1039(14), 1018(4), 1002(29), 958(<1), 887(12), 872(15), 856(72), 838(21), 809(26), 781(22), 763(30), 751(81), 736(1), 720(1), 693(2), 682(<1), 675(9), 658(3), 624(<1), 618(4), 599(2), 589(7), 572(1), 530(14), 521(6), 481(11).

HRMS (APCI, $[M]^+$): calculated = 1014.2732 m/z, observed = 1014.2734 m/z, error = 0.24 ppm

X-ray: Crystals were grown from a hexane solution. $C_{38}H_{60}BiN_4SbSi_4$ (M =1029.93 g/mol): monoclinic, space group $C2/c$ (no. 15), a = 20.7764(8) Å, b = 9.9748(4) Å, c = 42.2992(15) Å, β = 100.049(2)°, V = 8631.6(6) Å^3, Z = 8, T = 120.0 K, μ(CuKα) = 14.180 mm^{-1}, D_{calc} = 1.585 g/cm^3, 60586 reflections measured (4.242° $\leq 2\theta \leq$ 144.412°), 8363 unique (R_{int} = 0.0536, R_{sigma} = 0.0306) which were used in all calculations. The final R_1 was 0.0334 ($I > 2\sigma(I)$) and wR_2 was 0.0809 (all data). CCDC No. 1975979.

Compound 5.2:

Yield: 0.3975 mg, 69%

^{1}H NMR (300 MHz, benzene-d_6): δ 7.30-7.09 (m, 12H, Ar-H), 1.39-1.33 (m, 6H, 2 x iPr_3Si), 1.15-1.13 (d, 18H, 2 x iPr_3Si), 0.99-0.97 (d, 18H, 2 x iPr_3Si), 0.17 (s, 18H, 2 x Me_3Si).

$^{13}C\{^1H\}$ (75 MHz, benzene-d_6): δ 153.7 (CAr), 151.8 (CAr), 138.2 (CAr), 137.7 (CAr), 136.9 (CAr), 124.8 (CAr), 124.0 (CAr), 122.4 (CAr), 120.5 (CAr), 117.6 (CAr), 116.5 (CAr), 19.2 (2 x iPr_3Si), 19.1 (2 x iPr_3Si), 14.9 (2 x iPr_3Si), 3.27 (2 x Me_3Si).

FTIR (cm^1 (relative int.)): 3053(13), 2945(60), 2927(1), 2924(1), 2889(4), 2865(25), 1959(24), 1598(3), 1578(2), 1556(63), 1465(19), 1425(22), 1384(12), 1370(33), 1325(24), 1313(6), 1270(100), 1248(22), 1173(5), 1165(2), 1124(5), 1098(1), 1059(68), 1049(8), 1039(8), 1016(7), 988(3), 884(15), 868(36), 842(100), 794(33), 780(16), 758(47), 748(6), 734(23), 674(4), 654(19), 557(7), 524(20), 515(3).

HRMS (APCI, $[M]^+$): calculated = 1098.3671 m/z, observed = 1098.3634 m/z, error

= 3.32 ppm

X-ray: Crystals were grown from benzene solutions. $C_{47}H_{75}BiN_4SbSi_4$ (M =1139.20 g/mol): monoclinic, space group $P2_1/n$ (no. 14), a = 11.7148(10) Å, b = 24.8374(17) Å, c = 17.6977(10) Å, β = 98.486(2)°, V = 5093.0(6) Å^3, Z = 4, T = 120.0 K, μ(CuKα) = 12.067 mm^{-1}, D_{calc} = 1.486 g/cm^3, 82000 reflections measured (6.178° $\leq 2\theta \leq$ 127.002°), 8287 unique (R_{int} = 0.0579, R_{sigma} = 0.0298) which were used in all calculations. The final R_1 was 0.0592 ($I > 2\sigma(I)$) and wR_2 was 0.1426 (all data). CCDC No. 1975980.

Compound 5.3:

Yield: 0.2609 g, 58%

^{1}H NMR (300 MHz, benzene-d_6): δ 7.31-7.08 (m, 12H, Ar-H), 0.91-0.80 (m, 36H, 4 x Et_3Si), 0.77-0.70 (m, 24H, 4 x Et_3Si).

$^{13}C\{^1H\}$ (75 MHz, benzene-d_6): δ 154.9 (CAr), 151.5 (CAr), 138.0 (CAr), 137.7 (CAr), 136.5 (CAr), 126.5 (CAr), 124.5 (CAr), 124.3 (CAr), 122.2 (CAr), 120.3 (CAr), 117.4 (CAr), 115.5 (CAr), 7.5 (1 x Et_3Si), 7.1 (1 x Et_3Si), 6.9 (2 x Et_3Si).

FTIR (cm^{-1} (relative int.)): 2950(20), 2932(2), 2920(3), 2906(1), 2870(8), 2851(1), 1959(23), 1556(17), 1463(2), 1454(7), 1434(2), 1413(8), 1384(17), 1370(6), 1322(1), 1311(11), 1271(4), 1235(100), 1205(2), 1182(3), 1153(8), 1127(17), 1062(16), 1039(13), 1019(4), 999(29), 984(8), 879(23), 860(13), 845(27), 804(47), 788(17), 779(8), 763(8), 747(36), 719(11), 691(14), 652(2), 588(5), 530(4), 521(8).

HRMS (APCI, $[M]^+$): calculated = 1098.3671 m/z, observed = 1098.3680 m/z, error = 0.89 ppm.

X-ray: Crystals were grown from hexane solutions. This structure was solved in triclinic, space group P_1 (no. 1) due to a Bi/Sb substitutional disorder. $C_{44}H_{71}BiN_4SbSi_4$ (M =1099.64 g/mol): triclinic, space group P_1 (no. 1), a = 10.5482(4) Å, b = 12.2644(5) Å, c = 19.2011(8) Å, α = 90.033(2)°, β = 78.3440(10)°, γ = 89.997(2)°, V = 2432.77(17) Å^3, Z = 2, T = 115.0 K, μ(CuKα) = 12.609 mm^{-1}, D_{calc} = 1.501 g/cm^3, 134707 reflections measured (4.698° $\leq 2\theta \leq$ 144.452°), 18345 unique (R_{int}

= 0.0521, R_{sigma} = 0.0293) which were used in all calculations. The final R_1 was 0.0973 ($I > 2\sigma(I)$) and wR_2 was 0.2513 (all data). CCDC No. 1980822.

Compound 5.4:

Compound **5.1** (0.2561 g, 0.252 mmol) was dissolved in toluene (ca. 5 mL) and added to a pressure vessel containing S_8 (0.0081 g, 0.031 mmol). The solution was heated to 100 °C and stirred for 1 hour. The solvent was removed and the residual solid was dissolved in pentane and placed in the freezer for recrystallization at –25 °C which gave the respective thiobismuthanylstibane as a brown solid.

Yield: 46%

^{1}H NMR (300 MHz, benzene-d_6): δ 7.43-7.09 (m, 12H, Ar-H), 0.87-0.80 (m, 18H, 2 x Et_3Si), 0.79-0.71 (m, 12H, 2 x Et_3Si), 0.21 (s, 18H, 2 x Me_3Si).

$^{13}C\{^1H\}$ (75 MHz, benzene-d_6): δ 148.1 (CAr), 145.6 (CAr), 137.9 (CAr), 137.7 (CAr), 132.1 (CAr), 127.1 (CAr), 126.4 (CAr), 123.6 (CAr), 121.8 (CAr), 119.7 (CAr), 118.0 (CAr), 116.2 (CAr), 7.2 (2 x Et_3Si), 6.0 (2 x Et_3Si), 2.6 (2 x Me_3Si).

FTIR (cm^{-1} (relative int.)): 3223(10), 3054(17), 3027(6), 2955(108), 2933(3), 2874(21), 2029(11), 1959(43), 1598(5), 1579(10), 1562(78), 1512(14), 1494(21), 1460(33), 1453(5), 1420(51), 1416(2), 1384(14), 1375(40), 1332(11), 1313(17), 1293(6), 1274(100), 1263(5), 1251(37), 1175(6), 1162(2), 1154(6), 1092(2), 1080(6), 1059(111), 1043(17), 1031(8), 1017(6), 1002(27), 870(32), 859(2), 842(92), 815(40), 783(13), 767(30), 755(127), 730(16), 698(60), 659(3), 648(2), 627(2), 621(10), 605(32), 588(8), 532(13).

HRMS (APCI): decomposed in spectrometer.

X-ray: Crystals were grown from a saturated hexane solution. $C_{38}H_{60}BiN_4SSbSi_4$ (M =917.87 g/mol): monoclinic, space group $P2_1/c$ (no. 14), a = 16.5940(6) Å, b = 12.7708(4) Å, c = 21.9816(8) Å, β = 108.2140(10)°, V = 4424.9(3) Å^3, Z = 4, T = 116 K, μ(CuKα) = 14.183 mm^{-1}, D_{calc} = 1.378 g/cm^3, 106069 reflections measured ($5.606° \leq 2\theta \leq 144.504^1$), 8717 unique ($R_{int}$ = 0.0309, R_{sigma} = 0.0126) which were used in all calculations. The final R_1 was 0.0178 ($I > 2\sigma(I)$) and wR_2 was 0.0440 (all data). CCDC No. 1975978.

Compound $(EtSb)_4Sb_8$:

Spectroscopic data could not be obtained for this product due to poor solubility and a mixture of solids precipitating out of solution. Note that this compound was formed as a byproduct and is not of immediate interest to the findings of this study.

Xray: Crystals were grown from a solution of ether. $C_{30}H_{40}N_2Sb_3Si_2$ (M =850.07 g/mol): monoclinic, space group $P2_1$ (no. 4), a = 18.3686(6) Å, b = 11.8349(4) Å, c = 25.5125(8) Å, β = 92.574(2)°, V = 5540.6(3) Å^3, Z = 8, T = 125.0 K, μ(MoKα) = 3.016 mm^{-1}, D_{calc} = 2.038 g/cm^3, 147121 reflections measured (3.972°$\leq 2\theta \leq$ 53.406°), 22856 unique (R_{int} = 0.0470, R_{sigma} = 0.0261) which were used in all calculations. The final R_1 was 0.0200 ($I > 2\sigma(I)$) and wR_2 was 0.0411 (all data). CCDC No. 1975977.

5.4.3 Computational Details

All calculations were performed using the 2017 Amsterdam Density Functional (ADF) suite.[154]

EDA calculations: The BP86 functional was used with Grimme's D3[147] correction and Becke-Johnson dampening. The TZ2P basis set was employed with a small frozen core approximation and scalar relativistic correction. Homolytic dissociation of the Sb-Bi bond into two doublet fragments was assumed due to their similar electronegativities. All optimized species were confirmed as minima by frequency analysis.[206]

NBO calculations: The BP86 functional was used with Grimme's D3[147] correction and Becke-Johnson dampening. The TZ2P basis set was employed without any frozen core approximation. Scalar relativistic correction was employed. NBO analysis homolytic dissociation of the Sb-Bi bond into two doublet fragments was assumed due to their similar electronegativities.

Chapter 6

Selective Insertion of Carbon Dioxide Into Bismuth Nitrogen Bonds

6.1 Introduction

The capture and functionalization of CO_2, a potent greenhouse gas, is widely regarded to be a major challenge of the twenty-first century.[212] CO_2 capture and functionalization possess many challenges, such as the intrinsic reaction barrier of CO_2-activation, particularly when considering operative ambient reaction conditions.[213] The high polarity of the C=O bond makes it kinetically susceptible towards reactions with strong dipoles.[214] As such, facile insertion into very polarized M-N bonds has led to the conversion of CO_2 to organic carbamates; a class of compounds with applications in the synthesis of polymers,[215] insecticides,[216] and pharmaceuticals.[217]

Uncatalyzed insertion of CO_2 into polar metal amide bonds of heavy main-group elements is much less common than the analogous insertion reaction involving electropositive s-, d-, and f-block metal amides.[214218219219220221] As part of our exploration of chemistry at heavy Group 15 centers, we were interested in exploring the facility of selective CO_2 insertion into bismuth amide bonds. The reaction of CO_2 with Bi–O and Bi–C bonds is known to yield carbonates and carboylates, respectively (Figure 6.1).[222223224225226227] In some instances, the captured CO_2 equivalent

has been transferred to organic fragments (e.g. epoxides).[227,228] The insertion of CO_2 into a Bi–N bond has been comparatively minimally explored, with the two known studies demonstrating uncontrolled, multiple, insertion under excess CO_2 conditions.[229,230] Bismuth carbamates are also known to be made through alkoxide/carbamate methathesis.[225]

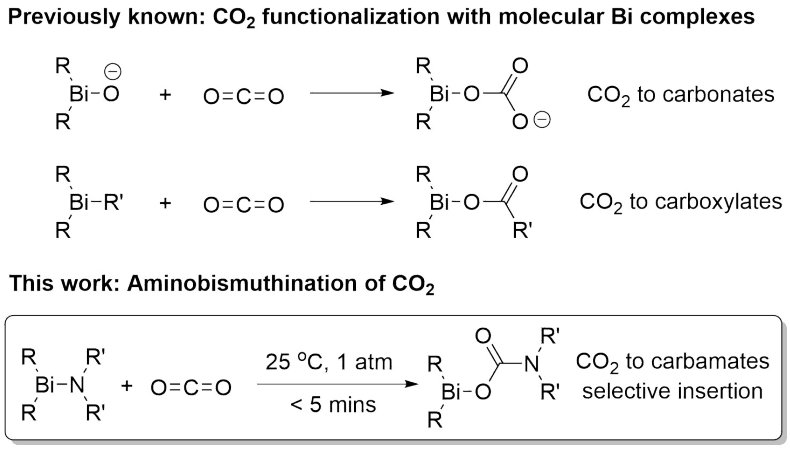

Figure 6.1: Conversion of CO_2 to carbonates, carboxylates and carbamates with molecular Bi complexes

6.2 Results and Discussion

The homoleptic bismuth amide **6.1a** contains three polar Bi–N bonds, potentially allowing for single, double, and triple insertion of CO_2 (Figure 6.2). As previously reported,[229] the addition of one molar equivalent of CO_2 to yellow coloured solutions of **6.1a** in THF gave a colourless solution, characteristic of formation of **6.1b**. Monitoring of reaction mixtures via ^{1}H NMR spectroscopy revealed sole formation of **6.1b**, even when a 3:1 stoichiometry of **6.1a**:CO_2 was used.

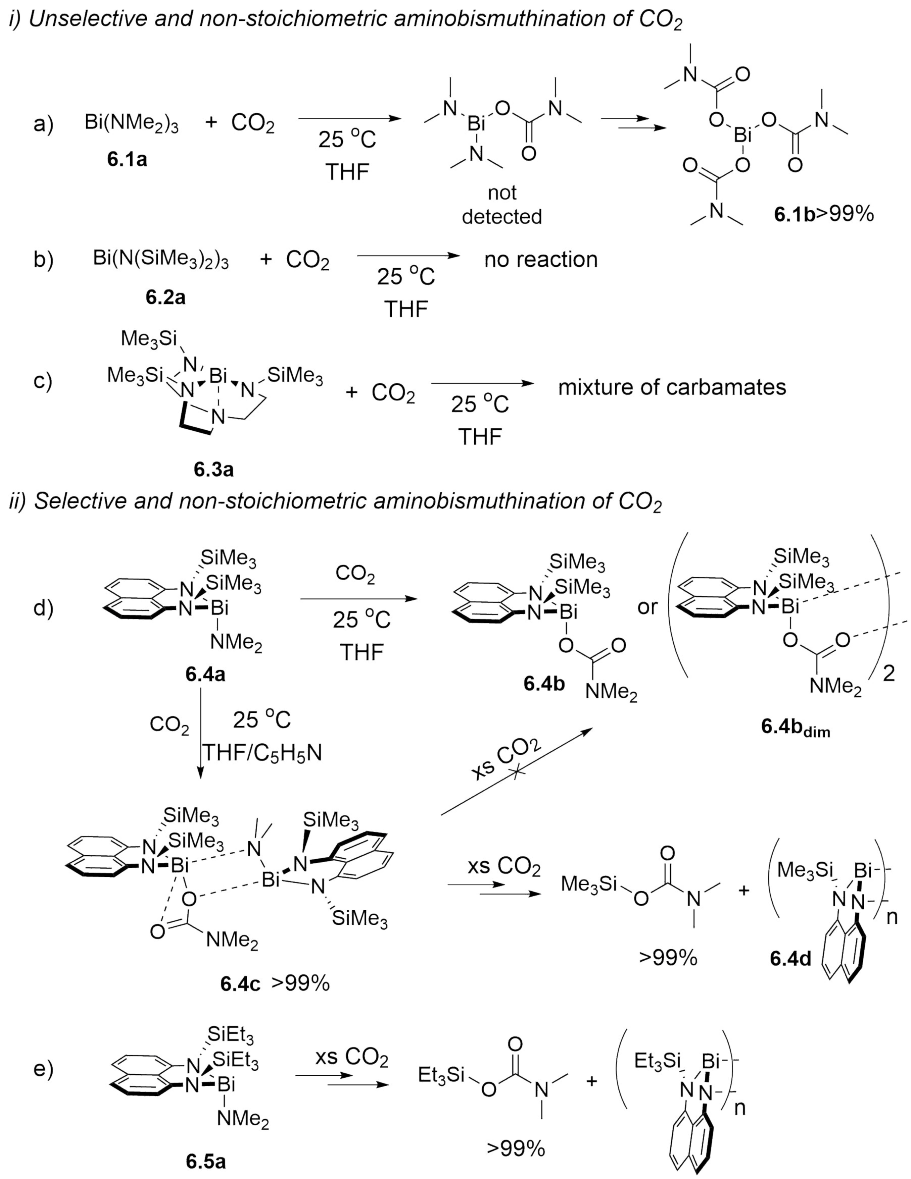

Figure 6.2: i) Unselective and non-stoichiometric insertion of CO_2 into Bi–N bonds, ii) selective but non-stoichiometric insertion of CO_2 into Bi–N bonds.

The analogous reaction of $Bi(N(SiMe_3)_2)_3$ with CO_2 was unproductive based on ^1H NMR spectroscopy, even after prolonged exposure to the gas. This was presumably because of the significant increase in steric bulk around the Bi center and lower basicity of the $N(SiMe_3)_2$ group relative to NMe_2. We then considered triamide $N(CH_2CH_2N(SiMe_3))_3Bi$[231] (6.3b, Figure 6.2c), where the steric bulk is pinned back with a trenamine ligand. Exposure of solutions containing **6.3a** to one molar equivalent of CO_2 gave a complex mixture of compounds. Although CO_2 insertion was confirmed via vibrational spectroscopy (Figure D.9), the specific identities of the products remain unknown.

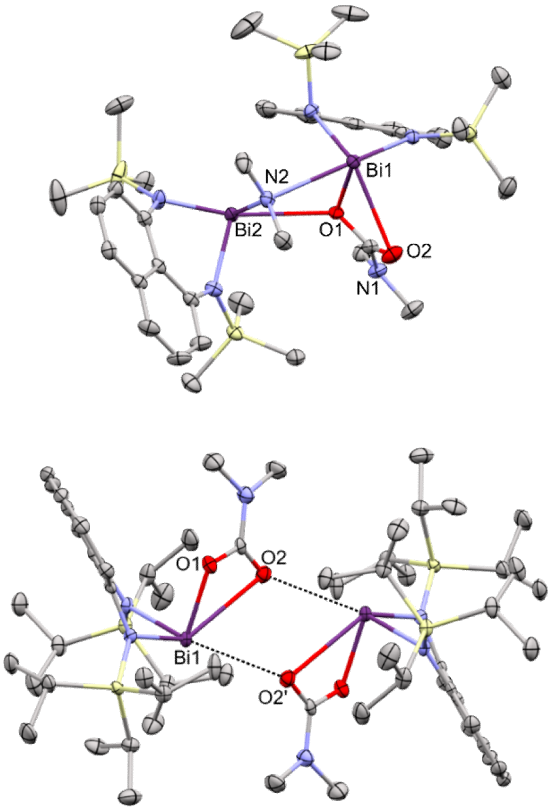

Figure 6.3: View of the structures of **6.4c** (top) and **6.6b$_{dim}$** (bottom) in the solid state. Hydrogen atoms have been omitted for clarity and thermal ellipsoids are shown at the 50% probability level.

We then sought to better control the selectivity of CO_2 insertion through the use of bismuth amide **6.4a**, which features a diaminonaphthalene ligand framework and terminal -NMe_2 group.[232233234235236237]The greater basicity of alkylamides relative to arylamides and the chelating nature of the backbone ultimately gave more define

reactivity. Exposure of **6.4a** to one molar equivalent of CO_2 (Figure 6.6) led to the immediate formation of **6.4c** in quantitative yield by ^{1}H NMR spectroscopy. Single-crystal X-ray analysis revealed selective insertion of CO_2 into the terminal Bi–NMe_2 bond. Despite the 1:1 stiochiometry of the reactants, a different stoichiometry of the products was obtained, resulting in what we refer to as "non-stoichiometric" insertion. Compound **6.4c** is instead viewed as an adduct between **6.4a** and transiently formed **6.4b**. Bi1 is coordinated to the carbamate in its primary coordination sphere and is five-coordinate due to interaction with both oxygen atoms [Bi1–O2 = 2.837(3) Å]. It is additionally coordinated to the NMe_2 moiety of an unreacted equivalent of **6.4b** [Bi1–N2 = 2.712(3) Å, Bi2–N2 = 2.228(3) Å].

A variable temperature ^{1}H NMR study revealed only one NMe_2 resonance, integrating to 12 protons, for redissolved crystals of **6.4b** in benzene-d_6, tetrahydrofuran-d_8, or pyridine-d_5 at 300 K, but two environments at 206 K, implicating a dynamic process that renders the two NMe_2 groups equivalent (Figure 6.4).

DFT calculations (Figure 6.5) indicate that formation of a dispersion adduct between **6.4a** and CO_2 (Int1) is followed by a nearly barrierless (TS1) nucleophilic attack by the amide upon the electrophilic carbon in CO_2, templated by a weak Bi—O interaction (Int2). A small barrier leads to the key insertion transition state (TS2), featuring both Bi–N and Bi–O interactions, and culminates in the formation of Int3 where the carbamate is bound to the metal via a pronounced Bi–O bond and a tenuous Bi—N interaction. The pyramidal NMe_2 group in Int3 then rotates around the nascent C–N bond via TS3 to enable N(lp)$\rightarrow CO_2$ π^* conjugation, furnishing **6.4b**, which has a planar carbamate substituent. Coordination of **6.4b** to **6.4a** (giving **6.4c**) is favoured over dimerization of **6.4b** (giving $\mathbf{6.4b_{dim}}$) by 11 kcal/mol, consistent with the exclusive observation of the adduct **6.4c**. Noting that the 11 kcal/mol energy difference is modest, that we anticipated being able to steer the reaction towards stoichiometric CO_2 insertion by one of three routes.

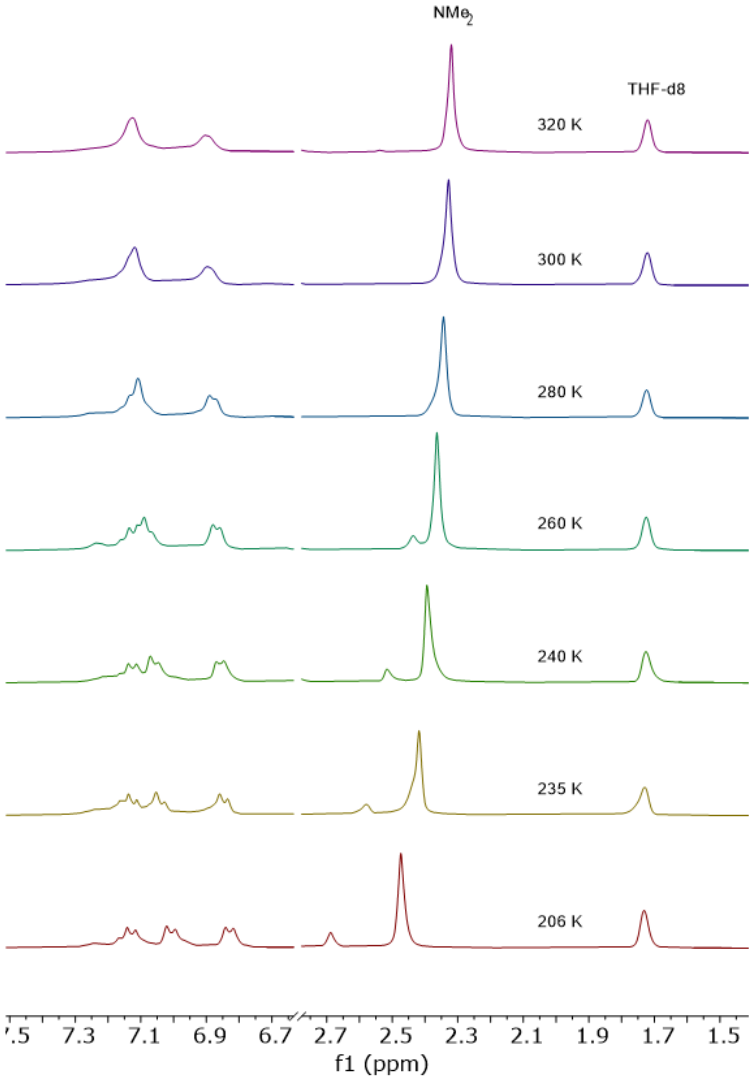

Figure 6.4: ^{1}H NMR spectra of **6.4c** as a function of temperature showing partial resolution of the NMe_2 resonance at low temperature into new peaks.

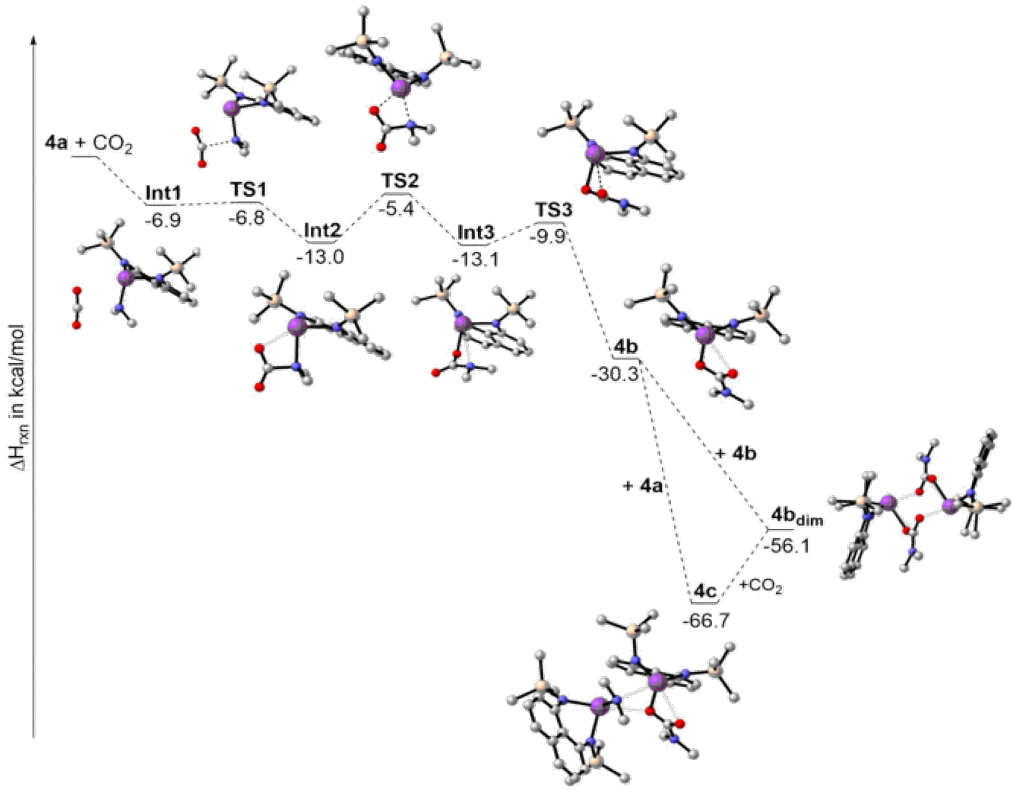

Figure 6.5: Reaction coordinate for the reaction of **6.4a** and CO_2. Enthalpy values given in the gas phase at 298 K. Hydrogen atoms are omitted for clarity.

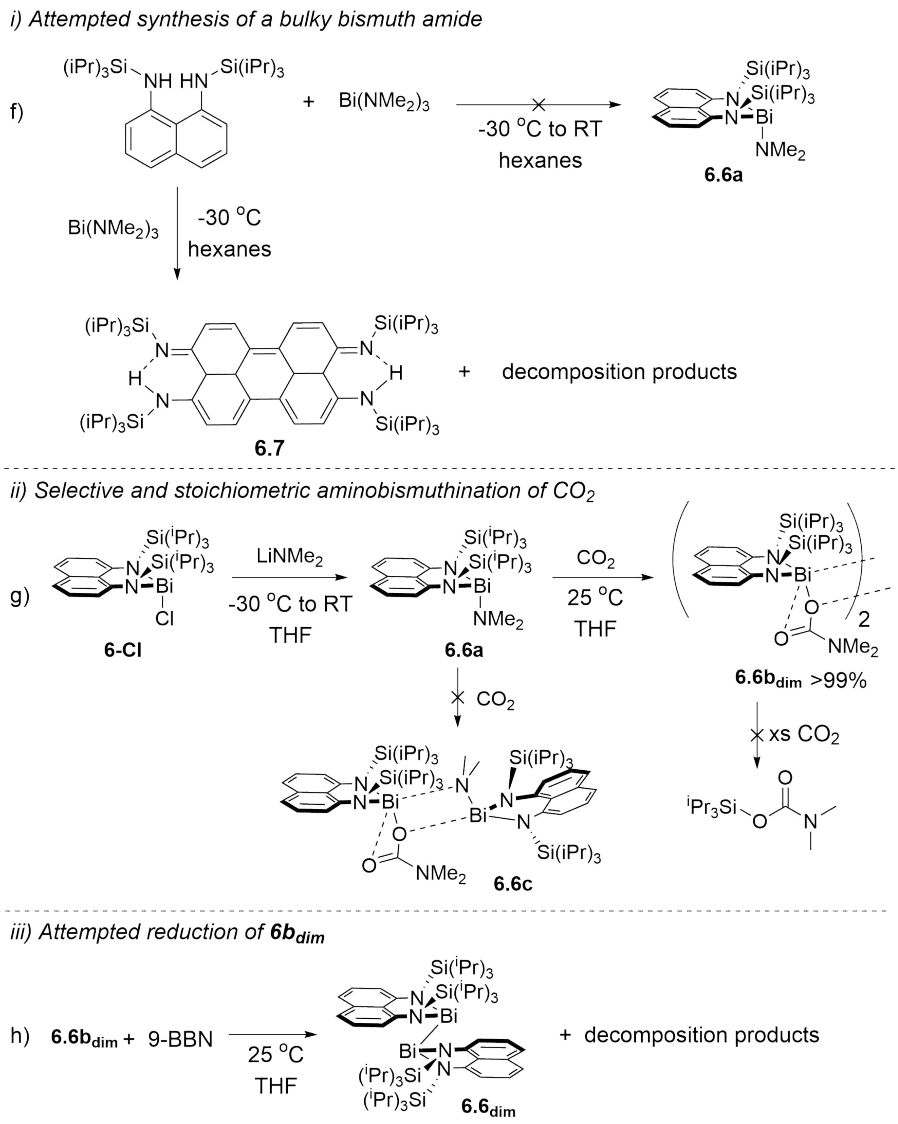

Figure 6.6: i) Attempted synthesis of a bulky bismuth amide. ii) Selective and stoichiometric aminobismuthination of CO_2. iii) Attempted reduction of $\mathbf{6b_{dim}}$.

First, **6.4a** was exposed to CO_2 in pyridine - a strongly coordinating solvent - to try and disrupt intermolecular association and liberate free **6.4a** for further reaction with CO_2. Unfortunately, this also yielded **6.4c** as the main product. We then treated a dilute solution of **6.4a** with a 10-fold excess of CO_2, to try and favour reactivity with the gas, rather than formation of **6.4c**. This yielded the silyl carbamate Me_3Si–$OC(O)NMe_2$, indicating decomposition of **6.4c** through N–Si bond scission. Formation of the undesired silylcarbamate must occur with concurent formation of **6.4d** or related oligomers.

When the above two routes failed, we turned towards the bulkier compounds **6.5a** and **6.6a**. Exposure of **6.5a** to excess CO_2 led to formation of the corresponding triethylsilylcarbamate, indicating that the progression from methyl to ethyl substitutes was not sufficient. Targeting the even bulkier $Si(^iPr)_3$ derivative required the addition of $LiNMe_2$ to **4.11b**, as the attempted syntheses via an aminolysis reaction between $Bi(NMe_2)_3$ and the corresponding naphthalenediamine did not yield the targeted bismuth amide.

Fortunately, the exposure of **6.6** to CO_2 gave quantitative and rapid formation of a single species as evidenced by ^1H NMR spectroscopy. Single-crystal X-ray diffraction confirmed this species as being the targeted stoichiometric dimer $\mathbf{6.6b_{dim}}$. Weak intermolecular Bi—O interactions (2.91(1)–3.10(1) A) hold the two monomeric components together. Adding excess CO_2 did not give the corresponding silylcarbamate. Attempts to reduce **6.6b** with phenylsilane, triethylsilane, and ammonia borane yielded **6.7**, due to the instability of Bi–H bonds,[238] and unidentified decomposition products.

6.3 Conclusions

Selective insertion of one molecule of CO_2 into a bismuth-nitrogen bond yielded the corresponding bismuth carbamates under mild conditions. This thorough study revealed the importance of ligand choice and bulk in obtaining selective insertion. These findings now motivate our pursuit of catalytic functionalization strategies to

valorize this greenhouse gas using rationally designed bismuth amides.

6.4 Experimental

6.4.1 General

Synthetic procedures.All manipulations were performed using standard Schlenk and glovebox techniques under an atmosphere of dry nitrogen. Solvents were dried over Na/benzophenone (tetrahydrofuran, pentanes, hexanes, benzene-d_6) or over activated 3 Åmolecular sieves (THF-d_8, C_6D_6, C_5D_5N, o-difluorobenzene). Reaction glassware was baked in a 160 °C oven for at least 1 h prior to use and assembled under nitrogen while hot.

Solution NMR Spectroscopy. Nuclear magnetic resonance spectra are referenced to tetramethylsilane (^1H, ^{13}C) on a Bruker AV-300 spectrometer or a Bruker AV-500 spectrometer with residual solvent used for chemical shift calibration. Samples for NMR spectroscopy were prepared and sealed inside the glovebox with Parafilm or in a J-Young tube before removal into ambient atmosphere.

Vibrational Spectroscopy. Infrared spectra were obtained on a Thermo Scientific Nicolet NXR 9650 FT-Infrared Spectrometer instrument equipped with a 1064 nm Nd:YVO4 laser and InGaAs detector, on KBr plates. Details for individual compounds are given with their characterization data. Peak intensities are normalized to 100 and given in parentheses.

Melting Points. Melting points were obtained for samples sealed in glass capillaries and are uncorrected.

Crystallography. Single crystal diffraction experiments were performed on a Bruker D8-Quest Photon II diffractometer. The data was processed using the APEX III GUI software The XPREP program was used to confirm unit cell dimensions and crystal lattices. All calculations were carried out using the SHELXTL-plus and the Olex2 software packages for structure determination (ShelXT/Intrinsic phasing), solution refinement (ShelXL/Least squares), and molecular graphics. Space group

choices were confirmed using Platon. The final refinements were obtained by introducing anisotropic thermal parameters and the recommended weightings for all atoms except the hydrogen atoms, which were placed at locations derived from a difference map and refined as riding contributions with isotropic displacement parameters that were 1.2 times those of the attached carbon atoms. Details for individual compounds are given with their characterization data.

Mass Spectrometry. Electro-Spray Ionization (ESI) and Atmospheric Pressure Chemical Ionization (APCI) spectra were obtained on a Bruker MicroTOF. In all cases, decomposition to the ligand occurred and precluded detection of the desired compounds.

Commercial reagents. 1,8-Naphthalene diamine was obtained from Oakwood Chemicals. Chlorosilanes were obtained from Alfa. *n*Butylltihium (1.6 M in hexanes) was obtained from Acros. $SbCl_3$ and $BiCl_3$ were obtained from Alfa and sublimed prior to use. $LiNMe_2$ was obtained from Sigma Aldrich and used as recieved. CO_2 gas was passed through a column packed with activated 3 Åmolecular sieves prior to use.

Computational Chemistry. Geometry optimizations and frequency calculations were performed using the Gaussian 16 suite. The PBE1 functional was used with Becke-Johnson dispersion dampening.

Known starting materials. Compounds **6.1a**, **6.2a**, **6.3a**, **6.4a**, and 1,8-bis-[(triisopropylsilyl)amino]naphthalene were prepared as per literature procedures.[182]

6.4.2 Synthesis and Characterization

Representative procedure for adding CO_2. Inside a glovebox, 0.1 mmol of an amide was transferred to a J-Young valved NMR tube and ca. 0.6 mL of solvent was added. The sealed tube was removed from the glovebox and attached to a Schlenk manifold. The sample was degassed using 3 freeze-pump-thaw cycles and then refilled with 1 atm of CO_2 and sealed at room temperature. The headspace of the tube at 1 atm holds approximately 0.1 mmol of an ideal gas. If required, additional equivalents of CO_2 were introduced by reopening the J-Young tube (with sample

under static vacuum due to consumption of previously added gas) briefly to the CO_2 stream until 1 atm internal pressure was again achieved. The sealed tube was inverted several times to mix the gas. Reactions generally began immediately and were completed within 5 minutes of mixing, as monitored by ^{1}H NMR spectroscopy.

Synthesis of 6.1b A yellow solution of **6.1a** (0.1 mmol) was prepared in 0.5 mL of tetrahydrofuran-d_8 and CO_2 (0.3 mmol) was added as per the representative procedure to obtain a colourless solution within 5 minutes, which showed a single ^{1}H NMR resonance. Removal of solvent under vacuum yielded **6.1b** as colourless crystals. Spectroscopic data matched previously reported values for this compound.[239]

Attempted reaction of 6.2a with CO_2 A yellow solution of **6.2a** (0.1 mmol) was prepared in 0.5 mL of tetrahydrofuran-d_8 and CO_2 (0.3 mmol) was added as per the representative procedure. No reaction was observed over 24 h.

Reaction of 6.3a with CO_2 A pale yellow solution of **6.1a** (0.1 mmol) was prepared in 0.5 mL of tetrahydrofuran-d_8 and CO_2 (0.3 mmol) was added as per the representative procedure to obtain a colourless solution within 5 minutes, which showed a multitude of ^{1}H NMR resonances attributed to multiple products. Isolation was not attempted due to the complex speciation. Removal of solvent left an oily solid, which was assayed by IR spectroscopy to determine the C=O stretching frequencies (Figure D.9).

IR (KBr plate, cm^{-1}): 2957(27), 2923(1), 2902(4), 2868(3), 1660(66), 1608(12), 1454(9), 1335(50), 1335(50), 1335(50), 1251(82), 1251(82), 1211(5), 1120(41), 1036(4), 1014(33), 938(7), 911(3), 848(100), 787(13), 757(9), 743(4), 705(3).

Synthesis of 6.4c: A dark orange solution of **6.4a** (0.18 mmol) was prepared in pyridine and CO_2 (ca. 0.2 mmol) was added as per the representative procedure. A slight change in colour to dark yellow was observed within 5 minutes and the conversion to **6.4c** was complete as per ^{1}H NMR spectroscopy. The reaction mixture was dried under vacuum and the residue was extracted with 5 mL of hexanes to obtain a bright yellow-orange solution. Cooling this solution to –25 °C yielded the product as a fine yellow powder.

Yield: 0.101 mg, 48%

Melting Point: 159–162 °C

^{1}H NMR (500 MHz, C_6D_6): 0.34 (s, 36 H, Me_3Si), 2.16 (s, 12 H, NMe_2), 7.17 (dd, 7.3/1.4 Hz, 4 H, Ar), 7.29 (t, 7.4 Hz, 4 H, Ar), 7.41 (dd, 7.5/1.3 Hz, 4 H, Ar).

^{13}C{^{1}H} (126 MHz, C_6D_6): 2.6 (Me_3Si), 36.0 (NMe_2), 115.6 (Ar), 120.3 (Ar), 126.8, (Ar), 130.9 (Ar), 138.2 (Ar), 147.8 (Ar), 162.7 (COO).

IR (KBr plate, cm^{-1}): 3050(10), 2949(37), 2894(2), 1558(98), 1484(20), 1440(12), 1426(3), 1397(50), 1373(15), 1329(21), 1275(80), 1249(30), 1233(1), 1175(5), 1061(71), 1040(12), 885(5), 868(28), 836(100), 803(5), 783(17), 757(37).

X-Ray: Crystals were grown from a hexane solutions. $C_{37}H_{60}Bi_2N_6O_2Si_4$ (M =1151.23 g/mol): monoclinic, space group $P21/c$ (no. 14), a = 10.2425(4) Å, b = 31.6554(12) Å, c = 28.1041(10) Å, β = 92.3920(10)°, V = 9104.3(6) Å^3, Z = 8, T = 116.0 K, μ(CuKα) = 16.299 mm-1, D_{calc} = 1.680 g/cm^3, 140891 reflections measured (4.206° $\leq 2\,\theta \leq$ 144.354°), 17919 unique (R_{int} = 0.0592, R_{sigma} = 0.0322) which were used in all calculations. The final R_1 was 0.0281 ($I > 2\sigma(I)$) and wR_2 was 0.0726 (all data). CCDC No. 2063353.

Synthesis of 1,8-bis[(triisopropylsilyl)amino]bismuth chloride: Naphthalene diamine (0.6328 g, 4 mmol) was dissolved in THF (ca. 25 mL) and cooled to –78 °C. To this, 5.1 mL of a solution of *n*-Butyllithium (1.6M in hexanes, 8 mmol) was slowly added, resulting in formation of a dark brown solution. The solution was warmed to room temperature and stirred for 14 hours. Next, a solution of $BiCl_3$ (1.2565 g, 4 mmol) in THF (ca. 25 mL) was prepared and cooled to –78 °C. The solution of $BiCl_3$ was added dropwise to a cooled solution of the lithiated ligand, which resulted in the formation of a dark red to black solution. The reaction was warmed to room temperature and stirred for 12 hours. The reaction was evaporated to dryness and the residue dissolved in ca. 20mL of hexanes then filtered, yielding a deep-red solution. Recrystallization at –25 °C gave the respective bismuth chloride as a red powder used without further purification.

Yield: 1.474 g, 52%

Melting Point: 118–123 °C

^{1}H NMR (300 MHz, C_6D_6): 1.05 (d, 6.8 Hz, 18 H, $CH(CH_3)_2$), 1.14 (d, 6.9 Hz, 18 H, $CH(CH_3)_2$), 1.29 (sept, 6 H, $CH(CH_3)_2$), 7.13 (m, 2 H, Ar), 7.27 (t, 7.5 Hz, 2 H, Ar), 7.36 (d, 8.1 Hz, 2 H, Ar.

$^{13}C\{^{1}H\}$ (75 MHz, C_6D_6): 15.2 ($CH(CH_3)_2$), 19.2 ($CH(CH_3)_2$), 116.8 (Ar), 121.8 (Ar), 126.1 (Ar), 137.8 (Ar), 145.9 (Ar).

IR (KBr plate, cm^{-1}): 3376(10), 3053(5), 2945(100), 2890(5), 2726(3), 1650(11), 1588(82), 1566(11), 1510(5), 1463(67), 1416(22), 1391(12), 1365(12), 1297(14), 1260(45), 1168(12), 1099(7), 1045(63), 1016(23), 996(6), 920(20), 882(68), 838(1), 790(34), 749(22), 735(6), 678(12), 640(25).

X-Ray: Crystals were grown from hexanes solutions. $C_{28}H_{48}BiClN_2Si_2$ (M =713.29 g/mol): orthorhombic, space group $P2_12_12_1$ (no. 19), a = 11.3776(3) Å, b = 11.6456(3) Å, c = 23.0890(5) Å, V = 3059.27(13) Å^3, Z = 4, T = 100.0 K, μ(CuKα) = 12.993 mm^{-1}, D_{calc} = 1.549 g/cm^3, 56544 reflections measured ($7.658^o \leq 2\theta \leq 144.348^o$), 6028 unique ($R_{int} = 0.0362$, $R_{sigma} = 0.0169$) which were used in all calculations. The final R_1 was 0.0231 ($I > 2\sigma(I)$) and wR_2 was 0.0548 (all data). CCDC No. 2063350.

Synthesis of 6.5a: Lithium dimethylamide (0.1023 mg, 2mmol) was dissolved in THF (ca. 10 mL) and cooled to –25 °C. This was added dropwise to a solution of 1,8-bis[(triisopropylsilyl)amino]bismuth chloride (1.4261 g, 2 mmol) in THF cooled to –25 °C, which resulted in the formation of a brown-green solution. The reaction was warmed to room temperature and stirred for 30 minutes. The reaction was evaporated to dryness and the residue dissolved in ca. 50 mL of pentanes then filtered, yielding a yellow-green solution. Recrystallization at –25 °C gave the respective bismuth amide as a yellow-green powder.

Yield: 0.3605 g, 26%

Melting Point: 148 °C (decomposition)

^{1}H NMR (300 MHz, C_6D_6): 1.12 (d, 7.2 Hz, 18 H, $CH(CH_3)_2$), 1.22 (d, 7.2 Hz, 18 H, $CH(CH_3)_2$), 1.42 (sept, 7.2 Hz, 6 H, $CH(CH_3)_2$), 3.00 (s, 6 H, NMe_2), 7.23 (m, 4 H, Ar), 7.38 (m, 2 H, Ar)

$^{13}C\{^1H\}$ (75 MHz, C_6D_6): 15.5 ($CH(CH_3)_2$), 19.5 ($CH(CH_3)_2$), 19.6 ($CH(CH_3)_2$), 43.2 (NMe_2), 117.1 (Ar), 121.2 (Ar), 126.1 (Ar), 129.7 (Ar), 138.4 (Ar), 148.1 (Ar)

IR (KBr plate, cm^{-1}): 3235(10), 2944(8), 2866(19), 2388(7), 2375(2), 2280(100), 1618(21), 1557(11), 1454(21), 1391(5), 1330(56), 1270(14), 1162(10), 1052(14), 884(7), 867(3), 812(79), 786(5), 758(3), 732(6).

Synthesis of 6.5b: A dark green-brown solution of **6.5a** (0.15 mmol) was prepared in THF and CO_2 (ca. 0.15 mmol) was added as per the representative procedure. A slight change in colour to brown-orange was observed within 5 minutes and the conversion to **6.5b** was quantitative as per ^{1}H NMR spectroscopy. Addition of an additional molar equivalent of CO_2 (1.5 mmol) did not result in further reaction. The reaction mixture was dried under vacuum and extracted with 5 mL of hexanes to obtain a bright yellow-orange solution. Cooling this solution to –25 °C yielded the product as a fine yellow powder.

Yield: 62%

Melting Point: 164-–175 °C

^{1}H NMR (300 MHz, C_6D_6): 1.14 (d, 7.6 Hz, 18 H, $CH(CH_3)_2$), 1.23 (d, 7.5 Hz, 18 H, $CH(CH_3)_2$), 1.37 (sept, 7.6 Hz, 6 H, $CH(CH_3)_2$), 2.18 (s, 6 H, NMe_2), 7.15 (m, 2 H, Ar), 7.28 (t, 8.1 Hz, 2 H, Ar), 7.36 (d, 7.8 Hz, 2 H, Ar).

$^{13}C\{^1H\}$ (75 MHz, C_6D_6): 15.3 ($CH(CH_3)_2$), 19.2 ($CH(CH_3)_2$), 19.3 ($CH(CH_3)_2$), 36.1 (NMe_2), 116.5 (Ar), 121.0 (Ar), 126.1 (Ar), 130.1 (Ar), 137.7 (Ar), 147.3 (Ar), 162.6 (COO).

IR (KBr plate, cm^{-1}): 3052(7), 2944(68), 2889(6), 2866(100), 2360(14), 2341(3), 2067(7), 1685(3), 1587(50), 1559(25), 1509(5), 1464(62), 1396(34), 1270(69), 1226(6), 1171(5), 1050(66), 1014(17), 919(12), 882(53), 867(9), 836(17), 787(45), 756(17), 735(35).

X-Ray: Crystals were grown from 1,2-difluorobenzene. $C_{31}H_{54}BiN_3O_2Si_2$ (M =765.93 g/mol): triclinic, space group $P_{\bar{1}}$ (no. 2), a = 12.0403(7) Å, b = 14.8836(12) Å, c = 19.5472(15) Å, $\alpha = 81.850(5)^o$, $\beta = 85.510(5)^o$, $\Gamma = 77.107(5)^o$, V = 3376.2(4) $Å^3$, Z = 4, T = 115.0 K, μ(CuKα) = 11.159 mm-1, D_{calc} = 1.507 g/cm^3, 99481 reflections measured ($4.572^o \leq 2\theta \leq 144.316^o$), 13241 unique ($R_{int}$ = 0.0373, R_{sigma} = 0.0211) which were used in all calculations. The final R_1 was 0.0213 ($I > 2\sigma(I)$) and wR_2 was 0.0533 (all data). CCDC No. 2063352.

Chapter 7

Synthesis of a Perfluorinated Phenoxyphosphorane and Conversion to its Hexacoordinate Anions

This project was explored at the beginning of my Ph.D. program; however, it was abandoned in favour of studying Group 15 amides after the targeted compounds failed to perform as expected under commercially relevant conditions (tested in collaboration with Prof. Jeff Dahn). This work is included here to provide an account of research completed based on Ph.D. funding proposals. Even though it does not fit within the overarching themes of the report, it did provide valuable insight into the requirements for computing the Lewis acidity at main-group centers that was recalled frequently throughout this report.

Portions of this work have appeared in **K. M. Marczenko**, C. L. Johnson,† S. S. Chitnis, Chem. Eur. J., 2019, 25, 8865-8874 (Full Paper; DOI: 10.1002/chem.201901333).

Contributions to the manuscript: KMM completed all experimental synthesis, most of the computational work, and wrote the first draft of the manuscript. CLJ conducted reactivity studies. SSC completed some computational work, wrote the final version of the manuscript, and supervised the project. † denotes undergraduate author.

7.1 Introduction

Strong Lewis Acids are essential as catalysts in industrial and academic chemistry.[136137240] Lewis acids are precursors to weakly coordinating anions (WCAs) - species that can improve the overall performance of batteries used in consumer electronics.[241138] In academic chemistry, strong Lewis acids and the WCAs derived from them allow for the isolation of fundamentally interesting molecules that push the boundaries of knowledge and may have future applications. The discovery of a new collection of Lewis acids and WCAs, and the evaluation of their performance as catalysts and materials for battery technology, is crucial for advancing these areas.

The replacement of halide groups with less reactive organic electronegative groups such as C_6F_5 or OC_6F_6 was successful in producing potent, non-corrosive Lewis acids using Group 13 elements (Figure 7.1a).[142242243141244139245] The most widely used classes of WCAs based on tetrahedral polyfluorinated borates[246] and aluminates were developed using this conversion strategy.[247248249] Strong neutral Lewis acids containing group 14 centers and pseudohalide substituents have also recently emerged.[110250] While this halide-to-pseudohalide conversion strategy is well-developed for Group 13 elements, and to a lesser extent group 14 elements, it has limited precedence for Group 15 elements.[60251252253] Besides the binary pentahalides, the best example of a neutral yet potent pnictogen (V) Lewis acid is the teflate derivatives (Figure 7.1b).[254255] Their fluoride ion affinities surpass the value for SbF_5, classifying them as Lewis superacids.[137] The corresponding $[M(OTeF_5)_6]$- anions show very low basicity, which has enabled the isolation of reactive carbo- and xeno-cations.[256257258] However, these Lewis acids require the handling of elemental fluorine in their synthesis, are extremely moisture sensitive, thermally unstable, and difficult to handle, limiting their practical utility.[256] In contrast, numerous examples of hexacoordinate phosphorus(V) anions featuring organic substituents have been reported - six of which feature bidentate monoaryl substituents (Figure 7.1c).[259260261262263] As a result, the degree of halogenation is quite low, and they are also formed as racemates rather than pure compounds. Nevertheless, some derivatives have successfully been used as the anionic components of polymerization initiators.[264265] The only achiral P(V) WCAs are those derived from perfluoroalkyl trifluorophosphates and

the tetracyano(difluoro)phosphate ion.[266] Due to the practical challenges associated with introducing perfluoroalkyl, cyanide, $OTeF_5$, or C_6F_5 substituents, we focused

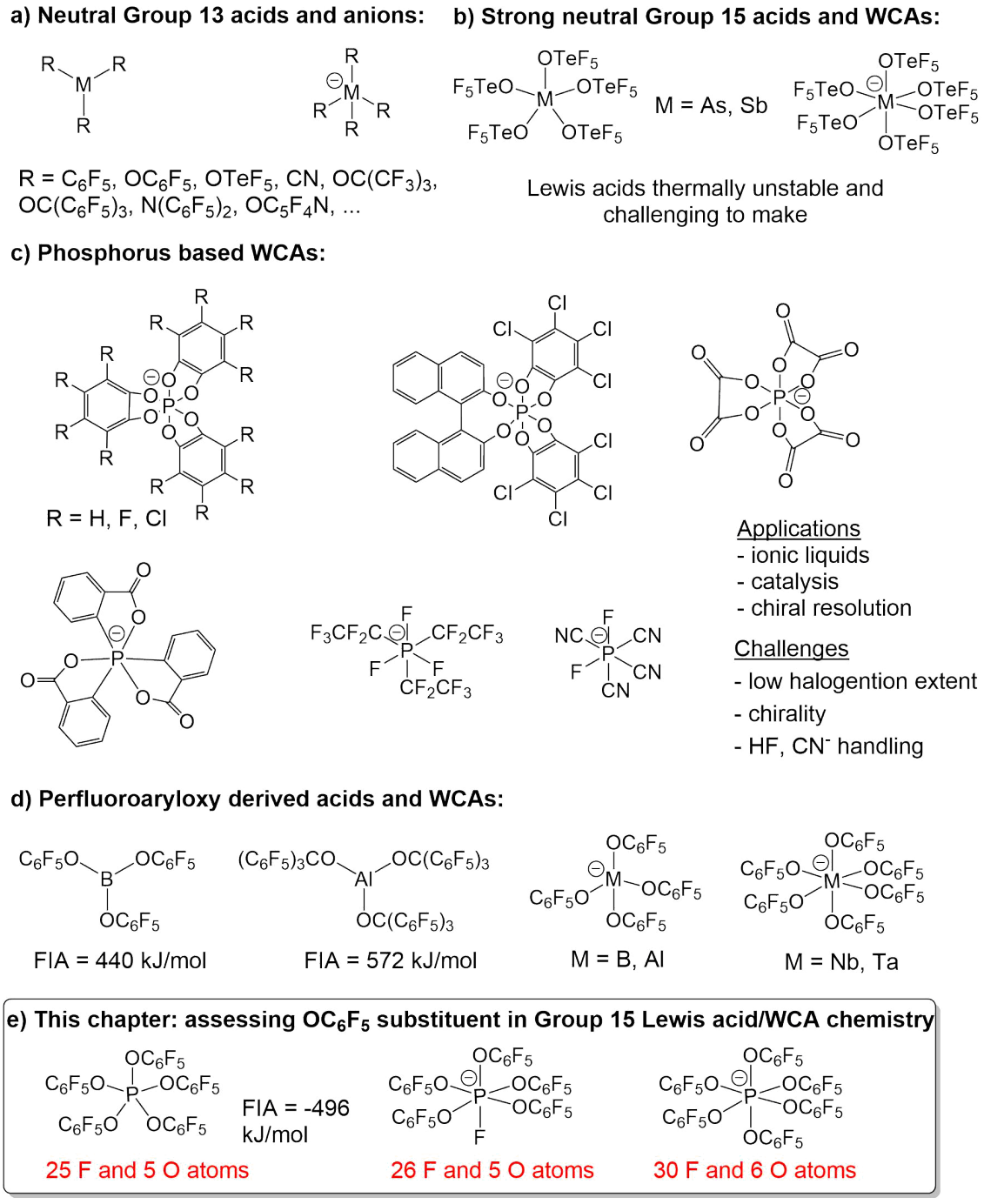

Figure 7.1: Select examples of pseudo-halide derived Lewis acids and WCAs. FIA refers to the Fluoride Ion Affinity and is a measure of Lewis acidity. See text for references.

on the easily accessible OC_6F_5 substituent to prepare neutral P(V) Lewis acids and anions. Marks *et al.* showed that the octahedral $[M(OC_6F_6)_6]^{-1}$ (M = Nb, Ta) anions are comparable to the $[B(C_6F_5)_4]^-$ anion in their ability to stabilize electrophilic metallocenium ions catalysts. This provided additional motivation for choosing the OC_6F_5 substituent.[249] Our goal was to prepare and test the $[P(OC_5F_5)_6]^-$ anion as a potential new WCA and a Li-ion battery electrolyte additive to enhance metal ion mobility, as has been reported successfully with the $[Al(OC(CF_3)_3)_4]^-$ anion.[241]

7.2 Results and Discussion

7.2.1 Syntheses

The reaction of commercially available PCl_5 with five equivalents of $LiOC_6F_5$ in CH_2Cl_2 at room temperature led to straightforward synthesis of $P(OC_6F_5)_5$ (**7.1**) in 70% isolated yield (Figure 7.2a). Compound **7.1** was purified by recrystallization from CH_2Cl_2 at –30 °C. It was found to be stable and soluble in acetonitrile, CH_2Cl_2, and 1,2-difluorobenzene. During the reaction, several intermediates were observed by NMR spectroscopy, and these were assigned the generic formula $P(OC_6F_5)_xCl_{5-x}$. The most stable mixed pseudohalide/halide intermediate was identified as $P(OC_6F_5)_4Cl$ (**7.2**) by independent synthesis. Addition of $NBu_4SiPh_3F_2$ to a solution of **2.1** in CH_2Cl_2 yielded $NBu_4P(OC_6F_5)_5F$ (**7.3**) in 87% isolated yield (Figure 7.2b). The anionic portion of **7.3** represents the fluoride adduct of **7.1**. Unexpectedly, $NBu_4P(OC_6F_5)_6$ (**7.4**) was formed as a minor product (5%) of this reaction, and varying the concentration, rate of addition, and order of addition did not affect the product ratios. Compound **7.1** was treated with one equivalent of $LiOC_6F_5$ in CH_2Cl_2 in an attempt to rationally form **2.4**, but no reaction was observed. We hypothesized that the lack of a reaction was due to lower nucleophilicity of the OC_6F_5 anion in poorly coordinating solvent, in which Li—O bridged oligomers could form. However, no reaction was observed between **7.1** and $LiOC_6F_5$, even in the more coordinating solvent Et_2O. Cooling this reaction mixture yielded a small amount of crystalline solid identified crystallographically as the tetramer $(LiOC_6F_5)_4{\cdot}(Et_2O)_3$ (**7.5**). This outcome suggested that aggregation

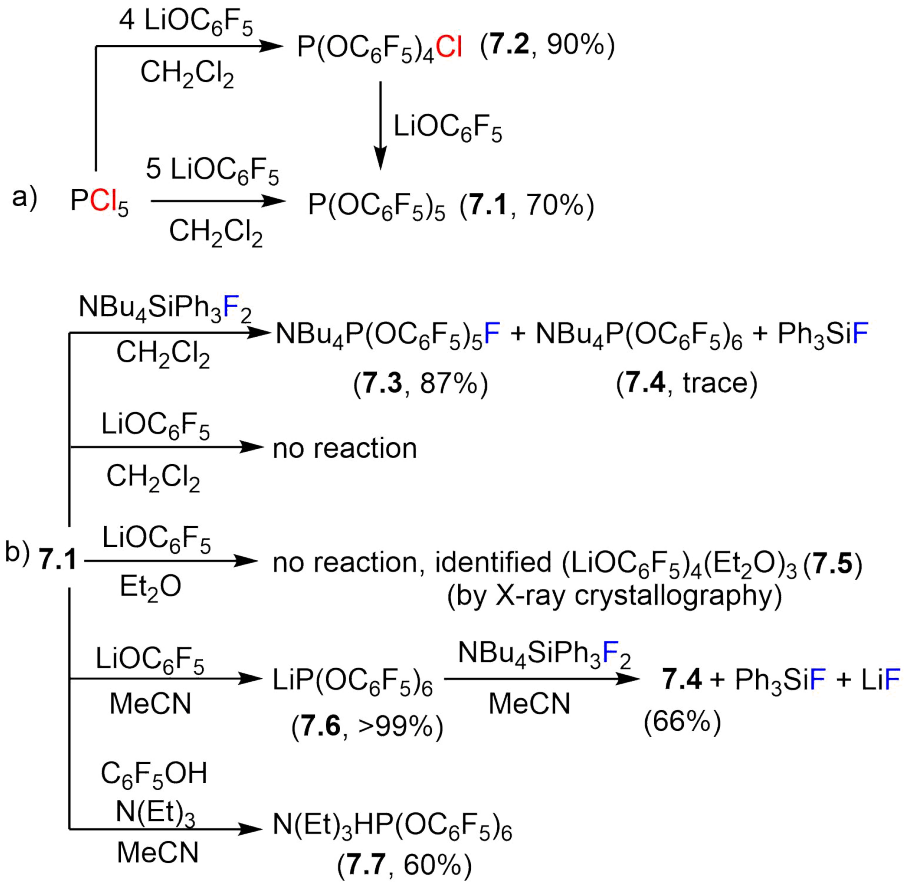

Figure 7.2: Synthesis of compounds **7.1-7.7**.

remains an obstacle, even in Et_2O.

In contrast, treatment of **7.1** with one equivalent of $LiOC_6F_5$ in even more coordinating solvent CH_3CN gave $LiP(OC_6F_5)_6$ (**7.6**) in nearly quantitative yield. Compound **7.6** is susceptible to cation exchange with $NBu_4SiPh_3F_2$ in acetonitrile to give $NBu_4P(OC_6F_5)$ (**7.4**). It was possible to prepare the tertiary ammonium salt $NEt_3HP(OC_6F_5)_6$ (**7.7**) in 60% yield by addition of the amine to an equimolar mixture of **7.1** and C_6F_5OH.

Compounds **7.1**–**7.4**, **7.6**, and **7.7** were isolated and comprehensively characterized by multinuclear NMR spectroscopy, vibrational spectroscopy, and elemental analysis. Compounds **7.1**–**7.5** were also structurally characterized by X-ray crystallography.

7.2.2 X-ray Crystallography

The single-crystal X-ray structures of compounds **7.1**–**7.5** were obtained. The structures of **7.1** (Figure 7.3a) and **7.2** (Figure 7.3b) have a trigonal-bipyramid PX_5 coordination geometry. The bond lengths in **7.1** (axial; 1.655(1), 1.675(1), equatorial; 1.590(1), 1.618(1), and 1.623(1) Å) are comparable to those in **7.2** (axial; 1.657(2) Å, equatorial; 1.593(2), 1.594(2), 1.595(2) Å). No secondary bonding interactions exist between the phosphorus center and the fluorine atoms of the OC_6F_5 groups in the structure of **7.1** or **7.2**.

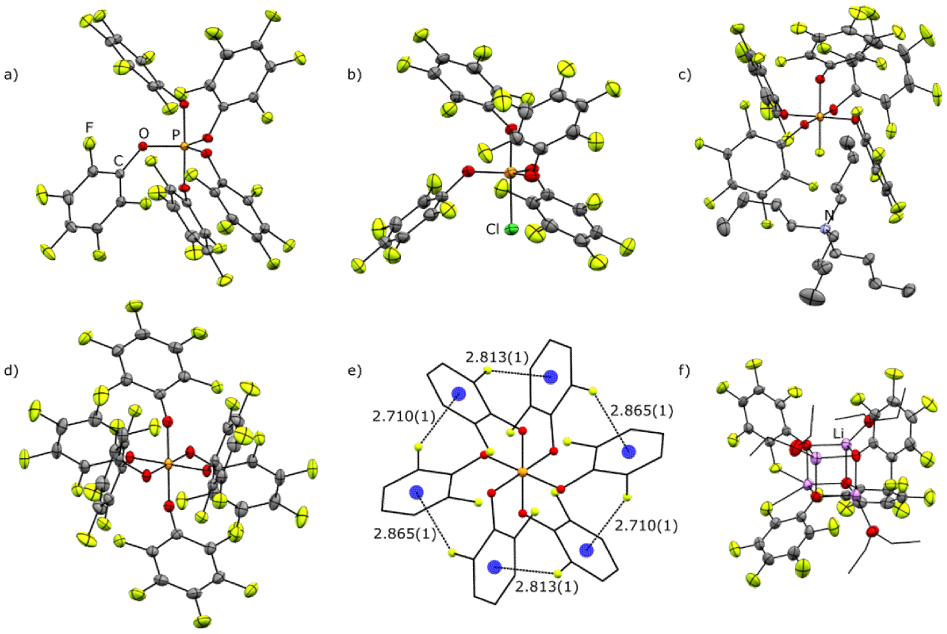

Figure 7.3: Single-crystal X-ray structure of a) **7.1**, b) **7.2**, c) the $[P(OC_6F_5)_5F]^-$ anion in **7.3** d) the $[P(OC_6F_5)_6]^-$ anion in **7.4**, e) select portions of the $[P(OC_6F_5)_6]^-$ anion in **7.4** showing the fluorine-π_{arene} interaction involving the *ortho* C–F groups, and f) **7.5**. Thermal ellipsoids are shown at the 50% probability level. Disordered CH_2Cl_2 solvent in b) and hydrogen atoms in c) have been omitted for clarity.

The $[P(OC_6F_5)_5F]^-$ anion in **7.3** (Figure 7.3c) has an octahedral PX_6 coordination geometry in which three short P–O bonds [1.698(1), 1.701(1) Å] and a P–F bond comprise the equatorial plane, and two P–O bonds [1.712(1) Å] define the axis. The P–O bonds in **7.3** are significantly elongated with respect to the corresponding values in **7.1**, consistent with the trans influence exerted by the substituents in the octahedral geometry. To the best of our knowledge, **7.3** contains the first

example of a structurally characterized mono-fluorophosphate anion. The crystal structure of **7.3** reveals two F—H contacts (2.365, 2.416 Å) between the tetrabutylammonium cation and the phosphorus bound fluorine atom. In the solid-state, all OC_6F_5 groups are participating in intramolecular *ortho*-F—π interactions (2.988, 2.988, 3.055, 3.180 Å, from the *ortho*-F to the centroid of OC_6F_5 participating in a π-interaction).

The geometry of the anion in the single-crystal X-ray structure of $NBu_4P(OC_6F_5)_6$ has an octahedral PX_6 coordination geometry with C_s symmetry (Figure 7.3d). Both the axial and equatorial P–O bond lengths are comparable to those found in the $[P(OC_6F_5)_5F]^-$ anion, indicating that replacement of a fluoride with OC_6F_5 did not introduce significant steric strain. No significant P—F contacts exist within the anion and the only interactions between the tetrabutylammonium cation and the $[P(OC_6F_5)_6]$ anion are H—F hydrogen bonds with the *ortho* and *meta* fluorine atoms of the OC_6F_5 groups. In the solid-state, all OC_6F_5 groups are participating in intramolecular *ortho*-F—π interactions with the *ortho*-F acting as a donor to the centroid of an adjacent electron-deficient C_6F_5 ring (π-hole).[267] The F—π interactions in **7.4** (2.710, 2.813, 2.865 Å) are shorter than those observed in **7.3** (2.988(1), 2.988(1), 3.055(1), 3.180(1) Å).

7.2.3 NMR Spectroscopy

^{19}F and ^{31}P NMR spectroscopic data for compounds **7.1**–**7.7** are summarized in Table 7.1. The ^{19}F NMR spectra of compounds **7.1** and **7.2** only show one set of *ortho*, *meta*, and *para* fluorine signals due to rapid rotation of the $-OC_6F_5$ substituents in solution.

The ^{19}F NMR spectrum of **7.3** and **7.4** were challenging to interpret at room temperature due to signal broadening and overlap. A variable temperature ^{19}F NMR study was conducted to assess the dynamic behaviour in solution. Upon cooling, the five aromatic C–F resonances observed in the ^{19}F NMR spectra of **7.3** split into seven signals (Figure 7.4). Based on the observed integrals, three of the signals are due to *ortho*, *meta*, and *para*-fluoro substituents of a single OC_6F_5 group trans to the fluoride. The remaining four signals arise from the aromatic fluorine

Compound	**^{31}P**	**^{19}F**	**J_{PF}**
7.1	-86.3	-154.0, -160.2, -162.9	
7.2	-65.3	-153.5, -158.8, -162.8	
7.3	-145.4	-66.6, -150.5, -154.4, -167.6, -168.0, -168.6	895.6 Hz
7.4	-148.2	-152.2, -167.5, -168.4	
7.6	-148.2	-152.5, -166.9, -167.9	
7.7	-147.0	-152.6, -167.0, -168.0	

Table 7.1: ^{31}P and ^{19}F NMR resonances for $P(OC_6F_5)_5$ (**7.1**), $P(OC_6F_5)_4Cl$ (**7.2**), $[NBu_4][P(OC_6F_5)_5F]$ (**7.3**), $[NBu_4][P(OC_6F_5)_6]$ (**7.4**), $[Li][P(OC_6F_5)_6]$ (**7.6**), and $[N(Et)_3][HP(OC_6F_5)_6]$ (**7.7**).

atoms of the equatorial OC_6F_5 substituents. Two of those are due to two *ortho* fluorine atoms residing *syn* or *anti* to the P–F bond and the remaining two signals are assigned to one para and two equivalent *meta* resonances per OC_6F_5 group. The ^{19}F NMR spectrum of the $[P(OC_6F_5)_6]$ anion showed splitting of a broad *ortho* resonance upon cooling to 250K (Figure 7.5). The observation of two distinct *ortho* C–F environments are consistent with the F–π arene interactions observed by X-ray crystallography. The experimentally determined $\Delta G^{\ddagger}$ value of 48 kJ mol^{-1} for the exchange process is considerably higher than values determined for F—π_{arene} interactions in "molecular balances" experiments (typically 6 kJ mol^{-1}),[159] which is consistent with the shorter ortho F—centroid$_{arene}$ distances observed in the $[P(OC_6F_5)_6]^-$ anion (2.710(1)–2.865(1) Å) than in molecular balances (3.06(1)–3.14(1) Å).[159]

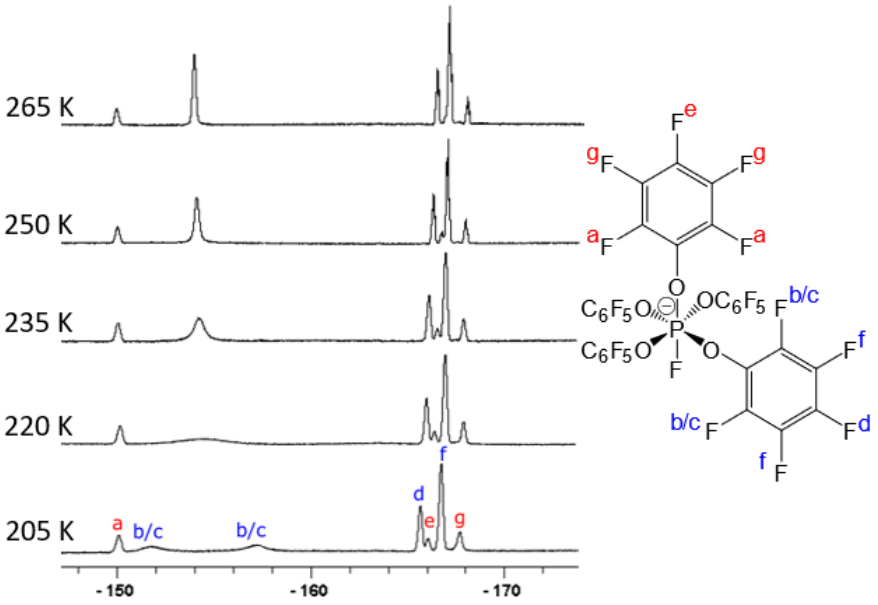

Figure 7.4: Variable temperature ^{19}F NMR spectra of **7.3** in CH_2Cl_2.

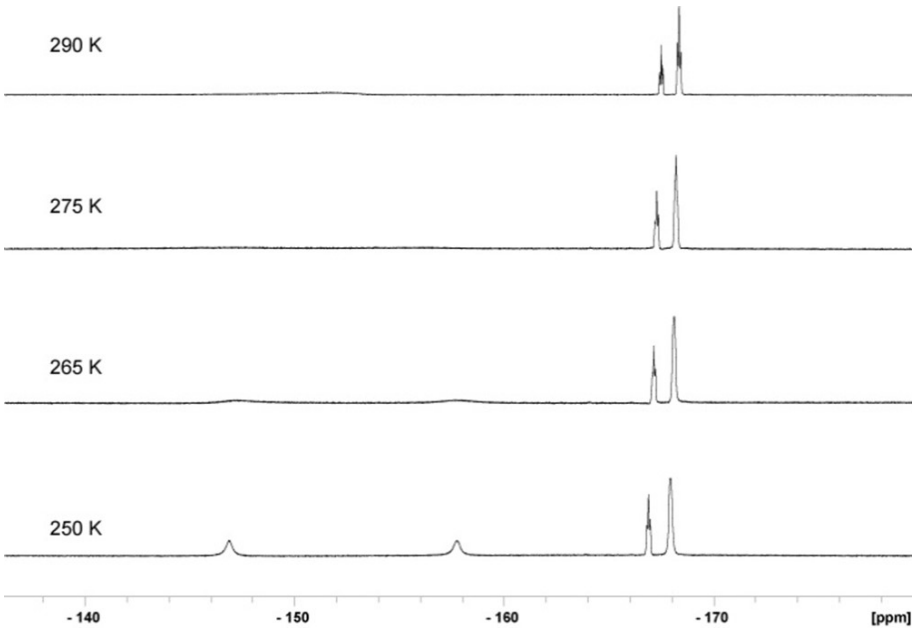

Figure 7.5: Variable temperature ^{19}F NMR spectra of **7.4** in CH_2Cl_2.The *ortho* C-F peaks are at -146.1 and -157.8 ppm in the 250 K spectrum.

7.2.4 Evaluation the Lewis Acid Strength of $P(OC_6F_5)_5$

Dispersion-corrected DFT calculations were used to study the structure of **7.1** in the gas-phase. The Lewis acidities of the $E(OC_6F_5)_5$ (E=P, As, Sb) family of compounds were evaluated by computing their Fluoride Ion Affinities (FIAs) at the BP8694/def2-SV(P)[149] level with Grimme D3 dispersion correction.[147] Def2-SV(P) is a split valence basis set with polarization functions on heavy atoms (not hydrogen). This basis set was chosen to facilitate direct comparison with previously reported data in the field.[268269270] FIAs were calculated by considering the sum of the reactions:

$$LA + COF_3^- \rightarrow LAF^- + COF_2$$

$$\underline{COF_2 + F^- \rightarrow COF_3^-}$$

$$LA + F \rightarrow LAF$$

where LA=$E(OC_6F_5)_5$ and LAF=$[E(OC_6F_5)F]^-$, and the experimental gas-phase FIA value of COF_2 is known to be 209 kJ mol^{-1}.[271] These calculations yielded an exceptionally high value of 497 kJ mol^{-1} for $P(OC_6F_5)_5$ in the gas phase, with the FIA value increasing down the group (Table E.1). For comparison, the calculated FIA of SbF_5 is 489 kJ mol^{-1}, defining the threshold of Lewis super acidity. An attempt was made to measure the Lewis acidity of **7.1** using the Gutmann-Beckett test.[272273] The Gutmann-Beckett test uses triethyl phosphine oxide as a probe molecule by relating the change in the ^{31}P chemical shift upon complexation to a Lewis acid. The combination of **7.1** with Et_3PO in CH_2Cl_2 revealed no evidence of interaction after 24 hours. The lack of evidence for complexation could be due to steric bulk, which has been shown to influence the observed chemical shift in the Gutmann-Becket methodology.[244]

We then experimentally bracketed the Lewis acidity of **7.1** through attempted fluoride abstraction from known anions. Although fluoride transfer from $[BF_4]^-$ to $P(OC_6F_5)_5$ was accomplished, no reaction was observed in the presence of the $[PF_6]^-$ anion. This experimentally observed trend of $FIA(BF_3) < FIA(7.1) < FIA(PF_5)$

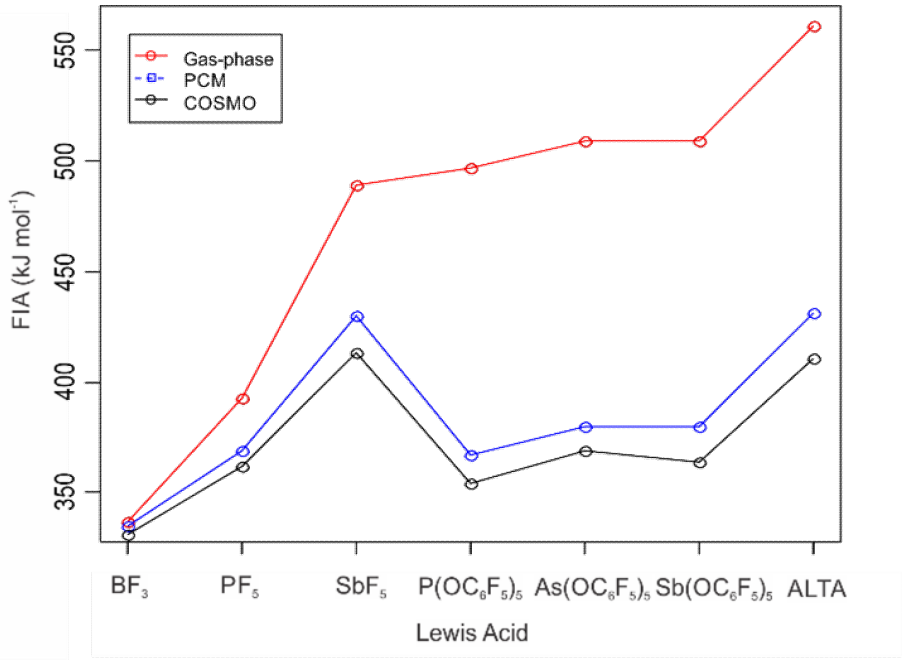

Figure 7.6: Calculated FIA (BP86/SV(P)) of BF_3, PF_5, SbF_5, $P(OC_6F_5)_5$ (**7.1**), $As(OC_6F_5)_5$, $Sb(OC_6F_5)_5$, and $Al(N(C_6F_5)_2)_3$ (ALTA) in the gas phase, with a PCM solvent model and with a COSMO solvent model.

does not agree with the calculated FIAs, which show that FIA(BF_3 = 337 kJ mol^{-1}) < FIA(PF_5 = 390 kJ mol^{-1}) < FIA(2.1 = 497 kJ mol^{-1}). The lack of agreement prompted us to investigate the influence of solvent inclusion on the calculated FIAs of these Lewis acids. The literature has noted a significant dampening of the FIA by the enthalpy of solvation (ΔH_{solv}) for cationic Lewis acids, but not neutral Lewis acids.[137] In contrast, significantly lower FIAs for all Group 15 $E(OC_6F_5)_5$ (E = P, As, Sb) Lewis acids were computed when implicit solvation was included. Both the Polarizable Continuum Model (PCM)[274] or a Conductor-like Screening Model (COSMO)[275] solvent models were evaluated using a field of CH_2Cl_2 (Figure 7.6). The FIA attenuation upon solvent model inclusion is strongly correlated with the size of the Lewis acid (Figure 7.6) with larger Lewis acids experiencing a more significant lowering of their FIA values when a solvent model is employed. For example, the gas-phase FIA of PF_5 is reduced by only 20 kJ/mol, but the gas-phase FIA of 7.1 is reduced by 140 kJ/mol in a field of CH_2Cl_2. Large reductions from the calculated FIAs are also observed for $As(OC_6F_5)_5$ and $Sb(OC_6F_5)_5$ but not for AsF_5 or SbF_5 (Table E.1). These results highlight the limitation of an often employed tool in this

field.

Given that FIA values specifically measure the fluorophilicity of a Lewis acid, we used Parr's global electrophilicity index (GEI)[276277278131] (Equation 7.1) to study derivatives of $E(OC_6F_5)_5$ (E = P, As, Sb). As with the FIA calculations, the calculated GEIs implied that **7.1** (GEI = 2.1 eV) is a much stronger electrophile than both PF_5 and BF_3 (GEI for both = 1.5 eV) in the gas-phase. Importantly, the inclusion of solvation did not reduce the GEI of the Lewis acids by a significant amount (Figure E.10). The lack of reduction in the predicted Lewis acidity could be because this method does not involve ions as part of the assessment or because it ignores steric crowding. Our results show that although the GEI has been proposed to be a convenient computational alternative to FIA calculations when assessing intrinsic electrophilicity,[278131] its use as a predictor for the outcomes of reactions is limited, even when solvation is considered.

$$GEI = \frac{[0.5(E_{\mathrm{HOMO}} + E_{\mathrm{LUMO}})]^2}{2(E_{\mathrm{LUMO}} - E_{\mathrm{HOMO}})} \tag{7.1}$$

7.2.5 Scope of $[P(OC_6F_5)_5F]^-$ and $[P(OC_6F_5)_6]^-$ as WCAs

The viability of $[P(OC_6F_5)_5F]^-$ and $[P(OC_6F_5)_6]^-$ as new weakly coordinating anions were also assessed. The Molecular Electrostatic Potential Surface (MEPS) of $[P(OC_6F_5)_6]^-$, $[P(OC_6F_5)_5F]^-$, $[Al(OC(CF_3)_3)_4]^-$, $[B(C_6F_5)_4]^-$, $[SbF_6]^-$, and $[BF_4]^-$ were calculated at the BP86-D3/SV(P) level (Figure 7.8). The small classical anions, like $[SbF_6]^-$ and $[BF_4]^-$, show significant charge localization on the fluorine atoms, which highlights their tendency to interact strongly with electrophiles and transfer a fluoride anion. In comparison, the larger and bulkier perfluoroarylborate and perfluoroalkoxyaluminate anions effectively disperse the negative charge and offer fewer sites for electrophile coordination.

The MEPS of $[P(OC_6F_5)_5F]^-$ and $[P(OC_6F_5)_6]^-$ are comparable to that of the heavily fluorinated borate and aluminate anions suggesting that this phosphorus based anion is comparable in its charge dispersal efficiency.

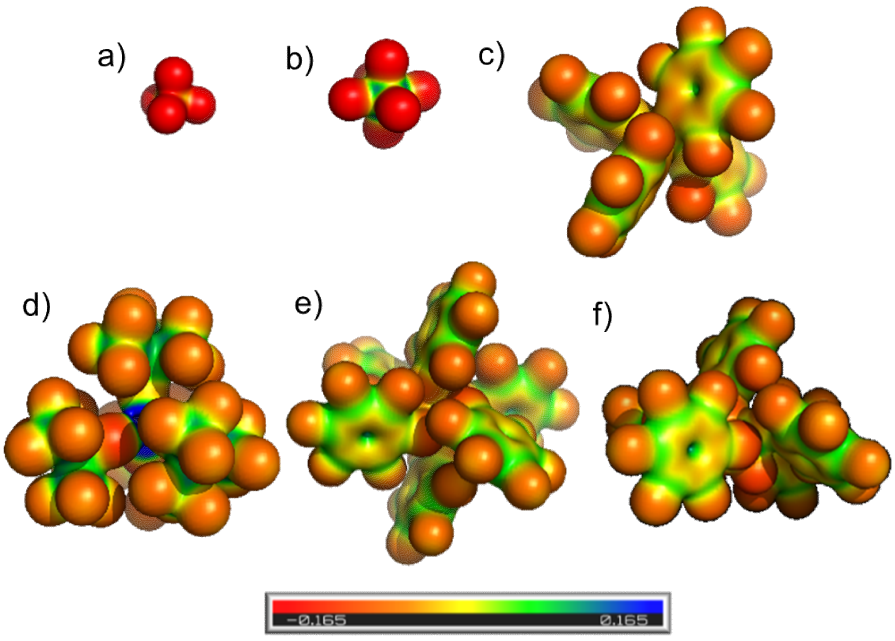

Figure 7.7: Molecular electrostatic potential surface (BP86-D3/SV(P)) at the 0.025 e^- Bohr isodensity surface for a) $[BF_4]^-$, b) $[SbF_6]^-$, c) $[B(C_6F_5)_4]^-$, d) $[Al(OC(CF_3)_3)_4]^-$, e) $[P(OC_6F_5)_6]^-$, and f) $[P(OC_6F_5)_5F]^-$.

These predictions were tested experimentally. The introduction of a strong electrophile, such as the trityl cation or unsolvated lithium cation, resulted in OC_6F_5 group transfer. These experiments provide evidence for lability of the OC_6F_5 groups in the $[P(OC_6F_5)_6]^-$ and $[P(OC_6F_5)_5F]^-$ anions, rendering them unsuitable as WCAs, despite their favourable calculated MEPS. The small atomic radius of phosphorus and the high steric pressure created by five or six aryl groups presumably drive the extrusion of an OC_6F_5 group in the presence of electrophiles.

7.3 Conclusions

To conclude, we reported the synthesis and structural characterization of a neutral P(V) Lewis acid, $P(OC_6F_5)_5$, and related $[P(OC_6F_5)_5F]^-$ and $[P(OC_6F_5)_6]^-$ anions. A rare intramolecular F-π_{arene} interaction was detected in the solid-state structure of $[P(OC_6F_5)_6]^-$. The strength of this interaction in the solution phase was established quantitatively by VT NMR experiments. Fluoride ion abstraction experiments were used to assess the Lewis acid strength of $P(OC_6F_5)_5$, which revealed that $P(OC_6F_5)_5$

is a weaker fluoride acceptor than PF5, despite the favourable gas-phase FIA and GEI calculations. This discrepancy prompted an investigation into solvation effects, which revealed that when solvation is taken into account, the FIA of $P(OC_6F_5)_5$ is indeed smaller than PF5. The impact of FIA dampening upon solvation is size and charge-dependent. Although the $[P(OC_6F_5)_5F]^-$ and $[P(OC_6F_5)_6]^-$ anions effectively delocalize negative charge, they are susceptible to OC_6F_5 group abstraction by cationic electrophiles (e.g. trityl cation or uncoordinated lithium cation). Although not discussed in this report, all attempts at preparing the antimony derivatives $Sb(OC_6F_5)_5$ and $[Sb(OC_6F_5)_6]^-$ have thus far failed. The tri- and tetracoordinate intermediates, $Sb(OC_6F_5)_3$ and $[Sb(OC_6F_5)_4]^-$, were isolated but could not be converted to their penta- and hexa-coordinate derivatives, presumably due to the increased stability of the +3 oxidation state. Guided by these findings, we continue to explore other electronegative substituents for expanding the scope of neutral Group 15 Lewis acid and WCA chemistry.

Chapter 8

Conclusion

To conclude, this work highlighted the use of multidentate ligands to create novel electronic structures at main group centers. Lewis acidity at planar trivalent antimony/bismuth triamides tethered with an N,N,N-triamide ligand (Chapters 2 and 3) was investigated. These compounds were examined in the solid, solution, and gas-phase. Gas-phase calculations were used to assess the Lewis acidity of the planar bismuth Lewis acid, considering both steric and electronic effects. These results complement our findings of a new class of antimony hydrides that participate in the first example of additive-free hydrostibanation of C≡C, C=C, C=O, and N=N bonds (Chapter 4). These hydrometallation reactions were unlocked by frontier orbital engineering through the careful choice of a bis(silylamino)naphthalene ligand. Hydrostibination of phenylacetylene was shown to proceed via a radical mechanism. Studies on the use of catalytic amounts of stibanyl hydrides for the syntheses of z-olefins are currently underway. These results further the non-intuitive concept of a diagonal relationship between the lightest Group 13 and the heaviest Group 15 elements.

The reactivity of Sb–H bonds was found to be surprisingly diverse. This led to the one-step, high yield synthesis of thermally-robust bismuthanylstibanes, which provided the first examples of neutral Bi–Sb σ-bonds in the solid-state (Chapter 5). The reaction chemistry of the Bi–Sb bond was debuted by showing the insertion of a sulfur atom, providing the first documented example of a Bi–S–Sb bonding moiety.

DFT calculations indicated that the bis(silylamino)naphthalene scaffold is particularly efficient in increasing interaction energies through a combination of inductive effects and dispersion donor effects, foreshadowing the use of this ligand in the isolation of other labile bonding motifs, such as bismuth carbamates. Selective insertion of one molecule of CO_2 into a bismuth-nitrogen bond yielded the corresponding bismuth carbamates under mild conditions (Chapter 6). The importance of ligand choice and bulk in obtaining selective insertion was highlighted. These findings now motivate our pursuit of catalytic functionalization strategies to valorize this greenhouse gas usisng rationally designed bismuth amides.

Neutral Group 15 Lewis acid and WCA chemistry was also explored using a combination of experimental and computational methods (Chapter 7), which demonstrated the importance of solvent effects in predicting the Lewis acid strength of bulky, neutral species. The targeted properties were not accessed and so this project has been temporarily abandoned.

Appendix A

Supporting Information for Chapter 2

*Procedure for determining thermodynamic parameters for **2.1-Sb**, **2.1-Sb$_{dim}$**, and **2.1-Sb$_{dim'}$**:*

Compound **2.1-Sb** was found to crystallize as **2.1-Sb$_{dim}$**. This dimerization was investigated using variable temperature NMR. It was found that the dimerization process involved the formation of an intermediate species **2.1-Sb$_{dim'}$** (Figure 2.6 in manuscript). First, raw integral values for the three species from Figure 2.6 were obtained. Integration of a residual DCM signal at 4.27 ppm and subsequent integrations were made of a peak for **2.1-Sb** (0.284 ppm, RT to 193 K), for **3dim'** (0.452 ppm, RT to 193 K), and **2.1-Sb$_{dim}$** (0.414 ppm, 253 K to 193 K). The integration value for **2.1-Sb** was divided by two to reflect the symmetry of the species from Figure 2.6. These raw data integrals (Table A.1) were turned into mol fraction (χ) data (Table A.2) for each species. The mol fraction data was then used to calculate the equilibrium constants (K_1 and K_2) (Table A.3) at the given temperatures following equations (A.1) and (A.2).

$$K_1 = \frac{\chi_{\text{ 2.1-Sbdim'}}}{\chi_{2.1-Sb}{}^2} \tag{A.1}$$

$$K_2 = \frac{\chi_{\text{ 2.1-Sbdim}}}{\chi_{\text{ 2.1-Sbdim'}}} \tag{A.2}$$

Temperature (K)	**2.1-Sb**	**2.1-Sb$_{dim'}$**	**2.1-Sb$_{dim}$**
193	19.1789	4.9943	40.0834
203	27.01365	6.0375	34.2246
213	37.0426	9.129	26.6784
223	43.5643	15.5529	16.1791
233	44.43125	22.5523	7.8907
243	55.5955	21.8196	5.7346
253	63.5968	17.6842	3.4268
263	72.6891	12.1046	0
273	79.2468	7.6881	0
283	80.44825	4.7408	0
293	91.0552	2.9314	0

Table A.1: Raw integral values for **2.1-Sb**, **2.1-Sb$_{dim'}$**, and **2.1-Sb$_{dim}$**. The values for **2.1-Sb** shown have already been divided by two.

Temperature (K)	χ **2.1-Sb**	χ **2.1-Sbdim'**	χ **2.1-Sbdim**
193	0.28899641	0.10700864	0.60399495
203	0.40079094	0.09143208	0.50777698
213	0.51692879	0.11077464	0.37229657
223	0.59331861	0.18633214	0.22034926
233	0.57238583	0.32109517	0.106519
243	0.66861937	0.26241345	0.06896718
253	0.75077856	0.20876708	0.04045436
263	0.85724647	0.14275353	0
273	0.91156486	0.08843514	0
283	0.94434966	0.05565034	0
293	0.96881045	0.03118955	0

Table A.2: Mol fraction data for **2.1-Sb**, **2.1-Sb$_{dim'}$**, and **2.1-Sb$_{dim}$** calculated from the raw integral data.

Temperature	K_1	K_2
203	-	5.66867081
213	-	2.92237923
223	-	1.04026259
243	-	0.26281875
253	0.37037212	-
263	0.19425645	-
273	0.10642648	-
283	0.06240253	-
293	0.03323009	-

Table A.3: Equillibrium constants at select temperatures.

The van't Hoff plot for each equilibrium was constructed using ln[K] versus 1/T data and are shown in Figure 2.8. ΔH and ΔS data were calculated using the gas constant R = 8.314 J mol^{-1} K^{-1} multiplied by the slope or y-intercept, respectively. ΔG_{298K} and ΔG_{193K} were calculated using the ΔH and ΔS values. Error propagation was employed following the equations below.

$$\sigma_{\Delta\ \mathrm{H}} = \frac{8.314 Jmol^{-1} K^{-1} * \sigma_{\mathrm{slope}}}{1000 * 4184 kJkcal^{-1}} \tag{A.3}$$

$$\sigma_{\Delta\ \mathrm{H}} = \frac{8.314 Jmol^{-1} K^{-1} * \sigma_{\mathrm{y\text{-}int}}}{1000 * 4184 kJkcal^{-1}} \tag{A.4}$$

$$\sigma_{\Delta\ \mathrm{G}} = \sqrt{(\sigma_{\Delta\ \mathrm{H}})^2 + (\sigma_{\Delta\ \mathrm{S}} * T)^2} \tag{A.5}$$

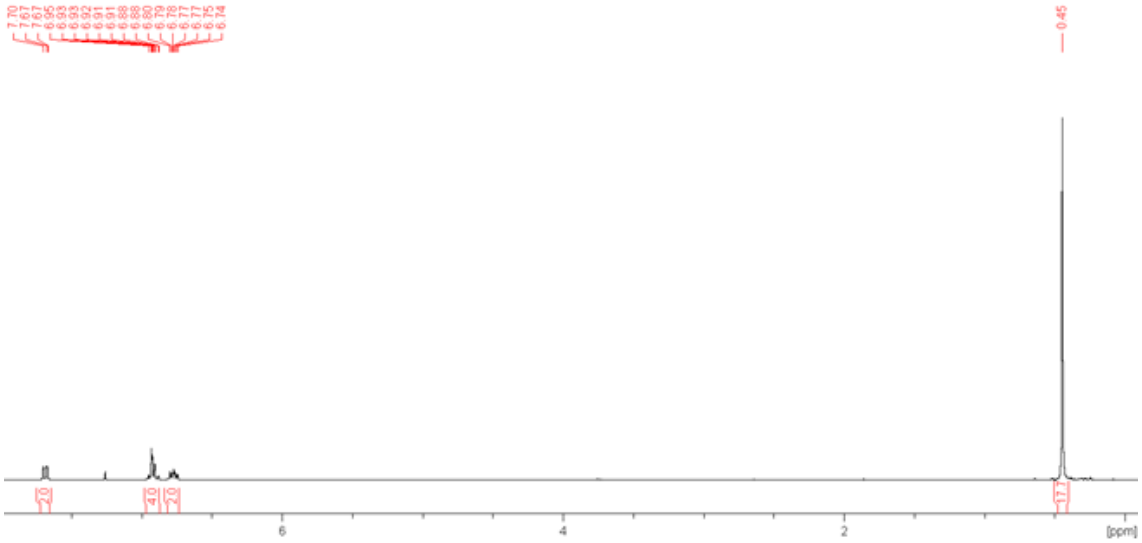

Figure A.1: ^{1}H NMR spectrum of **2.1-Sb** in $CDCl_3$.

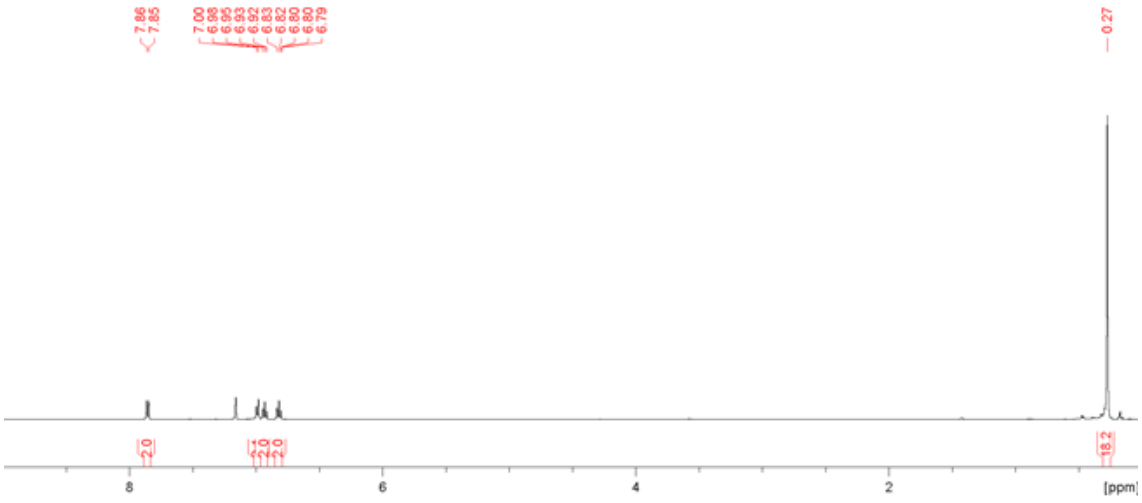

Figure A.2: ^{1}H NMR spectrum of **2.1-Sb** in C_6D_6.

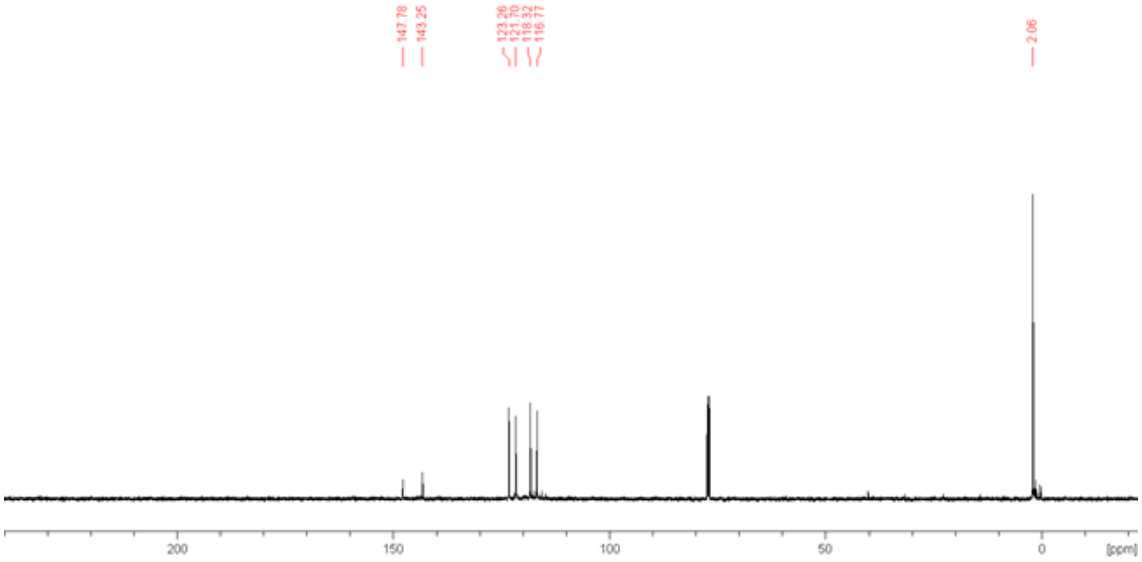

Figure A.3: $^{13}C\{^{1}H\}$ spectrum of **2.1-Sb** in C_6D_6.

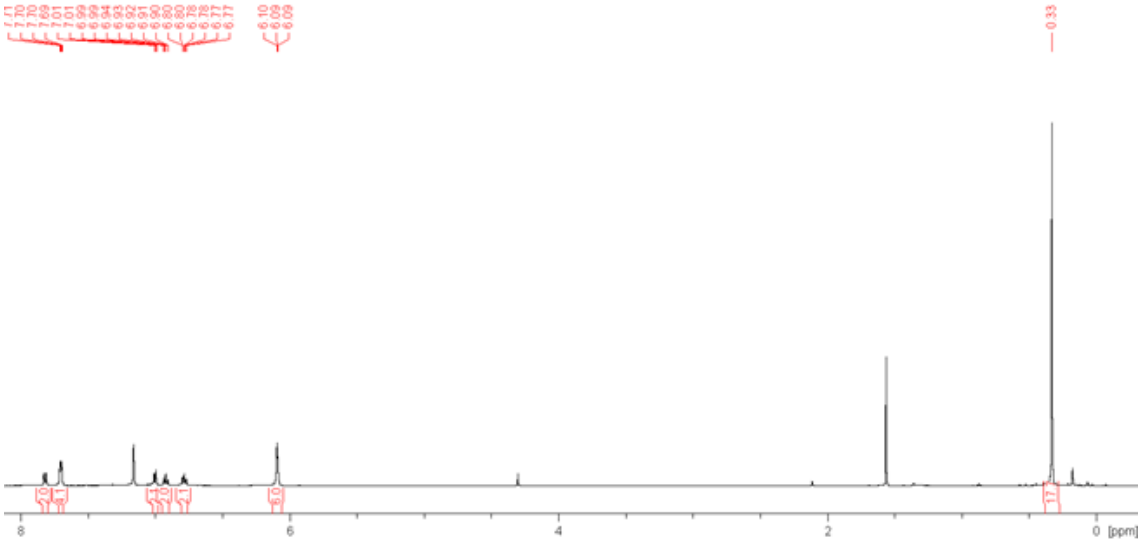

Figure A.4: ^{1}H NMR spectrum of **2.1-Sb-(pyo)$_2$** in C_6D_6. Signals at 1.56 ppm (acetone) and 4.30 ppm (DCM) are from residual solvent in the glovebox atmosphere.

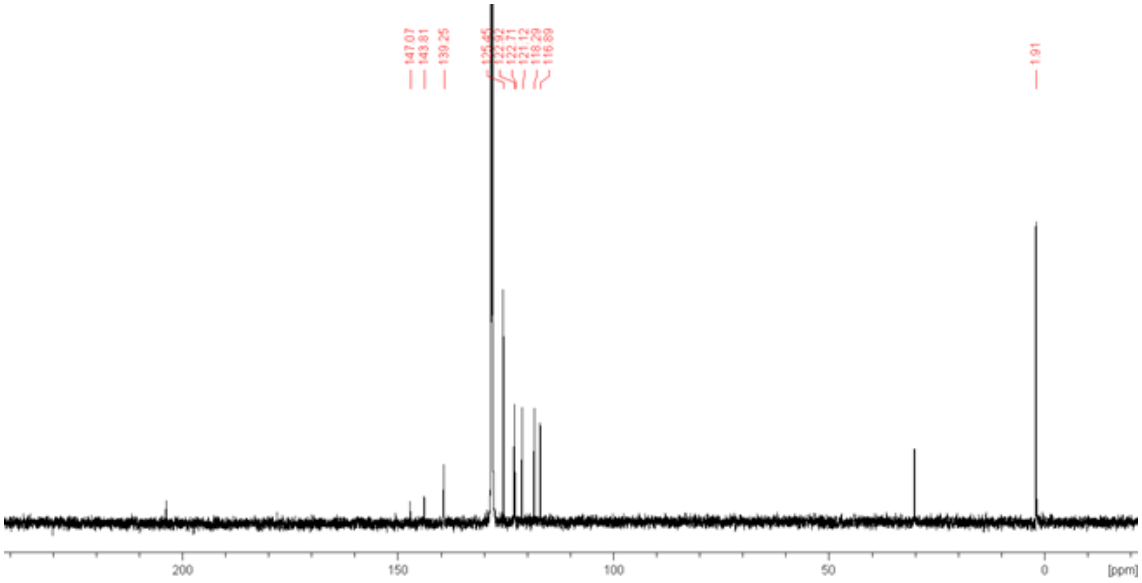

Figure A.5: $^{13}C\{^{1}H\}$ spectrum of **2.1-Sb-(pyo)$_2$** in C_6D_6. The two unpicked signals are from residual solvent (acetone) in the glovebox atmosphere.

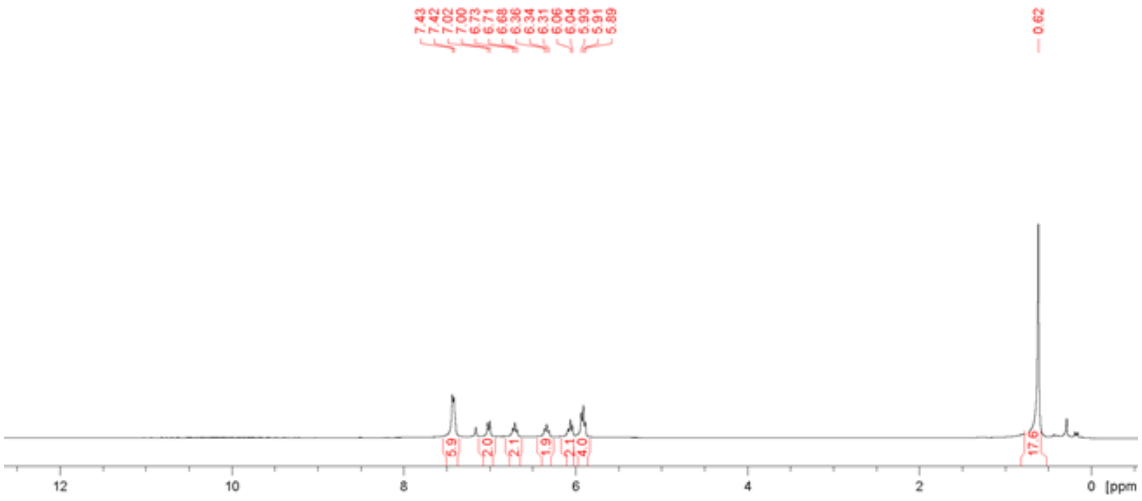

Figure A.6: ^{1}H NMR spectrum of **2.1-Bi-(pyo)$_2$** in C_6D_6.

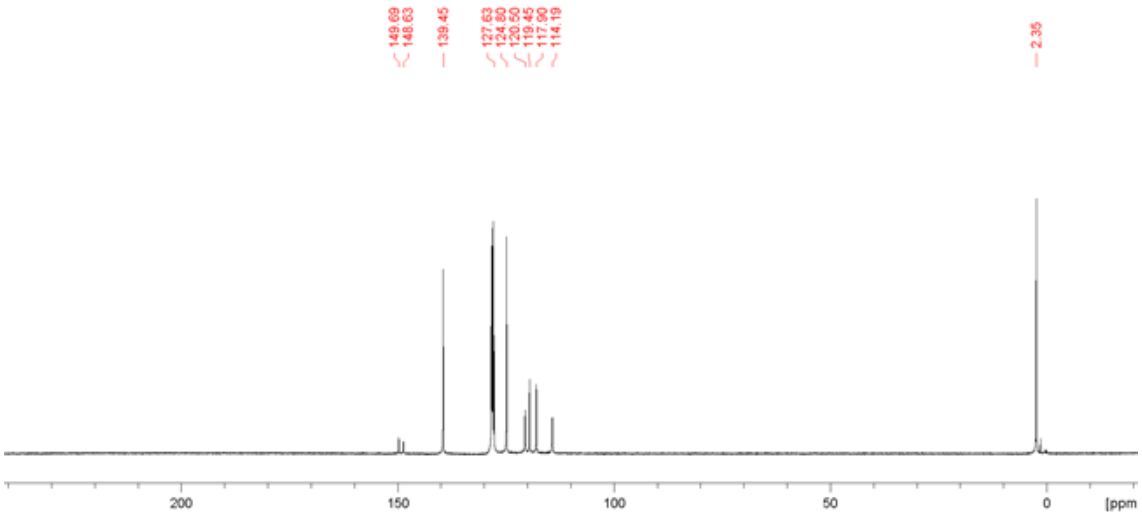

Figure A.7: $^{13}C\{^{1}H\}$ spectrum of **2.1-Bi-(pyo)$_2$** in C_6D_6.

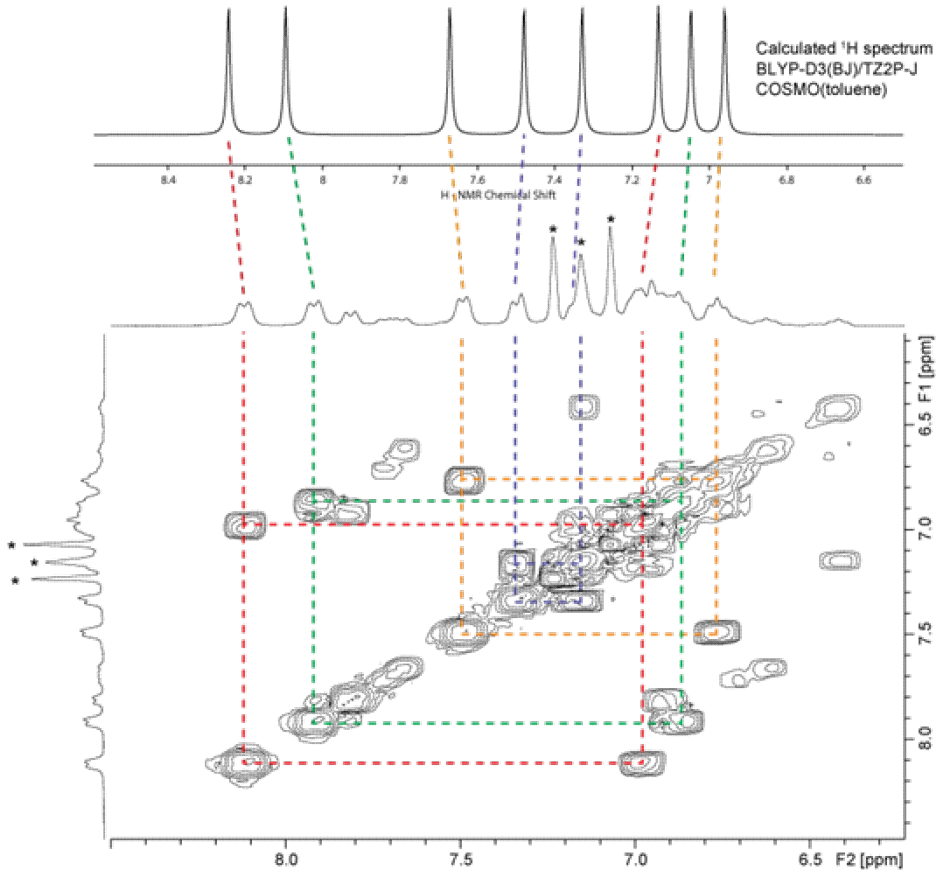

Figure A.8: Comparison of the calculated (top) and experimental (bottom) ^{1}H NMR spectra for **2.1-Sb$_{dim}$**. The bottom spectrum also shows the COSY cross-peaks between the peaks assigned to **2$_{dim}$**.

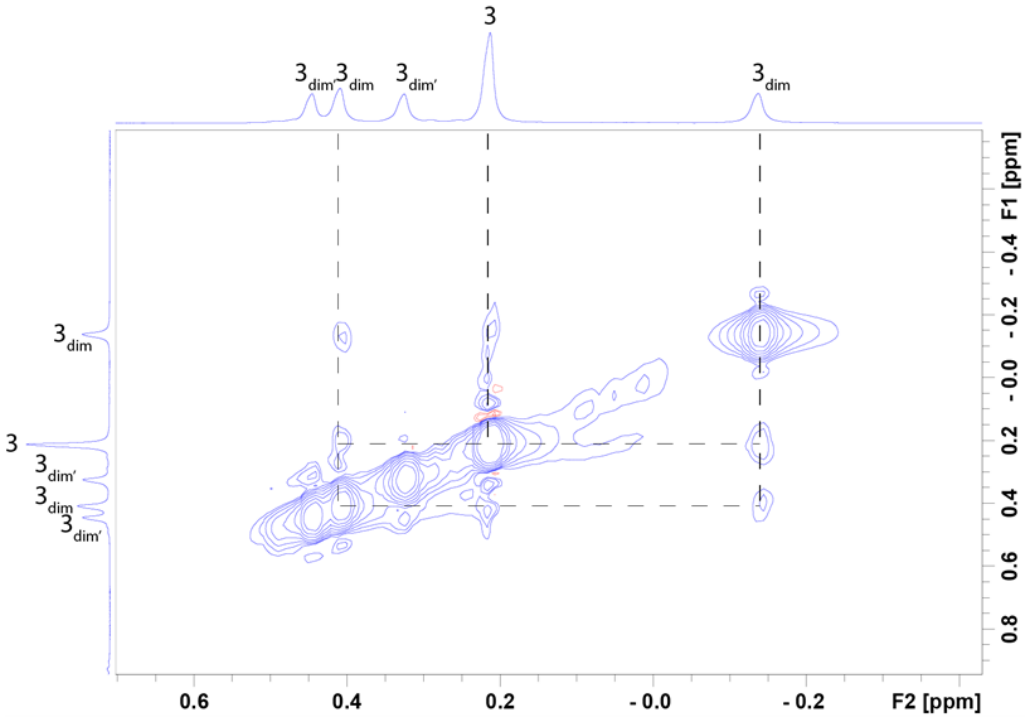

Figure A.9: EXSY crosspeaks observed between the TMS protons of **2.1-Sb** and **2.1-Sb$_{dim}$**. As **2.1-Sb$_{dim}$'**, is an intermediate, it exchanges too rapidly with both **2.1-Sb** and **2.1-Sb$_{dim}$** and therefore EXSY crosspeaks are not seen with the same acquisition parameters needed to see the peaks between **2.1-Sb** and **2.1-Sb$_{dim}$**.

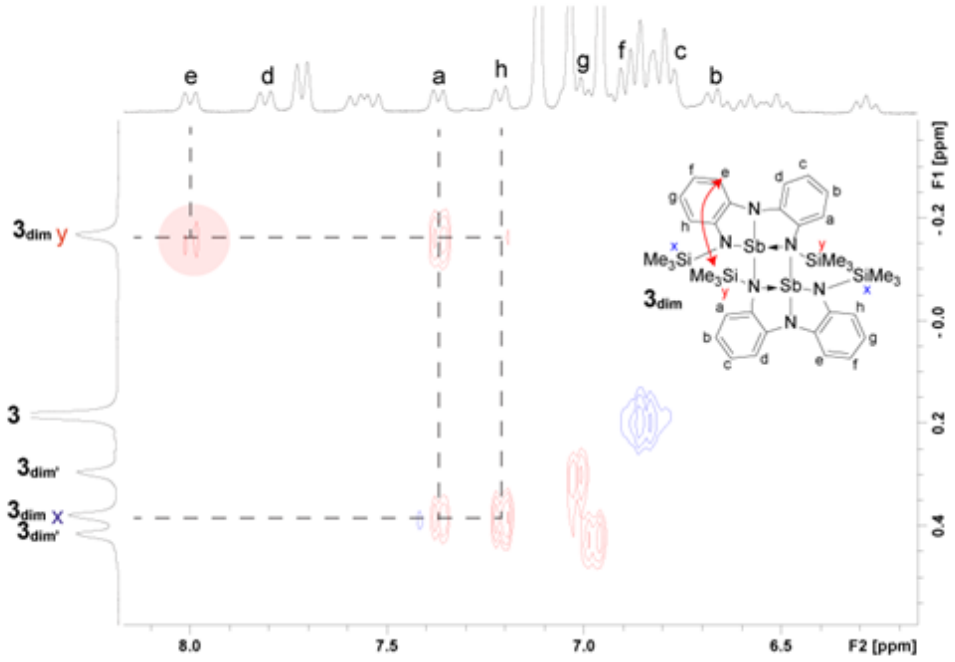

Figure A.10: NOESY experiment showing the spatial proximity of one of the TMS group protons (labelled y on the vertical spectrum) in **2.1-Sb$_{dim}$**, to the one of the protons ortho to the central N (labelled **e** on the horizontal spectrum).

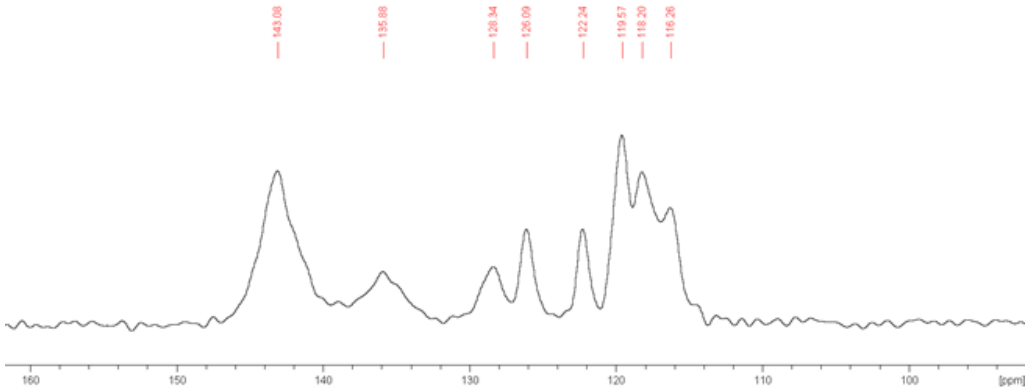

Figure A.11: ^{13}C CP-MAS ssNMR spectrum of **2.1-Sb** at 6.5 kHz spinning frequency.

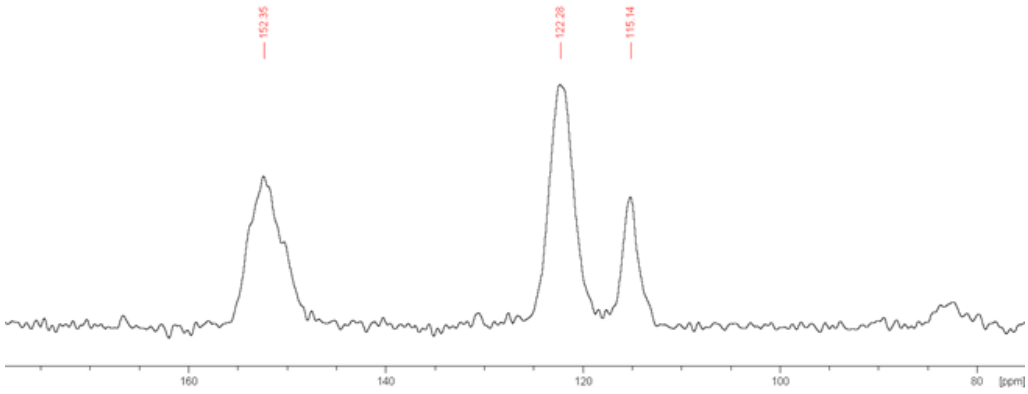

Figure A.12: ^{13}C CP-MAS ssNMR spectrum of **2.1-Bi** at 6.5 kHz spinning frequency.

Geometry optimizations and frequency calculations for compounds **2.1-P**, **2.1-As**, **2.1-Sb**, and **2.1-Bi** (bent and planar geometries) were carried out at the PBE0-D3/def2-tzvpd level in Gaussian 16. NBO calculations were performed on structures optimized at the PBE0-D3/def2-tzvpd level for monomers and PBE0-D3/def2-tzvp level for dimers.

EDA calculations were performed using geometries optimized at the PBE0-D3/def2-tzvp//SCRF(Toluene) level in Gaussian 16. These geometries were exported to the Amsterdam Density Functional (ADF) suite where energy calculations were done at the PBE1-D3/TZ2P//COSMO(Toluene) level with scalar relativistic correction. No significant difference was observed between small-core and large-core calculations and therefore, all calculations were performed using the large-core approximation for time efficiency.

UV-VIS calculations were performed using geometries optimized at the PBE0-D3/def2-tzvp//SCRF(Toluene) level in Gaussian 16. These geometries were exported to the Amsterdam Density Functional (ADF) suite where energy calculations were done using TD-DFT at the BLYP-D3(BJ)/TZ2P//COSMO(Toluene) level with scalar relativistic correction and large-core approximation. Davidson method was used and with 10 singlet-triplet excitations were calculated.

NMR calculations were performed using geometries optimized at the PBE0-D3/def2-tzvp//SCRF(Toluene) level in Gaussian 16. These geometries were exported to the Amsterdam Density Functional (ADF) suite where energy calculations were done using TD-DFT at the BLYP-D3(BJ)/TZ2P-J //COSMO(Toluene) level with scalar relativistic correction and large-core approximation.

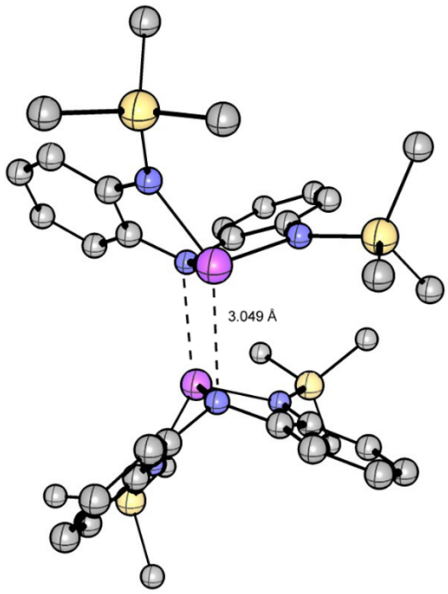

Figure A.13: Optimized structure of the **2.1-Sb$_{\mathbf{dim}}$**, at the PBE0/def2-TZVP level.

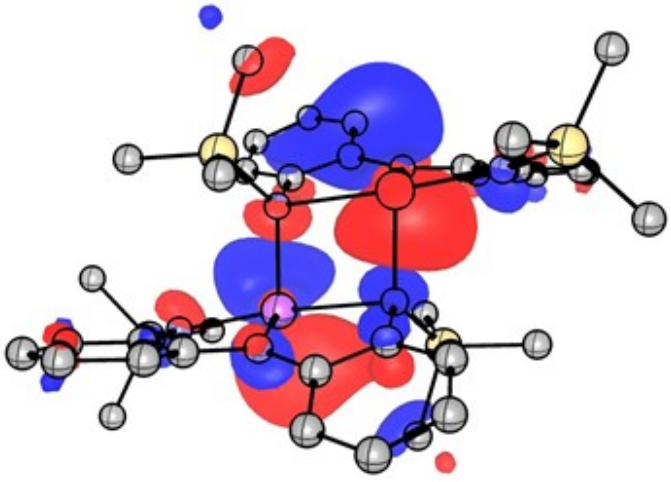

Figure A.14: Calculated LUMO of **2.1-Sb$_{\mathbf{dim}}$**, which is antibonding with respect to the Sb-N bonds between the two units.

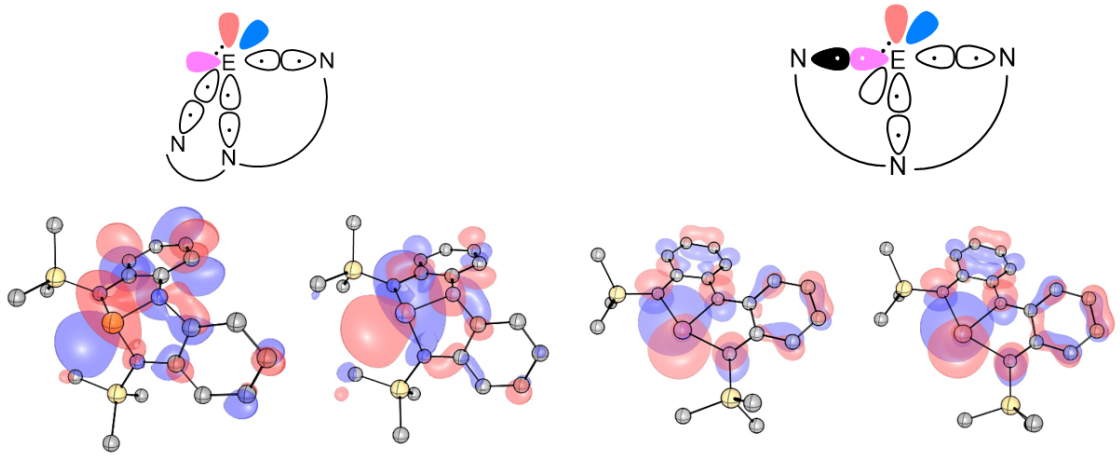

Figure A.15: Top: Bonding schemes for bent and planar geometries. Bottom: LUMOs of **2.1-P**, **2.1-As**, **2.1-Sb**, and **2.1-Bi** (left to right, respectively) in their minimum geometries.

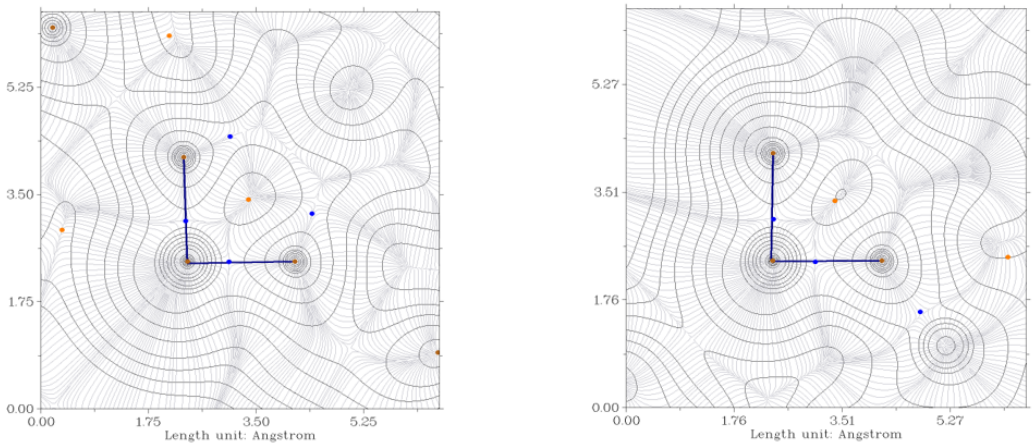

Figure A.16: Electron density gradient plots of the two PN_2C_2 heterocycles in **2.1-P**. The dark blue line denotes the N–P–N interaction. Blue circles represent bond critical points and orange circles denote ring critical points.

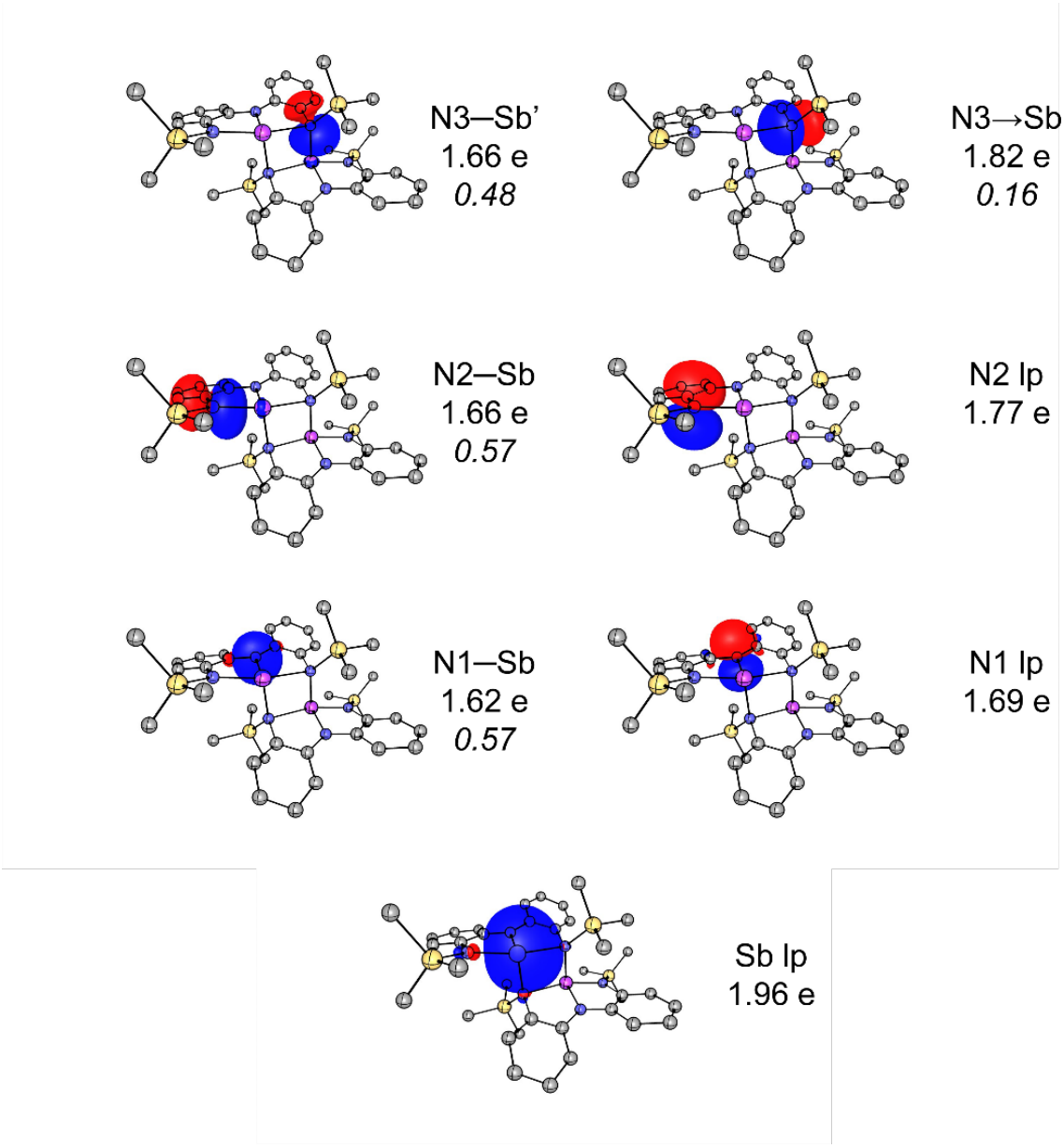

Figure A.17: Key NBOs involving the antimony and nitrogen atoms in **2.1-Sb$_{\mathbf{dim}}$**. Values in italics denote Wiberg Bond Indices. Note that the WBI for the N3-Sb' interaction is greater than the WBI for the dative N3-Sb interaction.

Appendix B

Supporting Information for Chapter 4

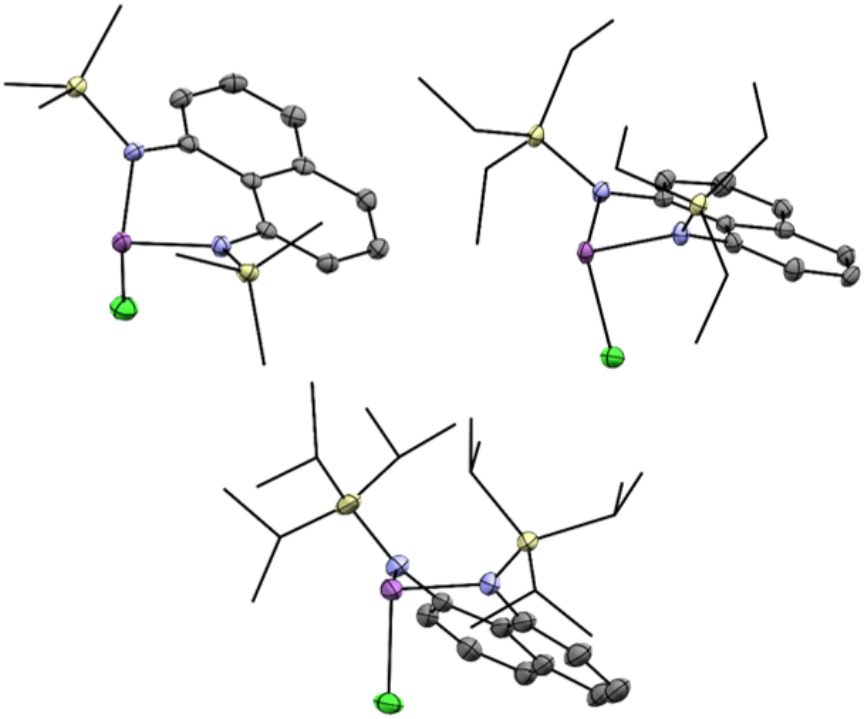

Figure B.1: Molecular structures of **4.2a-c** in the solid state as determined by crystallography. Ellipsoids are drawn at the 50% probability level. Carbon atoms on silyl groups are shown in wireframe for clarity and hydrogen atoms are omitted.

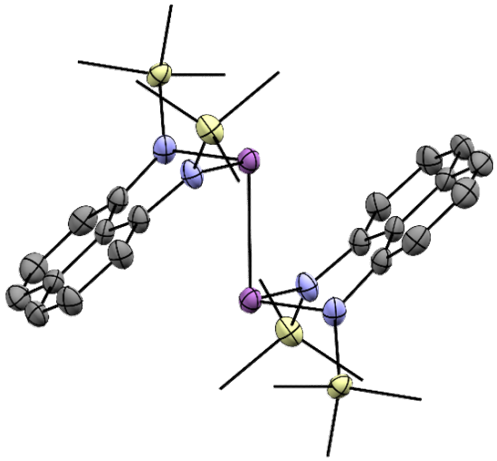

Figure B.2: Molecular structure of **4.4** in the solid state as determined by crystallography. Ellipsoids are drawn at the 50% probability level. Carbon atoms on silyl groups are shown in wireframe for clarity and hydrogen atoms are omitted.

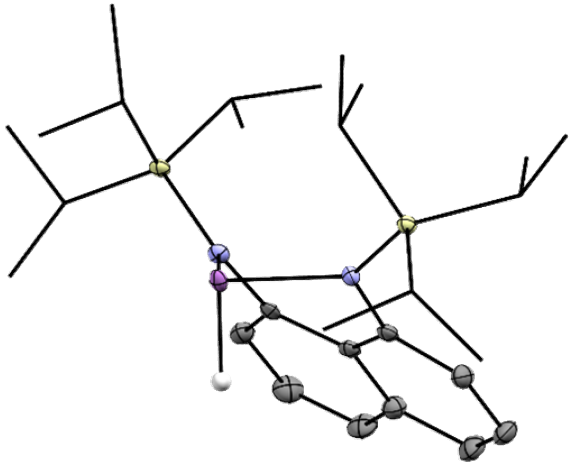

Figure B.3: Molecular structure of **4.3c** in the solid state as determined by crystallography. Ellipsoids are drawn at the 50% probability level. Carbon atoms on silyl groups are shown in wireframe for clarity and hydrogen atoms are omitted.

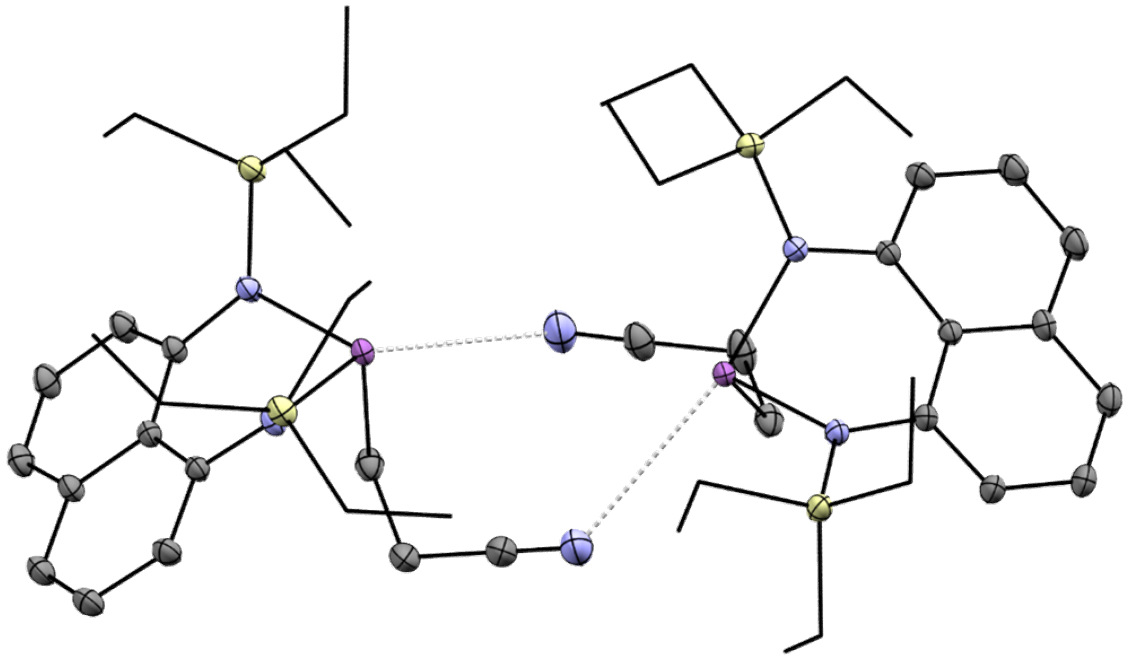

Figure B.4: The dimeric molecular structure of **4.7** in the solid state as determined by crystallography. Ellipsoids are drawn at the 50% probability level. Carbon atoms on silyl groups are shown in wireframe for clarity and hydrogen atoms are omitted.

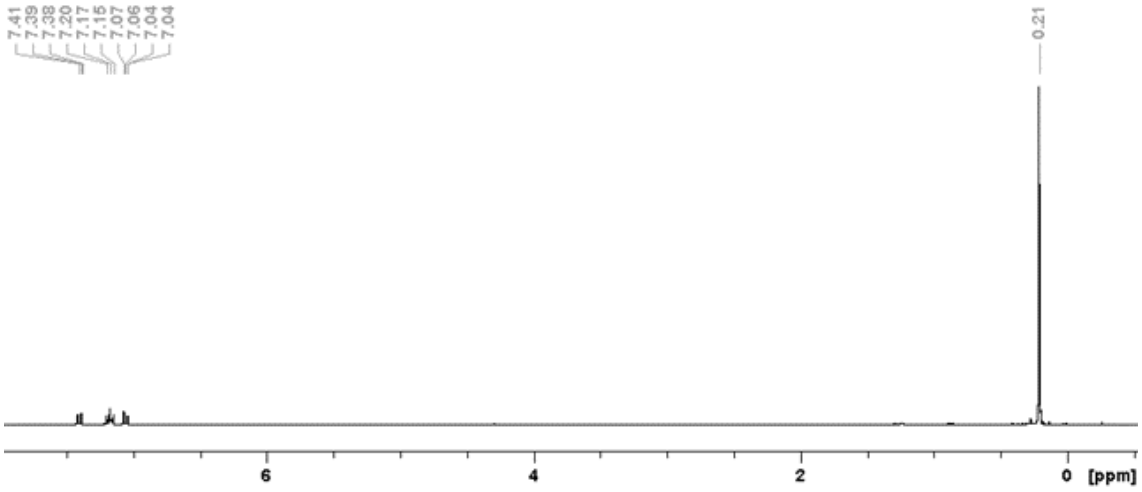

Figure B.5: ^{1}H NMR spectrum of **4.2a**.

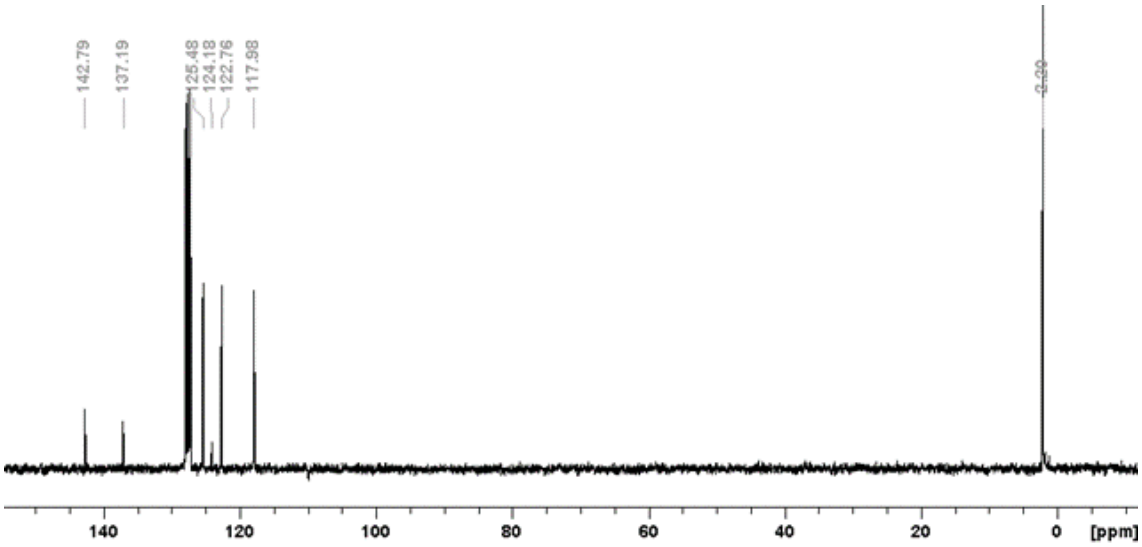

Figure B.6: ^{13}C NMR spectrum of **4.2a**.

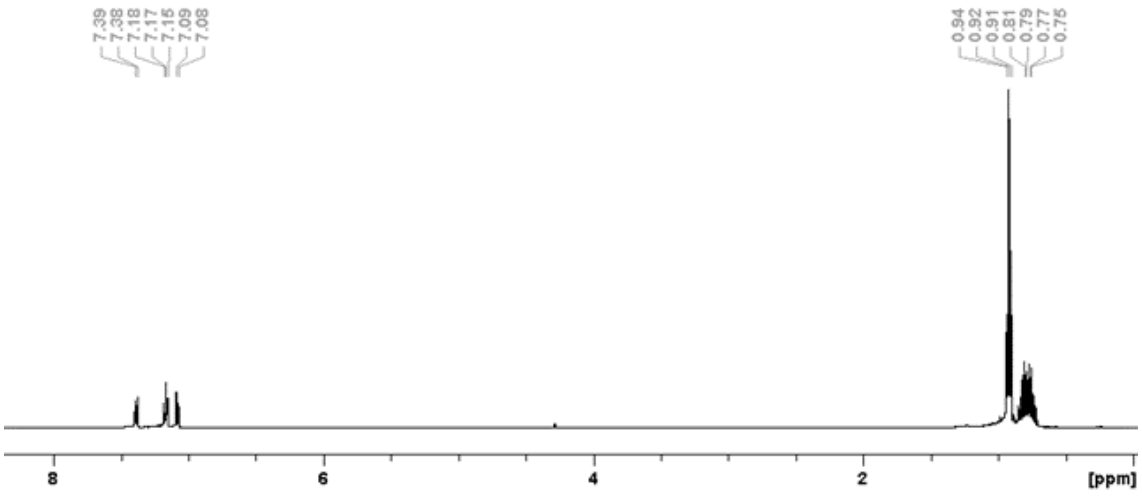

Figure B.7: ^{1}H NMR spectrum of **4.2b**.

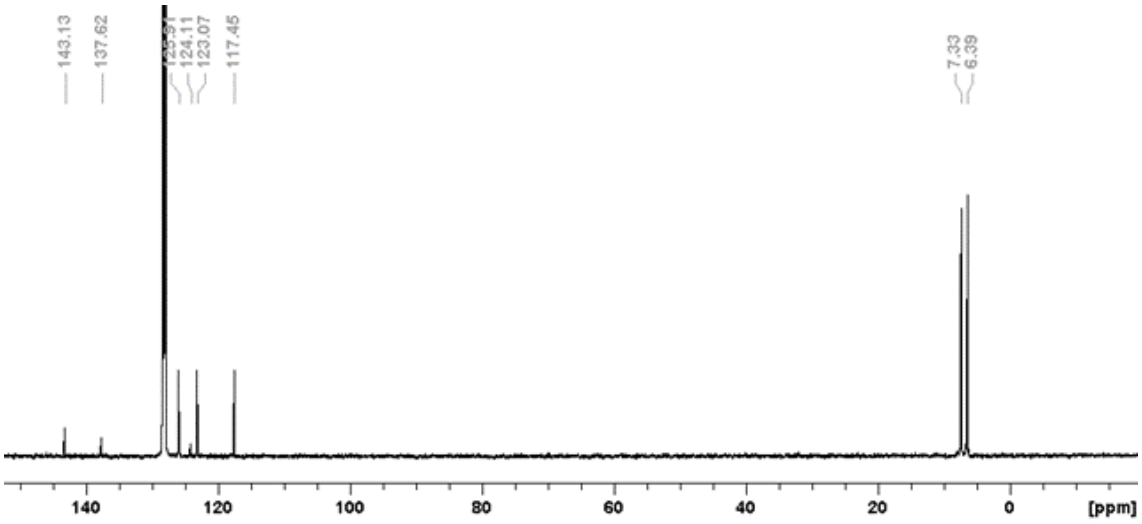

Figure B.8: ^{13}C NMR spectrum of **4.2b**.

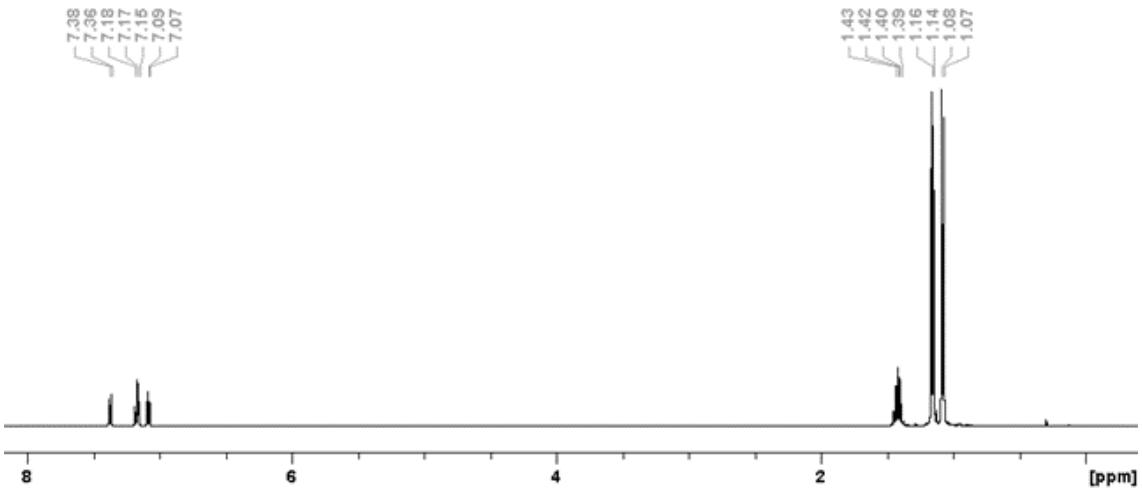

Figure B.9: ^{1}H NMR spectrum of **4.2c**.

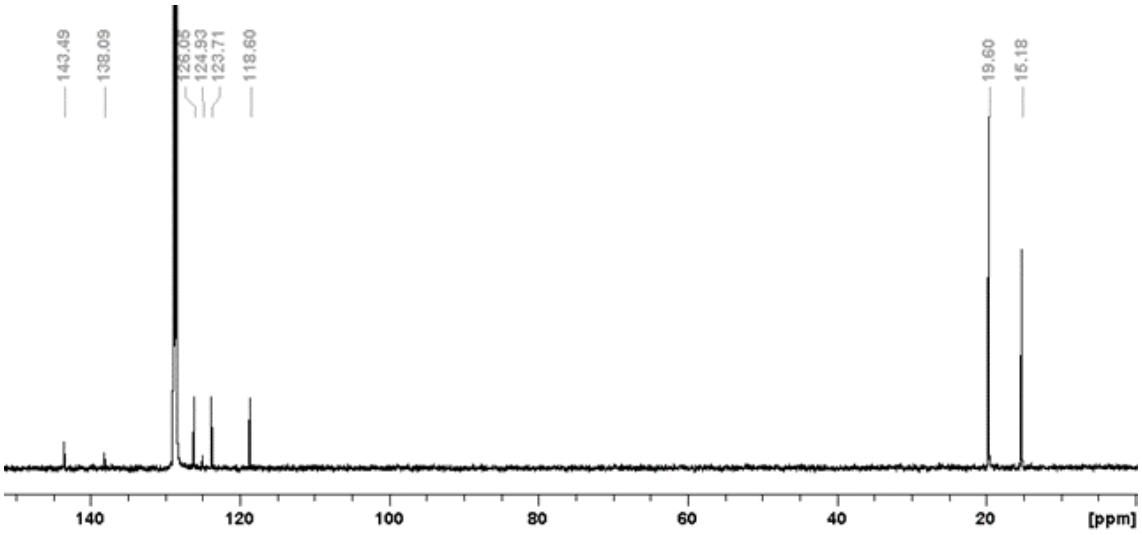

Figure B.10: ^{13}C NMR spectrum of **4.2c**.

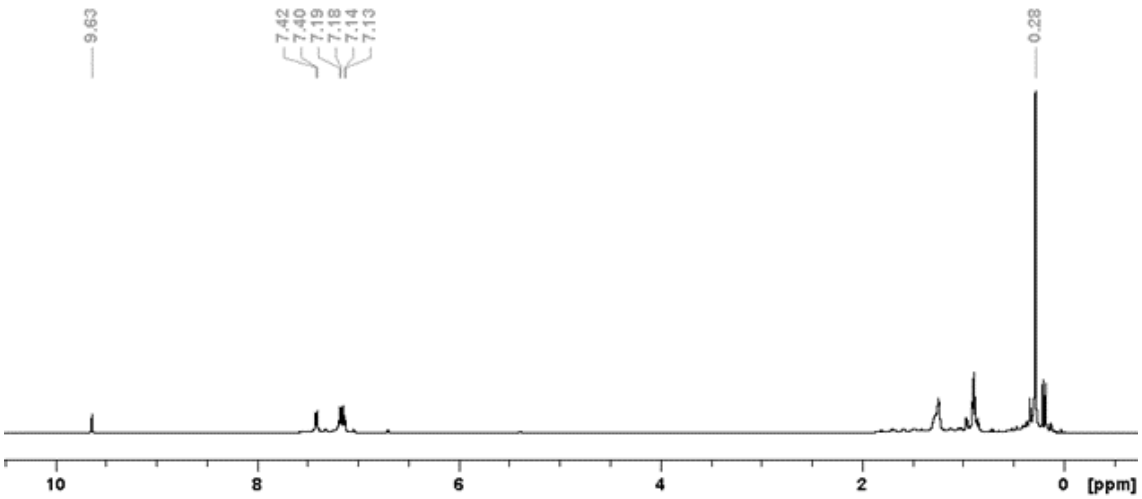

Figure B.11: ^{1}H NMR spectrum of **4.3a**. *This compound was not isolated due to thermal instability and has only been characterized spectroscopically in freshly prepared solutions.*

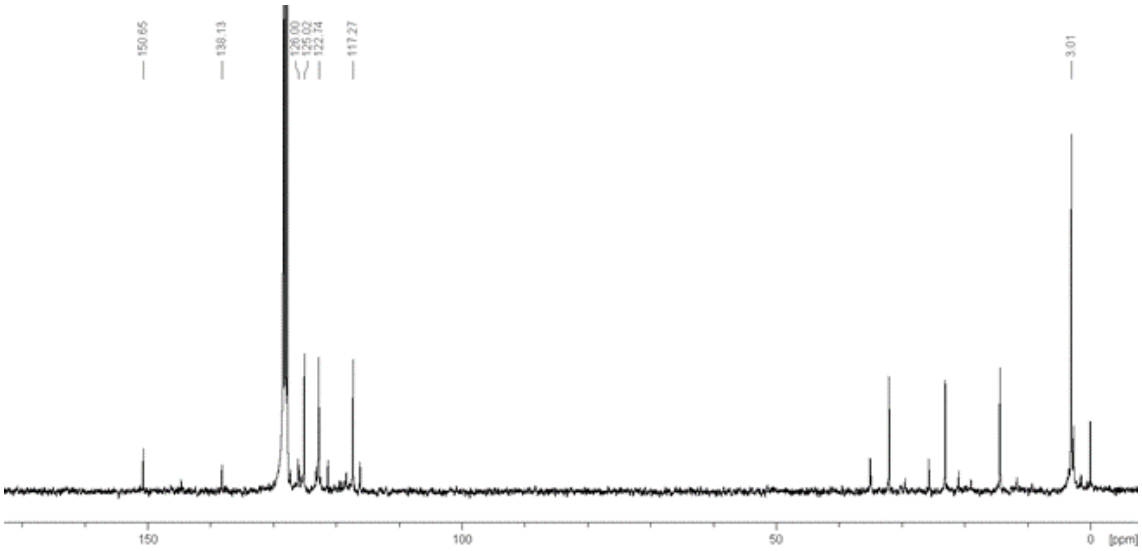

Figure B.12: ^{13}C NMR spectrum of **4.3a**. *This compound was not isolated due to thermal instability and has only been characterized spectroscopically in freshly prepared solutions.*

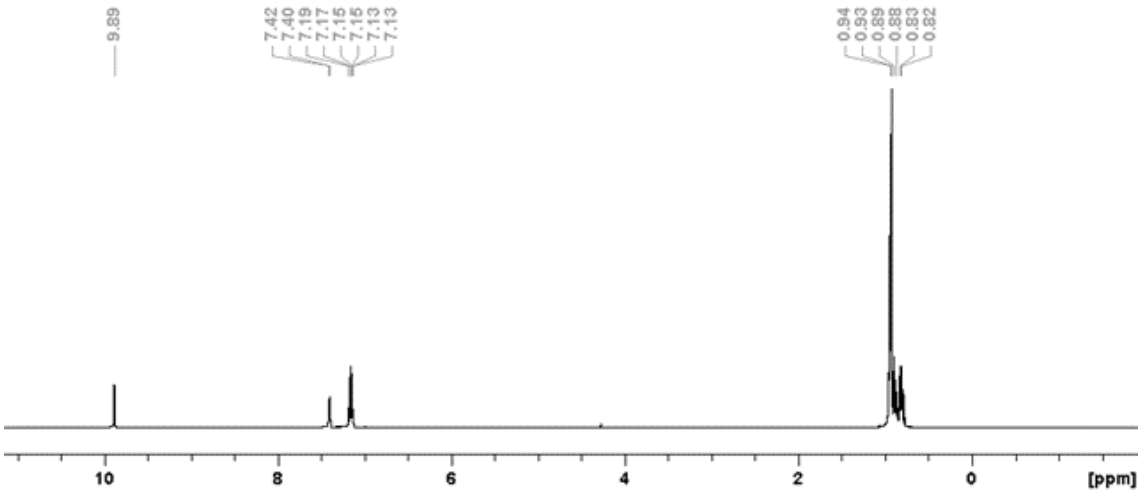

Figure B.13: ^{1}H NMR spectrum of **4.3b**.

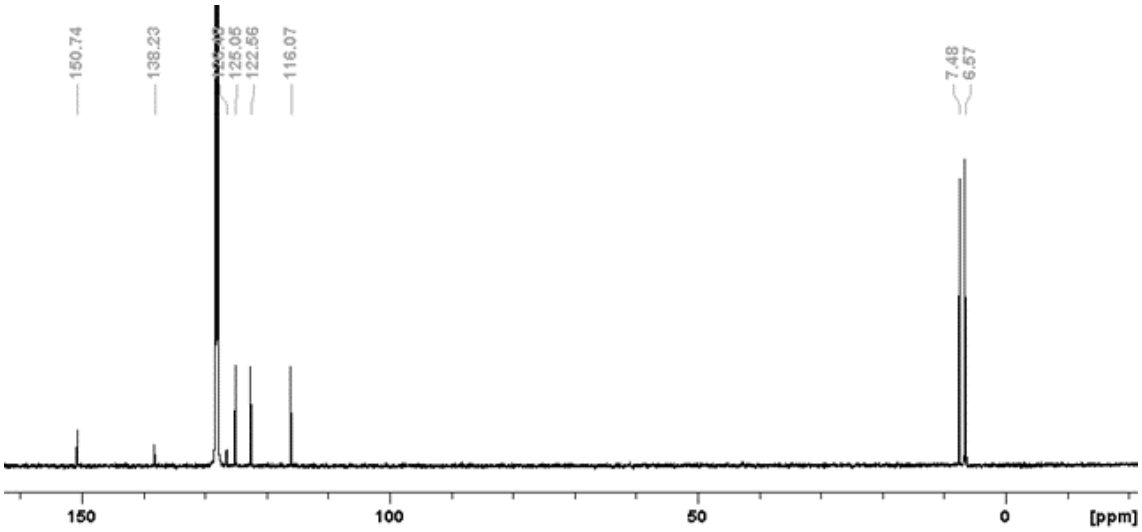

Figure B.14: ^{13}C NMR spectrum of **4.3b**.

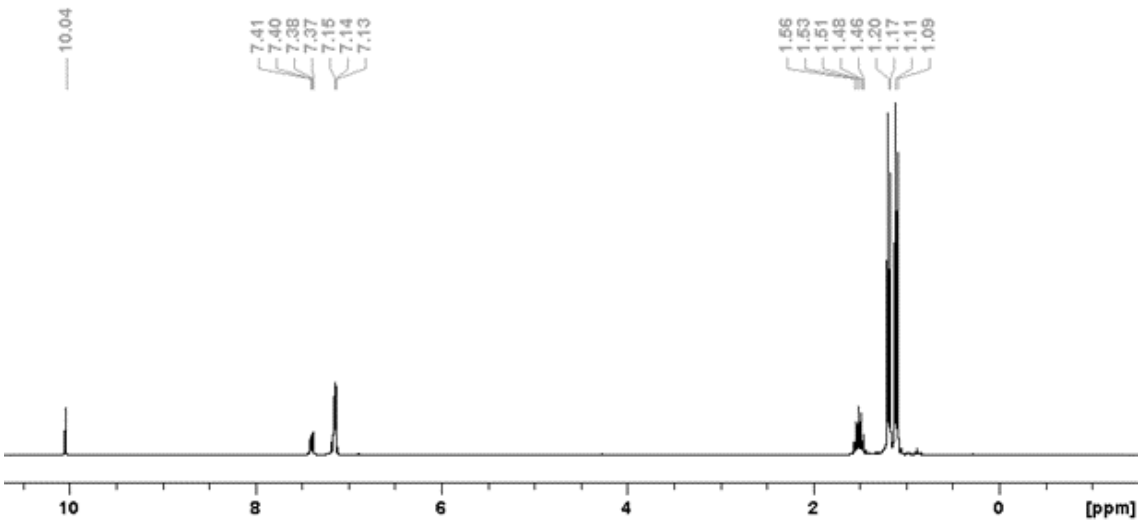

Figure B.15: ^{1}H NMR spectrum of **4.3c**.

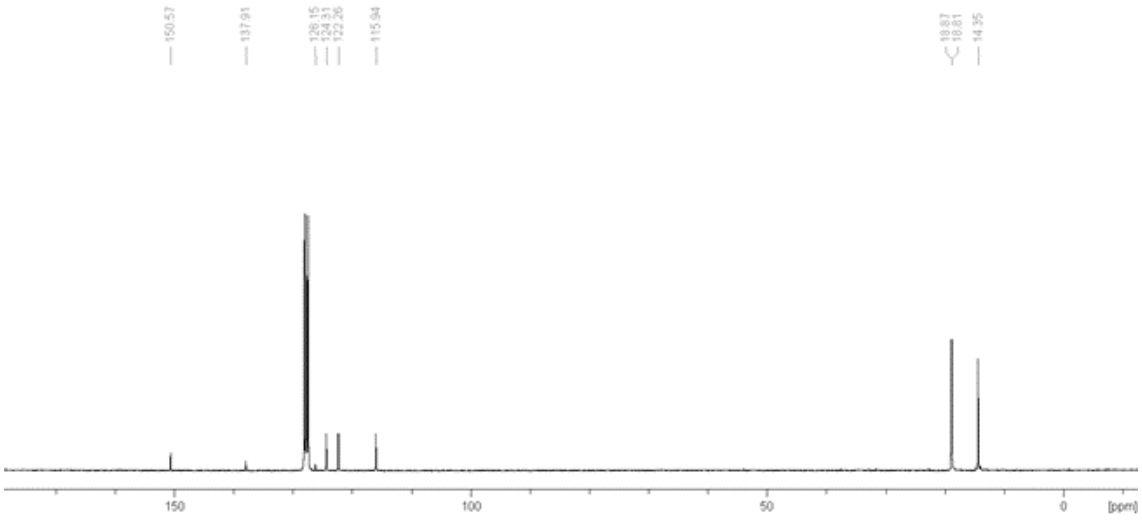

Figure B.16: $^{13}C\{^{1}H\}$ spectrum of **4.3c**.

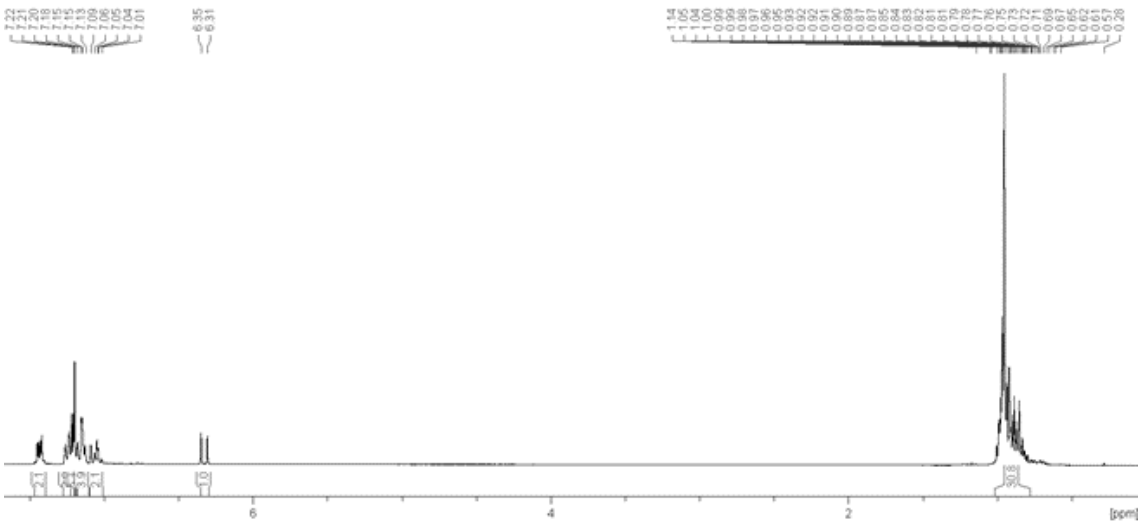

Figure B.17: ^{1}H NMR spectrum of **4.5**.

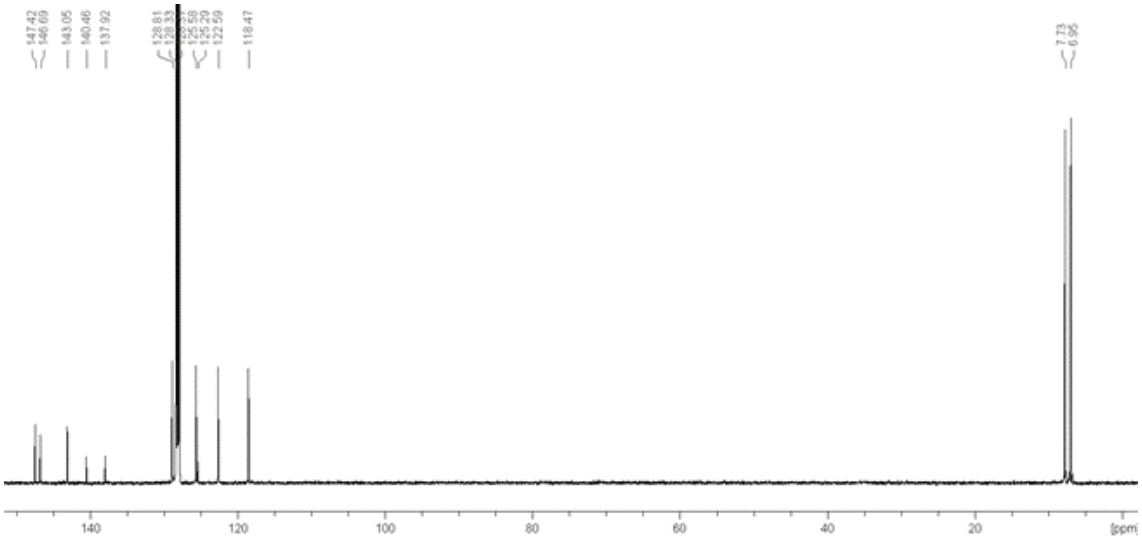

Figure B.18: $^{13}C\{^{1}H\}$ spectrum of **4.5**.

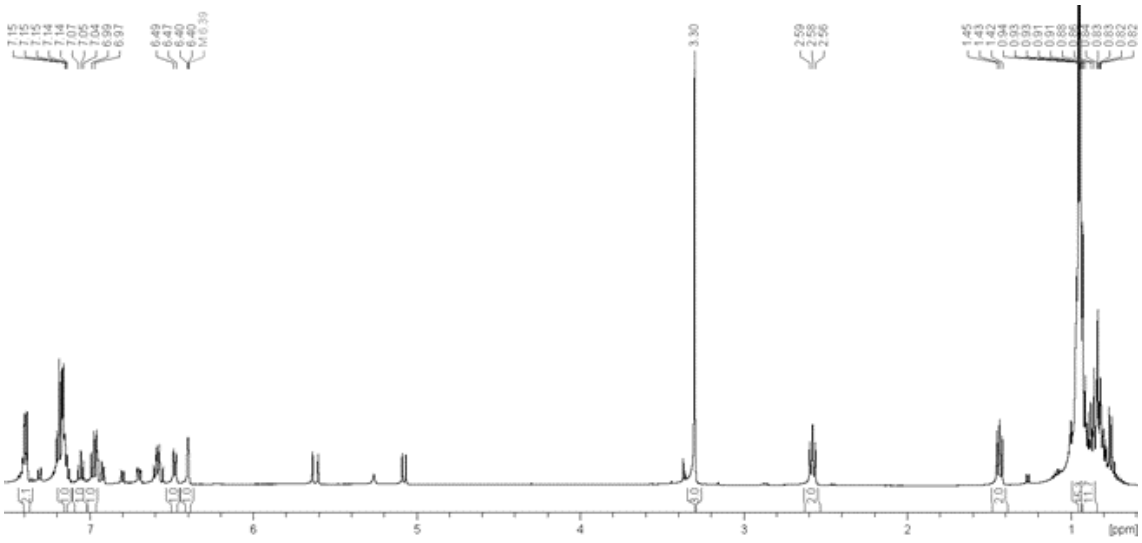

Figure B.19: ^{1}H NMR spectrum of the reaction mixture containing **4.6** after 140 h at ambient temperature. Unpicked peaks are due to **4.3b**, 3-vinylanisole, and **4.2b** (from thermal decomposition of **4.3b**).

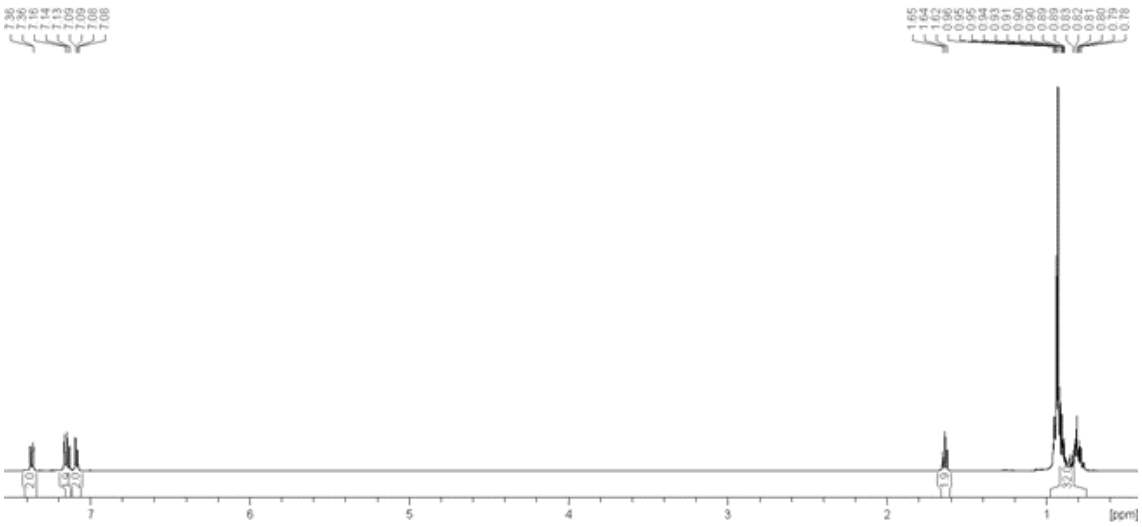

Figure B.20: ^{1}H NMR spectrum of **4.7**.

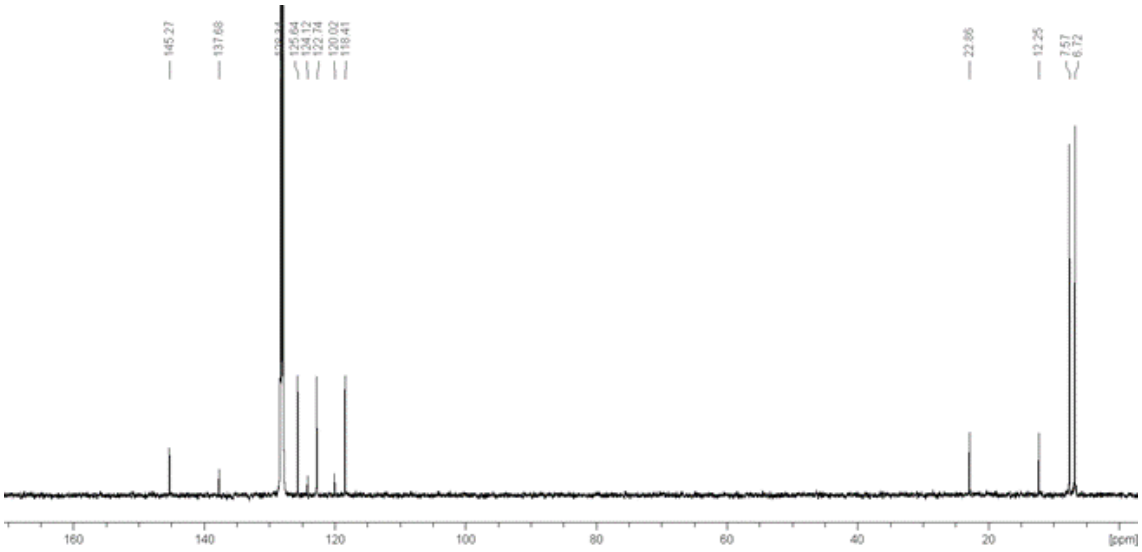

Figure B.21: ^{13}C{^{1}H} spectrum of **4.7**.

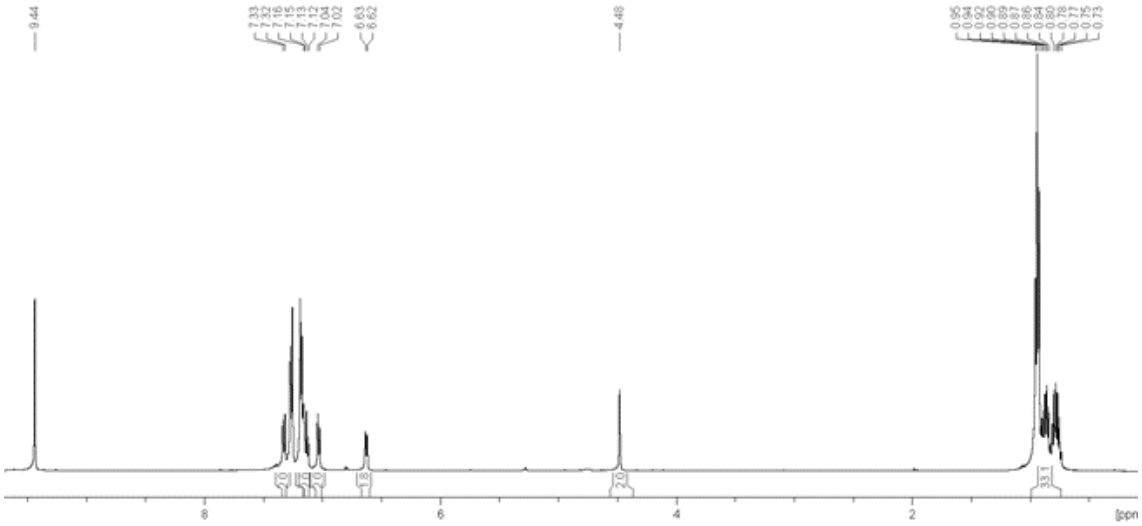

Figure B.22: ^{1}H NMR spectrum of the reaction mixture containing **4.8** and excess p-trifluoromethyl benzaldehyde (used as co-solvent). All unintegrated peaks are due to the excess benzaldehyde.

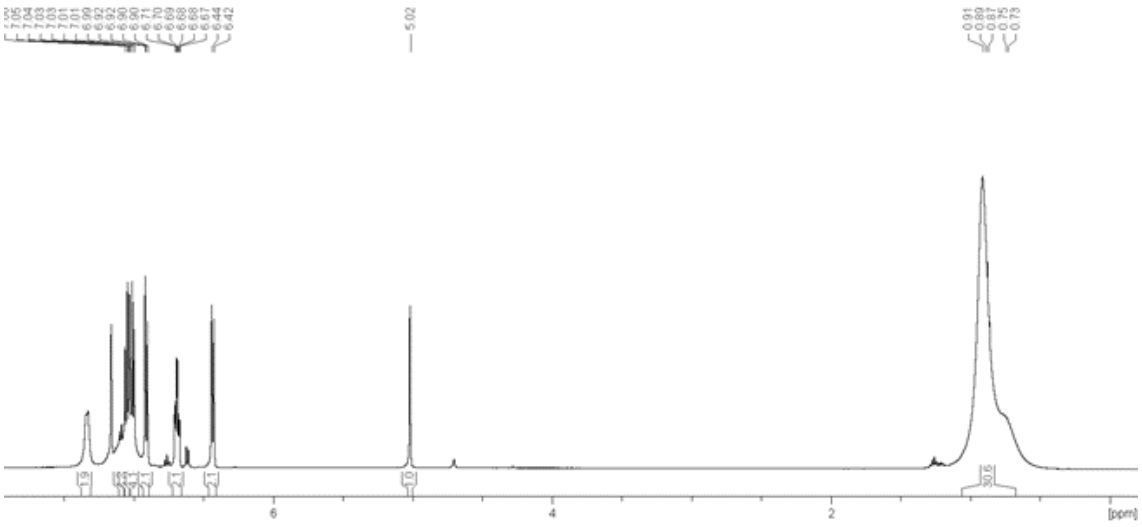

Figure B.23: ^{1}H NMR spectrum of **4.9**.

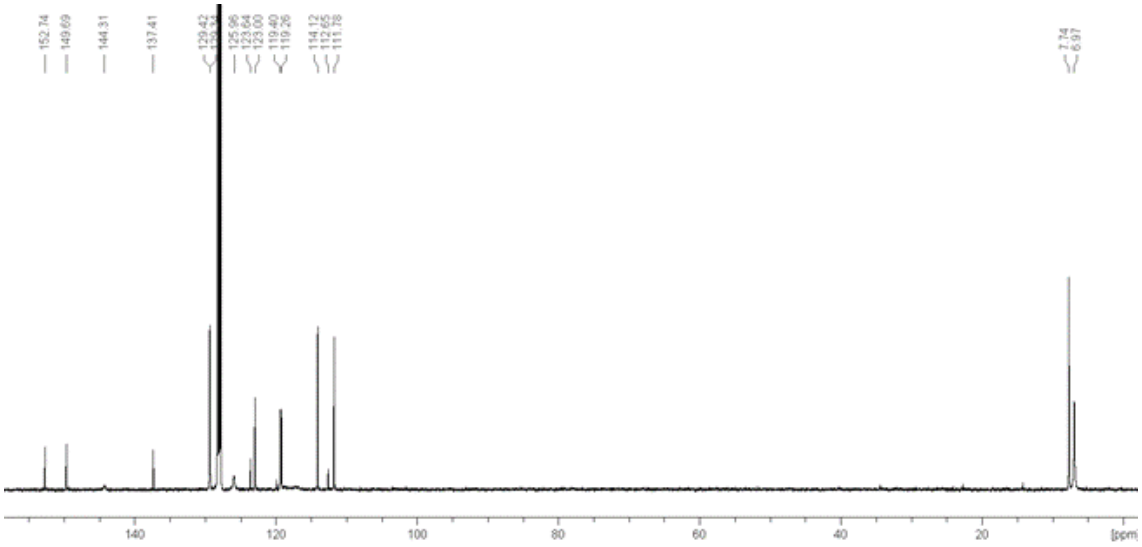

Figure B.24: $^{13}C\{^{1}H\}$ spectrum of **4.9**.

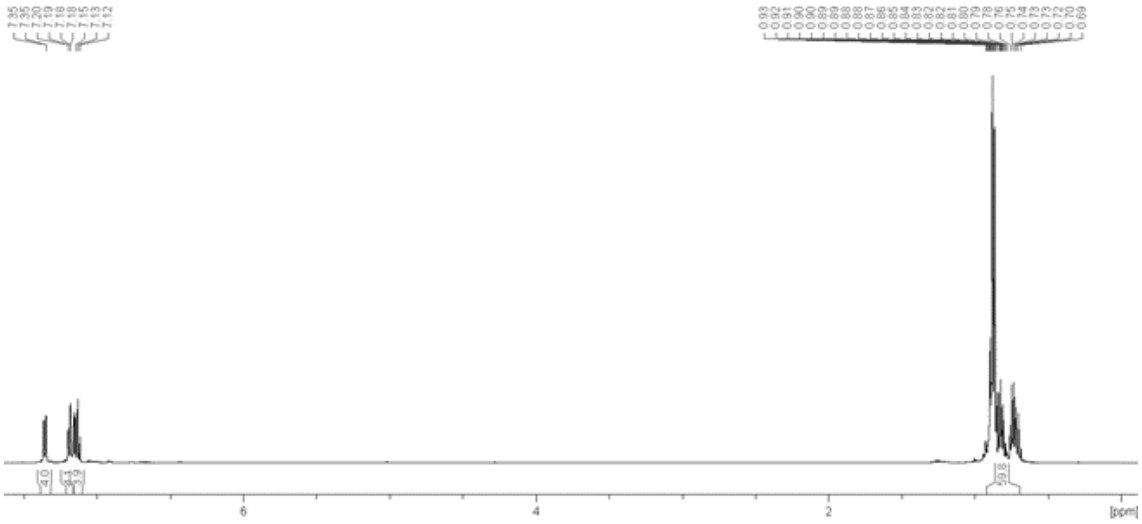

Figure B.25: ^{1}H NMR spectrum of **4.10**.

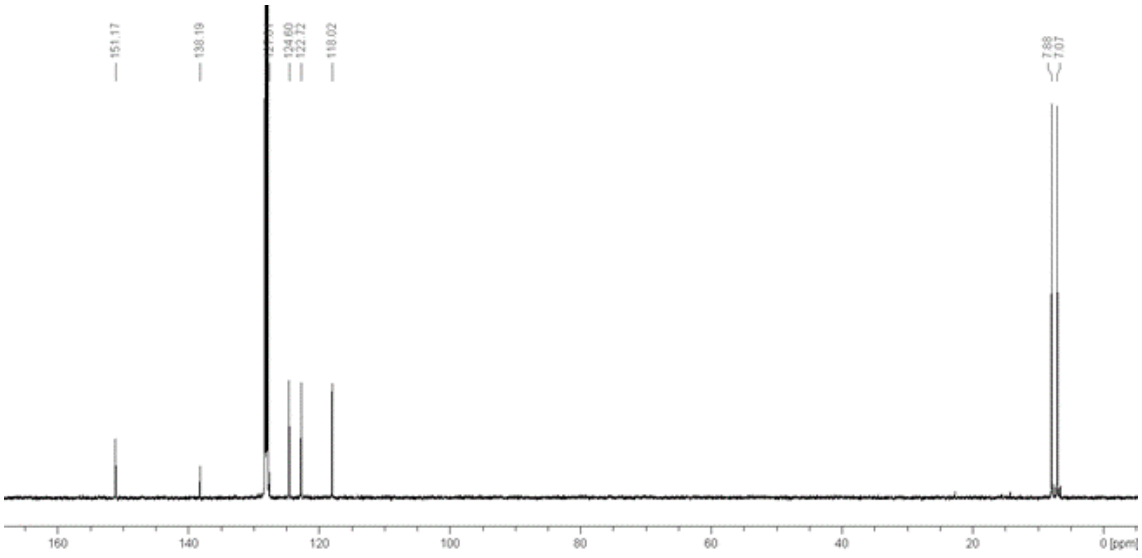

Figure B.26: $^{13}C\{^{1}H\}$ spectrum of **4.10**.

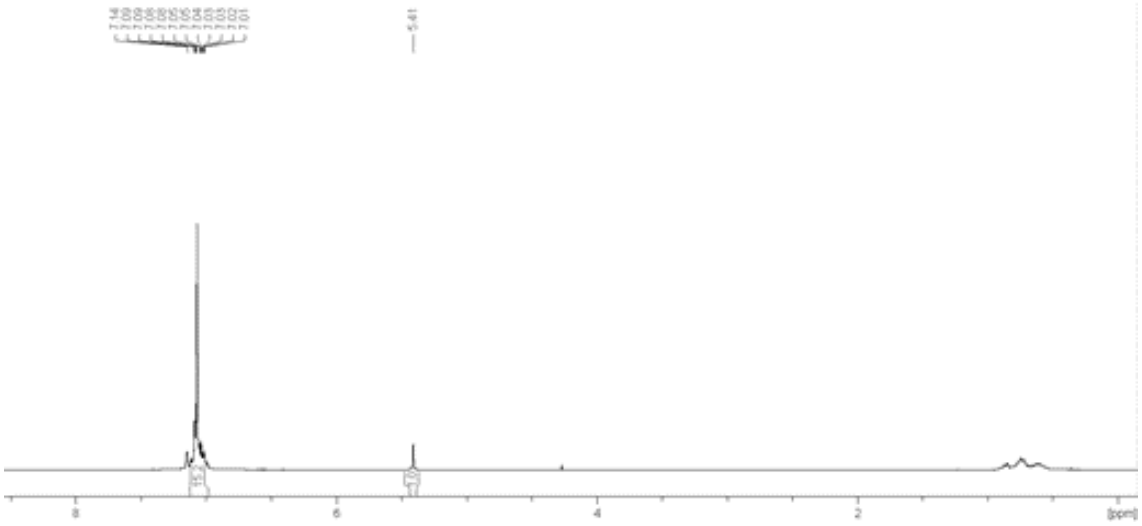

Figure B.27: ^{1}H NMR spectrum obtained upon combining $Ph_3CB(C_6F_5)_4$ with **4.3b** in C_6D_6. The picked peaks match with the literature spectrum of Ph_3CH. This reaction also produces an insoluble black material presumably from decomposition of the generated two-coordinate bent stibenium.

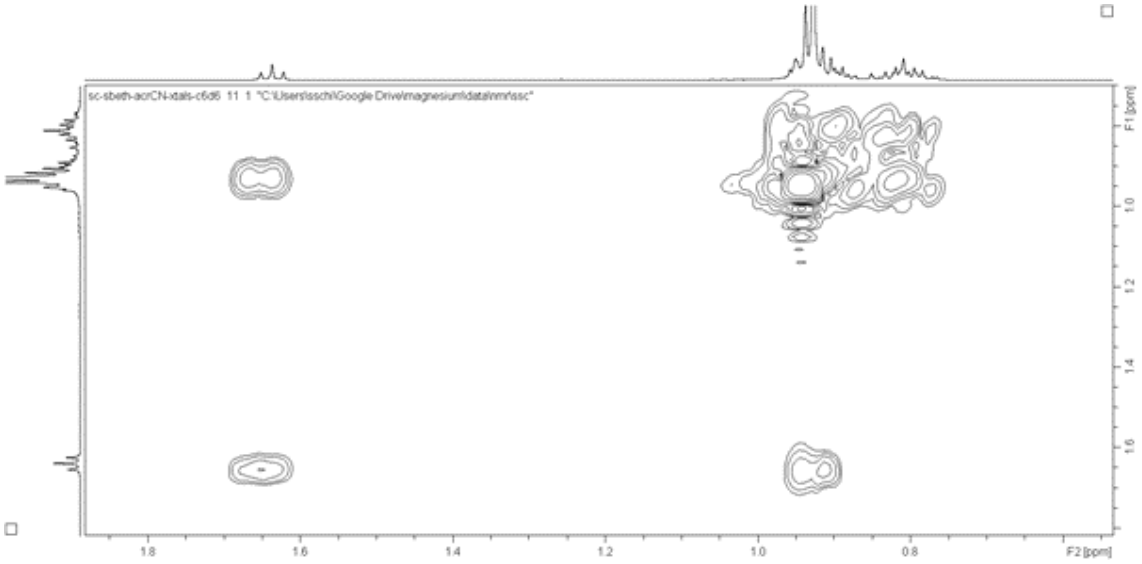

Figure B.28: Portion of the ^{1}H-COSY spectrum of **4.7** showing a methylene region under the Et_3Si resonances.

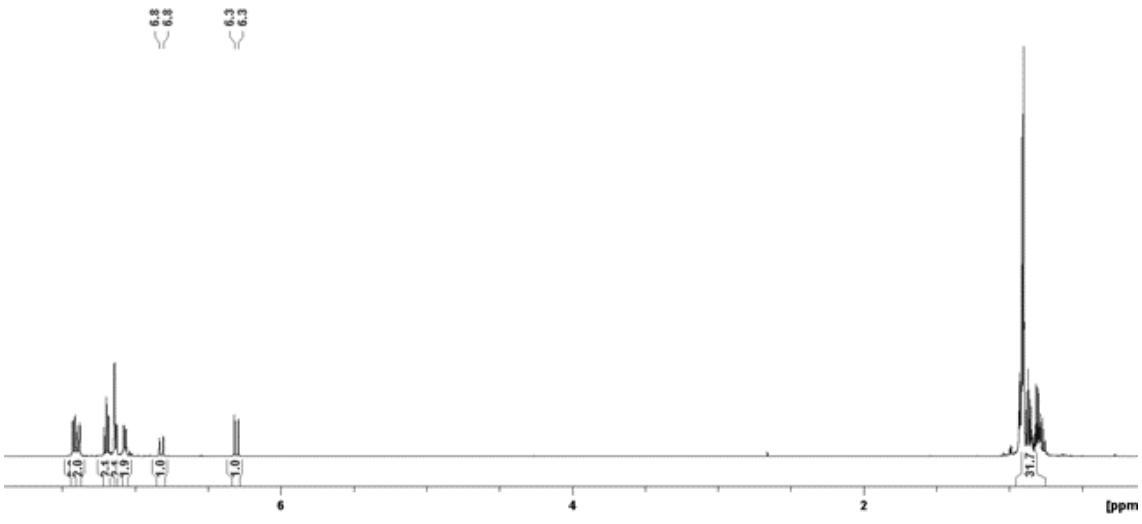

Figure B.29: ^{1}H NMR spectrum of the crude reaction (in C_6D_6) between p-CF3-phenylacetylene and **4.3b**. Only the alkene C–H peaks have been labelled. The $^{3}J_{HH}$ coupling constant is 12.7 Hz (c.f. 12.7 Hz for compound **4.5**).

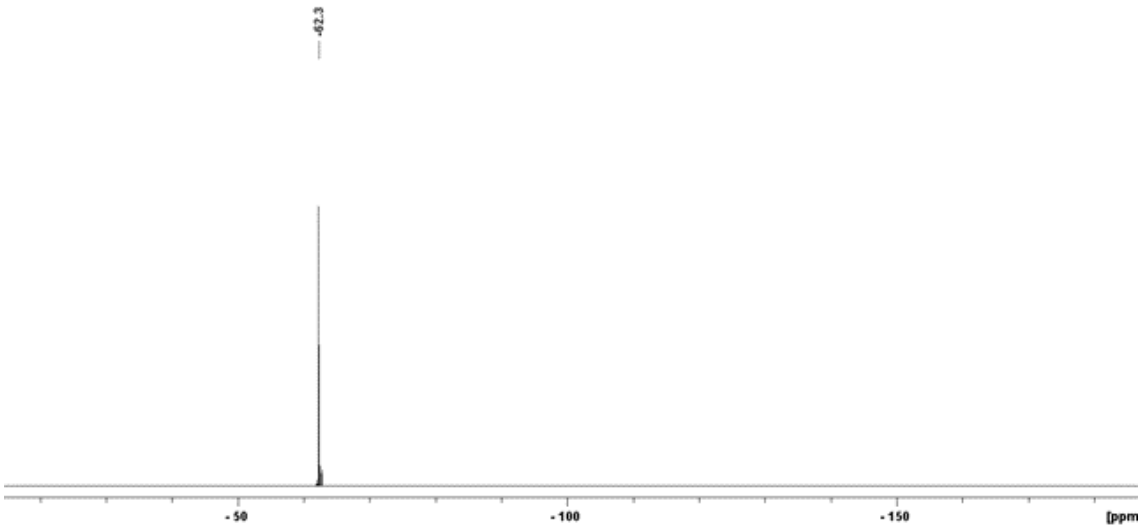

Figure B.30: ^{19}F NMR spectrum of the crude reaction (in C_6D_6) between p-CF_3-phenylacetylene and **4.3b**.

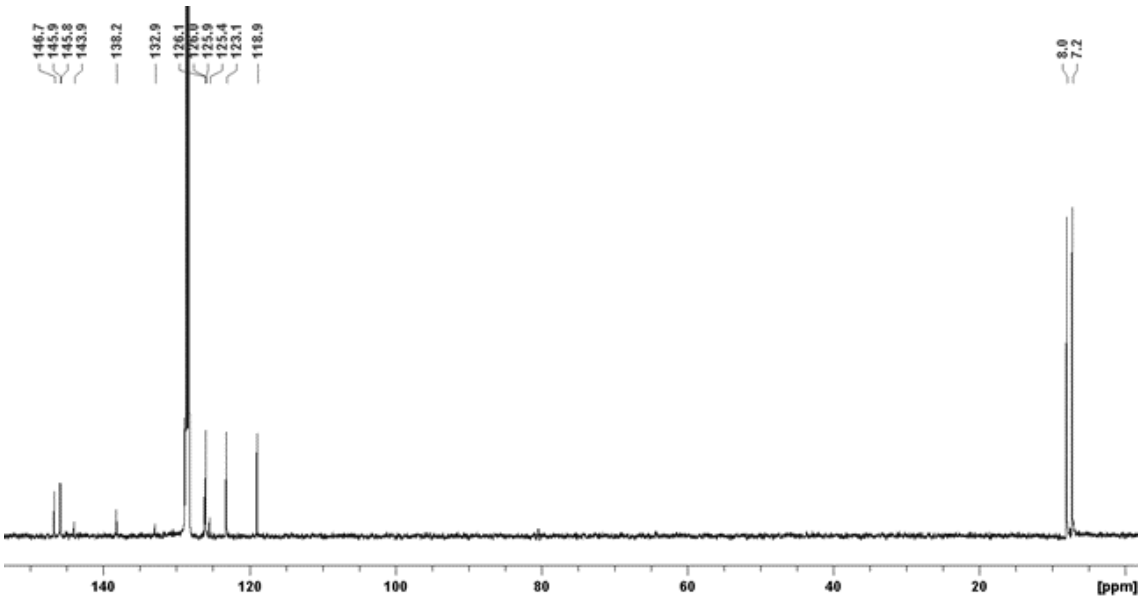

Figure B.31: $^{13}C\{^1H\}$ spectrum of the crude reaction (in C_6D_6) between p-CF_3-phenylacetylene and **4.3b**.

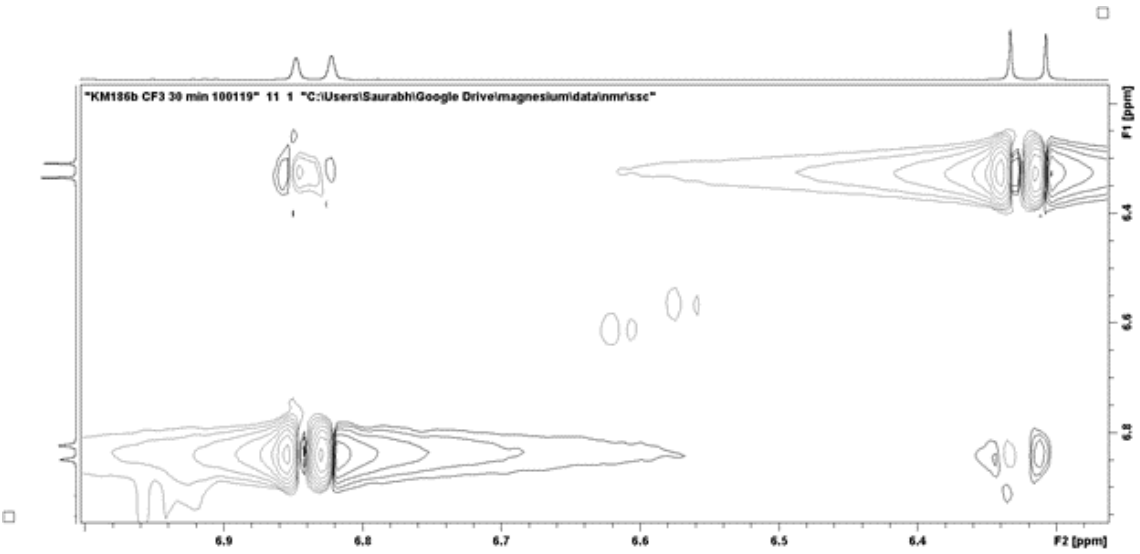

Figure B.32: NOESY spectrum of the crude reaction (in C_6D_6) mixture between p-CF_3-phenylacetylene and **4.3b** showing cross-peaks between the protons of the Z-alkene.

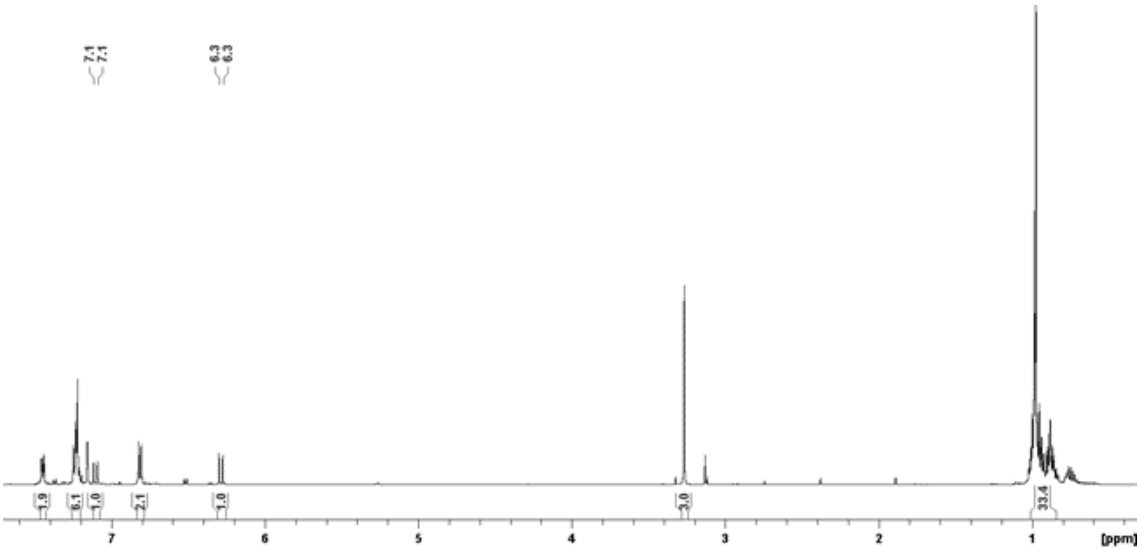

Figure B.33: Spectrum of the crude reaction (in C_6D_6) between p-Me-phenylacetylene and **4.3b**. Only the alkene C-H peaks have been labelled. The $^3J_{HH}$ coupling constant is 12.4 Hz (c.f. 12.7 Hz for compound **4.5**). The small doublet at 6.5 ppm arises from the small amount of unreacted p-Me-phenylacetylene.

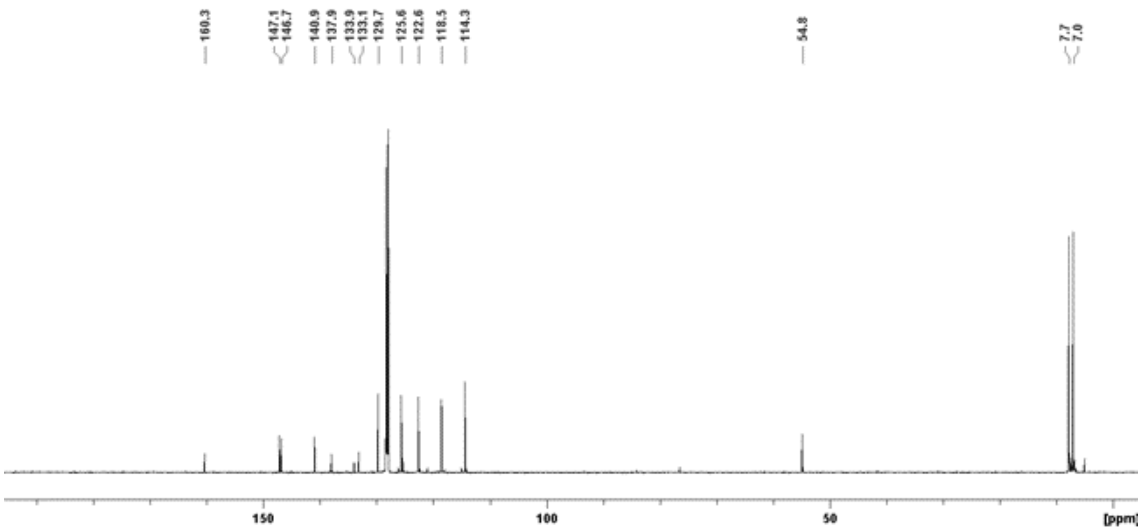

Figure B.34: $^{13}C\{^{1}H\}$ spectrum of the crude reaction (in C_6D_6) between p-Me-phenylacetylene and **4.3b** showing the 15 peaks expected for a single isomer.

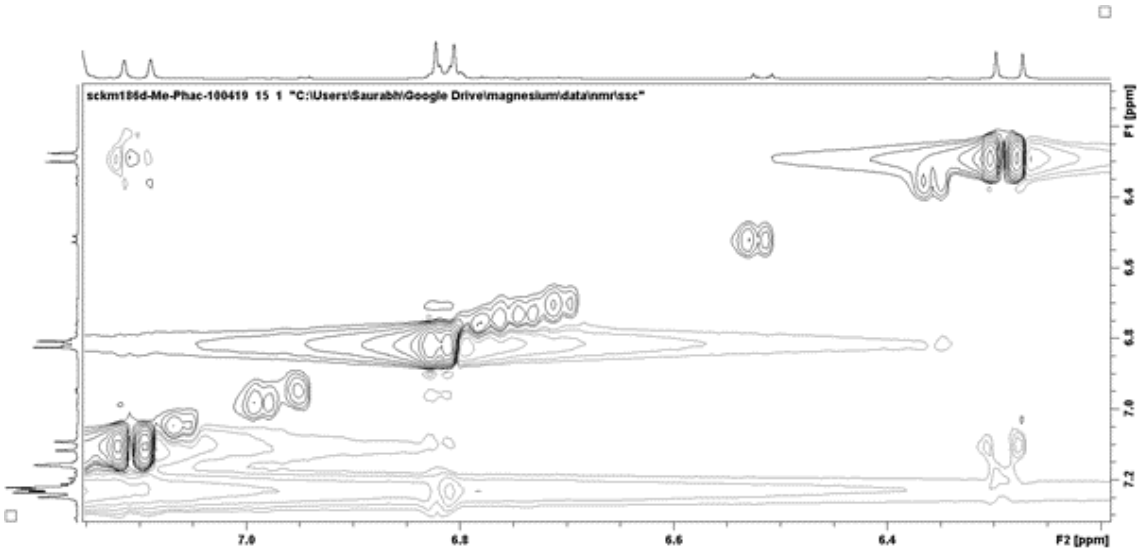

Figure B.35: NOESY spectrum of the crude reaction (in C_6D_6) mixture between p-Me-phenylacetylene and **4.3b** showing cross-peaks between the protons of the Z-alkene.

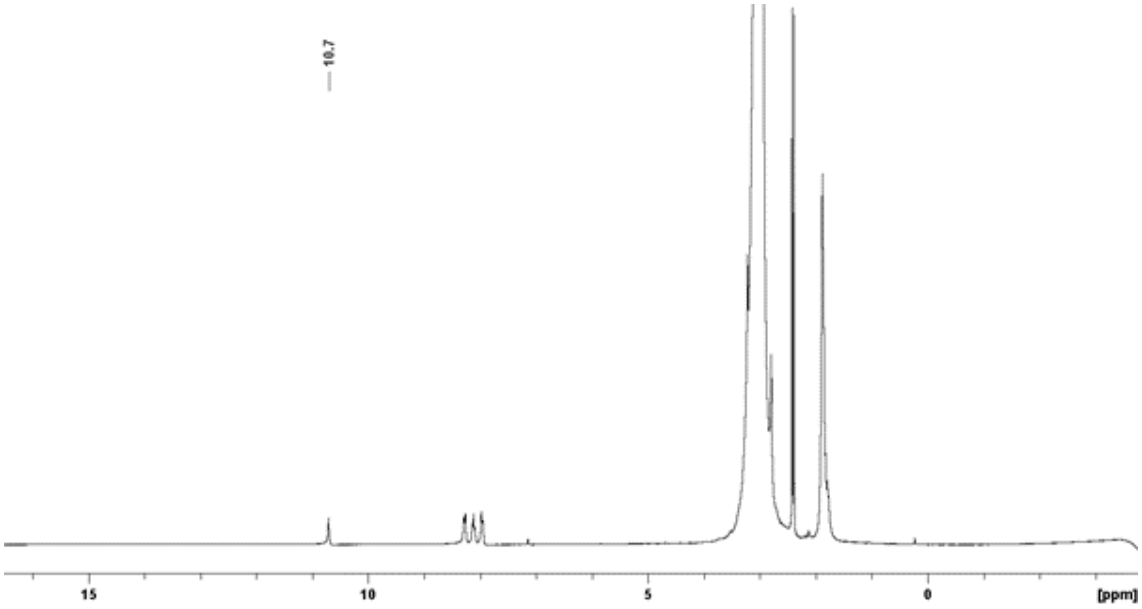

Figure B.36: ^{1}H NMR spectrum of **4.3b** dissolved in neat acetone after 24 h – no reaction has taken place. The intact Sb–H resonance is labelled. The peak at 7.16 ppm is due to a C_6D_6 capillary used for locking.

All calculations for our paper titled "Hydrostibination"[211] were performed using Gaussian 16. Geometry optimizations and frequency calculations were carried out at the PBE0-D3/def2-TZVP level (coordinates shown below) in a simulated field of toluene (SCRF).

NBO calculations: The BP86 functional was used with Grimme's D3 correction and Becke-Johnson dampening. The TZ2P basis set was employed without any frozen core approximation. Scalar relativistic corrections were employed.

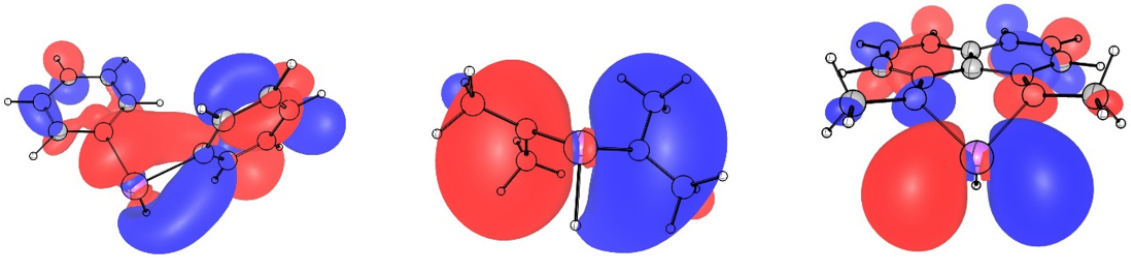

Figure B.37: View of the LUMOs of Ph_2SbH (left), $(Me_2N)_2SbH$ (middle), and N,N'−(dimethyl)naphthyl)SbH (right) at the PBE1/def2-tzvp level.

Appendix C

Supporting Information for Chapter 5

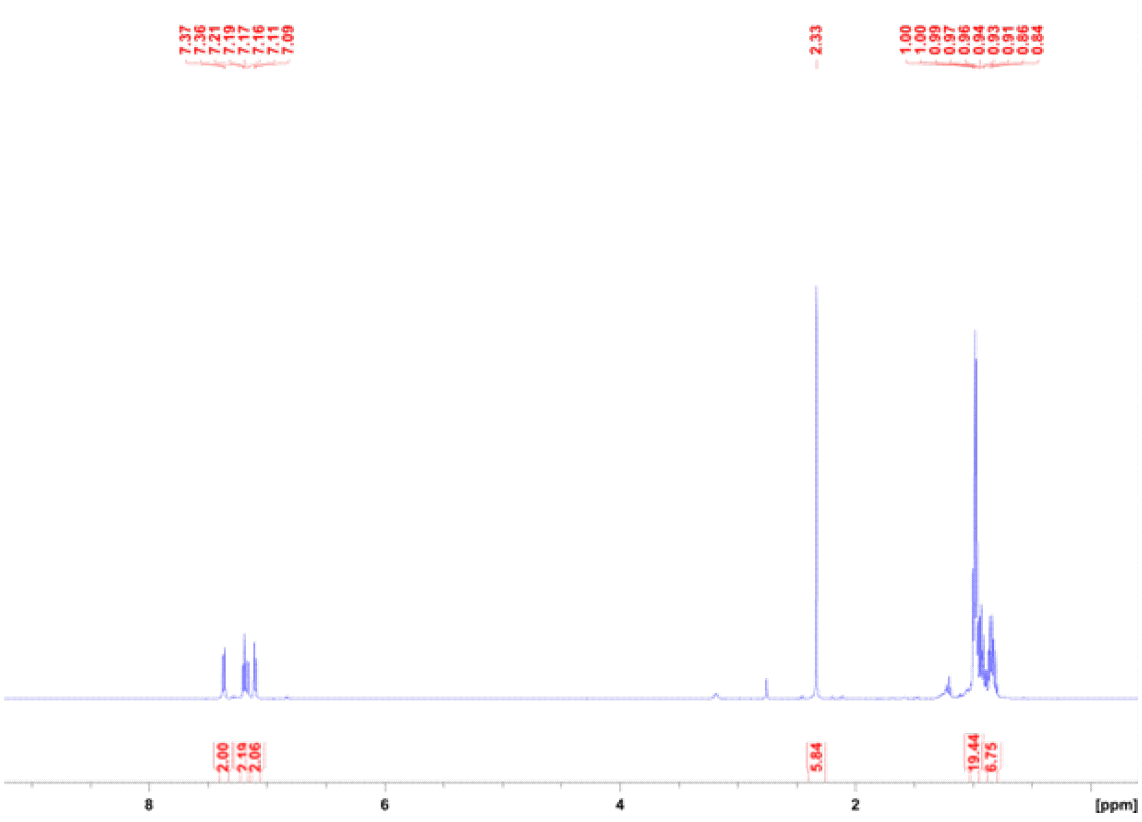

Figure C.1: Crude ^{1}H NMR spectrum of $EtSbNMe_2$ obtained from the combination of $LiNMe_2$ and **4.2b**.

c

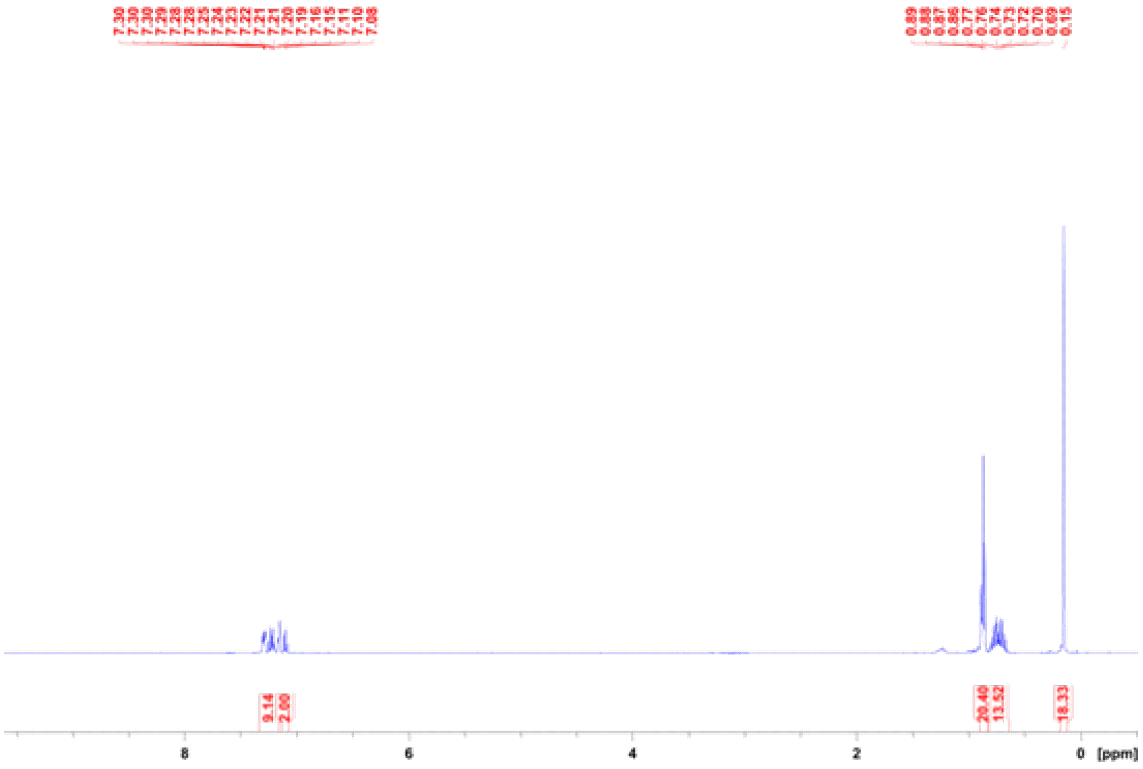

Figure C.2: ^{1}H NMR spectrum of **5.1**.

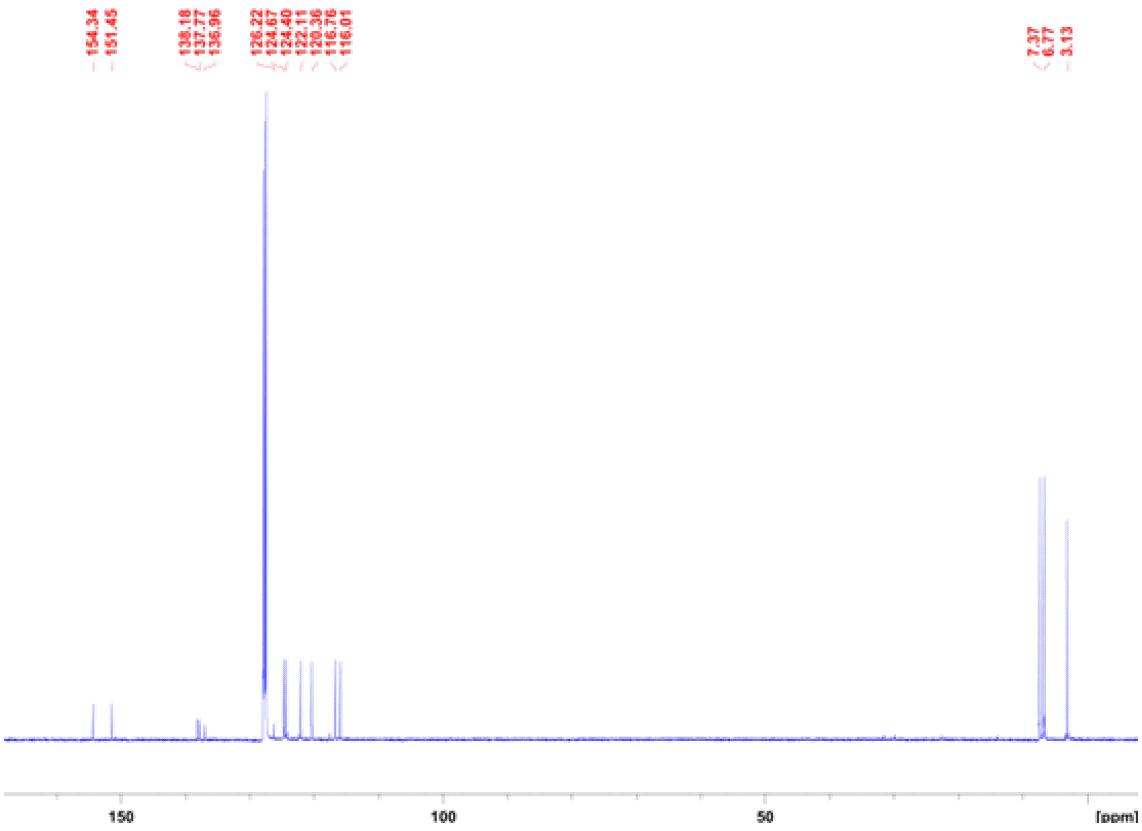

Figure C.3: $^{13}C\{^{1}H\}$ spectrum of **5.1**.

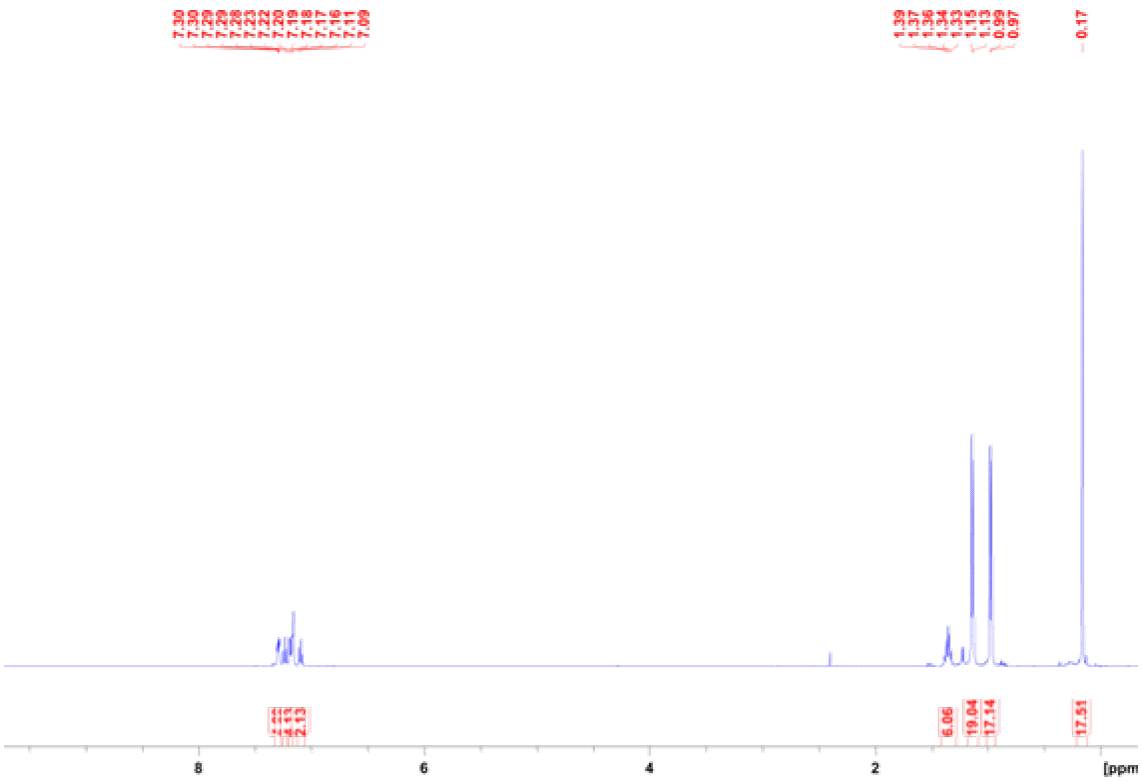

Figure C.4: ^{1}H NMR spectrum of **5.2**.

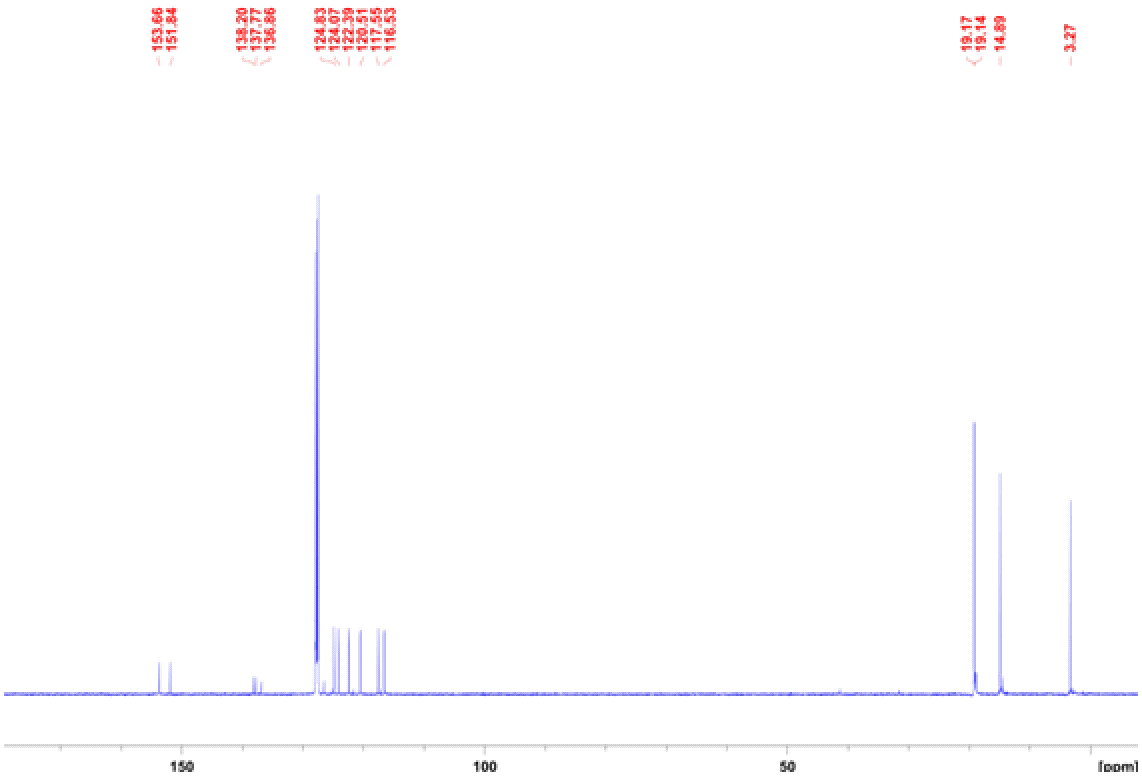

Figure C.5: $^{13}C\{^{1}H\}$ spectrum of **5.2**.

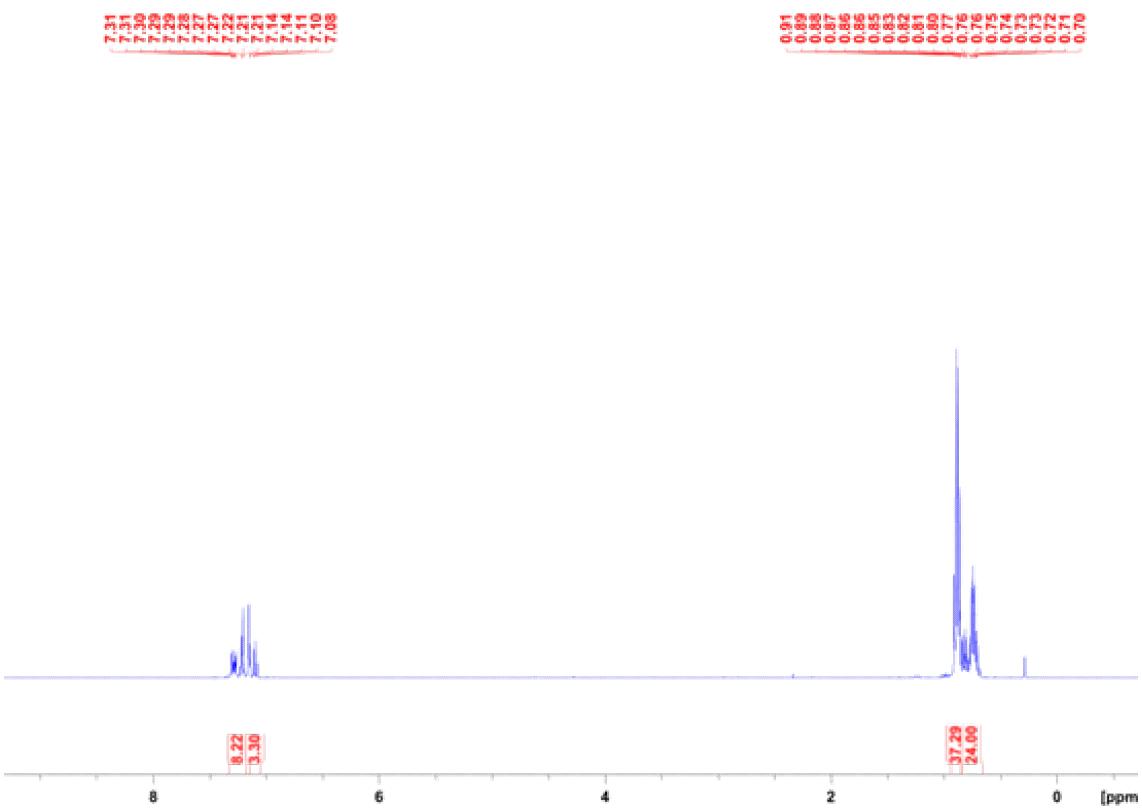

Figure C.6: ^{1}H NMR spectrum of **5.3**.

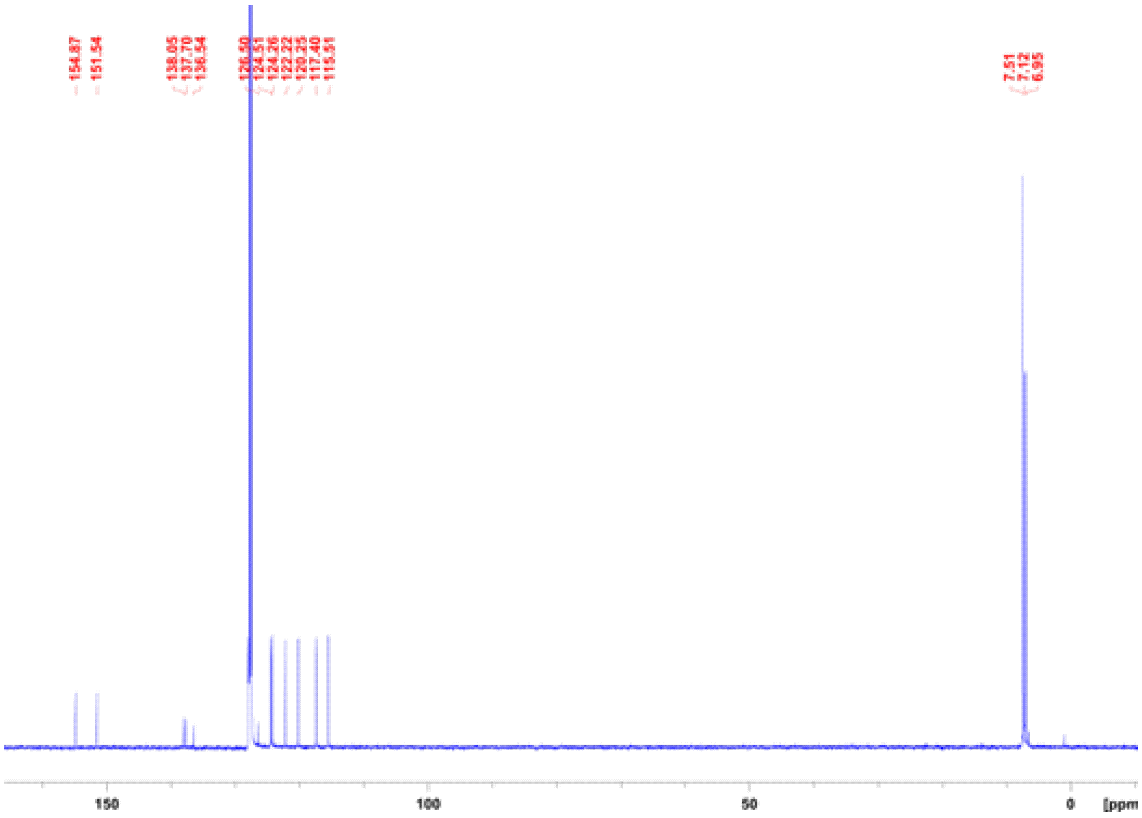

Figure C.7: $^{13}C\{^{1}H\}$ spectrum of **5.3**.

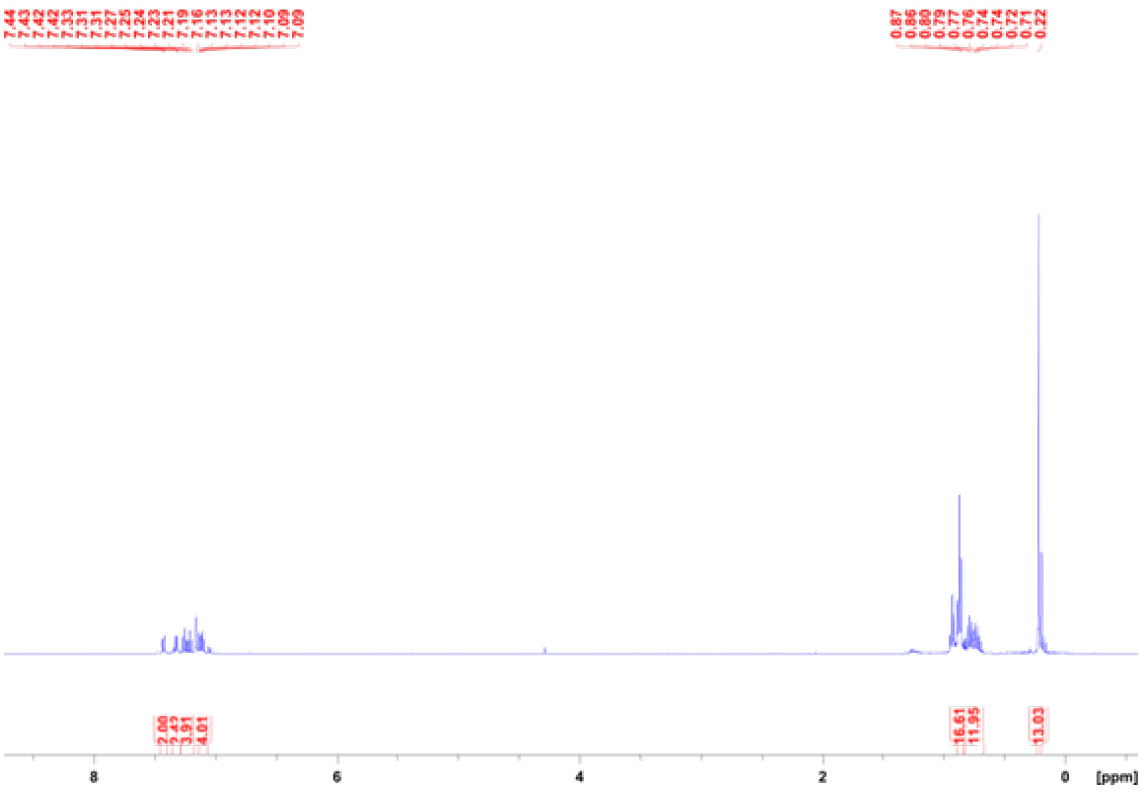

Figure C.8: ^{1}H NMR spectrum of **5.4**.

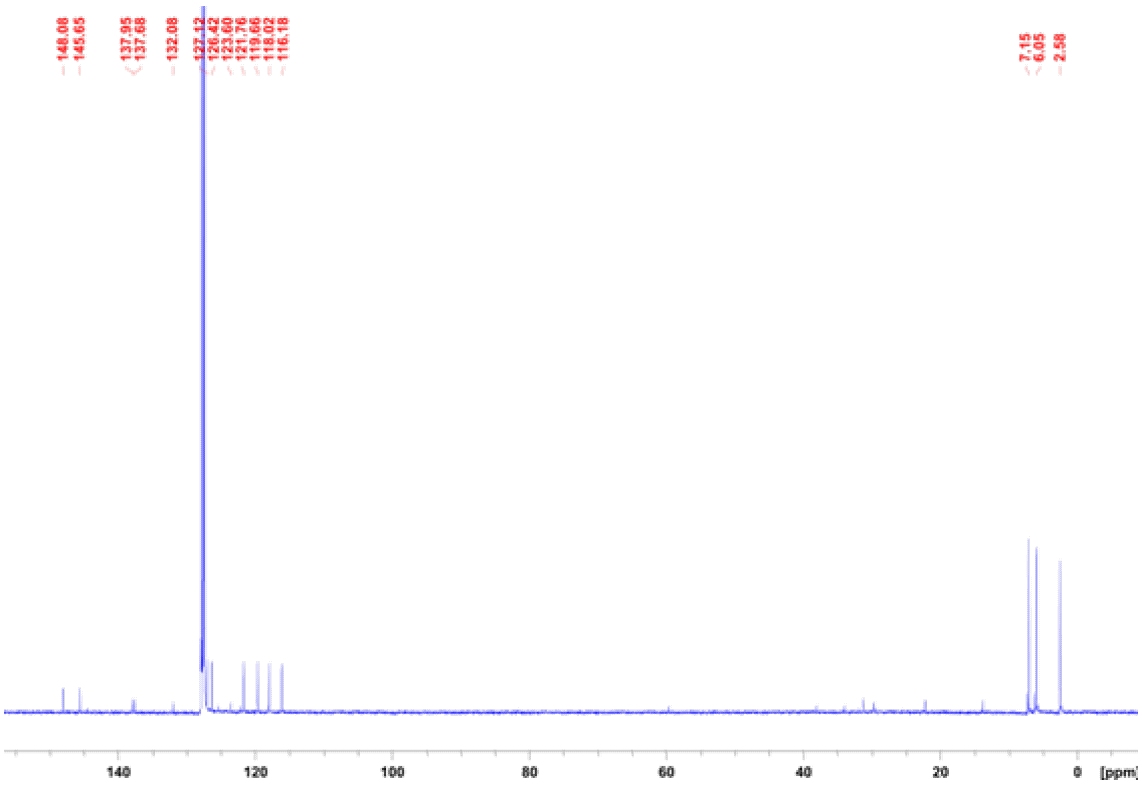

Figure C.9: $^{13}C\{^{1}H\}$ spectrum of **5.4**.

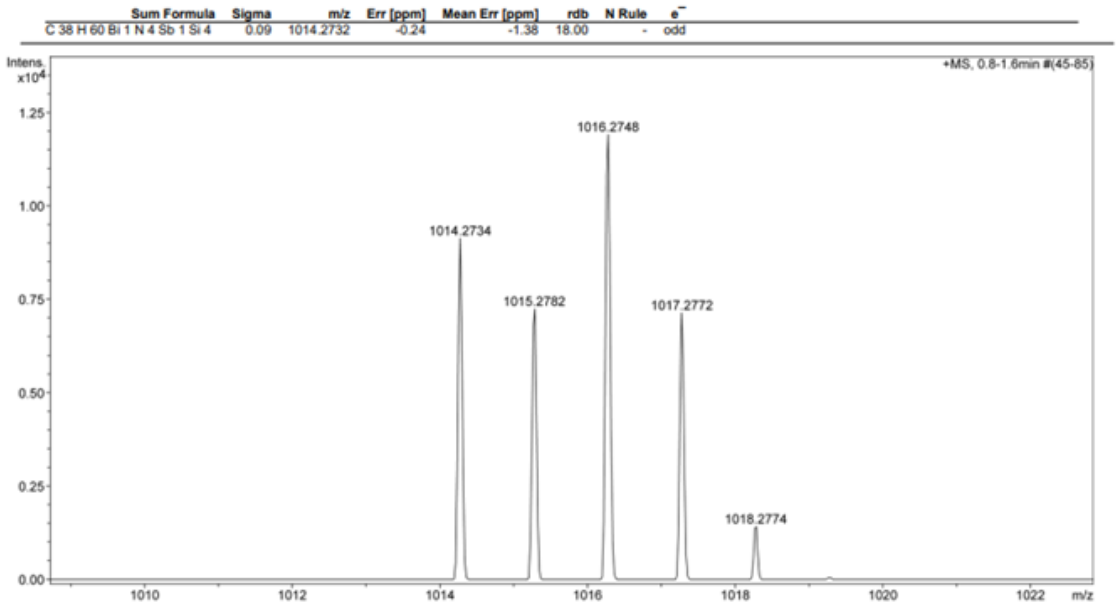

Figure C.10: HRMS of **5.1**.

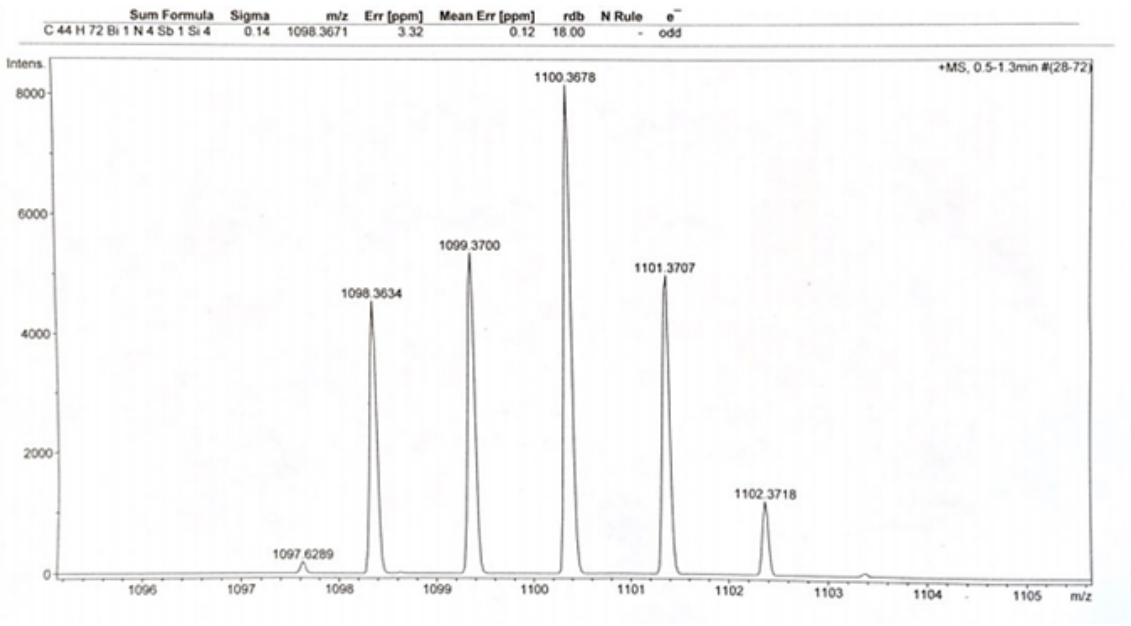

Figure C.11: HRMS of **5.2**.

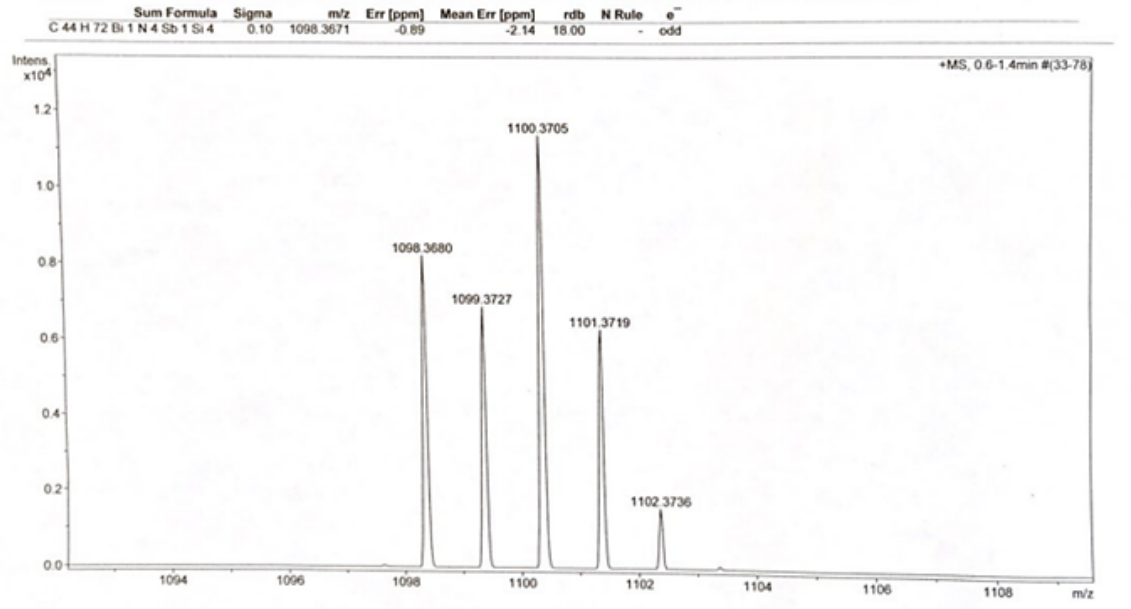

Figure C.12: HRMS of **5.3**.

Appendix D

Supporting Information for Chapter 6

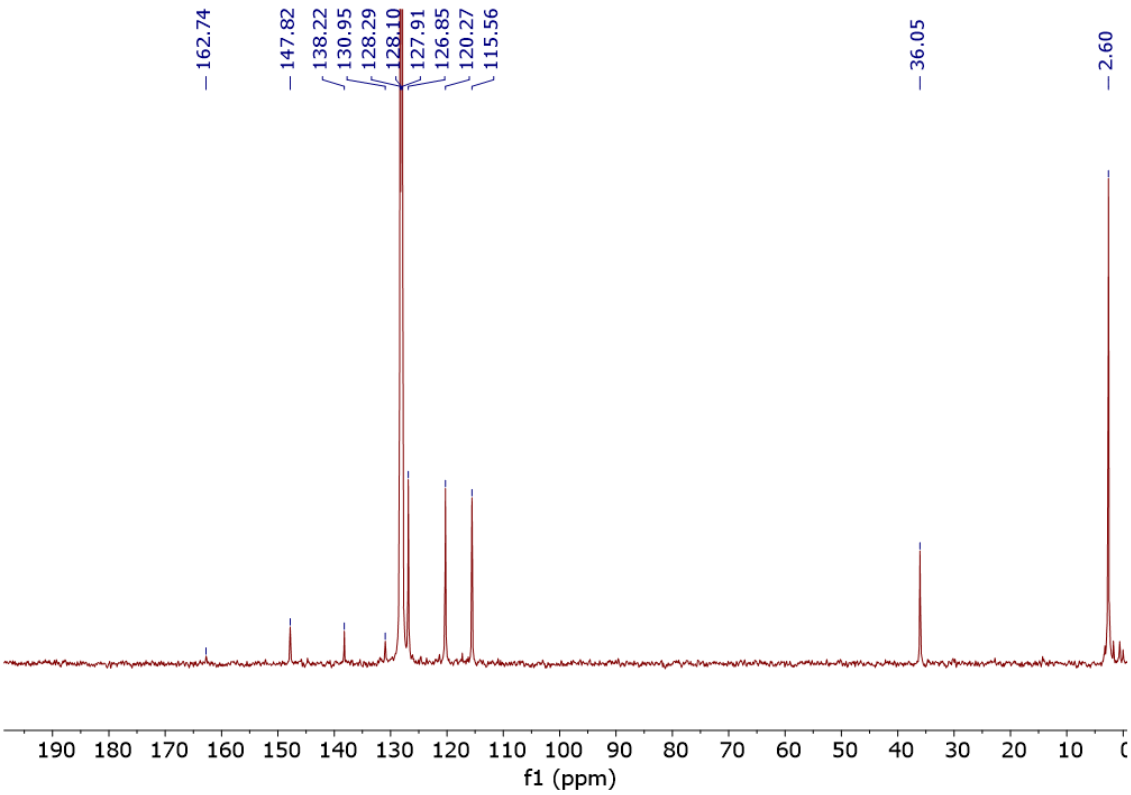

Figure D.1: $^{13}C\{^{1}H\}$ spectrum of **6.4c** in C_6D_6.

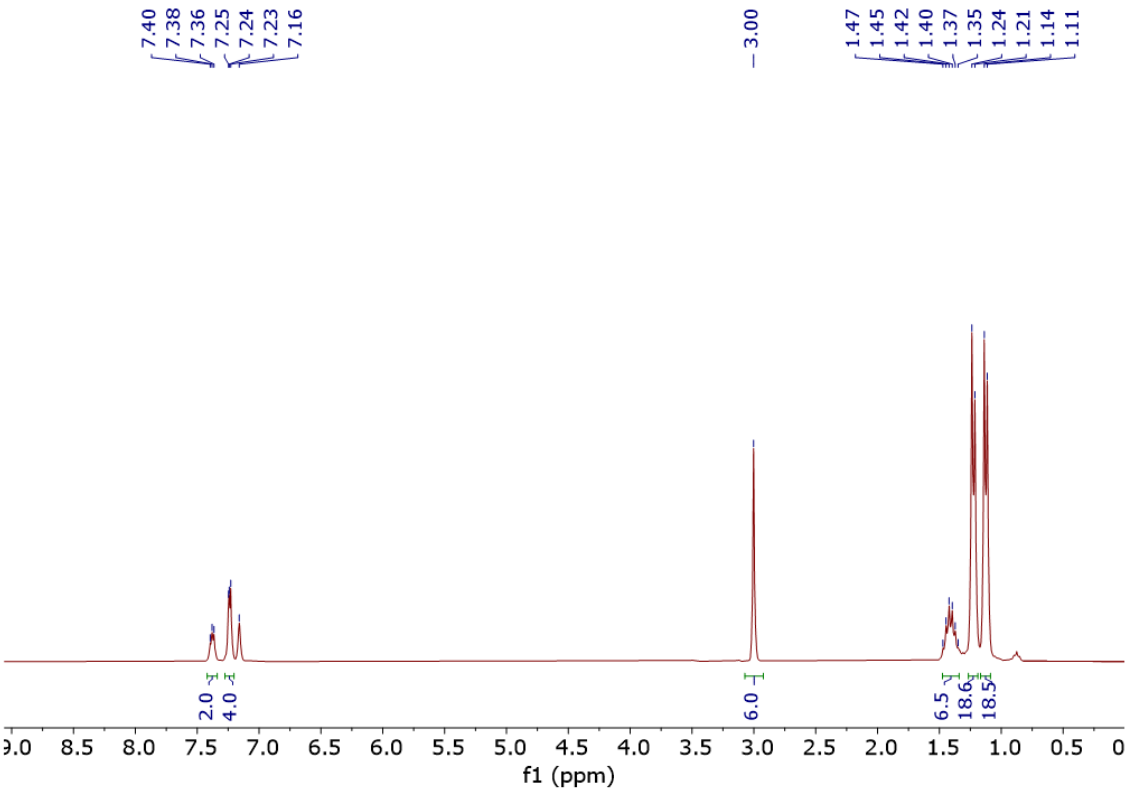

Figure D.2: ^{1}H NMR spectrum of **6.5a** in C_6D_6.

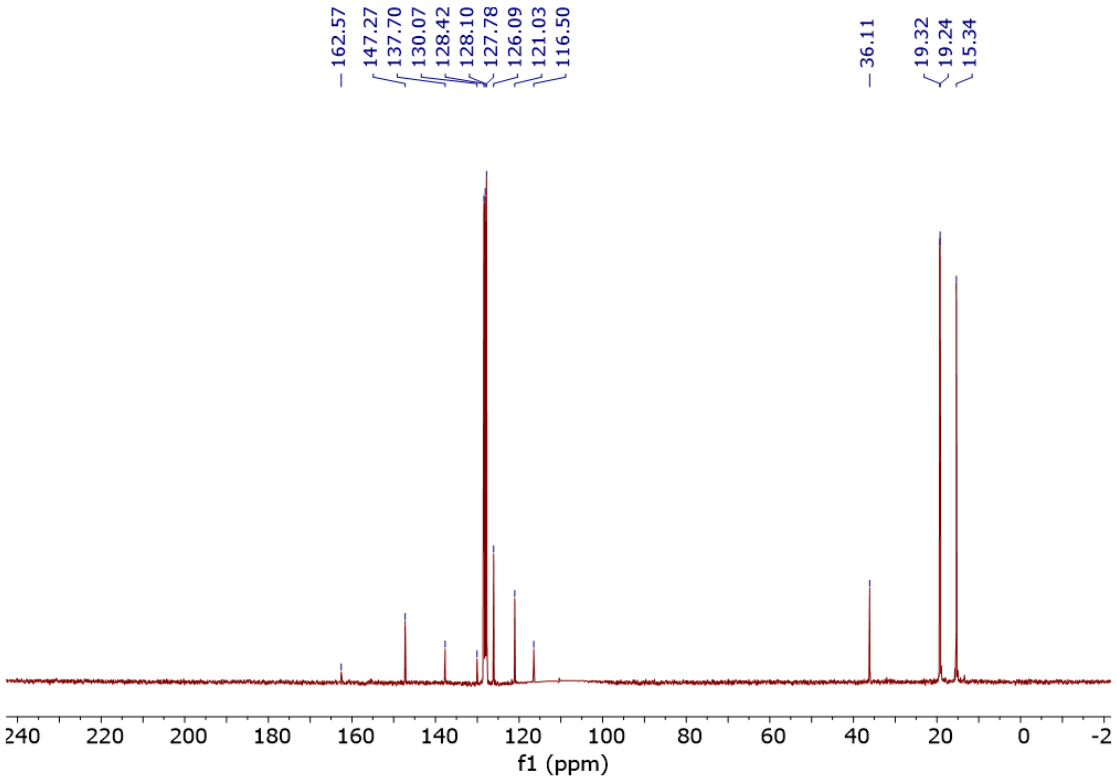

Figure D.3: $^{13}C\{^{1}H\}$ spectrum of **6.5a** in C_6D_6. An instrument artifact at 110 ppm has been suppressed.

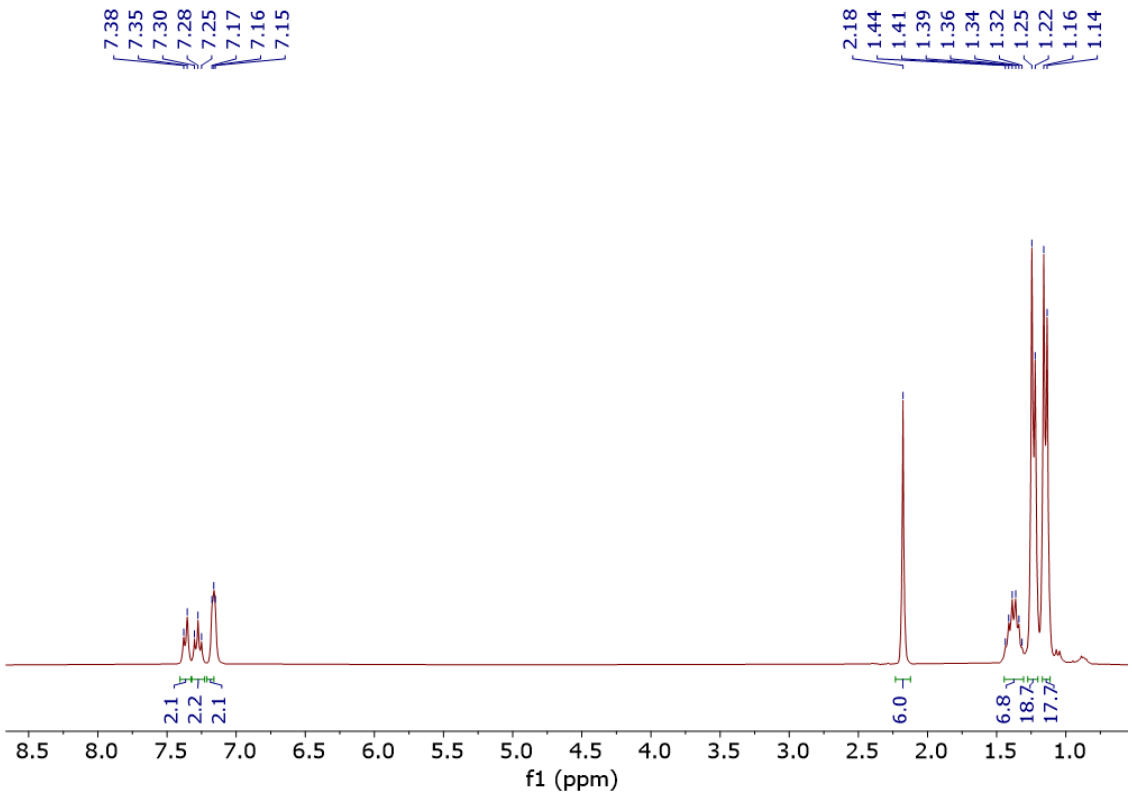

Figure D.4: ^{1}H NMR spectrum of **6.5b** in C_6D_6.

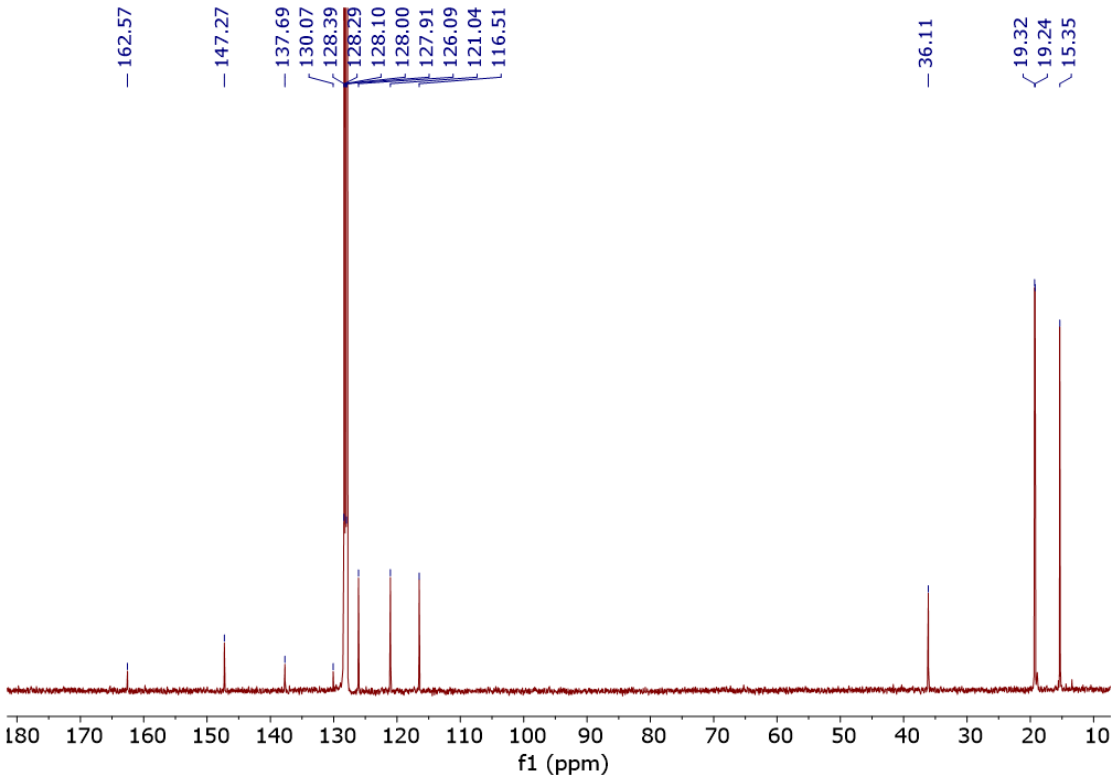

Figure D.5: $^{13}C\{^{1}H\}$ spectrum of **6.5b** in C_6D_6.

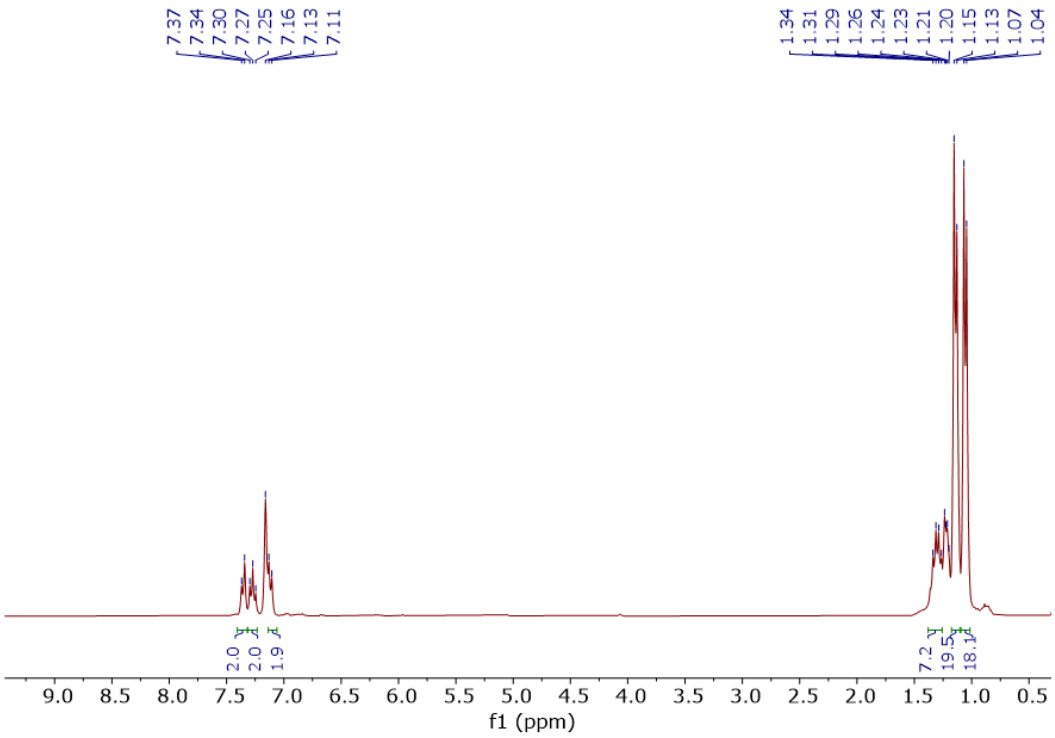

Figure D.6: ^{1}H NMR spectrum of **6-Cl** in C_6D_6.

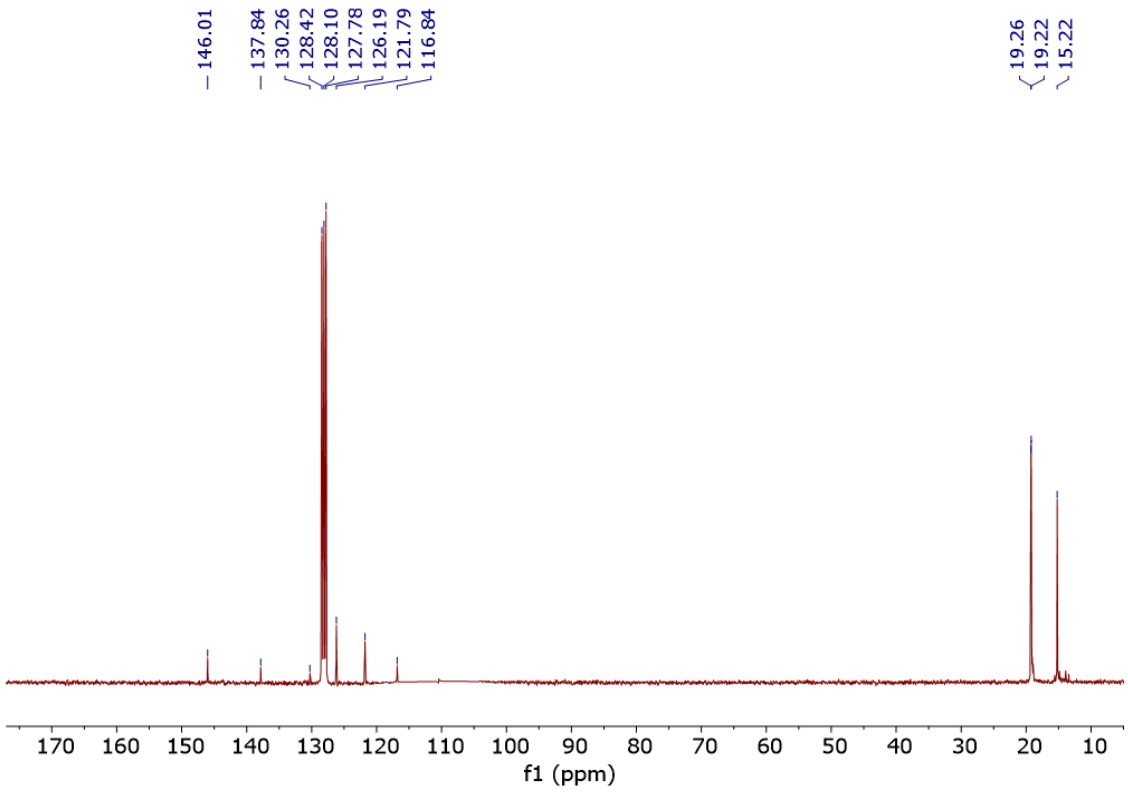

Figure D.7: $^{13}C\{^{1}H\}$ spectrum of **6-Cl** in C_6D_6. An instrument artifact at 110 ppm has been suppressed.

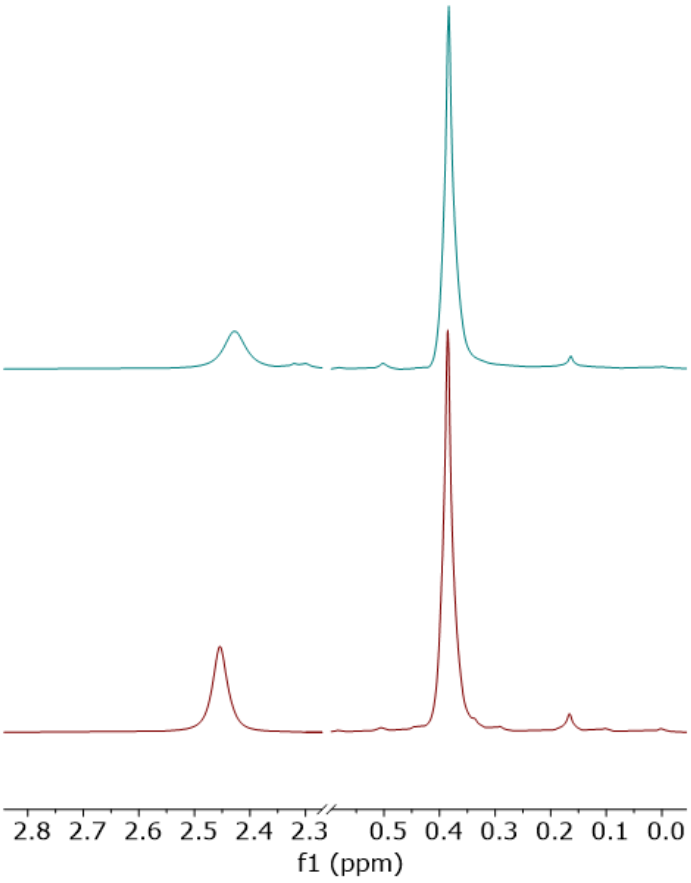

Figure D.8: Comparison of the diagnostic region of the ^{1}H NMR spectra of crystals of **6.4c** in pyridine-d_5 (top) and reaction of **6.4a** with CO_2 in pyridine-d_5 (bottom) showing that the same product is formed in each case.

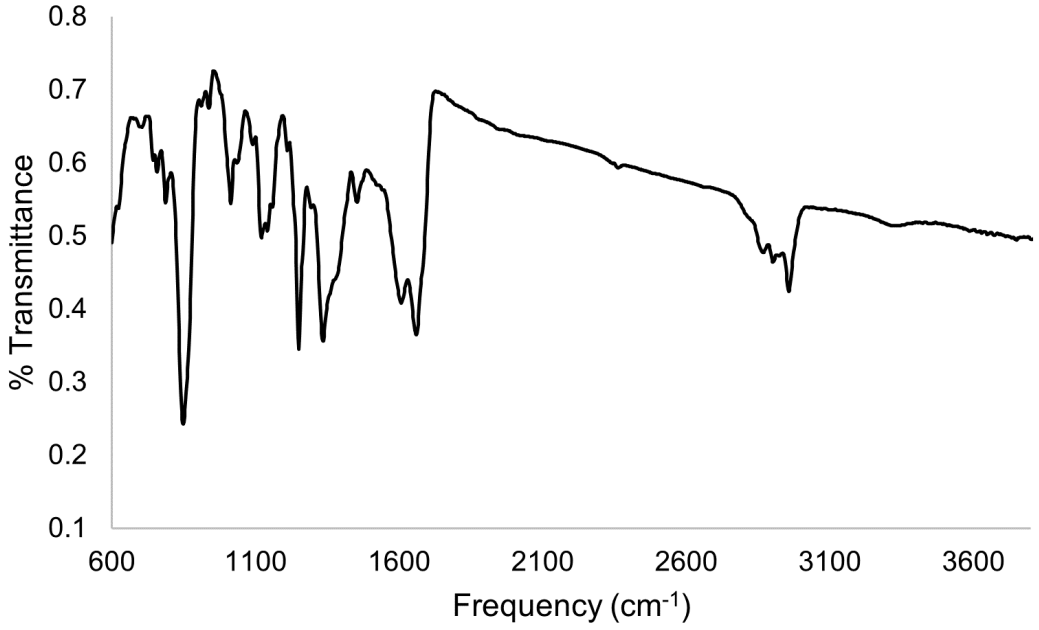

Figure D.9: IR spectrum of the reaction of **6.3a** with CO_2.

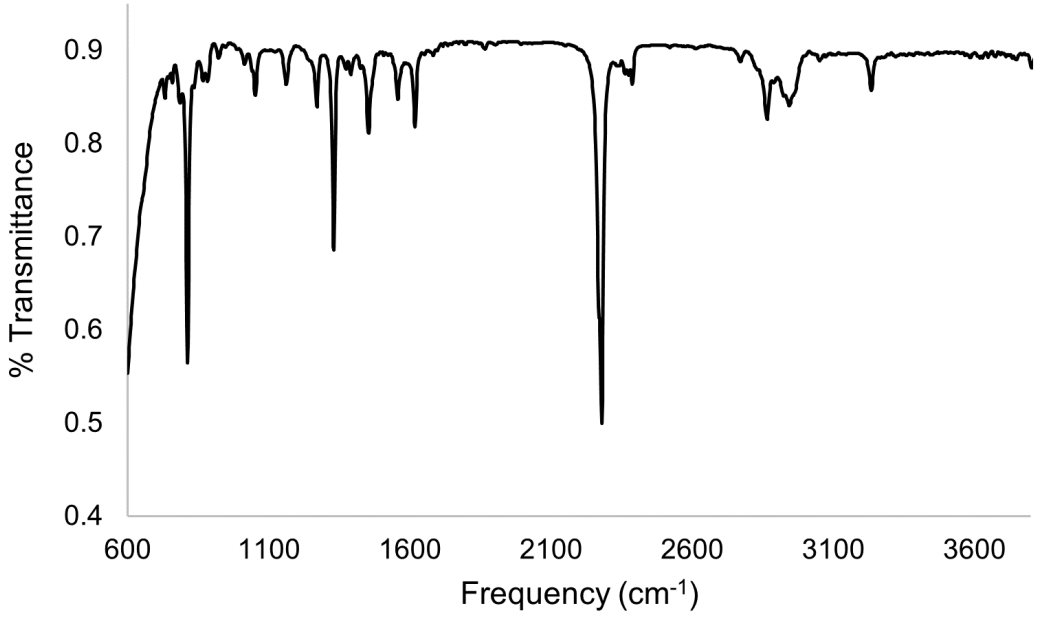

Figure D.10: IR spectrum of **6.5a**.

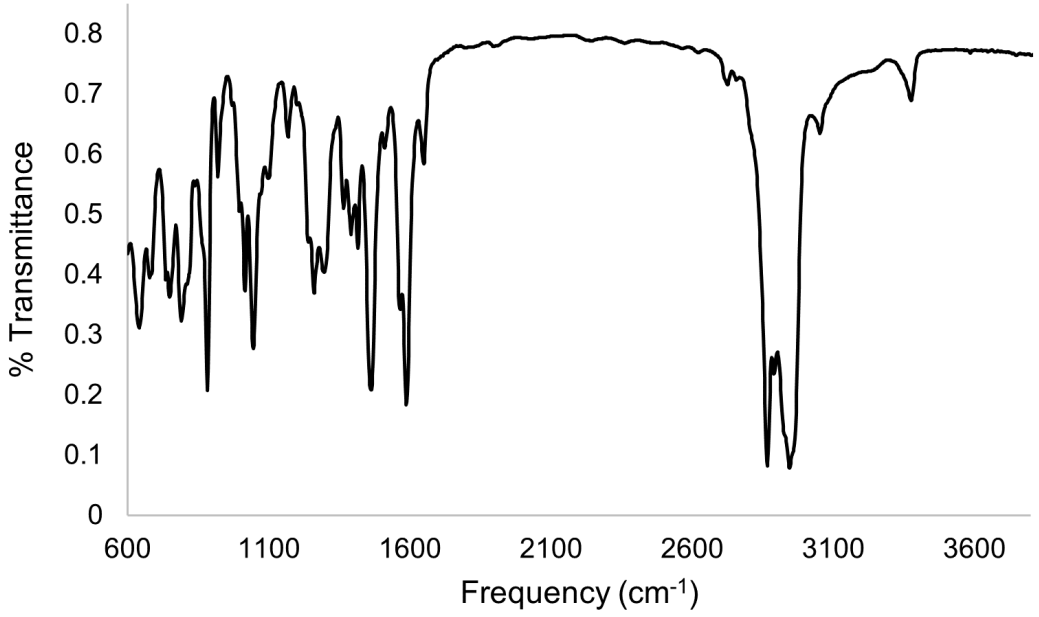

Figure D.11: IR spectrum of **6-Cl**.

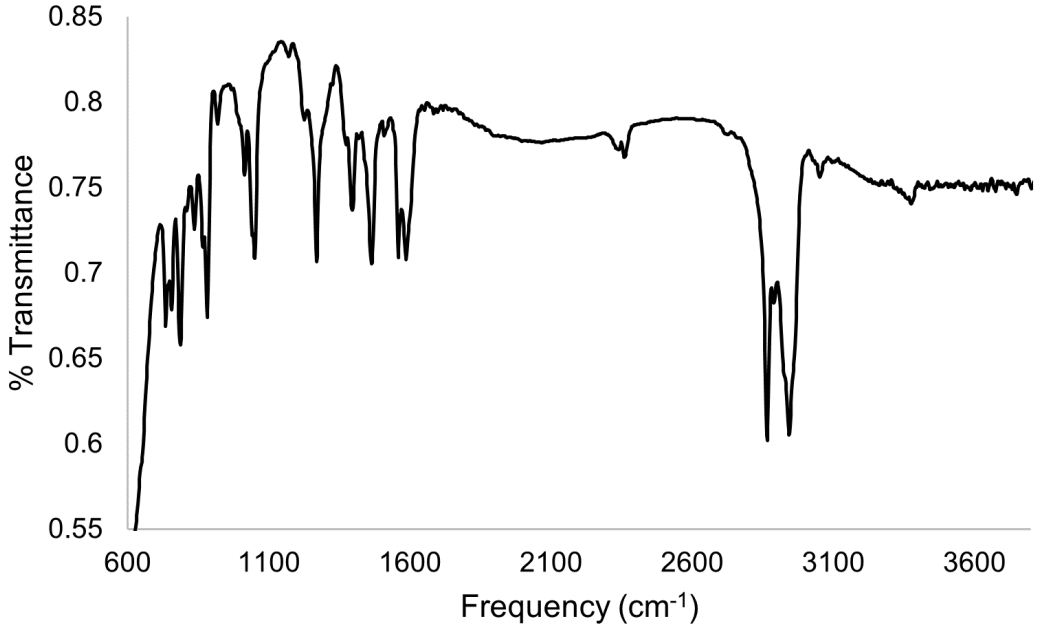

Figure D.12: IR spectrum of $\mathbf{6b_{dim}}$.

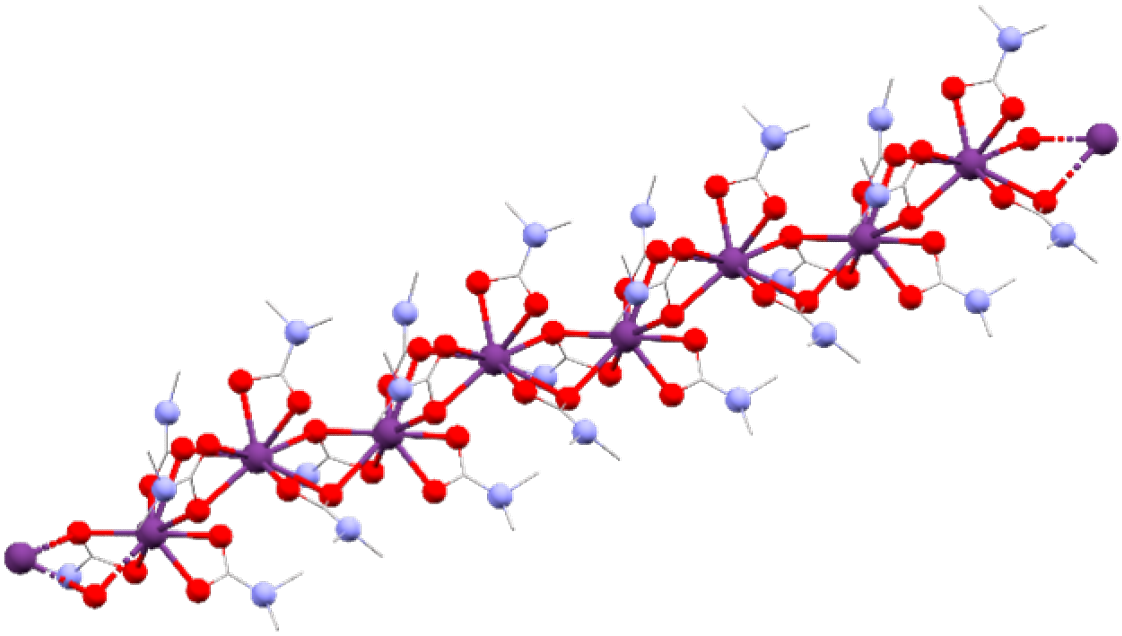

Figure D.13: View of the polymeric structure of **6.1b** in the solid state. Hydrogen atoms have been omitted and carbon atoms shown in wireframe for clarity. A ball and stick representation is used because disorder in the diffraction data limited refinement to isotropic treatment.

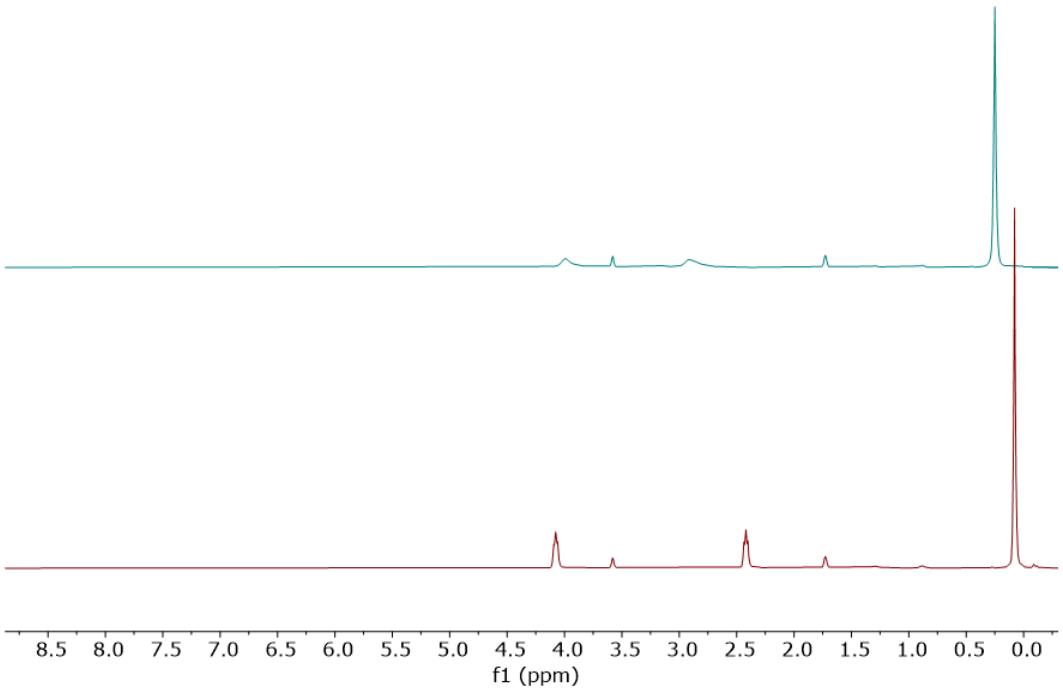

Figure D.14: ^{1}H NMR spectra of **6.3a** (bottom) and the reaction **6.3a** + CO_2 (top) in tetrahydrofuran-d_8. Broad ill-defined species are formed as seen in the top spectrum, likely due to oligomerization through the highly flexible ligand backbone.

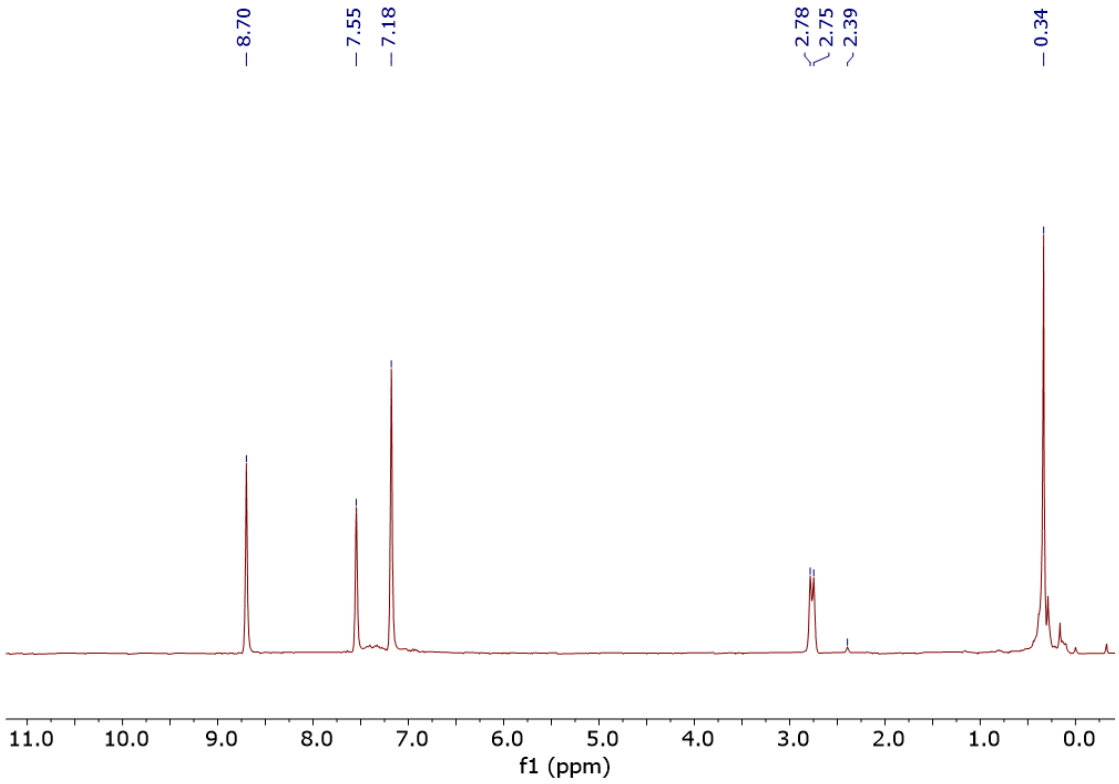

Figure D.15: ^{1}H NMR spectrum after addition of excess CO_2 to **6.4a** in pyridine. The resonances at 2.76 ppm and 0.34 ppm correspond to $Me_3SiO_2CNMe_2$. The resonance at 2.76 ppm arises from the NMe_2 portion of the carbamate and appears as a doublet due to significant contribution from the iminium resonance form (partial C=N double bond) of the molecule.

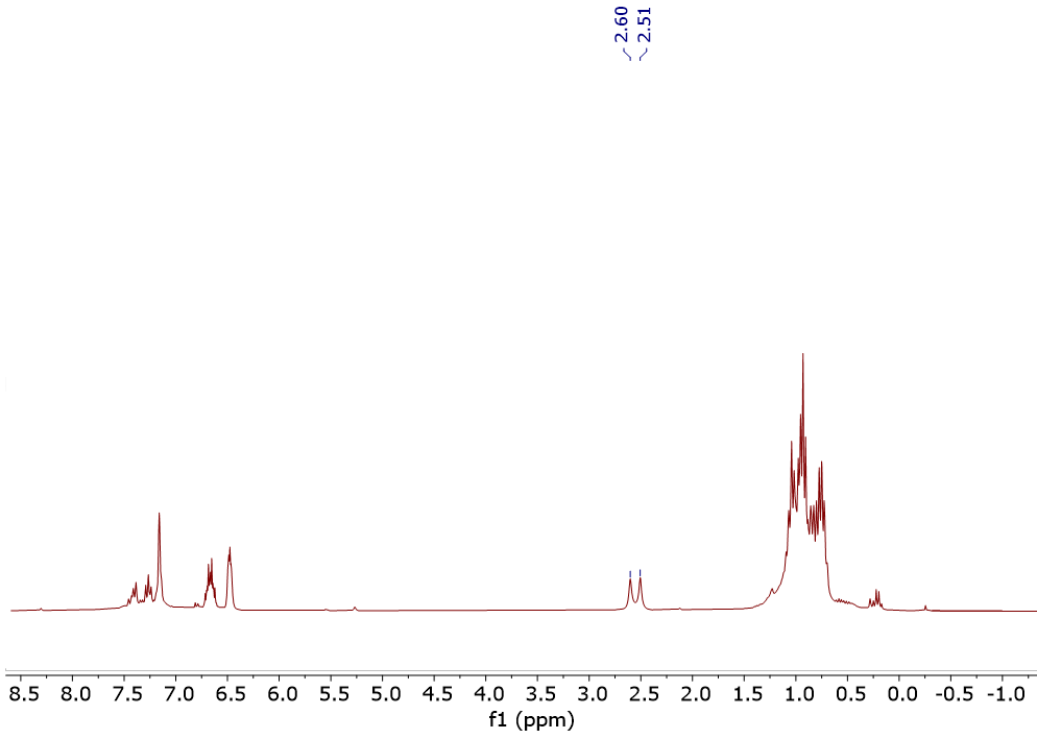

Figure D.16: ^{1}H NMR spectrum of the reaction between **6.5a** and CO_2. The peak-picked signal shows exclusive formation of $Et_3SiO_2CNMe_2$.

Appendix E

Supporting Information for Chapter 7

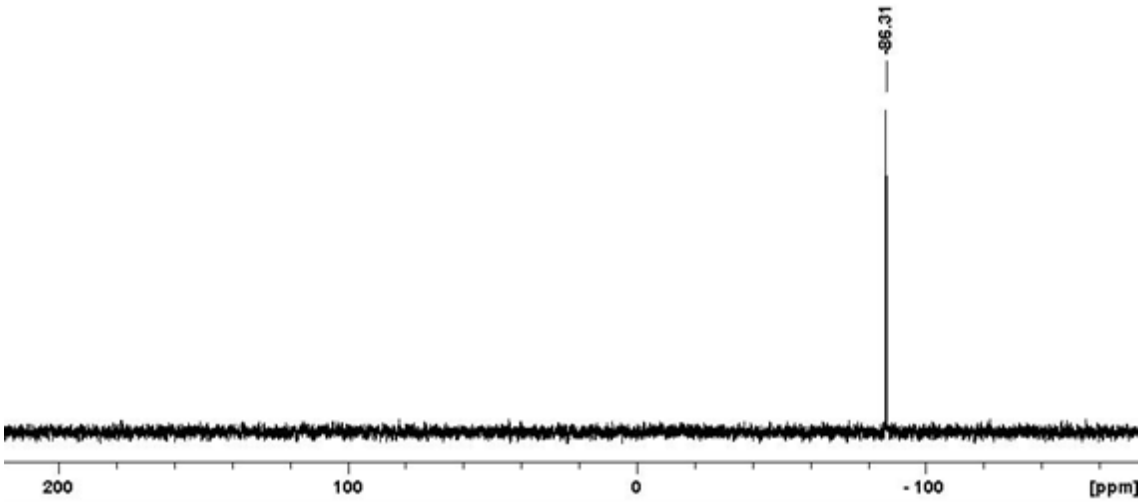

Figure E.1: ^{31}P NMR spectrum of $P(OC_6F_5)_5$ in dichloromethane.

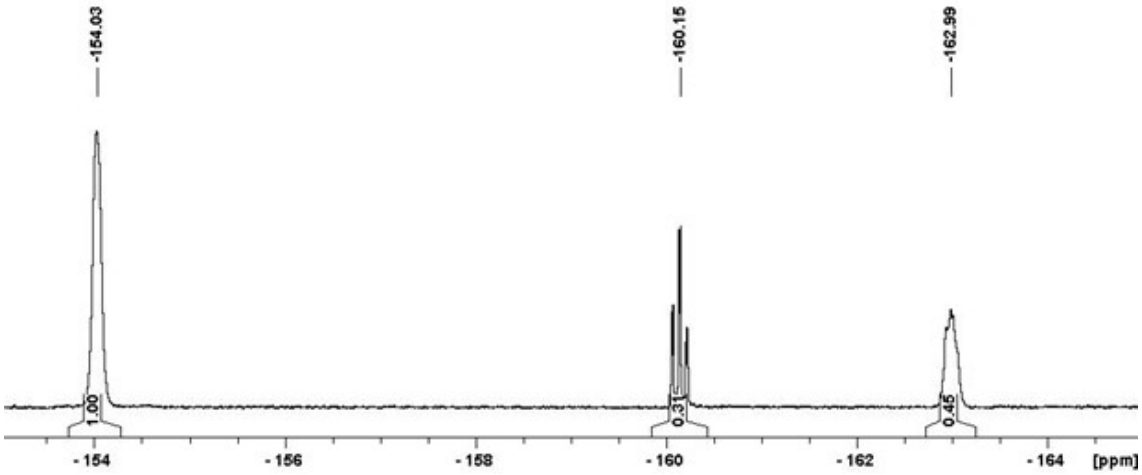

Figure E.2: ^{19}F NMR spectrum of $P(OC_6F_5)_5$ in dichloromethane.

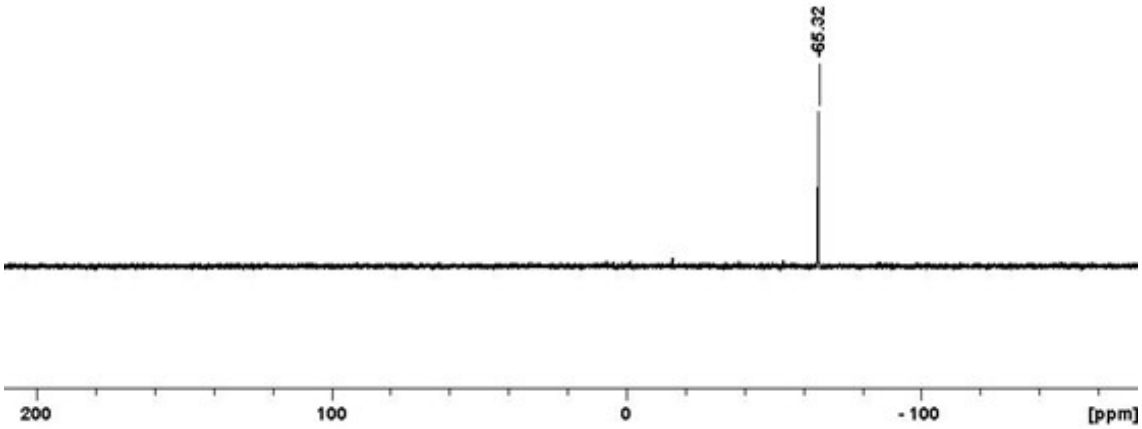

Figure E.3: ^{31}P NMR spectrum of $P(OC_6F_5)_4Cl$ in dichloromethane.

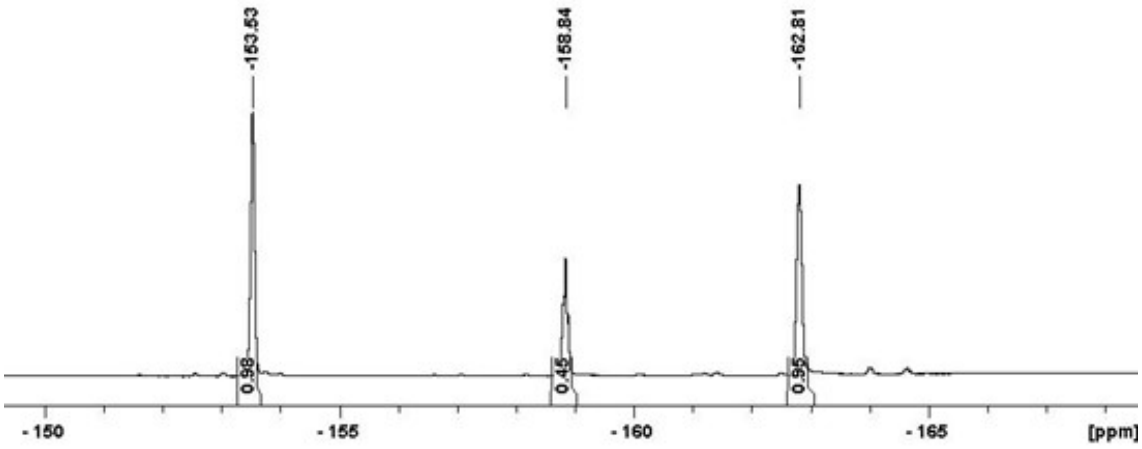

Figure E.4: ^{19}F NMR spectrum of $P(OC_6F_5)_4Cl$ in dichloromethane.

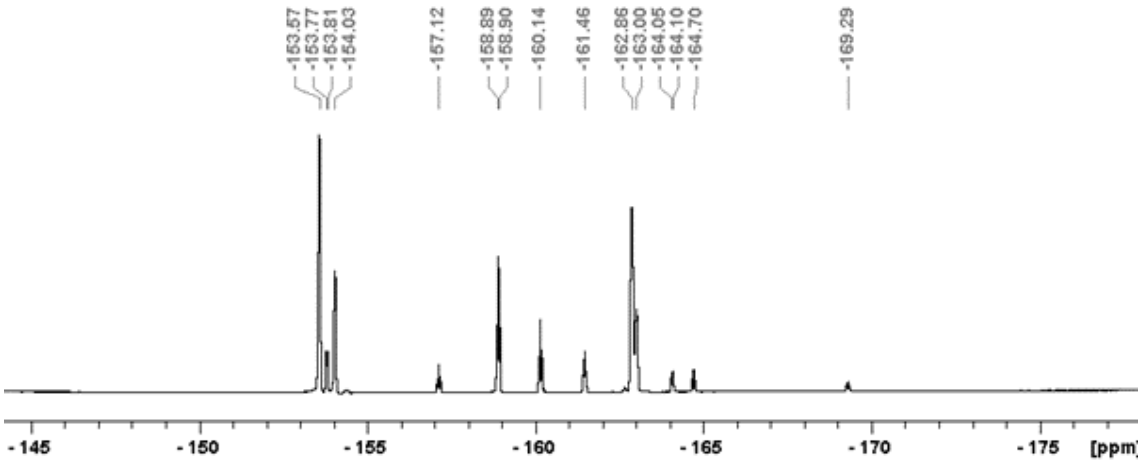

Figure E.5: ^{19}F NMR spectrum of reaction intermediates $P(OC_6F_5)_xCl_{x-n}$ in dichloromethane.

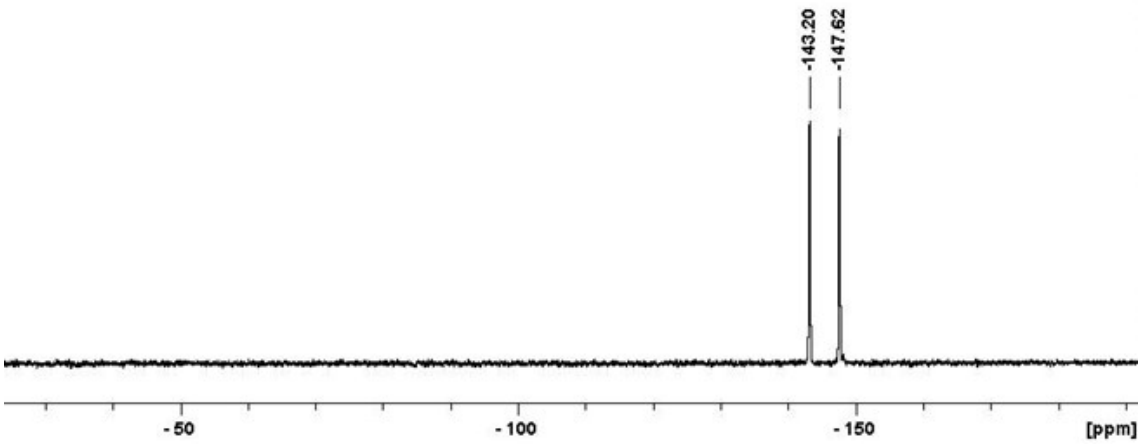

Figure E.6: ^{31}P NMR spectrum of $NBu_4P(OC_6F_5)_5F$ in dichloromethane at 303K.

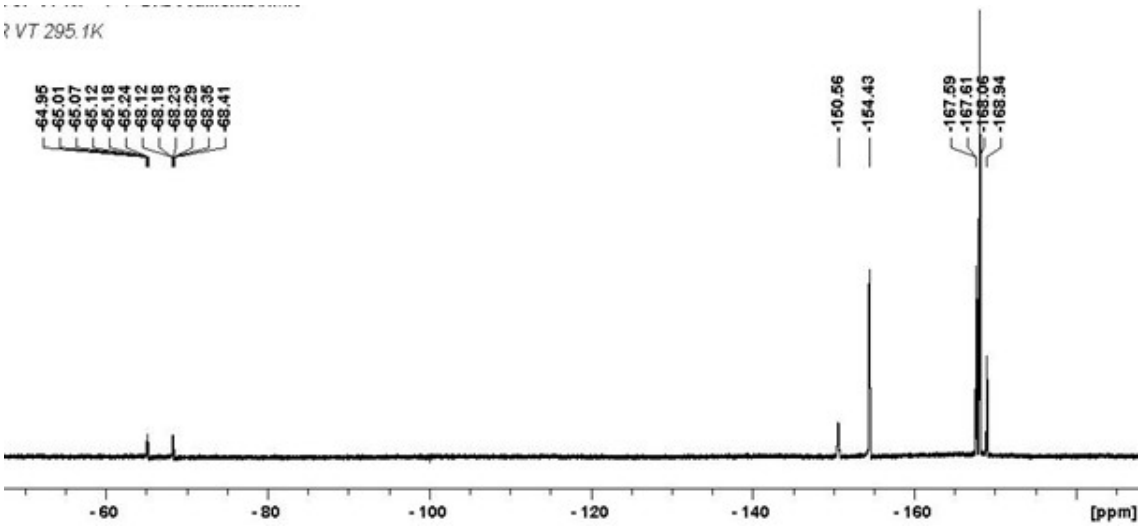

Figure E.7: ^{19}F NMR spectrum of $NBu_4P(OC_6F_5)_5F$ in dichloromethane at 303K.

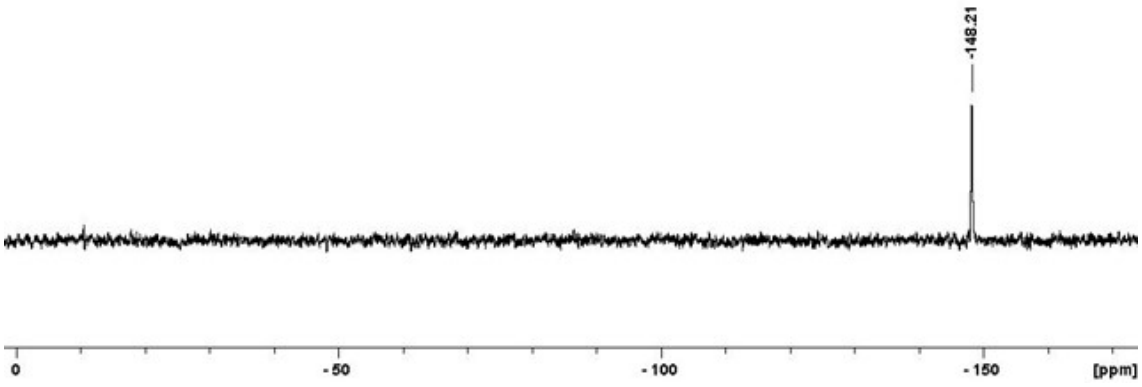

Figure E.8: ^{31}P NMR spectrum of $NBu_4P(OC_6F_5)_6$ in dichloromethane at 303K.

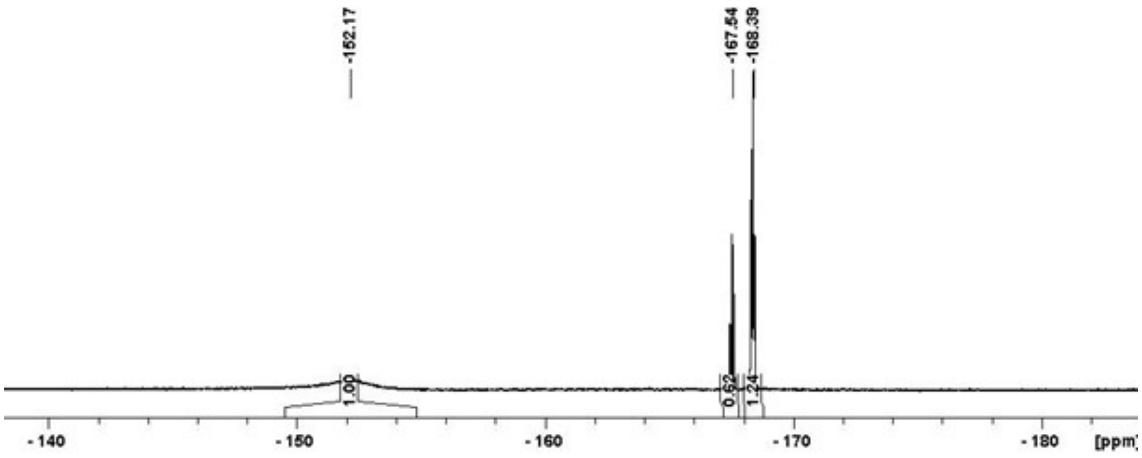

Figure E.9: ^{19}F NMR spectrum of $NBu_4P(OC_6F_5)_6$ in dichloromethane at 303K.

All calculations were performed using Gaussian 09. Geometry optimizations and frequency calculations were carried out at the BP86-D3/SV(P) level for FIA calculations and B3LYP-D3/tzvp for GEI calculations. Optimizations in the presence of a solvent model (PCM or COSMO) were computed in dichloromethane.

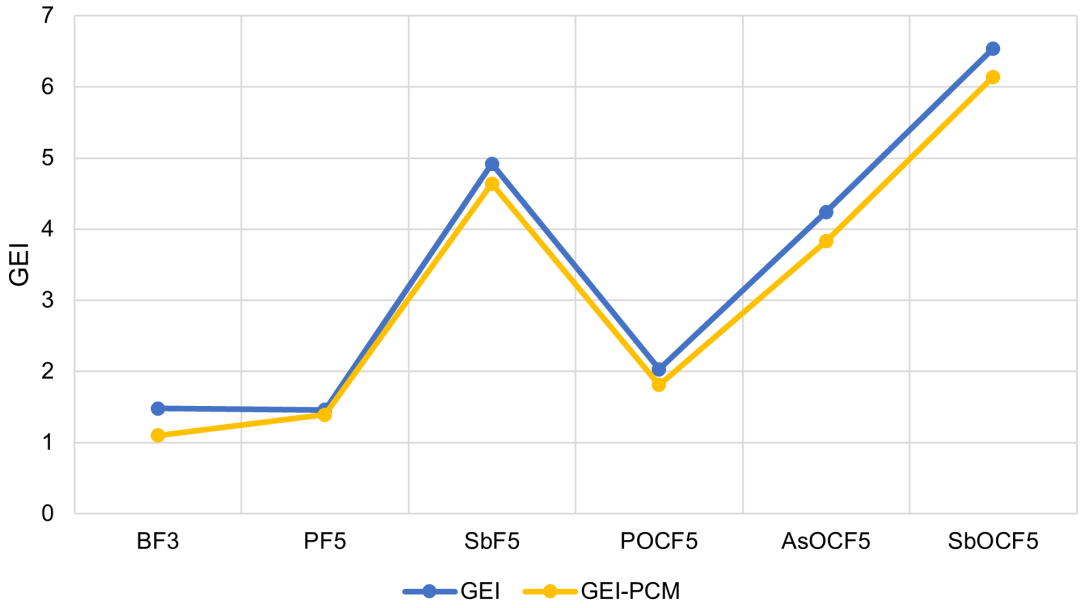

Figure E.10: Calculated GEI (B3LYP-def2tzvp; OCF = OC_6F_5) of BF_3, PF_5, SbF_5, $P(OC_6F_5)_5$, $As(OC_6F_5)_5$, and $Sb(OC_6F_5)_5$ as free molecules and with a PCM solvent model.

Compound	**Gas-phase**	**PCM**	**COSMO**	**GEI**
BF_3	337	335	331	1.48
PF_5	393	369	362	1.46
SbF_5	489	430	413	4.92
$P(OC_6F_5)_5$	497	367	354	2.03
$As(OC_6F_5)_5$	509	380	369	4.24
$Sb(OC_6F_5)_5$	509	380	364	6.54
$Al(N(C_6F_5)_2)_3$	561	431	411	NA

Table E.1: Calculated FIA's (kJ mol^{-1}; BP96-SV(P)) of BF_3, PF_5, SbF_5, $P(OC_6F_5)_5$, $As(OC_6F_5)_5$, $Sb(OC_6F_5)_5$, and $Al(N(C_6F_5)_2)_3$ as free molecules, with a PCM solvent model and with a COSMO solvent model, and the corresponding GEI values (without solvation effects).

Appendix F

Copyright Agreement Letters

JOHN WILEY AND SONS LICENSE TERMS AND CONDITIONS

May 18, 2021

This Agreement between Katherine Marczenko ("You") and John Wiley and Sons ("John Wiley and Sons") consists of your license details and the terms and conditions provided by John Wiley and Sons and Copyright Clearance Center.

License Number	5056000537143
License date	Apr 25, 2021
Licensed Content Publisher	John Wiley and Sons
Licensed Content Publication	Chemistry - A European Journal
Licensed Content Title	Periodicity in Structure, Bonding, and Reactivity for p-Block Complexes of a Geometry Constraining Triamide Ligand
Licensed Content Author	Katherine M. Marczenko, Joseph A. Zurakowski, Marcus B. Kindervater, et al
Licensed Content Date	Nov 26, 2019
Licensed Content Volume	25
Licensed Content Issue	71
Licensed Content Pages	11
Type of Use	Dissertation/Thesis
Requestor type	Author of this Wiley article
Format	Print and electronic
Portion	Full article
Will you be translating?	Yes, including English rights
Number of languages	1
Title	Thesis
Institution name	Dalhousie University
Expected presentation date	Jul 2021
Specific Languages	English
Requestor Location	Katherine Marczenko 5691 Rhuland St Apt 7 Halifax, NS B3J1B5 Canada Attn: Katherine Marczenko
Publisher Tax ID	EU826007151
Total	**0.00 CAD**
Terms and Conditions	

TERMS AND CONDITIONS

This copyrighted material is owned by or exclusively licensed to John Wiley & Sons, Inc. or one of its group companies (each a"Wiley Company") or handled on behalf of a society with which a Wiley Company has exclusive publishing rights in relation to a particular work (collectively "WILEY"). By clicking "accept" in connection with completing this licensing transaction, you agree that the following terms and conditions apply to this transaction (along with the billing and payment terms and conditions established by the Copyright Clearance Center Inc., ("CCC's Billing and Payment terms and conditions"), at the time that you opened your RightsLink account (these are available at any time at http://myaccount.copyright.com).

Terms and Conditions

- The materials you have requested permission to reproduce or reuse (the "Wiley Materials") are protected by copyright.

- You are hereby granted a personal, non-exclusive, non-sub licensable (on a stand-alone basis), non-transferable, worldwide, limited license to reproduce the Wiley Materials for the purpose specified in the licensing process. This license, **and any CONTENT (PDF or image file) purchased as part of your order,** is for a one-time use only and limited to any maximum distribution number specified in the license. The first instance of republication or reuse granted by this license must be completed within two years of the date of the grant of this license (although copies prepared before the end date may be distributed thereafter). The Wiley Materials shall not be used in any other manner or for any other purpose, beyond what is granted in the license. Permission is granted subject to an appropriate acknowledgement given to the author, title of the material/book/journal and the publisher. You shall also duplicate the copyright notice that appears in the Wiley publication in your use of the Wiley Material. Permission is also granted on the understanding that nowhere in the text is a previously published source acknowledged for all or part of this Wiley Material. Any third party content is expressly excluded from this permission.

- With respect to the Wiley Materials, all rights are reserved. Except as expressly granted by the terms of the license, no part of the Wiley Materials may be copied, modified, adapted (except for minor reformatting required by the new Publication), translated, reproduced, transferred or distributed, in any form or by any means, and no derivative works may be made based on the Wiley Materials without the prior permission of the respective copyright owner.**For STM Signatory Publishers clearing permission under the terms of the STM Permissions Guidelines only, the terms of the license are extended to include subsequent editions and for editions in other languages, provided such editions are for the work as a whole in situ and does not involve the separate exploitation of the permitted figures or extracts,** You may not alter, remove or suppress in any manner any copyright, trademark or other notices displayed by the Wiley Materials. You may not license, rent, sell, loan, lease, pledge, offer as security, transfer or assign the Wiley Materials on a stand-alone basis, or any of the rights granted to you hereunder to any other person.

- The Wiley Materials and all of the intellectual property rights therein shall at all times remain the exclusive property of John Wiley & Sons Inc, the Wiley Companies, or their respective licensors, and your interest therein is only that of having possession of and the right to reproduce the Wiley Materials pursuant to Section 2 herein during the continuance of this Agreement. You agree that you own no right, title or interest in or to the Wiley Materials or any of the intellectual property rights therein. You shall have no rights hereunder other than the license as provided for above in Section 2. No right, license or interest to any trademark, trade name, service mark or other branding ("Marks") of WILEY or its licensors is granted hereunder, and you agree that you shall not assert any such right, license or interest with respect thereto

- NEITHER WILEY NOR ITS LICENSORS MAKES ANY WARRANTY OR REPRESENTATION OF ANY KIND TO YOU OR ANY THIRD PARTY, EXPRESS, IMPLIED OR STATUTORY, WITH RESPECT TO THE MATERIALS OR THE ACCURACY OF ANY INFORMATION CONTAINED IN THE MATERIALS, INCLUDING, WITHOUT LIMITATION, ANY IMPLIED WARRANTY OF MERCHANTABILITY, ACCURACY, SATISFACTORY QUALITY, FITNESS FOR A PARTICULAR PURPOSE, USABILITY, INTEGRATION OR NON-INFRINGEMENT AND ALL SUCH WARRANTIES ARE HEREBY EXCLUDED BY WILEY AND ITS LICENSORS AND WAIVED BY YOU.

- WILEY shall have the right to terminate this Agreement immediately upon breach of this Agreement by you.

- You shall indemnify, defend and hold harmless WILEY, its Licensors and their respective directors, officers, agents and employees, from and against any actual or threatened claims, demands, causes of action or proceedings arising from any breach of this Agreement by you.

- IN NO EVENT SHALL WILEY OR ITS LICENSORS BE LIABLE TO YOU OR ANY OTHER PARTY OR ANY OTHER PERSON OR ENTITY FOR ANY SPECIAL, CONSEQUENTIAL, INCIDENTAL, INDIRECT, EXEMPLARY OR PUNITIVE DAMAGES, HOWEVER CAUSED, ARISING OUT OF OR IN CONNECTION WITH THE DOWNLOADING, PROVISIONING, VIEWING OR USE OF THE MATERIALS REGARDLESS OF THE FORM OF ACTION, WHETHER FOR BREACH OF CONTRACT, BREACH OF WARRANTY, TORT, NEGLIGENCE, INFRINGEMENT OR OTHERWISE (INCLUDING, WITHOUT LIMITATION, DAMAGES BASED ON LOSS OF PROFITS, DATA, FILES, USE, BUSINESS OPPORTUNITY OR CLAIMS OF THIRD PARTIES), AND WHETHER OR NOT THE PARTY HAS BEEN ADVISED OF THE POSSIBILITY OF SUCH DAMAGES. THIS LIMITATION SHALL APPLY NOTWITHSTANDING ANY FAILURE OF ESSENTIAL PURPOSE OF ANY LIMITED REMEDY PROVIDED HEREIN.

- Should any provision of this Agreement be held by a court of competent jurisdiction to be illegal, invalid, or unenforceable, that provision shall be deemed amended to achieve as nearly as possible the same economic effect as the original provision, and the legality, validity and enforceability of the remaining provisions of this Agreement shall not be affected or impaired thereby.

- The failure of either party to enforce any term or condition of this Agreement shall not constitute a waiver of either party's right to enforce each and every term and condition of this Agreement. No breach under this agreement shall be deemed waived or excused by either party unless such waiver or consent is in writing signed by the party granting such waiver or consent. The waiver by or consent of a party to a breach of any provision of this Agreement shall not operate or be construed as a waiver of or consent to any other or subsequent breach by such other party.

- This Agreement may not be assigned (including by operation of law or otherwise) by you without WILEY's prior written consent.

- Any fee required for this permission shall be non-refundable after thirty (30) days from receipt by the CCC.

- These terms and conditions together with CCC's Billing and Payment terms and conditions (which are incorporated herein) form the entire agreement between you and WILEY concerning this licensing transaction and (in the absence of fraud) supersedes all prior agreements and representations of the parties, oral or written. This Agreement may not be amended except in writing signed by both parties. This Agreement shall be binding upon and inure to the benefit of the parties' successors, legal representatives, and authorized assigns.

- In the event of any conflict between your obligations established by these terms and conditions and those established by CCC's Billing and Payment terms and conditions, these terms and conditions shall prevail.

- WILEY expressly reserves all rights not specifically granted in the combination of (i) the license details provided by you and accepted in the course of this licensing transaction, (ii) these terms and conditions and (iii) CCC's Billing and Payment terms and conditions.

- This Agreement will be void if the Type of Use, Format, Circulation, or Requestor Type was misrepresented during the licensing process.

- This Agreement shall be governed by and construed in accordance with the laws of the State of New York, USA, without regards to such state's conflict of law rules. Any legal action, suit or proceeding arising out of or relating to these Terms and Conditions or the breach thereof shall be instituted in a court of competent jurisdiction in New York County in the State of New York in the United States of America and each party hereby consents and submits to the personal jurisdiction of such court, waives any objection to venue in such court and consents to service of process by registered or certified mail, return receipt requested, at the last known address of such party.

WILEY OPEN ACCESS TERMS AND CONDITIONS

Wiley Publishes Open Access Articles in fully Open Access Journals and in Subscription journals offering Online Open. Although most of the fully Open Access journals publish open access articles under the terms of the Creative Commons Attribution (CC BY) License only, the subscription journals and a few of the Open Access Journals offer a choice of Creative Commons Licenses. The license type is clearly identified on the article.

The Creative Commons Attribution License

The Creative Commons Attribution License (CC-BY) allows users to copy, distribute and transmit an article, adapt the article and make commercial use of the article. The CC-BY license permits commercial and non-

Creative Commons Attribution Non-Commercial License

The Creative Commons Attribution Non-Commercial (CC-BY-NC)License permits use, distribution and reproduction in any medium, provided the original work is properly cited and is not used for commercial purposes.(see below)

Creative Commons Attribution-Non-Commercial-NoDerivs License

The Creative Commons Attribution Non-Commercial-NoDerivs License (CC-BY-NC-ND) permits use, distribution and reproduction in any medium, provided the original work is properly cited, is not used for commercial purposes and no modifications or adaptations are made. (see below)

Use by commercial "for-profit" organizations

Use of Wiley Open Access articles for commercial, promotional, or marketing purposes requires further explicit permission from Wiley and will be subject to a fee.

Further details can be found on Wiley Online Library http://olabout.wiley.com/WileyCDA/Section/id-410895.html

Other Terms and Conditions:

High Lewis Acidity at Planar, Trivalent, and Neutral Bismuth Centers

Author: Katherine M. Marczenko, Samantha Jee, Saurabh S. Chitnis

Publication: Organometallics

Publisher: American Chemical Society

Date: Dec 1, 2020

PERMISSION/LICENSE IS GRANTED FOR YOUR ORDER AT NO CHARGE

This type of permission/license, instead of the standard Terms & Conditions, is sent to you because no fee is being charged for your order. Please note the following:

- Permission is granted for your request in both print and electronic formats, and translations.
- If figures and/or tables were requested, they may be adapted or used in part.
- Please print this page for your records and send a copy of it to your publisher/graduate school.
- Appropriate credit for the requested material should be given as follows: "Reprinted (adapted) with permission from (COMPLETE REFERENCE CITATION). Copyright (YEAR) American Chemical Society." Insert appropriate information in place of the capitalized words.
- One-time permission is granted only for the use specified in your request. No additional uses are granted (such as derivative works or other editions). For any other uses, please submit a new request.

BACK CLOSE WINDOW

JOHN WILEY AND SONS LICENSE TERMS AND CONDITIONS

May 18, 2021

This Agreement between Katherine Marczenko ("You") and John Wiley and Sons ("John Wiley and Sons") consists of your license details and the terms and conditions provided by John Wiley and Sons and Copyright Clearance Center.

License Number	5071930873829
License date	May 18, 2021
Licensed Content Publisher	John Wiley and Sons
Licensed Content Publication	Angewandte Chemie International Edition
Licensed Content Title	Hydrostibination
Licensed Content Author	Saurabh S. Chitnis, Joshua W. M. MacMillan, Karlee L. Bamford, et al
Licensed Content Date	Oct 24, 2019
Licensed Content Volume	58
Licensed Content Issue	50
Licensed Content Pages	6
Type of Use	Dissertation/Thesis
Requestor type	Author of this Wiley article
Format	Print and electronic
Portion	Full article
Will you be translating?	No
Title	Thesis
Institution name	Dalhousie University
Expected presentation date	Jul 2021
Requestor Location	Katherine Marczenko 5691 Rhuland St Apt 7 Halifax, NS B3J1B5 Canada Attn: Katherine Marczenko
Publisher Tax ID	EU826007151
Total	**0.00 CAD**
Terms and Conditions	

TERMS AND CONDITIONS

This copyrighted material is owned by or exclusively licensed to John Wiley & Sons, Inc. or one of its group companies (each a"Wiley Company") or handled on behalf of a society with which a Wiley Company has exclusive publishing rights in relation to a particular work (collectively "WILEY"). By clicking "accept" in connection with completing this licensing transaction, you agree that the following terms and conditions apply to this transaction (along with the billing and payment terms and conditions established by the Copyright Clearance Center Inc., ("CCC's Billing and Payment terms and conditions"), at the time that you opened your RightsLink account (these are available at any time at http://myaccount.copyright.com).

Terms and Conditions

- The materials you have requested permission to reproduce or reuse (the "Wiley Materials") are protected by copyright.
- You are hereby granted a personal, non-exclusive, non-sub licensable (on a stand-alone basis), non-transferable, worldwide, limited license to reproduce the Wiley Materials for the purpose specified in the licensing process. This license, **and any CONTENT (PDF or image file) purchased as part of your order,** is for a one-time use only and limited to any maximum

distribution number specified in the license. The first instance of republication or reuse granted by this license must be completed within two years of the date of the grant of this license (although copies prepared before the end date may be distributed thereafter). The Wiley Materials shall not be used in any other manner or for any other purpose, beyond what is granted in the license. Permission is granted subject to an appropriate acknowledgement given to the author, title of the material/book/journal and the publisher. You shall also duplicate the copyright notice that appears in the Wiley publication in your use of the Wiley Material. Permission is also granted on the understanding that nowhere in the text is a previously published source acknowledged for all or part of this Wiley Material. Any third party content is expressly excluded from this permission.

- With respect to the Wiley Materials, all rights are reserved. Except as expressly granted by the terms of the license, no part of the Wiley Materials may be copied, modified, adapted (except for minor reformatting required by the new Publication), translated, reproduced, transferred or distributed, in any form or by any means, and no derivative works may be made based on the Wiley Materials without the prior permission of the respective copyright owner.**For STM Signatory Publishers clearing permission under the terms of the STM Permissions Guidelines only, the terms of the license are extended to include subsequent editions and for editions in other languages, provided such editions are for the work as a whole in situ and does not involve the separate exploitation of the permitted figures or extracts,** You may not alter, remove or suppress in any manner any copyright, trademark or other notices displayed by the Wiley Materials. You may not license, rent, sell, loan, lease, pledge, offer as security, transfer or assign the Wiley Materials on a stand-alone basis, or any of the rights granted to you hereunder to any other person.

- The Wiley Materials and all of the intellectual property rights therein shall at all times remain the exclusive property of John Wiley & Sons Inc, the Wiley Companies, or their respective licensors, and your interest therein is only that of having possession of and the right to reproduce the Wiley Materials pursuant to Section 2 herein during the continuance of this Agreement. You agree that you own no right, title or interest in or to the Wiley Materials or any of the intellectual property rights therein. You shall have no rights hereunder other than the license as provided for above in Section 2. No right, license or interest to any trademark, trade name, service mark or other branding ("Marks") of WILEY or its licensors is granted hereunder, and you agree that you shall not assert any such right, license or interest with respect thereto

- NEITHER WILEY NOR ITS LICENSORS MAKES ANY WARRANTY OR REPRESENTATION OF ANY KIND TO YOU OR ANY THIRD PARTY, EXPRESS, IMPLIED OR STATUTORY, WITH RESPECT TO THE MATERIALS OR THE ACCURACY OF ANY INFORMATION CONTAINED IN THE MATERIALS, INCLUDING, WITHOUT LIMITATION, ANY IMPLIED WARRANTY OF MERCHANTABILITY, ACCURACY, SATISFACTORY QUALITY, FITNESS FOR A PARTICULAR PURPOSE, USABILITY, INTEGRATION OR NON-INFRINGEMENT AND ALL SUCH WARRANTIES ARE HEREBY EXCLUDED BY WILEY AND ITS LICENSORS AND WAIVED BY YOU.

- WILEY shall have the right to terminate this Agreement immediately upon breach of this Agreement by you.

- You shall indemnify, defend and hold harmless WILEY, its Licensors and their respective directors, officers, agents and employees, from and against any actual or threatened claims, demands, causes of action or proceedings arising from any breach of this Agreement by you.

- IN NO EVENT SHALL WILEY OR ITS LICENSORS BE LIABLE TO YOU OR ANY OTHER PARTY OR ANY OTHER PERSON OR ENTITY FOR ANY SPECIAL, CONSEQUENTIAL, INCIDENTAL, INDIRECT, EXEMPLARY OR PUNITIVE DAMAGES, HOWEVER CAUSED, ARISING OUT OF OR IN CONNECTION WITH THE DOWNLOADING, PROVISIONING, VIEWING OR USE OF THE MATERIALS REGARDLESS OF THE FORM OF ACTION, WHETHER FOR BREACH OF CONTRACT, BREACH OF WARRANTY, TORT, NEGLIGENCE, INFRINGEMENT OR OTHERWISE (INCLUDING, WITHOUT LIMITATION, DAMAGES BASED ON LOSS OF PROFITS, DATA, FILES, USE, BUSINESS OPPORTUNITY OR CLAIMS OF THIRD PARTIES), AND WHETHER OR NOT THE PARTY HAS BEEN ADVISED OF THE POSSIBILITY OF SUCH DAMAGES. THIS LIMITATION SHALL APPLY NOTWITHSTANDING ANY FAILURE OF ESSENTIAL PURPOSE OF ANY LIMITED REMEDY PROVIDED HEREIN.

- Should any provision of this Agreement be held by a court of competent jurisdiction to be illegal, invalid, or unenforceable, that provision shall be deemed amended to achieve as nearly as possible the same economic effect as the original provision, and the legality, validity and enforceability of the remaining provisions of this Agreement shall not be affected or impaired thereby.

- The failure of either party to enforce any term or condition of this Agreement shall not constitute a waiver of either party's right to enforce each and every term and condition of this Agreement. No breach under this agreement shall be deemed waived or excused by either party unless such waiver or consent is in writing signed by the party granting such waiver or consent. The waiver by or consent of a party to a breach of any provision of this Agreement shall not operate or be construed as a waiver

of or consent to any other or subsequent breach by such other party.

- This Agreement may not be assigned (including by operation of law or otherwise) by you without WILEY's prior written consent.
- Any fee required for this permission shall be non-refundable after thirty (30) days from receipt by the CCC.
- These terms and conditions together with CCC's Billing and Payment terms and conditions (which are incorporated herein) form the entire agreement between you and WILEY concerning this licensing transaction and (in the absence of fraud) supersedes all prior agreements and representations of the parties, oral or written. This Agreement may not be amended except in writing signed by both parties. This Agreement shall be binding upon and inure to the benefit of the parties' successors, legal representatives, and authorized assigns.
- In the event of any conflict between your obligations established by these terms and conditions and those established by CCC's Billing and Payment terms and conditions, these terms and conditions shall prevail.
- WILEY expressly reserves all rights not specifically granted in the combination of (i) the license details provided by you and accepted in the course of this licensing transaction, (ii) these terms and conditions and (iii) CCC's Billing and Payment terms and conditions.
- This Agreement will be void if the Type of Use, Format, Circulation, or Requestor Type was misrepresented during the licensing process.
- This Agreement shall be governed by and construed in accordance with the laws of the State of New York, USA, without regards to such state's conflict of law rules. Any legal action, suit or proceeding arising out of or relating to these Terms and Conditions or the breach thereof shall be instituted in a court of competent jurisdiction in New York County in the State of New York in the United States of America and each party hereby consents and submits to the personal jurisdiction of such court, waives any objection to venue in such court and consents to service of process by registered or certified mail, return receipt requested, at the last known address of such party.

WILEY OPEN ACCESS TERMS AND CONDITIONS

Wiley Publishes Open Access Articles in fully Open Access Journals and in Subscription journals offering Online Open. Although most of the fully Open Access journals publish open access articles under the terms of the Creative Commons Attribution (CC BY) License only, the subscription journals and a few of the Open Access Journals offer a choice of Creative Commons Licenses. The license type is clearly identified on the article.

The Creative Commons Attribution License

The Creative Commons Attribution License (CC-BY) allows users to copy, distribute and transmit an article, adapt the article and make commercial use of the article. The CC-BY license permits commercial and non-

Creative Commons Attribution Non-Commercial License

The Creative Commons Attribution Non-Commercial (CC-BY-NC)License permits use, distribution and reproduction in any medium, provided the original work is properly cited and is not used for commercial purposes.(see below)

Creative Commons Attribution-Non-Commercial-NoDerivs License

The Creative Commons Attribution Non-Commercial-NoDerivs License (CC-BY-NC-ND) permits use, distribution and reproduction in any medium, provided the original work is properly cited, is not used for commercial purposes and no modifications or adaptations are made. (see below)

Use by commercial "for-profit" organizations

Use of Wiley Open Access articles for commercial, promotional, or marketing purposes requires further explicit permission from Wiley and will be subject to a fee.

Further details can be found on Wiley Online Library http://olabout.wiley.com/WileyCDA/Section/id-410895.html

Other Terms and Conditions:

v1.10 Last updated September 2015

Questions? customercare@copyright.com or +1-855-239-3415 (toll free in the US) or +1-978-646-2777.

JOHN WILEY AND SONS LICENSE TERMS AND CONDITIONS

May 18, 2021

This Agreement between Katherine Marczenko ("You") and John Wiley and Sons ("John Wiley and Sons") consists of your license details and the terms and conditions provided by John Wiley and Sons and Copyright Clearance Center.

License Number	5056000715276
License date	Apr 25, 2021
Licensed Content Publisher	John Wiley and Sons
Licensed Content Publication	Chemistry - A European Journal
Licensed Content Title	Hydrostibination of Alkynes: A Radical Mechanism**
Licensed Content Author	Saurabh S. Chitnis, Erin R. Johnson, Katherine M. Marczenko, et al
Licensed Content Date	Nov 11, 2020
Licensed Content Volume	26
Licensed Content Issue	71
Licensed Content Pages	9
Type of Use	Dissertation/Thesis
Requestor type	Author of this Wiley article
Format	Print and electronic
Portion	Full article
Will you be translating?	Yes, including English rights
Number of languages	1
Title	Thesis
Institution name	Dalhousie University
Expected presentation date	Jul 2021
Specific Languages	English
Requestor Location	Katherine Marczenko 5691 Rhuland St Apt 7 Halifax, NS B3J1B5 Canada Attn: Katherine Marczenko
Publisher Tax ID	EU826007151
Total	**0.00 USD**
Terms and Conditions	

TERMS AND CONDITIONS

This copyrighted material is owned by or exclusively licensed to John Wiley & Sons, Inc. or one of its group companies (each a"Wiley Company") or handled on behalf of a society with which a Wiley Company has exclusive publishing rights in relation to a particular work (collectively "WILEY"). By clicking "accept" in connection with completing this licensing transaction, you agree that the following terms and conditions apply to this transaction (along with the billing and payment terms and conditions established by the Copyright Clearance Center Inc., ("CCC's Billing and Payment terms and conditions"), at the time that you opened your RightsLink account (these are available at any time at http://myaccount.copyright.com).

Terms and Conditions

- The materials you have requested permission to reproduce or reuse (the "Wiley Materials") are protected by copyright.

- You are hereby granted a personal, non-exclusive, non-sub licensable (on a stand-alone basis), non-transferable, worldwide, limited license to reproduce the Wiley Materials for the purpose specified in the licensing process. This license, **and any CONTENT (PDF or image file) purchased as part of your order,** is for a one-time use only and limited to any maximum distribution number specified in the license. The first instance of republication or reuse granted by this license must be completed within two years of the date of the grant of this license (although copies prepared before the end date may be distributed thereafter). The Wiley Materials shall not be used in any other manner or for any other purpose, beyond what is granted in the license. Permission is granted subject to an appropriate acknowledgement given to the author, title of the material/book/journal and the publisher. You shall also duplicate the copyright notice that appears in the Wiley publication in your use of the Wiley Material. Permission is also granted on the understanding that nowhere in the text is a previously published source acknowledged for all or part of this Wiley Material. Any third party content is expressly excluded from this permission.

- With respect to the Wiley Materials, all rights are reserved. Except as expressly granted by the terms of the license, no part of the Wiley Materials may be copied, modified, adapted (except for minor reformatting required by the new Publication), translated, reproduced, transferred or distributed, in any form or by any means, and no derivative works may be made based on the Wiley Materials without the prior permission of the respective copyright owner.**For STM Signatory Publishers clearing permission under the terms of the STM Permissions Guidelines only, the terms of the license are extended to include subsequent editions and for editions in other languages, provided such editions are for the work as a whole in situ and does not involve the separate exploitation of the permitted figures or extracts,** You may not alter, remove or suppress in any manner any copyright, trademark or other notices displayed by the Wiley Materials. You may not license, rent, sell, loan, lease, pledge, offer as security, transfer or assign the Wiley Materials on a stand-alone basis, or any of the rights granted to you hereunder to any other person.

- The Wiley Materials and all of the intellectual property rights therein shall at all times remain the exclusive property of John Wiley & Sons Inc, the Wiley Companies, or their respective licensors, and your interest therein is only that of having possession of and the right to reproduce the Wiley Materials pursuant to Section 2 herein during the continuance of this Agreement. You agree that you own no right, title or interest in or to the Wiley Materials or any of the intellectual property rights therein. You shall have no rights hereunder other than the license as provided for above in Section 2. No right, license or interest to any trademark, trade name, service mark or other branding ("Marks") of WILEY or its licensors is granted hereunder, and you agree that you shall not assert any such right, license or interest with respect thereto

- NEITHER WILEY NOR ITS LICENSORS MAKES ANY WARRANTY OR REPRESENTATION OF ANY KIND TO YOU OR ANY THIRD PARTY, EXPRESS, IMPLIED OR STATUTORY, WITH RESPECT TO THE MATERIALS OR THE ACCURACY OF ANY INFORMATION CONTAINED IN THE MATERIALS, INCLUDING, WITHOUT LIMITATION, ANY IMPLIED WARRANTY OF MERCHANTABILITY, ACCURACY, SATISFACTORY QUALITY, FITNESS FOR A PARTICULAR PURPOSE, USABILITY, INTEGRATION OR NON-INFRINGEMENT AND ALL SUCH WARRANTIES ARE HEREBY EXCLUDED BY WILEY AND ITS LICENSORS AND WAIVED BY YOU.

- WILEY shall have the right to terminate this Agreement immediately upon breach of this Agreement by you.

- You shall indemnify, defend and hold harmless WILEY, its Licensors and their respective directors, officers, agents and employees, from and against any actual or threatened claims, demands, causes of action or proceedings arising from any breach of this Agreement by you.

- IN NO EVENT SHALL WILEY OR ITS LICENSORS BE LIABLE TO YOU OR ANY OTHER PARTY OR ANY OTHER PERSON OR ENTITY FOR ANY SPECIAL, CONSEQUENTIAL, INCIDENTAL, INDIRECT, EXEMPLARY OR PUNITIVE DAMAGES, HOWEVER CAUSED, ARISING OUT OF OR IN CONNECTION WITH THE DOWNLOADING, PROVISIONING, VIEWING OR USE OF THE MATERIALS REGARDLESS OF THE FORM OF ACTION, WHETHER FOR BREACH OF CONTRACT, BREACH OF WARRANTY, TORT, NEGLIGENCE, INFRINGEMENT OR OTHERWISE (INCLUDING, WITHOUT LIMITATION, DAMAGES BASED ON LOSS OF PROFITS, DATA, FILES, USE, BUSINESS OPPORTUNITY OR CLAIMS OF THIRD PARTIES), AND WHETHER OR NOT THE PARTY HAS BEEN ADVISED OF THE POSSIBILITY OF SUCH DAMAGES. THIS LIMITATION SHALL APPLY NOTWITHSTANDING ANY FAILURE OF ESSENTIAL PURPOSE OF ANY LIMITED REMEDY PROVIDED HEREIN.

- Should any provision of this Agreement be held by a court of competent jurisdiction to be illegal, invalid, or unenforceable, that provision shall be deemed amended to achieve as nearly as possible the same economic effect as the original provision, and the legality, validity and enforceability of the remaining provisions of this Agreement shall not be affected or impaired thereby.

- The failure of either party to enforce any term or condition of this Agreement shall not constitute a waiver of either party's right to enforce each and every term and condition of this Agreement. No breach under this agreement shall be deemed waived or

excused by either party unless such waiver or consent is in writing signed by the party granting such waiver or consent. The waiver by or consent of a party to a breach of any provision of this Agreement shall not operate or be construed as a waiver of or consent to any other or subsequent breach by such other party.

- This Agreement may not be assigned (including by operation of law or otherwise) by you without WILEY's prior written consent.
- Any fee required for this permission shall be non-refundable after thirty (30) days from receipt by the CCC.
- These terms and conditions together with CCC's Billing and Payment terms and conditions (which are incorporated herein) form the entire agreement between you and WILEY concerning this licensing transaction and (in the absence of fraud) supersedes all prior agreements and representations of the parties, oral or written. This Agreement may not be amended except in writing signed by both parties. This Agreement shall be binding upon and inure to the benefit of the parties' successors, legal representatives, and authorized assigns.
- In the event of any conflict between your obligations established by these terms and conditions and those established by CCC's Billing and Payment terms and conditions, these terms and conditions shall prevail.
- WILEY expressly reserves all rights not specifically granted in the combination of (i) the license details provided by you and accepted in the course of this licensing transaction, (ii) these terms and conditions and (iii) CCC's Billing and Payment terms and conditions.
- This Agreement will be void if the Type of Use, Format, Circulation, or Requestor Type was misrepresented during the licensing process.
- This Agreement shall be governed by and construed in accordance with the laws of the State of New York, USA, without regards to such state's conflict of law rules. Any legal action, suit or proceeding arising out of or relating to these Terms and Conditions or the breach thereof shall be instituted in a court of competent jurisdiction in New York County in the State of New York in the United States of America and each party hereby consents and submits to the personal jurisdiction of such court, waives any objection to venue in such court and consents to service of process by registered or certified mail, return receipt requested, at the last known address of such party.

WILEY OPEN ACCESS TERMS AND CONDITIONS

Wiley Publishes Open Access Articles in fully Open Access Journals and in Subscription journals offering Online Open. Although most of the fully Open Access journals publish open access articles under the terms of the Creative Commons Attribution (CC BY) License only, the subscription journals and a few of the Open Access Journals offer a choice of Creative Commons Licenses. The license type is clearly identified on the article.

The Creative Commons Attribution License

The Creative Commons Attribution License (CC-BY) allows users to copy, distribute and transmit an article, adapt the article and make commercial use of the article. The CC-BY license permits commercial and non-

Creative Commons Attribution Non-Commercial License

The Creative Commons Attribution Non-Commercial (CC-BY-NC)License permits use, distribution and reproduction in any medium, provided the original work is properly cited and is not used for commercial purposes.(see below)

Creative Commons Attribution-Non-Commercial-NoDerivs License

The Creative Commons Attribution Non-Commercial-NoDerivs License (CC-BY-NC-ND) permits use, distribution and reproduction in any medium, provided the original work is properly cited, is not used for commercial purposes and no modifications or adaptations are made. (see below)

Use by commercial "for-profit" organizations

Use of Wiley Open Access articles for commercial, promotional, or marketing purposes requires further explicit permission from Wiley and will be subject to a fee.

Further details can be found on Wiley Online Library http://olabout.wiley.com/WileyCDA/Section/id-410895.html

Other Terms and Conditions:

v1.10 Last updated September 2015

JOHN WILEY AND SONS LICENSE TERMS AND CONDITIONS

May 18, 2021

This Agreement between Katherine Marczenko ("You") and John Wiley and Sons ("John Wiley and Sons") consists of your license details and the terms and conditions provided by John Wiley and Sons and Copyright Clearance Center.

License Number	5056000647043
License date	Apr 25, 2021
Licensed Content Publisher	John Wiley and Sons
Licensed Content Publication	Chemistry - A European Journal
Licensed Content Title	Synthesis of a Perfluorinated Phenoxyphosphorane and Conversion to Its Hexacoordinate Anions
Licensed Content Author	Saurabh S. Chitnis, Chloe-Louise Johnson, Katherine M. Marczenko
Licensed Content Date	Jun 6, 2019
Licensed Content Volume	25
Licensed Content Issue	37
Licensed Content Pages	10
Type of Use	Dissertation/Thesis
Requestor type	Author of this Wiley article
Format	Print and electronic
Portion	Full article
Will you be translating?	Yes, including English rights
Number of languages	1
Title	Thesis
Institution name	Dalhousie University
Expected presentation date	Jul 2021
Specific Languages	English
Requestor Location	Katherine Marczenko 5691 Rhuland St Apt 7 Halifax, NS B3J1B5 Canada Attn: Katherine Marczenko
Publisher Tax ID	EU826007151
Total	**0.00 USD**
Terms and Conditions	

TERMS AND CONDITIONS

This copyrighted material is owned by or exclusively licensed to John Wiley & Sons, Inc. or one of its group companies (each a"Wiley Company") or handled on behalf of a society with which a Wiley Company has exclusive publishing rights in relation to a particular work (collectively "WILEY"). By clicking "accept" in connection with completing this licensing transaction, you agree that the following terms and conditions apply to this transaction (along with the billing and payment terms and conditions established by the Copyright Clearance Center Inc., ("CCC's Billing and Payment terms and conditions"), at the time that you opened your RightsLink account (these are available at any time at http://myaccount.copyright.com).

Terms and Conditions

- The materials you have requested permission to reproduce or reuse (the "Wiley Materials") are protected by copyright.

- You are hereby granted a personal, non-exclusive, non-sub licensable (on a stand-alone basis), non-transferable, worldwide, limited license to reproduce the Wiley Materials for the purpose specified in the licensing process. This license, **and any CONTENT (PDF or image file) purchased as part of your order,** is for a one-time use only and limited to any maximum distribution number specified in the license. The first instance of republication or reuse granted by this license must be completed within two years of the date of the grant of this license (although copies prepared before the end date may be distributed thereafter). The Wiley Materials shall not be used in any other manner or for any other purpose, beyond what is granted in the license. Permission is granted subject to an appropriate acknowledgement given to the author, title of the material/book/journal and the publisher. You shall also duplicate the copyright notice that appears in the Wiley publication in your use of the Wiley Material. Permission is also granted on the understanding that nowhere in the text is a previously published source acknowledged for all or part of this Wiley Material. Any third party content is expressly excluded from this permission.

- With respect to the Wiley Materials, all rights are reserved. Except as expressly granted by the terms of the license, no part of the Wiley Materials may be copied, modified, adapted (except for minor reformatting required by the new Publication), translated, reproduced, transferred or distributed, in any form or by any means, and no derivative works may be made based on the Wiley Materials without the prior permission of the respective copyright owner.**For STM Signatory Publishers clearing permission under the terms of the STM Permissions Guidelines only, the terms of the license are extended to include subsequent editions and for editions in other languages, provided such editions are for the work as a whole in situ and does not involve the separate exploitation of the permitted figures or extracts,** You may not alter, remove or suppress in any manner any copyright, trademark or other notices displayed by the Wiley Materials. You may not license, rent, sell, loan, lease, pledge, offer as security, transfer or assign the Wiley Materials on a stand-alone basis, or any of the rights granted to you hereunder to any other person.

- The Wiley Materials and all of the intellectual property rights therein shall at all times remain the exclusive property of John Wiley & Sons Inc, the Wiley Companies, or their respective licensors, and your interest therein is only that of having possession of and the right to reproduce the Wiley Materials pursuant to Section 2 herein during the continuance of this Agreement. You agree that you own no right, title or interest in or to the Wiley Materials or any of the intellectual property rights therein. You shall have no rights hereunder other than the license as provided for above in Section 2. No right, license or interest to any trademark, trade name, service mark or other branding ("Marks") of WILEY or its licensors is granted hereunder, and you agree that you shall not assert any such right, license or interest with respect thereto

- NEITHER WILEY NOR ITS LICENSORS MAKES ANY WARRANTY OR REPRESENTATION OF ANY KIND TO YOU OR ANY THIRD PARTY, EXPRESS, IMPLIED OR STATUTORY, WITH RESPECT TO THE MATERIALS OR THE ACCURACY OF ANY INFORMATION CONTAINED IN THE MATERIALS, INCLUDING, WITHOUT LIMITATION, ANY IMPLIED WARRANTY OF MERCHANTABILITY, ACCURACY, SATISFACTORY QUALITY, FITNESS FOR A PARTICULAR PURPOSE, USABILITY, INTEGRATION OR NON-INFRINGEMENT AND ALL SUCH WARRANTIES ARE HEREBY EXCLUDED BY WILEY AND ITS LICENSORS AND WAIVED BY YOU.

- WILEY shall have the right to terminate this Agreement immediately upon breach of this Agreement by you.

- You shall indemnify, defend and hold harmless WILEY, its Licensors and their respective directors, officers, agents and employees, from and against any actual or threatened claims, demands, causes of action or proceedings arising from any breach of this Agreement by you.

- IN NO EVENT SHALL WILEY OR ITS LICENSORS BE LIABLE TO YOU OR ANY OTHER PARTY OR ANY OTHER PERSON OR ENTITY FOR ANY SPECIAL, CONSEQUENTIAL, INCIDENTAL, INDIRECT, EXEMPLARY OR PUNITIVE DAMAGES, HOWEVER CAUSED, ARISING OUT OF OR IN CONNECTION WITH THE DOWNLOADING, PROVISIONING, VIEWING OR USE OF THE MATERIALS REGARDLESS OF THE FORM OF ACTION, WHETHER FOR BREACH OF CONTRACT, BREACH OF WARRANTY, TORT, NEGLIGENCE, INFRINGEMENT OR OTHERWISE (INCLUDING, WITHOUT LIMITATION, DAMAGES BASED ON LOSS OF PROFITS, DATA, FILES, USE, BUSINESS OPPORTUNITY OR CLAIMS OF THIRD PARTIES), AND WHETHER OR NOT THE PARTY HAS BEEN ADVISED OF THE POSSIBILITY OF SUCH DAMAGES. THIS LIMITATION SHALL APPLY NOTWITHSTANDING ANY FAILURE OF ESSENTIAL PURPOSE OF ANY LIMITED REMEDY PROVIDED HEREIN.

- Should any provision of this Agreement be held by a court of competent jurisdiction to be illegal, invalid, or unenforceable, that provision shall be deemed amended to achieve as nearly as possible the same economic effect as the original provision, and the legality, validity and enforceability of the remaining provisions of this Agreement shall not be affected or impaired thereby.

- The failure of either party to enforce any term or condition of this Agreement shall not constitute a waiver of either party's right to enforce each and every term and condition of this Agreement. No breach under this agreement shall be deemed waived or

excused by either party unless such waiver or consent is in writing signed by the party granting such waiver or consent. The waiver by or consent of a party to a breach of any provision of this Agreement shall not operate or be construed as a waiver of or consent to any other or subsequent breach by such other party.

- This Agreement may not be assigned (including by operation of law or otherwise) by you without WILEY's prior written consent.
- Any fee required for this permission shall be non-refundable after thirty (30) days from receipt by the CCC.
- These terms and conditions together with CCC's Billing and Payment terms and conditions (which are incorporated herein) form the entire agreement between you and WILEY concerning this licensing transaction and (in the absence of fraud) supersedes all prior agreements and representations of the parties, oral or written. This Agreement may not be amended except in writing signed by both parties. This Agreement shall be binding upon and inure to the benefit of the parties' successors, legal representatives, and authorized assigns.
- In the event of any conflict between your obligations established by these terms and conditions and those established by CCC's Billing and Payment terms and conditions, these terms and conditions shall prevail.
- WILEY expressly reserves all rights not specifically granted in the combination of (i) the license details provided by you and accepted in the course of this licensing transaction, (ii) these terms and conditions and (iii) CCC's Billing and Payment terms and conditions.
- This Agreement will be void if the Type of Use, Format, Circulation, or Requestor Type was misrepresented during the licensing process.
- This Agreement shall be governed by and construed in accordance with the laws of the State of New York, USA, without regards to such state's conflict of law rules. Any legal action, suit or proceeding arising out of or relating to these Terms and Conditions or the breach thereof shall be instituted in a court of competent jurisdiction in New York County in the State of New York in the United States of America and each party hereby consents and submits to the personal jurisdiction of such court, waives any objection to venue in such court and consents to service of process by registered or certified mail, return receipt requested, at the last known address of such party.

WILEY OPEN ACCESS TERMS AND CONDITIONS

Wiley Publishes Open Access Articles in fully Open Access Journals and in Subscription journals offering Online Open. Although most of the fully Open Access journals publish open access articles under the terms of the Creative Commons Attribution (CC BY) License only, the subscription journals and a few of the Open Access Journals offer a choice of Creative Commons Licenses. The license type is clearly identified on the article.

The Creative Commons Attribution License

The Creative Commons Attribution License (CC-BY) allows users to copy, distribute and transmit an article, adapt the article and make commercial use of the article. The CC-BY license permits commercial and non-

Creative Commons Attribution Non-Commercial License

The Creative Commons Attribution Non-Commercial (CC-BY-NC)License permits use, distribution and reproduction in any medium, provided the original work is properly cited and is not used for commercial purposes.(see below)

Creative Commons Attribution-Non-Commercial-NoDerivs License

The Creative Commons Attribution Non-Commercial-NoDerivs License (CC-BY-NC-ND) permits use, distribution and reproduction in any medium, provided the original work is properly cited, is not used for commercial purposes and no modifications or adaptations are made. (see below)

Use by commercial "for-profit" organizations

Use of Wiley Open Access articles for commercial, promotional, or marketing purposes requires further explicit permission from Wiley and will be subject to a fee.

Further details can be found on Wiley Online Library http://olabout.wiley.com/WileyCDA/Section/id-410895.html

Other Terms and Conditions:

v1.10 Last updated September 2015

Bibliography

[1] Guy Bertrand. Introduction to main group chemistry. *Chemical Reviews*, 110(7):3851–3851, 2010.

[2] Lili Zhao, Sudip Pan, Nicole Holzmann, Peter Schwerdtfeger, and Gernot Frenking. Chemical bonding and bonding models of main-group compounds. *Chemical Reviews*, 119(14):8781–8845, 2019.

[3] Terrance J. Hadlington, Markus Hermann, Gernot Frenking, and Cameron Jones. Two-coordinate group 14 element(II) hydrides as reagents for the facile, and sometimes reversible, hydrogermylation/hydrostannylation of unactivated alkenes and alkynes. *Chemical Science*, 6(12):7249–7257, 2015.

[4] Eric Rivard and Philip P. Power. Multiple bonding in heavier element compounds stabilized by bulky terphenyl ligands. *Inorganic Chemistry*, 46(24):10047–10064, 2007. PMID: 17975890.

[5] Robert West, Mark J. Fink, and Josef Michl. Tetramesityldisilene, a stable compound containing a silicon-silicon double bond. *Science*, 214(4527):1343–1344, 1981.

[6] Peter J. Davidson and Michael F. Lappert. Stabilisation of metals in a low coordinative environment using the bis(trimethylsilyl)methyl ligand; coloured Sn and Pb alkyls, $M[CH(SiMe_3)_2]_2$. *J. Chem. Soc., Chem. Commun.*, pages 317a–317a, 1973.

[7] Roland C. Fischer and Philip P. Power. π-bonding and the lone pair effect in multiple bonds involving heavier main group elements: Developments in the new millennium. *Chemical Reviews*, 110(7):3877–3923, 2010. PMID: 20672858.

[8] M. Yoshifuji, I. Shima, N. Inamoto, K. Hirotsu, and T. Higuchi. Synthesis and structure of bis(2,4,6-tri-tert-butylphenyl)diphosphene: isolation of a true phosphobenzene. *Journal of the American Chemical Society*, 103(15):4587–4589, 1981.

[9] Werner Kutzelnigg. Chemical bonding in higher main group elements. *Angewandte Chemie International Edition in English*, 23(4):272–295, 1984.

[10] Rebecca L. Melen. Frontiers in molecular p-block chemistry: From structure to reactivity. *Science*, 363(6426):479–484, 2019.

[11] Philip P. Power. Main-group elements as transition metals. *Nature*, 463(7278):171–177, 2010.

[12] Catherine Weetman and Shigeyoshi Inoue. The road travelled: After main-group elements as transition metals. *ChemCatChem*, 10(19):4213–4228, 2018.

[13] A. F. Wells. *Structural Inorganic Chemistry*. 5th e.d. Clarendon Press, 1986.

[14] Matthias Driess, Nicoleta Dona, and Klaus Merz. Novel hypervalent complexes of main-group metals by intramolecular ligand→metal electron transfer. *Chemistry – A European Journal*, 10(23):5971–5976, 2004.

[15] Stéphane Noury, Bernard Silvi, and Ronald J. Gillespie. Chemical bonding in hypervalent molecules: Is the octet rule relevant? *Inorganic Chemistry*, 41(8):2164–2172, 2002. PMID: 11952370.

[16] Linus. Pauling. The nature of the chemical bond. application of results obtained from the quantum mechanics and from a theory of paramagnetic susceptibility to the structure of molecules. *Journal of the American Chemical Society*, 53(4):1367–1400, 1931.

[17] Pekka Pyykko. Relativistic effects in structural chemistry. *Chemical Reviews*, 88(3):563–594, 1988.

[18] R. E. Rundle. On the problem structure of XeF_4 and XeF_2. *Journal of the American Chemical Society*, 85(1):112–113, 1963.

[19] Freich Keil and Werner Kutzelnigg. Chemical bond in phosphoranes. comparative ab initio study of difluorophosphorane phosphorane and the hypothetical molecules nitrogen difluoride trihydride and phosphorane. *Journal of the American Chemical Society*, 97(13):3623–3632, 1975.

[20] R. J. Gillespie. The Valence-Shell Electron-Pair Repulsion (VSEPR) theory of directed valency. *Journal of Chemical Education*, 40(6):295, 1963.

[21] Ronald J. Gillespie and Edward A. Robinson. Electron domains and the VSEPR model of molecular geometry. *Angewandte Chemie International Edition in English*, 35(5):495–514, 1996.

[22] R.J. Gillespie and E.A. Robinson. The importance of ligand–ligand interactions for molecular geometry and the ligand close-packing model. *Comptes Rendus Chimie*, 8(9):1631–1644, 2005. Aspects expériment aux, spectroscopiques et théoriques en chimie inorganique.

[23] R. J. Gillespie and P. L. A. Popelier. "Chemical bonding and molecular geometry": Comments on a book review. *Angewandte Chemie International Edition*, 42(29):3331–3334, 2003.

[24] Roger S. Grev. Structure and bonding in the parent hydrides and multiply bonded silicon and germanium compounds: From Mh_n to $R_2M{=}M'R_2$ and $RM{\equiv}M'R$. volume 33 of *Advances in Organometallic Chemistry*, pages 125–170. Academic Press, 1991.

[25] Georges Trinquier and Jean Paul Malrieu. Nonclassical distortions at multiple bonds. *Journal of the American Chemical Society*, 109(18):5303–5315, 1987.

[26] Hansjörg Grützmacher and Thomas F. Fässler. Topographical analyses of homonuclear multiple bonds between main group elements. *Chemistry – A European Journal*, 6(13):2317–2325, 2000.

[27] Jianrui Su, Xiao-Wang Li, R. Chad Crittendon, and Gregory H. Robinson. How short is a Ga–Ga triple bond? synthesis and molecular structure of $Na_2[Mes^*_2C_6H_3\text{-}GaGa\text{-}C_6H_3Mes^*_2]$ (Mes^* = 2,4,6-i-$Pr_3C_6H_2$): The first gallyne. *Journal of the American Chemical Society*, 119(23):5471–5472, 1997.

[28] Geoffrey H. Spikes, James C. Fettinger, and Philip P. Power. Facile activation of dihydrogen by an unsaturated heavier main group compound. *Journal of the American Chemical Society*, 127(35):12232–12233, 2005. PMID: 16131195.

[29] Philip P. Power. Bonding and reactivity of heavier group 14 element alkyne analogues. *Organometallics*, 26(18):4362–4372, 2007.

[30] Zhongliang Zhu, Xinping Wang, Yang Peng, Hao Lei, James C. Fettinger, Eric Rivard, and Philip P. Power. Addition of hydrogen or ammonia to a low-valent group 13 metal species at 25°c and 1 atmosphere. *Angewandte Chemie International Edition*, 48(11):2031–2034, 2009.

[31] Yang Peng, Marcin Brynda, Bobby D. Ellis, James C. Fettinger, Eric Rivard, and Philip P. Power. Addition of H_2 to distannynes under ambient conditions. *Chem. Commun.*, pages 6042–6044, 2008.

[32] Guido D. Frey, Vincent Lavallo, Bruno Donnadieu, Wolfgang W. Schoeller, and Guy Bertrand. Facile splitting of hydrogen and ammonia by nucleophilic activation at a single carbon center. *Science*, 316(5823):439–441, 2007.

[33] Preston A. Chase and Douglas W. Stephan. Hydrogen and amine activation by a frustrated lewis pair of a bulky N-heterocyclic carbene and $B(C_6F_5)_3$. *Angewandte Chemie International Edition*, 47(39):7433–7437, 2008.

[34] Victor Sumerin, Felix Schulz, Martin Nieger, Markku Leskelä, Timo Repo, and Bernhard Rieger. Facile heterolytic H_2 activation by amines and $B(C_6F_5)_3$. *Angewandte Chemie International Edition*, 47(32):6001–6003, 2008.

[35] Dirk Holschumacher, Thomas Bannenberg, Cristian G. Hrib, Peter G. Jones, and Matthias Tamm. Heterolytic dihydrogen activation by a frustrated carbene–borane lewis pair. *Angewandte Chemie International Edition*, 47(39):7428–7432, 2008.

[36] Victor Sumerin, Felix Schulz, Michiko Atsumi, Cong Wang, Martin Nieger, Markku Leskelä, Timo Repo, Pekka Pyykkö, and Bernhard Rieger. Molecular tweezers for hydrogen: Synthesis, characterization, and reactivity. *Journal of the American Chemical Society*, 130(43):14117–14119, 2008. PMID: 18826306.

[37] Gregory C. Welch, Ronan R. San Juan, Jason D. Masuda, and Douglas W. Stephan. Reversible, metal-free hydrogen activation. *Science*, 314(5802):1124–1126, 2006.

[38] Aaron J. Boutland, Deepak Dange, Andreas Stasch, Laurent Maron, and Cameron Jones. Two-coordinate magnesium(i) dimers stabilized by super bulky amido ligands. *Angewandte Chemie International Edition*, 55(32):9239–9243, 2016.

[39] Cameron Jones. Dimeric Magnesium(I) β-diketiminates: a new class of quasi-universal reducing agent. *Nature Reviews Chemistry*, 1(8):0059, 2017.

[40] Shaun P. Green, Cameron Jones, and Andreas Stasch. Stable Magnesium(I) compounds with Mg–Mg bonds. *Science*, 318(5857):1754–1757, 2007.

[41] Ralf Köppe, Patrick Henke, and Hansgeorg Schnöckel. MgCl and Mg_2Cl_2: From theoretical and thermodynamic considerations to spectroscopy and chemistry of species with Mg–Mg bonds. *Angewandte Chemie International Edition*, 47(45):8740–8744, 2008.

[42] Yanyan Liu, Shaoguang Li, Xiao-Juan Yang, Peiju Yang, and Biao Wu. Magnesium-magnesium bond stabilized by a doubly reduced α-diimine: Synthesis and structure of $[K(THF)_3]_2$[LMg-MgL] (L = $[(2,6\text{-}iPr_2C_6H_3)NC(Me)]_2^{2-}$). *Journal of the American Chemical Society*, 131(12):4210–4211, 2009.

[43] Mark R. Crimmin and Michael S. Hill. *Homogeneous Catalysis with Organometallic Complexes of Group 2*, pages 191–241. Springer Berlin Heidelberg, Berlin, Heidelberg, 2013.

[44] Sandeep Yadav, Sumana Saha, and Sakya S. Sen. Compounds with low-valent p-block elements for small molecule activation and catalysis. *ChemCatChem*, 8(3):486–501, 2016.

[45] Jeffrey M. Lipshultz, Gen Li, and Alexander T. Radosevich. Main group redox catalysis of organopnictogens: Vertical periodic trends and emerging opportunities in group 15. *Journal of the American Chemical Society*, 143(4):1699–1721, 2021. PMID: 33464903.

[46] Kin-ya Akiba, Hideyuki Ohnari, and Katsuo Ohkata. Oxidation of α-hydroxyketones with triphenylantimony dibromide and its catalytic cycle. *Chemistry Letters*, 14(10):1577–1580, 1985.

[47] Shuji Yasuike, Yoshihito Kishi, Shin ichiro Kawara, and Jyoji Kurita. Catalytic action of triarylstibanes: Oxidation of benzoins into benzyls using triarylstibanes under an aerobic condition. *Chemical and Pharmaceutical Bulletin*, 53(4):425–427, 2005.

[48] Feng Wang, Oriol Planas, and Josep Cornella. Bi(i)-catalyzed transfer-hydrogenation with ammonia-borane. *Journal of the American Chemical Society*, 2019.

[49] Petr Šimon, Roman Jambor, Aleš Růžička, and Libor Dostál. Oxidative addition of organic disulfides to low valent N,C,N-chelated organobismuth(I) compound: Isolation, structure and coordination capability of substituted bismuth(III) bis(arylsulfides). *Journal of Organometallic Chemistry*, 740:98–103, 2013.

[50] Petr Šimon, Frank de Proft, Roman Jambor, Aleš Růžička, and Libor Dostál. Monomeric organoantimony(I) and organobismuth(I) compounds stabilized by an NCN chelating ligand: Syntheses and structures. *Angewandte Chemie International Edition*, 49(32):5468–5471, 2010.

[51] Martin Hejda, Robert Jirásko, Aleš Růžička, Roman Jambor, and Libor Dostál. Probing the limits of oxidative addition of C(sp^3)–X bonds toward selected N,C,N-chelated Bismuth(I) compounds. *Organometallics*, 39(23):4320–4328, 2020.

[52] Petr Šimon, Roman Jambor, Aleš Růžička, and Libor Dostál. Oxidative addition of diphenyldichalcogenides PhEEPh (E = S, Se, Te) to low-valent CN- and NCN-chelated organoantimony and organobismuth compounds. *Organometallics*, 32(1):239–248, 2013.

[53] Iva Urbanova, Roman Jambor, Ales Ruzicka, Robert Jirasko, and Libor Dostal. Synthesis and structure of N,C-chelated Organoantimony(V) and Organobismuth(V) compounds. *Dalton Transactions*, 43(2):505–512, 2014.

[54] Yue Pang, Markus Leutzsch, Nils Nöthling, and Josep Cornella. Catalytic activation of N_2O at a low-valent bismuth redox platform. *Journal of the American Chemical Society*, 142(46):19473–19479, 2020. PMID: 33146996.

[55] Derek H. R. Barton, William B. Motherwell, and Alan Stobie. A catalytic method for α-glycol cleavage. *J. Chem. Soc., Chem. Commun.*, pages 1232–1233, 1981.

[56] Jacqueline Ramler, Ivo Krummenacher, and Crispin Lichtenberg. Well-defined, molecular bismuth compounds: Catalysts in photochemically induced radical dehydrocoupling reactions. *Chemistry – A European Journal*, 26(64):14551–14555, 2020.

[57] Oriol Planas, Feng Wang, Markus Leutzsch, and Josep Cornella. Fluorination of arylboronic esters enabled by bismuth redox catalysis. *Science*, 367(6475):313–317, 2020.

[58] Daniel Tofan and François P. Gabbaï. Fluorinated Antimony(V) derivatives: strong lewis acidic properties and application to the complexation of formaldehyde in aqueous solutions. *Chemical Science*, 7(11):6768–6778, 2016.

[59] Holger Braunschweig, Rian D. Dewhurst, Florian Hupp, and Justin Wolf. Unprecedented oxidative addition and metal-only lewis pair chemistry of antimony trihalides. *Chemistry – A European Journal*, 21(5):1860–1862, 2015.

[60] Baofei Pan and Francois P. Gabbai. $Sb(C_6F_5)_4B(C_6F_5)_4$: An air stable, lewis acidic stibonium salt that activates strong element-fluorine bonds. *Journal of the American Chemical Society*, 136(27):9564–9567, 2014.

[61] Pekka Pyykkö. Relativistic effects in chemistry: More common than you thought. *Annual Review of Physical Chemistry*, 63(1):45–64, 2012.

[62] Robert Pollice and Peter Chen. A universal quantitative descriptor of the dispersion interaction potential. *Angewandte Chemie*, 131(29):9860–9871, 2019.

[63] Hafida Gaspard-Iloughmane and Christophe Le Roux. Bismuth(III) triflate in organic synthesis. *European Journal of Organic Chemistry*, 2004(12):2517–2532, 2004.

[64] Holger Braunschweig, Paul Cogswell, and Katrin Schwab. Synthesis, structure and reactivity of complexes containing a transition metal–bismuth bond. *Coordination Chemistry Reviews*, 255(1):101–117, 2011.

[65] Gábor Balázs, Hans Joachim Breunig, Enno Lork, and Werner Offermann. Two stable hydrides of antimony: $RSbH_2$ and R(H)Sb-Sb(H)R (R = $(Me_3Si)_2CH$). *Organometallics*, 20(13):2666–2668, 2001.

[66] G Balazs, HJ Breunig, E Lork, and W Offermann. Two stable hydrides of antimony: $RSbH_2$ and R(H)Sb-Sb(H)R (R = $(Me_3Si)_2CH$). *Organometallics*, 20(13):2666–2668, 2001.

[67] P. Braunstein. Hollemann, wiberg and wiberg: Lehrbuch der anorganischen chemie. von hollemann-wiberg. walter de gruyter verlag and co. berlin – new york 1984. isbn 3-11-007511-3. *Nachrichten aus Chemie, Technik und Laboratorium*, 33(8):727–727, 1985.

[68] Fred E. Saalfeld and Harry J. Svec. The mass spectra of volatile hydrides II. some higher hydrides of the group IVB and VB elements. *Inorganic Chemistry*, 2(1):50–53, 1963.

[69] Alan Berry. The synthesis and characterization of isobutylantimony compounds. *Polyhedron*, 18(20):2609–2615, 1999.

[70] Alan H. Cowley, Richard A. Jones, Christine M. Nunn, and Donald L. Westmoreland. $[Mes_2SbCu(PMe_3)_2]_2$: The first CuI antimonide. *Angewandte Chemie International Edition in English*, 28(8):1018–1019, 1989.

[71] Brendan Twamley, Cheong-Soo Hwang, Ned J. Hardman, and Philip P. Power. Sterically encumbered terphenyl substituted primary pnictanes $ArEH_2$

and their metallated derivatives ArE(H)Li (Ar=(C_6H_3-2,6-Trip)$_2$; Trip=2,4,6-triisopropylphenyl; E=N, P, As, Sb). *Journal of Organometallic Chemistry*, 609(1):152–160, 2000.

[72] Ryan J. Schwamm, Alison J. Edwards, Christopher M. Fitchett, and Martyn P. Coles. A study of di(amino)stibines with terminal Sb(III) hydrogen-ligands by x-ray- and neutron-diffraction. *Dalton Transactions*, 48(9):2953–2958, 2019.

[73] Robert J. Baker, Markus Brym, Cameron Jones, and Mark Waugh. 9-triptycenyl complexes of group 13 and 15 halides and hydrides. *Journal of Organometallic Chemistry*, 689(4):781–790, 2004.

[74] H. J. Breunig, E. Lork, O. Moldovan, and C. I. Rat. Syntheses of a stable tristibine and of related antimony compounds with the 2,6-dimesitylphenyl (Dmp) substituent. *Journal of Organometallic Chemistry*, 693(15):2527–2534, 2008.

[75] Jon M. Bellama and Alan G. MacDiarmid. Synthesis of the hydrides of germanium, phosphorus, arsenic, and antimony by the solid-phase reaction of the corresponding oxide with lithium aluminum hydride. *Inorganic Chemistry*, 7(10):2070–2072, 1968.

[76] HJ Breunig, V Breuniglyriti, and TP Knobloch. Simple synthesis of tetramethyldistibane and tetraethyldistibane. *Chemiker-Zeitung*, 101(9):399–400, 1977.

[77] HJ Breunig. Synthesis of tetrakis(trimethylgermyl)-distibane. *Zeitschrift Fur Naturforschung Section B - A Journal of Chemical Sciences*, 33(2):244–245, 1978.

[78] HJ Breunig and TP Knobloch. Polymeric metal carbonyl complexes with bridging distibine ligands. *Journal of Inorganic and Nuclear Chemistry*, 42(4):505–507, 1980.

[79] HJ Breunig and D Muller. Reactions of tetrapropyldibismuthane with chalcogens and tetramethyldistibane. *Zeitschrift Fur Naturforschung Section B - A Journal of Chemical Sciences*, 41(9):1129–1132, 1986.

[80] Eberhard Amberger. Hydride des wismuts. *Chemische Berichte*, 94(6):1447–1452, 1961.

[81] Ned J. Hardman, Brendan Twamley, and Philip P. Power. (2,6-$Mes_2H_3C_6$)$_2$BiH, a stable, molecular hydride of a main group element of the sixth period, and its conversion to the dibismuthene (2,6-$Mes_2H_3C_6$)BiBi(2,6-$Mes_2C_6H_3$).

[82] Benedikt Ritschel, Jordi Poater, Hannah Dengel, F. Matthias Bickelhaupt, and Crispin Lichtenberg. Double CH activation of a masked cationic bismuth amide. *Angewandte Chemie International Edition*, 57(14):3825–3829, 2018.

[83] Marian Olaru, Daniel Duvinage, Enno Lork, Stefan Mebs, and Jens Beckmann. Heavy carbene analogues: Donor-free bismuthenium and stibenium ions. *Angewandte Chemie International Edition*, 57(32):10080–10084, 2018.

[84] Bijan Nekoueishahraki, Prinson P. Samuel, Herbert W. Roesky, Daniel Stern, Julia Matussek, and Dietmar Stalke. Organobismuth(III) and dibismuthine complexes bearing N,N'-disubstituted 1,8-diaminonaphthalene ligand: Synthesis, structure, and reactivity. *Organometallics*, 31(18):6697–6703, 2012.

[85] D Nusshar, R Garbe, F Weller, J Pebler, and K Dehnicke. $[Sb(NPPh_3)_4]\equiv SbF_6^-$ - synthesis, crystal-structure, and Sb-^{121} mossbauer spectrum. *Zeitschrift Fur Anorganische Und Allgemeine Chemie*, 620(1):67–72, 1994.

[86] Michael A. Beswick, Alexander D. Hopkins, Marta E. G. Mosquera, Paul R. Raithby, Alexander Rothenberger, Andrew J. Wheatley, Dominic S. Wright, Nick Choi, Mary McPartlin, and Dietmar Stalke. Direct synthesis of heterocyclic $[(RP)E]^-$ anions using $[E(NMe_2)_3]$ (E = Sb, As); implications to the mechanism of formation of zintl compounds. *Chemical Communications*, (22):2485–2486, 1998.

[87] Saurabh S. Chitnis and Neil Burford. Phosphine complexes of lone pair bearing lewis acceptors. *Dalton Transactions*, 44(1):17–29, 2015.

[88] Alasdair P. M. Robertson, Paul A. Gray, and Neil Burford. Interpnictogen cations: Exploring new vistas in coordination chemistry. *Angewandte Chemie International Edition*, 53(24):6050–6069, 2014.

[89] Saurabh S. Chitnis, Neil Burford, Jan J. Weigand, and Robert McDonald. Reductive catenation of phosphine antimony complexes. *Angewandte Chemie International Edition*, 54(27):7828–7832, 2015.

[90] Saurabh S. Chitnis, Alasdair P. M. Robertson, Neil Burford, Jan J. Weigand, and Roland Fischer. Synthesis and reactivity of cyclo-tetra(stibinophosphonium) tetracations: redox and coordination chemistry of phosphine-antimony complexes. *Chemical Science*, 6(4):2559–2574, 2015.

[91] *Bismuth: Inorganic Chemistry*, pages 1–32.

[92] William Clegg, Neville A. Compton, R. John Errington, George A. Fisher, Marjorie E. Green, David C. R. Hockless, and Nicholas C. Norman. X-ray crystal structure of bismuth dimethylamide. *Inorganic Chemistry*, 30(24):4680–4682, 1991.

[93] Hannah Dengel and Crispin Lichtenberg. Cationic bismuth amides: Accessibility, structure, and reactivity. *Chemistry – A European Journal*, 22(51):18465–18475, 2016.

[94] Phillip Sayer, Martin Gouterman, and Charles R. Connell. Metalloid porphyrins and phthalocyanines. *Accounts of Chemical Research*, 15(3):73–79, 1982.

[95] Tanya Barbour, Warwick J. Belcher, Penelope J. Brothers, Clifton E. F. Rickard, and David C. Ware. Preparation of group 15 (phosphorus, antimony, and bismuth) complexes of meso-tetra-p-tolylporphyrin (TTP) and x-ray crystal structure of $[Sb(TTP)(OCH(CH_3)_2)_2]Cl$. *Inorganic Chemistry*, 31(5):746–754, 1992.

[96] William Clegg, Mark R. J. Elsegood, Nicholas C. Norman, and Nigel L. Pickett. Anionic phosphine complexes of Antimony(III) and Bismuth(III) halogenoanions. *Journal of the Chemical Society, Dalton Transactions*, (12):1753–1757, 1994.

[97] Gerald R. Willey, Leo T. Daly, and Michael G. B. Drew. Phosphorus donor complexes of Bismuth(III). structural characterisation of $[Bi_2Cl_6(Ph_2PCH_2PPh_2)_2]$, $[Bi_2Cl_6(Ph_2PCH_2CH_2PPh_2)_2]$ and $[Bi_2Cl_6(Ph_2PCH_2CH_2PPh_2)_3]$. *Journal of the Chemical Society, Dalton Transactions*, (6):1063–1067, 1996.

[98] Subrata Kundu. Pincer-type ligand-assisted catalysis and small-molecule activation by non-vsepr main-group compounds. *Chemistry – An Asian Journal*, 15(20):3209–3224, 2020.

[99] Eduardo Peris and Robert H. Crabtree. Key factors in pincer ligand design. *Chem. Soc. Rev.*, 47:1959–1968, 2018.

[100] Terry Chu and Georgii I. Nikonov. Oxidative addition and reductive elimination at main-group element centers. *Chemical Reviews*, 118(7):3608–3680, 2018. PMID: 29558125.

[101] David M. Schubert, Marc A. Bandman, William S. Rees, Carolyn B. Knobler, Paul Lu, Wonwoo Nam, and M. Frederick Hawthorne. Synthesis of group 13 element metallacarboranes and related structure-reactivity correlations. *Organometallics*, 9(7):2046–2061, 1990.

[102] Holger Braunschweig, Krzysztof Radacki, Daniela Rais, and Fabian Seeler. Boron in the coordination spheres of three transition-metal atoms: Syntheses and structures of metalloborylenes stabilized by a transition-metal base. *Angewandte Chemie International Edition*, 45(7):1066–1069, 2006.

[103] Kexuan Huang, Jason L. Dutton, and Caleb D. Martin. Exploiting pincer ligands to perturb the geometry at boron. *Chemistry – A European Journal*, 23(44):10532–10535, 2017.

[104] Kexuan Huang, Jason L. Dutton, and Caleb D. Martin. Exploiting pincer ligands to perturb the geometry at boron. *Chemistry – A European Journal*, 23(44):10532–10535, 2017.

[105] Fabian Ebner, Hubert Wadepohl, and Lutz Greb. Calix[4]pyrrole aluminate: A planar tetracoordinate Aluminum(III) anion and its unusual lewis acidity. *Journal of the American Chemical Society*, 141(45):18009–18012, 2019.

[106] Fabian Ebner, Philipp Mainik, and Lutz Greb. Calix[4]pyrrolato aluminates: The effect of ligand modification on the reactivity of square-planar aluminum anions. *Chemistry – A European Journal*, 27(16):5120–5124, 2021.

[107] Fabian Ebner, Lukas Maximilian Sigmund, and Lutz Greb. Metal–ligand cooperativity of the calix[4]pyrrolato aluminate: Triggerable C–C bond formation and rate control in catalysis. *Angewandte Chemie International Edition*, 59(39):17118–17124, 2020.

[108] Gerhard. Bettermann and Anthony J. Arduengo. The chemistry and structure of a 10-Sn-4 system: Pseudo-trigonal-bipyramidal 4-coordinate, 10-electron tin centers. *Journal of the American Chemical Society*, 110(3):877–879, 1988.

[109] Matthias Driess, Nicoleta Muresan, and Klaus Merz. A novel type of pentacoordinate silicon complexes and unusual ligand coupling by intramolecular electron transfer. *Angewandte Chemie International Edition*, 44(41):6738–6741, 2005.

[110] R. Maskey, M. Schadler, C. Legler, and L. Greb. Bis(perchlorocatecholato)silane-a neutral silicon lewis super acid. *Angew Chem Int Ed Engl*, 57(6):1717–1720, 2018.

[111] Nina Kramer, Christoph Jöst, Alexandra Mackenroth, and Lutz Greb. Synthesis of electron-rich, planarized Silicon(IV) species and a theoretical analysis of dimerizing aminosilanes. *Chemistry – A European Journal*, 23(70):17764–17774, 2017.

[112] Shabana Khan, Reent Michel, Johannes M. Dieterich, Ricardo A. Mata, Herbert W. Roesky, Jean-Philippe Demers, Adam Lange, and Dietmar Stalke. Preparation of RSn(I)–Sn(I)R with two unsymmetrically coordinated Sn(I) atoms and subsequent gentle activation of P_4. *Journal of the American Chemical Society*, 133(44):17889–17894, 2011. PMID: 21958040.

[113] Scott Anthony Culley and Anthony J. Arduengo. Synthesis and structure of the first 10-P-3 species. *Journal of the American Chemical Society*, 106(4):1164–1165, 1984.

[114] Anthony J. Arduengo, Constantine A. Stewart, Fredric Davidson, David A. Dixon, James Y. Becker, Scott Anthony Culley, and Mark B. Mizen. The synthesis, structure, and chemistry of 10-Pn-3 systems: tricoordinate hypervalent pnicogen compounds. *Journal of the American Chemical Society*, 109(3):627–647, 1987.

[115] Matthias Driess, Nicoleta Muresan, Klaus Merz, and Michael Päch. Formation of a bowl-shaped, pentacyclic phosphonium cage by methylation of a nucleophilic phosphinidene. *Angewandte Chemie International Edition*, 44(41):6734–6737, 2005.

[116] Constantine A. Stewart, Joseph C. Calabrese, and Anthony J. Arduengo. Synthesis and structure of the first 20-bi-9 system: a discrete nine-coordinate 20-electron bismuth. *Journal of the American Chemical Society*, 107(11):3397–3398, 1985.

[117] Nicole L. Dunn, Minji Ha, and Alexander T. Radosevich. Main group redox catalysis: Reversible PIII/PV redox cycling at a phosphorus platform. *Journal of the American Chemical Society*, 134(28):11330–11333, 2012.

[118] Sean M. McCarthy, Yi-Chun Lin, Deepa Devarajan, Ji Woong Chang, Hemant P. Yennawar, Robert M. Rioux, Daniel H. Ess, and Alexander T. Radosevich. Intermolecular N-–H oxidative addition of ammonia, alkylamines, and arylamines to a planar σ^3-phosphorus compound via an entropy-controlled electrophilic mechanism. *Journal of the American Chemical Society*, 136(12):4640–4650, 2014. PMID: 24597970.

[119] Thomas P. Robinson, Daniel De Rosa, Simon Aldridge, and Jose M. Goicoechea. On the redox reactivity of a geometrically constrained Phosphorus(III) compound. *Chemistry – A European Journal*, 23(61):15455–15465, 2017.

[120] Thomas P. Robinson, Siu-Kwan Lo, Daniel De Rosa, Simon Aldridge, and Jose M. Goicoechea. On the ambiphilic reactivity of geometrically constrained Phosphorus(III) and Arsenic(III) compounds: Insights into their interaction with ionic substrates. *Chemistry – A European Journal*, 22(44):15712–15724, 2016.

[121] Manas Kumar Mondal, Li Zhang, Zhongtao Feng, Shuxuan Tang, Rui Feng, Yue Zhao, Gengwen Tan, Huapeng Ruan, and Xinping Wang. Tricoordinate nontrigonal pnictogen-centered radical anions: Isolation, characterization, and reactivity. *Angewandte Chemie International Edition*, 58(44):15829–15833, 2019.

[122] Marcus B. Kindervater, Katherine M. Marczenko, Ulrike Werner-Zwanziger, and Saurabh S. Chitnis. A redox-confused Bismuth(I/III) triamide with a t-shaped planar ground state. *Angewandte Chemie International Edition*, 58(23):7850–7855, 2019.

[123] Monika Kořenková, Martin Hejda, Milan Erben, Robert Jirásko, Roman Jambor, Aleš Růžička, Elena Rychagova, Sergey Ketkov, and Libor Dostál. Reversible C=C bond activation by an intramolecularly coordinated Antimony(I) compound. *Chemistry – A European Journal*, 0(ja).

[124] Manas Kumar Mondal, Li Zhang, Zhongtao Feng, Shuxuan Tang, Rui Feng, Yue Zhao, Gengwen Tan, Huapeng Ruan, and Xinping Wang. Tricoordinate nontrigonal pnictogen-centered radical anions: Isolation, characterization, and reactivity. *Angewandte Chemie International Edition*, 58(44):15829–15833, 2019.

[125] Andrew L. Hawley, C. André Ohlin, Lea Fohlmeister, and Andreas Stasch. Heavier group 13 Metal(I) heterocycles stabilized by sterically demanding diiminophosphinates: A structurally characterized monomer–dimer pair for gallium. *Chemistry – A European Journal*, 23(2):447–455, 2017.

[126] Katherine M. Marczenko, Joseph A. Zurakowski, Marcus B. Kindervater, Sam Jee, Toren Hynes, Nicholas Roberts, Seoyeon Park, U Werner-Zwanziger,

M Lumsden, David N. Langelaan, and Saurabh S. Chitnis. Periodicity in structure, bonding, and reactivity for p-block complexes of a geometry-constraining triamide ligand. *Chem. Eur. J.*, 25(71):16414–16424, 2019.

[127] Yi-Chun Lin, Emmanuel Hatzakis, Sean M. McCarthy, Kyle D. Reichl, Ting-Yi Lai, Hemant P. Yennawar, and Alexander T. Radosevich. P-–N cooperative borane activation and catalytic hydroboration by a distorted phosphorous triamide platform. *Journal of the American Chemical Society*, 139(16):6008–6016, 2017.

[128] Yohsuke Yamamoto, Xiang Chen, Satoshi Kojima, Keisuke Ohdoi, Mutsuko Kitano, Yasutaka Doi, and Kin-ya Akiba. Experimental investigation on edge inversion at trivalent bismuth and antimony: Great acceleration by intra- and intermolecular nucleophilic coordination. *Journal of the American Chemical Society*, 117(14):3922–3932, 1995.

[129] David A. Dixon and Anthony J. Arduengo. Periodic trends in the edge and vertex inversion barriers for tricoordinate pnicogen hydrides and fluorides. *Journal of the American Chemical Society*, 109(2):338–341, 1987.

[130] Albert P. Soran, Cristian Silvestru, Hans J. Breunig, Gabor Balazs, and Jennifer C. Green. Organobismuth(III) dihalides with T-shaped geometry stabilized by intramolecular N–Bi interactions and related diorganobismuth(III) halides. *Organometallics*, 26(5):1196–1203, 2007.

[131] Andrew R. Jupp, Timothy C. Johnstone, and Douglas W. Stephan. The global electrophilicity index as a metric for lewis acidity. *Dalton Transactions*, 47(20):7029–7035, 2018.

[132] Rui F. Munhá, Ryan A. Zarkesh, and Alan F. Heyduk. Tuning the electronic and steric parameters of a redox-active tris(amido) ligand. *Inorganic Chemistry*, 52(19):11244–11255, 2013.

[133] Richard R. Schrock, Jesse Lee, Lan-Chang Liang, and William M. Davis. The synthesis and structures of tantalum complexes that contain a triamido or a diamidoamine ligand. *Inorganica Chimica Acta*, 270(1):353–362, 1998.

[134] C. J. Carmalt, Neville A. Compton, R. J. Errington, G. A. Fisher, I. Moenandar, N. C. Norman, and Kenton H. Whitmire. *Homoleptic Bismuth Amides*, pages 98–101. Wiley, 2007.

[135] Hans Schumann. Synthese und spektroskopische charakterisierung von cyclopentadienyleisen-komplexen mit P-N-liganden des typs $(C_6H_5)_3-nP(NR_2)n$ (n = 0-3; R = CH_3, C_2H_5. *Journal of Organometallic Chemistry*, 299(2):169–178, 1986.

[136] Tobias A. Engesser, Martin R. Lichtenthaler, Mario Schleep, and Ingo Krossing. Reactive p-block cations stabilized by weakly coordinating anions. *Chemical Society Reviews*, 45(4):789–899, 2016.

[137] Lutz Greb. Lewis superacids: Classifications, candidates, and applications. *Chemistry – A European Journal*, 24(68):17881–17896, 2018.

[138] Alexander B. A. Rupp and Ingo Krossing. Ionic liquids with weakly coordinating $[M^{III}(ORF)_4]^-$ anions. *Accounts of Chemical Research*, 48(9):2537–2546, 2015.

[139] Ian M. Riddlestone, Sarah Keller, Florian Kirschenmann, Marcel Schorpp, and Ingo Krossing. Towards weakly coordinating anions with the extremely electron withdrawing perfluoropyridinoxy ligand $–OC_5F_4N$. *European Journal of Inorganic Chemistry*, 2019(1):59–67, 2019.

[140] Anne Kraft, Nils Trapp, Daniel Himmel, Hannes Böhrer, Peter Schlüter, Harald Scherer, and Ingo Krossing. Synthesis, characterization, and application of two $Al(ORF)_3$ lewis superacids. *Chemistry – A European Journal*, 18(30):9371–9380, 2012.

[141] Leif A. Körte, Jan Schwabedissen, Marcel Soffner, Sebastian Blomeyer, Christian G. Reuter, Yury V. Vishnevskiy, Beate Neumann, Hans-Georg Stammler, and Norbert W. Mitzel. Tris(perfluorotolyl)borane—a boron lewis superacid. *Angewandte Chemie International Edition*, 56(29):8578–8582, 2017.

[142] James R. Lawson and Rebecca L. Melen. Tris(pentafluorophenyl)borane and beyond: Modern advances in borylation chemistry. *Inorganic Chemistry*, 56(15):8627–8643, 2017.

[143] Makoto Yasuda, Sachiko Yoshioka, Hideto Nakajima, Kouji Chiba, and Akio Baba. Fine-tuning of boron complexes with cage-shaped ligand geometry: Rational design of triphenolic ligand as a template for structure control. *Organic Letters*, 10(5):929–932, 2008. PMID: 18220406.

[144] M. J. Frisch, G. W. Trucks, H. B. Schlegel, G. E. Scuseria, M. A. Robb, J. R. Cheeseman, G. Scalmani, V. Barone, G. A. Petersson, H. Nakatsuji, X. Li, M. Caricato, A. V. Marenich, J. Bloino, B. G. Janesko, R. Gomperts, B. Mennucci, H. P. Hratchian, J. V. Ortiz, A. F. Izmaylov, J. L. Sonnenberg, D. Williams-Young, F. Ding, F. Lipparini, F. Egidi, J. Goings, B. Peng, A. Petrone, T. Henderson, D. Ranasinghe, V. G. Zakrzewski, J. Gao, N. Rega, G. Zheng, W. Liang, M. Hada, M. Ehara, K. Toyota, R. Fukuda, J. Hasegawa, M. Ishida, T. Nakajima, Y. Honda, O. Kitao, H. Nakai, T. Vreven, K. Throssell, J. A. Montgomery, Jr., J. E. Peralta, F. Ogliaro, M. J. Bearpark, J. J. Heyd, E. N. Brothers, K. N. Kudin, V. N. Staroverov, T. A. Keith, R. Kobayashi, J. Normand, K. Raghavachari, A. P. Rendell, J. C. Burant, S. S. Iyengar, J. Tomasi, M. Cossi, J. M. Millam, M. Klene, C. Adamo, R. Cammi, J. W. Ochterski, R. L. Martin, K. Morokuma, O. Farkas, J. B. Foresman, and D. J. Fox. Gaussian 16 Revision C.01, 2016. Gaussian Inc. Wallingford CT.

[145] John P. Perdew, Kieron Burke, and Matthias Ernzerhof. Generalized gradient approximation made simple [phys. rev. lett. 77, 3865 (1996)]. *Physical Review Letters*, 78(7):1396–1396, 1997.

[146] John P. Perdew, Kieron Burke, and Matthias Ernzerhof. Generalized gradient approximation made simple. *Physical Review Letters*, 77(18):3865–3868, 1996.

[147] Stefan Grimme, Jens Antony, Stephan Ehrlich, and Helge Krieg. A consistent and accurate ab initio parametrization of density functional dispersion correction (DFT-D) for the 94 elements H-Pu. *The Journal of Chemical Physics*, 132(15):154104, 2010.

[148] Stefan Grimme, Stephan Ehrlich, and Lars Goerigk. Effect of the damping function in dispersion corrected density functional theory. *Journal of Computational Chemistry*, 32(7):1456–1465, 2011.

[149] Florian Weigend and Reinhart Ahlrichs. Balanced basis sets of split valence, triple zeta valence and quadruple zeta valence quality for h to rn: Design and assessment of accuracy. *Physical Chemistry Chemical Physics*, 7(18):3297–3305, 2005.

[150] Bernhard Metz, Hermann Stoll, and Michael Dolg. Small-core multiconfiguration-dirac–hartree–fock-adjusted pseudopotentials for post-d main group elements: Application to PbH and PbO. *The Journal of Chemical Physics*, 113(7):2563–2569, 2000.

[151] Tom Ziegler and Arvi Rauk. A theoretical study of the ethylene-metal bond in complexes between copper($^{1+}$), silver($^{1+}$), gold($^{1+}$), platinum(0) or platinum($^{2+}$) and ethylene, based on the Hartree-Fock-Slater transition-state method. *Inorganic Chemistry*, 18(6):1558–1565, 1979.

[152] Tom Ziegler and Arvi Rauk. Carbon monoxide, carbon monosulfide, molecular nitrogen, phosphorus trifluoride, and methyl isocyanide as σ donors and π acceptors. a theoretical study by the hartree-fock-slater transition-state method. *Inorganic Chemistry*, 18(7):1755–1759, 1979.

[153] F. Matthias Bickelhaupt and E. J. Baerends. *Kohn-Sham Density Functional Theory: Predicting and Understanding Chemistry*, pages 1–86.

[154] G. te Velde, F. M. Bickelhaupt, E. J. Baerends, C. Fonseca Guerra, S. J. A. van Gisbergen, J. G. Snijders, and T. Ziegler. Chemistry with adf. *Journal of Computational Chemistry*, 22(9):931–967, 2001.

[155] E. van Lenthe, E. J. Baerends, and J. G. Snijders. Relativistic regular two-component hamiltonians. *The Journal of Chemical Physics*, 99(6):4597–4610, 1993.

[156] Erik van Lenthe, Andreas Ehlers, and Evert-Jan Baerends. Geometry optimizations in the zero order regular approximation for relativistic effects. *The Journal of Chemical Physics*, 110(18):8943–8953, 1999.

[157] E. van Lenthe, E. J. Baerends, and J. G. Snijders. Relativistic total energy using regular approximations. *The Journal of Chemical Physics*, 101(11):9783–9792, 1994.

[158] Kirk A. Peterson. Systematically convergent basis sets with relativistic pseudopotentials. i. correlation consistent basis sets for the post-d group 13–15 elements. *The Journal of Chemical Physics*, 119(21):11099–11112, 2003.

[159] Ping Li, Josef M. Maier, Erik C. Vik, Christopher J. Yehl, Brent E. Dial, Amanda E. Rickher, Mark D. Smith, Perry J. Pellechia, and Ken D. Shimizu. Stabilizing fluorine–π interactions. *Angewandte Chemie International Edition*, 56(25):7209–7212, 2017.

[160] Katherine M. Marczenko, Chloe-Louise Johnson, and Saurabh S. Chitnis. Synthesis of a perfluorinated phenoxyphosphorane and conversion to its hexacoordinate anions. *Chemistry – A European Journal*, 25(37):8865–8874, 2019.

[161] Ralph G. Pearson. Absolute electronegativity and absolute hardness of lewis acids and bases. *Journal of the American Chemical Society*, 107(24):6801–6806, 1985.

[162] Albert Paparo, Cory D. Smith, and Cameron Jones. Diagonally related s- and p-block metals join forces: Synthesis and characterization of complexes with covalent beryllium–aluminum bonds. *Angewandte Chemie International Edition*, 58(33):11459–11463, 2019.

[163] William Levason, Seema Maheshwari, Raju Ratnani, Gillian Reid, Michael Webster, and Wenjian Zhang. Structural diversity in supramolecular complexes of mcl_3 (m = as, sb, bi) with constrained thio- and seleno-ether ligands. *Inorganic Chemistry*, 49(19):9036–9048, 2010.

[164] William Levason, Mark E. Light, Seema Maheshwari, Gillian Reid, and Wenjian Zhang. Unusual neutral ligand coordination to arsenic and antimony trifluoride. *Dalton Transactions*, 40(19):5291–5297, 2011.

[165] Sophie L. Benjamin, William Levason, Gillian Reid, Michael C. Rogers, and Robert P. Warr. Lewis base complexes of methyldihalobismuthines $BiMeX_2$ (X = Cl or Br). *Journal of Organometallic Chemistry*, 708:106–111, 2012.

[166] Saurabh S. Chitnis, Neil Burford, Robert McDonald, and Michael J. Ferguson. Prototypical phosphine complexes of antimony(iii). *Inorganic Chemistry*, 53(10):5359–5372, 2014.

[167] Hubert Schmidbaur and Annette Schier. π-complexation of post-transition metals by neutral aromatic hydrocarbons: The road from observations in the 19th century to new aspects of supramolecular chemistry. *Organometallics*, 27(11):2361–2395, 2008.

[168] Rory Waterman and T. Don Tilley. Catalytic antimony–antimony bond formation through stibinidene elimination from zirconocene and hafnocene complexes. *Angewandte Chemie International Edition*, 45(18):2926–2929, 2006.

[169] D. Greg Hendershot and Alan D. Berry. Primary and secondary trimethylsilylmethylstibines. synthesis, characterization and chemical vapor deposition properties. *Journal of Organometallic Chemistry*, 449(1):119–123, 1993.

[170] Christian Marquardt, Oliver Hegen, Matthias Hautmann, Gábor Balázs, Michael Bodensteiner, Alexander V. Virovets, Alexey Y. Timoshkin, and Manfred Scheer. Isolation and characterization of lewis base stabilized monomeric parent stibanylboranes. *Angewandte Chemie International Edition*, 54(44):13122–13125, 2015.

[171] Simon Aldridge and Anthony J. Downs. Hydrides of the main-group metals: New variations on an old theme. *Chemical Reviews*, 101(11):3305–3366, 2001.

[172] Tokitoh Norihiro, Arai Yoshimitsu, Harada Jun, and Okazaki Renji. Syntheses and crystal structures of novel antimony-containing cyclic polysulfides. *Chemistry Letters*, 24(10):959–960, 1995.

[173] H. J. Breunig and J. Probst. Reaktionen von ph_2sbh und p-$tolsbh_2$ mit organischen verbindungen. *Journal of Organometallic Chemistry*, 571(2):297–303, 1998.

[174] Yaozeng Huang, Yanchang Shen, and Chen Chen. Selective reduction of carbonyl compounds by diphenylstibine. *Tetrahedron Letters*, 26(42):5171–5172, 1985.

[175] A. N. Nesmeyanov, A. E. Borisov, and N. V. Novikova. Organometallic derivatives of ethylene. *Bulletin of the Academy of Sciences of the USSR, Division of chemical science*, 14(4):749–749, 1965.

[176] K.-H. Linke and W. Brandt. Beiträge zur chemie des hydrazins und seiner derivate. synthese P-, As- und Sb-substituierter hydrazine durch addition von P-H-, As-H- und Sb-H-funktionen an N-N-doppelbindungen. *Zeitschrift für anorganische und allgemeine Chemie*, 433(1):119–132, 1977.

[177] Heather A. Spinney, Ilia Korobkov, and Darrin S. Richeson. Diamidonaphthalene-supported pnictogenium cations: Synthesis of an N-heterocyclic stibenium cation by a novel protonation route. *Chemical Communications*, (16):1647–1649, 2007.

[178] Heather A. Spinney, Ilia Korobkov, Gino A. DiLabio, Glen P. A. Yap, and Darrin S. Richeson. Diamidonaphthalene-stabilized N-heterocyclic pnictogenium cations and their cation-cation solid-state interactions. *Organometallics*, 26(20):4972–4982, 2007.

[179] Kevin Dzialkowski, Alexander Gehlhaar, Christoph Wölper, Alexander A. Auer, and Stephan Schulz. Structure and reactivity of 1,8-bis(naphthalenediyl)dipnictanes. *Organometallics*, 38(15):2927–2942, 2019.

[180] H. F. T. Klare and M. Oestreich. *Dalton Trans.*, 39:9176, 2010.

[181] Antoine Simonneau, Tobias Biberger, and Martin Oestreich. The cyclohexadienyl-leaving-group approach toward donor-stabilized silylium ions. *Organometallics*, 34(16):3927–3929, 2015.

[182] Lutz H. Gade, Christian H. Galka, Konrad W. Hellmann, René M. Williams, Luisa De Cola, Ian J. Scowen, and Mary McPartlin. Tetraaminoperylenes: Their efficient synthesis and physical properties. *Chemistry – A European Journal*, 8(16):3732–3746, 2002.

[183] M. J. Frisch, G. W. Trucks, H. B. Schlegel, G. E. Scuseria, M. A. Robb, J. R. Cheeseman, G. Scalmani, V. Barone, G. A. Petersson, H. Nakatsuji, X. Li, M. Caricato, A. Marenich, J. Bloino, B. G. Janesko, R. Gomperts, B. Mennucci, H. P. Hratchian, J. V. Ortiz, A. F. Izmaylov, J. L. Sonnenberg, D. Williams-Young, F. Ding, F. Lipparini, F. Egidi, J. Goings, B. Peng, A. Petrone, T. Henderson, D. Ranasinghe, V. G. Zakrzewski, J. Gao, N. Rega, G. Zheng, W. Liang, M. Hada, M. Ehara, K. Toyota, R. Fukuda, J. Hasegawa, M. Ishida, T. Nakajima, Y. Honda, O. Kitao, H. Nakai, T. Vreven, K. Throssell, J. A. Montgomery, Jr., J. E. Peralta, F. Ogliaro, M. Bearpark, J. J. Heyd, E. Brothers, K. N. Kudin, V. N. Staroverov, T. Keith, R. Kobayashi, J. Normand, K. Raghavachari, A. Rendell, J. C. Burant, S. S. Iyengar, J. Tomasi, M. Cossi, J. M. Millam, M. Klene, C. Adamo, R. Cammi, J. W. Ochterski, R. L. Martin, K. Morokuma, O. Farkas, J. B. Foresman, , and D. J. Fox. Gaussian 09 Revision A.02, 2016. Gaussian Inc. Wallingford CT.

[184] A. Otero-de-la Roza and Erin R. Johnson. Non-covalent interactions and thermochemistry using xdm-corrected hybrid and range-separated hybrid density functionals. *The Journal of Chemical Physics*, 138(20):204109, 2013.

[185] Axel D. Becke. Density-functional thermochemistry. III. the role of exact exchange. *J. Chem. Phys.*, 98(7):5648–5652, 1993.

[186] Chengteh Lee, Weitao Yang, and Robert G. Parr. Development of the colle-salvetti correlation-energy formula into a functional of the electron density. *Physical Review B*, 37(2):785–789, 1988.

[187] E. R. Johnson. *The Exchange-Hole Dipole Moment Dispersion Model*, book section 5, pages 169–194. Elsevier, 2017.

[188] Nicholas P. Labello, Antonio M. Ferreira, and Henry A. Kurtz. Correlated, relativistic, and basis set limit molecular polarizability calculations to evaluate an augmented effective core potential basis set. *International Journal of Quantum Chemistry*, 106(15):3140–3148, 2006.

[189] Walter J. Stevens, Morris Krauss, Harold Basch, and Paul G. Jasien. Relativistic compact effective potentials and efficient, shared-exponent basis sets for the third-, fourth-, and fifth-row atoms. *Canadian Journal of Chemistry*, 70(2):612–630, 1992.

[190] Bernhard Metz, Hermann Stoll, and Michael Dolg. Small-core multiconfiguration-dirac–hartree–fock-adjusted pseudopotentials for post-d main group elements: Application to PbH and PbO. *J. Chem. Phys.*, 113(7):2563–2569, 2000.

[191] Dmitrij Rappoport and Filipp Furche. Property-optimized gaussian basis sets for molecular response calculations. *J. Chem. Phys.*, 133(13):134105, 2010.

[192] Florian Weigend and Reinhart Ahlrichs. Balanced basis sets of split valence, triple zeta valence and quadruple zeta valence quality for H to Rn: Design and assessment of accuracy. *Phys. Chem. Chem. Phys.*, 7(18):3297–3305, 2005.

[193] Giovanni Scalmani and Michael J. Frisch. Continuous surface charge polarizable continuum models of solvation. i. general formalism. *J. Chem. Phys.*, 132(11):114110, 2010.

[194] Katherine M. Marczenko and Saurabh S. Chitnis. Bismuthanylstibanes. *Chem. Commun.*, 56:8015–8018, 2020.

[195] Philip P. Power. Interaction of multiple bonded and unsaturated heavier main group compounds with hydrogen, ammonia, olefins, and related molecules. *Accounts of Chemical Research*, 44(8):627–637, 2011.

[196] Carsten Präsang and David Scheschkewitz. Reactivity in the periphery of functionalised multiple bonds of heavier group 14 elements. *Chemical Society Reviews*, 45(4):900–921, 2016.

[197] Henry B. Wedler, Paul Wendelboe, and Philip P. Power. Second-order jahn–teller (sojt) structural distortions in multiply bonded higher main group compounds. *Organometallics*, 37(18):2929–2936, 2018.

[198] Takahiro Sasamori, Nobuhiro Takeda, and Norihiro Tokitoh. Synthesis of a stable stibabismuthene; the first compound with an antimony–bismuth double bond. *Chemical Communications*, (15):1353–1354, 2000.

[199] III Ashe, Arthur J. and Jr. Ludwig, Edward G. The exchange reaction of tetramethyldiphosphine, -diarsine, -distibine, and -dibismuthine. *J. Organomet. Chem.*, 303(2):197–204, 1986.

[200] Bernhard Wahl, Lars Kloo, and Michael Ruck. The molecular cluster $[Bi_{10}Au_2](SbBi_3Br_9)_2$. *Angewandte Chemie International Edition*, 47(21):3932–3935, 2008.

[201] Siméon Ponou and Thomas F. Fässler. Nonclassical bonding in the novel structure of Ba_2Bi_3 and unexpected site preference in the coloring variant Ba2BiSb2. *Inorganic Chemistry*, 43(20):6124–6126, 2004.

[202] Eamonn Conrad, Neil Burford, Robert McDonald, and Michael J. Ferguson. Bismuthenium-pnictonium dications [R'BiPnR(3)](2≡) (pn = as, sb) containing carbenoid bismuth centers and rare Bi-Sb bonds. *Chemical Communications*, 46(25):4598–4600, 2010.

[203] Hans J. Breunig, Ioan Ghesner, Mihaiela E. Ghesner, and Enno Lork. Syntheses, structures, and dynamic behavior of chiral racemic organoantimony and -bismuth compounds RR'SbCl, RR'BiCl, and RR'SbM [R = $_2$−$(Me_2NCH_2)C_6H_4$, R' = $CH(Me_3Si)_2$, M = H, Li, Na]. *Inorganic Chemistry*, 42(5):1751–1757, 2003.

[204] HJ Breunig, R Rosler, and E Lork. Sb_8R_4, R = $(Me_3Si)_2CH$ - a polycyclic organostibane. *Angewandte Chemie-International Edition In English*, 36(20):2237–2238, 1997.

[205] Christoph Schoo, Sebastian Bestgen, Alexander Egeberg, Svetlana Klementyeva, Claus Feldmann, Sergey N. Konchenko, and Peter W. Roesky. Samarium polystibides derived from highly activated nanoscale antimony. *Angewandte Chemie International Edition*, 57(20):5912–5916, 2018.

[206] Kazuo Kitaura and Keiji Morokuma. A new energy decomposition scheme for molecular interactions within the hartree-fock approximation. *International Journal of Quantum Chemistry*, 10(2):325–340, 1976.

[207] J. Philipp Wagner and Peter R. Schreiner. London dispersion in molecular chemistry—reconsidering steric effects. *Angewandte Chemie International Edition*, 54(42):12274–12296, 2015.

[208] Alexander Hinz, Axel Schulz, and Alexander Villinger. Accessing heavy allyl-analogous $[(tern)_2e]^-$ (e = sb, bi) ions and their reactivity towards ecl_3. *Chemical Communications*, 51(57):11437–11440, 2015.

[209] Christian Ritter, Benjamin Ringler, Fabian Dankert, Matthias Conrad, Florian Kraus, and Carsten von Hänisch. Synthesis and crystal structures of novel tertiary butyl substituted (pseudo-)halogen bismuthanes. *Dalton Transactions*, 48(16):5253–5262, 2019.

[210] Hao Zhang, Jae Sung Son, Jaeyoung Jang, Jong-Soo Lee, Wee-Liat Ong, Jonathan A. Malen, and Dmitri V. Talapin. Bi1–xsbx alloy nanocrystals: Colloidal synthesis, charge transport, and thermoelectric properties. *ACS Nano*, 7(11):10296–10306, 2013.

[211] Katherine M. Marczenko, Joseph A. Zurakowski, Karlee L. Bamford, Joshua W. M. MacMillan, and Saurabh S. Chitnis. Hydrostibination. *Angewandte Chemie International Edition*, 58(50):18096–18101, 2019.

[212] Hironori Arakawa, Michele Aresta, John N. Armor, Mark A. Barteau, Eric J. Beckman, Alexis T. Bell, John E. Bercaw, Carol Creutz, Eckhard Dinjus, David A. Dixon, Kazunari Domen, Daniel L. DuBois, Juergen Eckert, Etsuko Fujita, Dorothy H. Gibson, William A. Goddard, D. Wayne Goodman, Jay Keller, Gregory J. Kubas, Harold H. Kung, James E. Lyons, Leo E. Manzer, Tobin J. Marks, Keiji Morokuma, Kenneth M. Nicholas, Roy Periana, Lawrence Que, Jens Rostrup-Nielson, Wolfgang M. H. Sachtler, Lanny D. Schmidt, Ayusman Sen, Gabor A. Somorjai, Peter C. Stair, B. Ray Stults, and William Tumas. Catalysis research of relevance to carbon management: Progress, challenges, and opportunities. *Chemical Reviews*, 101(4):953–996, 2001.

[213] John R. Rumble, David R. Lide, and Thomas J. Bruno. *CRC handbook of chemistry and physics : a ready-reference book of chemical and physical data*. 2018.

[214] Daniela Belli Dell'Amico, Fausto Calderazzo, Luca Labella, Fabio Marchetti, and Guido Pampaloni. Converting carbon dioxide into carbamato derivatives. *Chemical Reviews*, 103(10):3857–3898, 2003.

[215] Lise Maisonneuve, Océane Lamarzelle, Estelle Rix, Etienne Grau, and Henri Cramail. Isocyanate-free routes to polyurethanes and poly(hydroxy urethane)s. *Chemical Reviews*, 115(22):12407–12439, 2015.

[216] Rais Vohra. *Chapter 120. Organophosphorus and Carbamate Insecticides*. The McGraw-Hill Companies, New York, NY, 2012.

[217] Arun K. Ghosh and Margherita Brindisi. Organic carbamates in drug design and medicinal chemistry. *Journal of Medicinal Chemistry*, 58(7):2895–2940, 2015.

[218] Daniela Belli Dell' Amico, Fausto Calderazzo, Luca Labella, Fabio Marchetti, and Guido Pampaloni. N,n-dialkylcarbamato metal complexes, molecular inorganic precursors to functionalized inorganic matrices. *Inorganic Chemistry Communications*, 5(9):733–745, 2002.

[219] Clément Camp, Lucile Chatelain, Christos E. Kefalidis, Jacques Pécaut, Laurent Maron, and Marinella Mazzanti. CO_2 conversion to isocyanate via multiple N–Si bond cleavage at a bulky Uranium(III) complex. *Chemical Communications*, 51(84):15454–15457, 2015.

[220] Diane A. Dickie, Madeline T. Barker, Michael A. Land, Kira E. Hughes, Jason A. C. Clyburne, and Richard A. Kemp. Rapid, reversible, solid–gas and solution-phase insertion of CO_2 into In–P bonds. *Inorganic Chemistry*, 54(23):11121–11126, 2015.

[221] Luke J. Murphy, Katherine N. Robertson, Richard A. Kemp, Heikki M. Tuononen, and Jason A. C. Clyburne. Structurally simple complexes of co_2. *Chemical Communications*, 51(19):3942–3956, 2015.

[222] Jing Peng, Yongchao Geng, Hai-Jian Yang, Wei He, Zidong Wei, Jingkui Yang, and Cun-Yue Guo. Efficient solvent-free fixation of CO_2 into cyclic carbonates catalyzed by Bi(III) porphyrin/TBAI at atmospheric pressure. *Molecular Catalysis*, 432:37–46, 2017.

[223] Douglas R. Kindra, Ian J. Casely, Megan E. Fieser, Joseph W. Ziller, Filipp Furche, and William J. Evans. Insertion of CO_2 and COS into Bi–C bonds: Reactivity of a bismuth NCN pincer complex of an oxyaryl dianionic ligand, [2,6-$(Me_2NCH_2)_2C_6H_3$]Bi($C_6H_2tBu_2O$). *J. Am. Chem. Soc.*, 135(20):7777–7787, 2013.

[224] Douglas R. Kindra and William J. Evans. Bismuth-based cyclic synthesis of 3,5-di-tert-butyl-4-hydroxybenzoic acid via the oxyarylcarboxy dianion, $(O_2CC_6H_2tBu_2O)_2$. *Dalton Trans.*, 43(8):3052–3054, 2014.

[225] Shuang-Feng Yin, Junpei Maruyama, Takashi Yamashita, and Shigeru Shimada. Efficient fixation of carbon dioxide by hypervalent organobismuth oxide, hydroxide, and alkoxide. *Angew. Chem., Int. Ed.*, 47(35):6590–6593, 2008.

[226] Hans J. Breunig, Lucia Königsmann, Enno Lork, Mihai Nema, Nicky Philipp, Cristian Silvestru, Albert Soran, Richard A. Varga, and Roxana Wagner. Hypervalent Organobismuth(III) carbonate, chalcogenides and halides with the pendant arm ligands 2-$(Me_2NCH_2)C_6H_4$ and 2,6-$(Me_2NCH_2)_2C_6H_3$. *Dalton Transactions*, (14):1831–1842, 2008.

[227] Yi Chen, Renhua Qiu, Xinhua Xu, Chak-Tong Au, and Shuang-Feng Yin. Organoantimony and organobismuth complexes for co_2 fixation. *Rsc Advances*, 4(23):11907–11918, 2014.

[228] Renhua Qiu, Zhengong Meng, Shuangfeng Yin, Xingxing Song, Nianyuan Tan, Yongbo Zhou, Kun Yu, Xinhua Xu, Shenglian Luo, Chak-Tong Au, and Wai-Yeung Wong. Synthesis and structure of binuclear O/S-bridged organobismuth complexes and their cooperative catalytic effect on co_2 fixation. *ChemPlusChem*, 77(5):404–410, 2012.

[229] F. Ando, T. Hayashi, K. Ohashi, and J. Koketsu. Preparations and reactions of tris(dialkylamino)bismuthine. *Journal of Inorganic and Nuclear Chemistry*, 37(9):2011–2013, 1975.

[230] Samuel D. Cosham, Michael S. Hill, Graeme A. Horley, Andrew L. Johnson, Laura Jordan, Kieran C. Molloy, and David C. Stanton. Synthesis and materials chemistry of bismuth tris-(di-i-propylcarbamate): Deposition of photoactive bi_2o_3 thin films. *Inorganic Chemistry*, 53(1):503–511, 2014.

[231] Pavel L. Shutov, Sergey S. Karlov, Klaus Harms, Daniil A. Tyurin, Andrei V. Churakov, Jörg Lorberth, and Galina S. Zaitseva. Synthesis and characterization of the first azastibatranes and azabismatranes. *Inorganic Chemistry*, 41(23):6147–6152, 2002.

[232] K. M. Marczenko and S. S. Chitnis. Bismuthanylstibanes. *Chemical Communications*, 56(58):8015–8018, 2020.

[233] Bijan Nekoueishahraki, Prinson P. Samuel, Herbert W. Roesky, Daniel Stern, Julia Matussek, and Dietmar Stalke. Organobismuth(III) and dibismuthine complexes bearing N,N'-disubstituted 1,8-diaminonaphthalene ligand: Synthesis, structure, and reactivity. *Organometallics*, 31(18):6697–6703, 2012.

[234] Bijan Nekoueishahraki, Sankaranarayana Pillai Sarish, Herbert W. Roesky, Daniel Stern, Carola Schulzke, and Dietmar Stalke. Addition of dimethylaminobismuth to aldehydes, ketones, alkenes, and alkynes. *Angewandte Chemie International Edition*, 48(25):4517–4520, 2009.

[235] Bijan Nekoueishahraki, Anukul Jana, Herbert W. Roesky, Lallan Mishra, Daniel Stern, and Dietmar Stalke. Synthesis and structural characterization of heterobimetallic bismuth complexes with main group and transition metals. *Organometallics*, 28(19):5733–5738, 2009.

[236] Christina Knispel, Christian Limberg, and Burkhard Ziemer. Bismuth allyloxides. *Inorg. Chem.*, 49(9):4313–4318, 2010.

[237] Christina Knispel and Christian Limberg. C–H bond activation in a molybdenumoxo-bismuth compound. *Organometallics*, 30(14):3701–3703, 2011.

[238] Ned J. Hardman, Brendan Twamley, and Philip P. Power. (2,6-$Mes_2H_3C_6$)2BiH, a stable, molecular hydride of a main group element of the sixth period, and its conversion to the dibismuthene (2,6-$Mes_2H_3C_6$)BiBi(2,6-$Mes_2C_6H_3$). *Angewandte Chemie International Edition*, 39(15):2771–2773, 2000.

[239] Polly L. Arnold, Zöe R. Turner, Anne I. Germeroth, Ian J. Casely, Gary S. Nichol, Ronan Bellabarba, and Robert P. Tooze. Carbon monoxide and carbon dioxide insertion chemistry of f-block N-heterocyclic carbene complexes. *Dalton Transactions*, 42(5):1333–1337, 2013.

[240] Eugene You-Xian Chen and Tobin J. Marks. Cocatalysts for metal-catalyzed olefin polymerization: Activators, activation processes, and structure-activity relationships. *Chemical Reviews*, 100(4):1391–1434, 2000.

[241] Abhinandan Shyamsunder, Witali Beichel, Petra Klose, Quan Pang, Harald Scherer, Anke Hoffmann, Graham K. Murphy, Ingo Krossing, and Linda F. Nazar. Inhibiting polysulfide shuttle in lithium–sulfur batteries through low-ion-pairing salts and a triflamide solvent. *Angewandte Chemie International Edition*, 56(22):6192–6197, 2017.

[242] Gerhard Erker. Tris(pentafluorophenyl)borane: a special boron lewis acid for special reactions. *Dalton Transactions*, (11):1883–1890, 2005.

[243] Warren E. Piers and Tristram Chivers. Pentafluorophenylboranes: from obscurity to applications. *Chemical Society Reviews*, 26(5):345–354, 1997.

[244] George J. P. Britovsek, Juri Ugolotti, and Andrew J. P. White. From $B(C_6F_5)_3$ to $B(OC_6F_5)_3$: Synthesis of $(C_6F_5)_2BOC_6F_5$ and $C_6F_5B(OC_6F_5)_2$ and their relative lewis acidity. *Organometallics*, 24(7):1685–1691, 2005.

[245] Julius F. Kögel, Alexey Y. Timoshkin, Artem Schröder, Enno Lork, and Jens Beckmann. $Al(OCArF_3)_3$ – a thermally stable lewis superacid. *Chemical Science*, 9(43):8178–8183, 2018.

[246] Nishida Hiroshi, Takada Naoko, Yoshimura Masaji, Sonoda Takaaki, and Kobayashi Hiroshi. Tetrakis[3,5-bis(trifluoromethyl)phenyl]borate. highly lipophilic stable anionic agent for solvent-extraction of cations. *Bulletin of the Chemical Society of Japan*, 57(9):2600–2604, 1984.

[247] Svetlana M. Ivanova, Benjamin G. Nolan, Yoshihiro Kobayashi, Susie M. Miller, Oren P. Anderson, and Steven H. Strauss. Relative lewis basicities of six $Al(ORF)_4^-$ superweak anions and the structures of $LiAlOCH(CF_3)_{24}$ and [1-Et-3-Me-1,3-$C_3H_3N_2$][$Li(Al(OCH(CF_3)_2)_4)_2$]. *Chemistry – A European Journal*, 7(2):503–510, 2001.

[248] Kurt F. Hoffmann, Anja Wiesner, Noah Subat, Simon Steinhauer, and Sebastian Riedel. Salts of the weakly coordinating anion $[Al(OTeF_5)_4]^-$ containing reactive counterions. *Zeitschrift für anorganische und allgemeine Chemie*, 644(21):1344–1348, 2018.

[249] Yimin Sun, Matthew V. Metz, Charlotte L. Stern, and Tobin J. Marks. Al-, nb-, and ta-based perfluoroaryloxide anions as cocatalysts for metallocene-mediated ziegler-natta olefin polymerization. *Organometallics*, 19(9):1625–1627, 2000.

[250] Allegra L. Liberman-Martin, Robert G. Bergman, and T. Don Tilley. Lewis acidity of bis(perfluorocatecholato)silane: Aldehyde hydrosilylation catalyzed by a neutral silicon compound. *Journal of the American Chemical Society*, 137(16):5328–5331, 2015.

[251] Casey R. Wade and Francois P. Gabbai. Fluoride anion chelation by a bidentate stibonium-borane lewis acid. *Organometallics*, 30(17):4479–4481, 2011.

[252] Tzu-Pin Lin, Ryan C. Nelson, Tianpin Wu, Jeffrey T. Miller, and Francois P. Gabbai. Lewis acid enhancement by juxtaposition with an onium ion: the case of a mercury stibonium complex. *Chemical Science*, 3(4):1128–1136, 2012.

[253] Christopher B. Caputo, Lindsay J. Hounjet, Roman Dobrovetsky, and Douglas W. Stephan. Lewis acidity of organofluorophosphonium salts: Hydrodefluorination by a saturated acceptor. *Science*, 341(6152):1374–1377, 2013.

[254] Walter Tötsch and Neil Bartlett. Antimonypentafluoroorthotellurates: $Sb(OTeF_5)_3$, $Sb(OTeF_5)_5$ and salts of $Sb(OTeF_5)_6^-$. *Journal of Fluorine Chemistry*, 21(1):32, 1982.

[255] D. Lentz and K. Seppelt. Otef5-verbindungen von p, as und sb. *Zeitschrift für anorganische und allgemeine Chemie*, 502(7):83–88, 1983.

[256] Helene P. A. Mercier, Jeremy C. P. Sanders, and Gary J. Schrobilgen. Hexakis(pentafluorooxotellurato)pnictate(V) Anions, $M(OTeF_5)_6^-$ (M = As, Sb, Bi): A series of very weakly coordinating anions. *Journal of the American Chemical Society*, 116(7):2921–2937, 1994.

[257] Hélène P. A. Mercier, Matthew D. Moran, Gary J. Schrobilgen, Christoph Steinberg, and Reijo J. Suontamo. The syntheses of carbocations by use of the noble-gas oxidant, $[XeOTeF_5][Sb(OTeF_5)_6]$: The syntheses and characterization of the CX_3^+ (X = Cl, Br, $OTeF_5$) and $CBr(OTeF_5)_2^+$ cations and theoretical studies of CX_3^+ and BX_3 (X = F, Cl, Br, I, $OTeF_5$). *Journal of the American Chemical Society*, 126(17):5533–5548, 2004.

[258] Hélène P. A. Mercier, Matthew D. Moran, Jeremy C. P. Sanders, Gary J. Schrobilgen, and R. J. Suontamo. Synthesis, structural characterization, and computational study of the strong oxidant salt $[XeOTeF_5][Sb(OTeF_5)_6]\cdot SO_2ClF$. *Inorganic Chemistry*, 44(1):49–60, 2005.

[259] Jérôme Lacour. Chiral hexacoordinated phosphates: From pioneering studies to modern uses in stereochemistry. *Comptes Rendus Chimie*, 13(8):985–997, 2010.

[260] Jerome Vachon, Gerald Bernardinelli, and Jerome Lacour. Resolution of the first nonracemic diquats. *Chemistry - A European Journal*, 16(9):2797–2805, 2010.

[261] Samuel Constant and Jerome Lacour. *New Trends in Hexacoordinated Phosphorus Chemistry*, pages 1–41. Springer Berlin Heidelberg, Berlin, Heidelberg, 2005.

[262] Ulrich Wietelmann, Werner Bonrath, Thomas Netscher, Heinrich Nöth, Jan-Christoph Panitz, and Margret Wohlfahrt-Mehrens. Tris(oxalato)phosphorus acid and its lithium salt. *Chemistry – A European Journal*, 10(10):2451–2458, 2004.

[263] Hong Xue, Rajendar Verma, and Jean'ne M. Shreeve. Review of ionic liquids with fluorine-containing anions. *Journal of Fluorine Chemistry*, 127(2):159–176, 2006.

[264] Khatera Hazin and Derek P. Gates. A twist on Hellwinkel's salt, $[P(2,2'\text{-biphenyl})_2]^+[P(2,2'\text{-biphenyl})_3]^-$. *Canadian Journal of Chemistry*, 96(6):526–533, 2018.

[265] Khatera Hazin, Brian O. Patrick, and Derek P. Gates. Ammonium and potassium salts of a hexacoordinate Phosphorus(V) anion featuring P–O and P–C bonds. *Inorganic Chemistry*, 58(1):188–198, 2019.

[266] N. V. Ignat'ev, U. Welz-Biermann, A. Kucheryna, G. Bissky, and H. Willner. New ionic liquids with tris(perfluoroalkyl)trifluorophosphate (FAP) anions. *Journal of Fluorine Chemistry*, 126(8):1150–1159, 2005.

[267] Hui Wang, Weizhou Wang, and Wei Jun Jin. σ-hole bond vs π-hole bond: A comparison based on halogen bond. *Chemical Reviews*, 116(9):5072–5104, 2016.

[268] I. Krossing. The facile preparation of weakly coordinating anions: Structure and characterisation of silverpolyfluoroalkoxyaluminates $AgAl(ORF)_4$, calculation of the alkoxide ion affinity. *Chemistry – A European Journal*, 7:490–502, 2001.

[269] Ingo Krossing and Ines Raabe. Relative stabilities of weakly coordinating anions: A computational study. *Chemistry – A European Journal*, 10(20):5017–5030, 2004.

[270] Lutz O Müller, Daniel Himmel, Julia Stauffer, Gunther Steinfeld, John Slattery, Gustavo Santiso-Quiñones, Volker Brecht, and Ingo Krossing. Simple access to the non-oxidizing lewis superacid PhF-$Al(ORF)_3$ ($RF=C(CF_3)_3$). *Angewandte Chemie International Edition*, 47(40):7659–7663, 2008.

[271] Karl O. Christe, David A. Dixon, Douglas McLemore, William W. Wilson, Jeffrey A. Sheehy, and Jerry A. Boatz. On a quantitative scale for lewis acidity and recent progress in polynitrogen chemistry. *Journal of Fluorine Chemistry*, 101(2):151–153, 2000.

[272] Michael A. Beckett, Gary C. Strickland, John R. Holland, and K. Sukumar Varma. A convenient n.m.r. method for the measurement of lewis acidity at boron centres: correlation of reaction rates of lewis acid initiated epoxide polymerizations with lewis acidity. *Polymer*, 37(20):4629–4631, 1996.

[273] Ulrich Mayer, Viktor Gutmann, and Wolfgang Gerger. The acceptor number — a quantitative empirical parameter for the electrophilic properties of solvents. *Monatshefte für Chemie / Chemical Monthly*, 106(6):1235–1257, 1975.

[274] S. Miertuš, E. Scrocco, and J. Tomasi. Electrostatic interaction of a solute with a continuum. a direct utilizaion of ab initio molecular potentials for the prevision of solvent effects. *Chemical Physics*, 55(1):117–129, 1981.

[275] Aleksandr V. Marenich, Christopher J. Cramer, and Donald G. Truhlar. Universal solvation model based on solute electron density and on a continuum model of the solvent defined by the bulk dielectric constant and atomic surface tensions. *The Journal of Physical Chemistry B*, 113(18):6378–6396, 2009.

[276] Robert G. Parr, László V. Szentpály, and Shubin Liu. Electrophilicity index. *Journal of the American Chemical Society*, 121(9):1922–1924, 1999.

[277] Pratim Kumar Chattaraj, Santanab Giri, and Soma Duley. Update 2 of: Electrophilicity index. *Chemical Reviews*, 111(2):PR43–PR75, 2011.

[278] Andrew R. Jupp, Timothy C. Johnstone, and Douglas W. Stephan. Improving the global electrophilicity index (GEI) as a measure of lewis acidity. *Inorganic Chemistry*, 57(23):14764–14771, 2018.